UNIVERSIDAD POLITÉCNICA DE MADRID
Escuela Técnica Superior de Ingenieros Industriales

Engineering design methodology for shape-morphing medical devices triggered by degradation

DOCTORAL THESIS

Submitted for the degree of Doctor by:

William Gabriel Solórzano Requejo
Bachelor's degree in Mechanical-Electrical Engineering
Master's degree in Mechanical Engineering

Madrid, 2025

UNIVERSIDAD POLITÉCNICA DE MADRID
Escuela Técnica Superior de Ingenieros Industriales

Doctoral Degree in Mechanical Engineering

Engineering design methodology for shape-morphing medical devices triggered by degradation

DOCTORAL THESIS

Submitted for the degree of Doctor by:

William Gabriel Solórzano Requejo
Bachelor's degree in Mechanical-Electrical Engineering
Master's degree in Mechanical Engineering

Under the supervision of:
Prof. Dr. Andrés Díaz Lantada
Full Professor Ph.D. in Mechanical Engineering

Madrid, 2025

Title: Engineering design methodology for shape-morphing medical devices triggered by degradation

Author: William Gabriel Solórzano Requejo

Doctoral Programme: Mechanical Engineering

Thesis Supervision:

Prof. Dr. Andrés Díaz Lantada

Full Professor, Ph.D. in Mechanical Engineering at UPM

External Reviewers:

Thesis Defense Committee:

Thesis Defense Date:

This PhD thesis has been funded by the European Union's Horizon Europe research and innovation programme under project number No 101047008 (BIOMET4D project: Smart 4D biodegradable metallic shape-shifting implants for dynamic tissue restoration), coordinated by Dr. Jennifer Patterson from IMDEA Materials Institute. BIOMET4D's project partners are acknowledged for inspiring comments, fruitful discussions and material-technological support for the technological validation of the thesis research.

A mi madre, que con sus manos me dio alas, y con su amor, el rumbo

Si puedes mantener en su lugar tu cabeza cuando todos a tu alrededor,

han perdido la suya y te culpan de ello.

Si crees en ti mismo cuando todo el mundo duda de ti,

pero también dejas lugar a sus dudas.

Si puedes esperar y no cansarte de la espera;

o si, siendo engañado, no respondes con engaños,

o si, siendo odiado, no te domina el odio

Y aun así no te las das de bueno ni de sabio.

Si puedes soñar y no hacer de los sueños tu amo;

Si puedes pensar y no hacer de tus pensamientos tu único objetivo;

Si puedes conocer al triunfo y la derrota,

y tratar de la misma manera a esos dos impostores.

Si puedes soportar oír toda la verdad que has dicho,

tergiversada por malhechores para engañar a los necios.

O ver cómo se destruye todo aquello por lo que has dado la vida,

y agacharte para reconstruirlo con herramientas maltrechas.

Si puedes amontonar todo lo que has ganado

y arriesgarlo todo en una sola jugada;

y perderlo, y empezar de nuevo desde el principio

y no decir ni una palabra sobre tu pérdida.

Si puedes forzar tu corazón y tus nervios y tus tendones,

para seguir adelante mucho después de haberlos perdido,

y resistir cuando no haya nada en ti

salvo la voluntad que te dice: "¡Resiste!"

Si puedes hablar a las masas y conservar tu virtud

o caminar junto a reyes, sin menospreciar por ello a la gente común.

Si ni amigos ni enemigos pueden herirte.

Si todos cuentan contigo, pero ninguno demasiado.

Si puedes llenar el inexorable minuto,

con sesenta segundos que valieron la pena recorrer...

Tuya es la Tierra y todo lo que hay en ella,

y, lo que es más: serás un hombre, hijo mío.

"If" – Rudyard Kipling

Acknowledgement

"Todo lo que soy o espero ser, se lo debo al ángel de mi madre"

Abraham Lincoln

Mi reina eres, sin duda, mi primer y mejor referente. Vuelvo con nostalgia a aquella infancia en la que me leías cuentos para dormir, me llevabas al colegio y repasabas a mi lado cada lección. Hacías que los viajes que contabas se convirtieran en horizontes posibles; asegurabas que un día viviría mis propias aventuras, y no te equivocaste.

Impulsado por tu fe en mí, dejé la comodidad de casa para saltar de un mundo a otro, aprender de los demás y encontrarme a mí mismo. No sé dónde habría acabado sin tu respaldo incondicional. Primero me diste la vida, luego tu amor y, por último, la libertad. Sé lo difícil que fue soltar mi mano, pero tu amor fue más grande y me permitiste equivocarme y, sobre todo, hacerme responsable de mis actos.

En esta etapa valoro aún más tu ejemplo, mientras yo jugaba, tú sacabas adelante tu tesis doctoral, conciliando capítulos de ciencia con meriendas y tareas escolares. Hoy comprendo los sacrificios que hiciste para ser una madre extraordinaria y, al mismo tiempo, una investigadora tenaz.

Gracias por estar siempre, por escucharme y aconsejarme, por esa rectitud que no admite medias tintas y por enseñarme que el trabajo bien hecho exige entregarse por completo. Aspiro cada día a reflejar tu cercanía sencilla y tu incansable afán de excelencia.

Te amo con todo mi corazón.

"Quizás te diga un día que dejé de quererte, aunque siga queriéndote más allá de la muerte; y acaso no comprendas, en esa despedida, que, aunque el amor nos une, nos separa la vida"

José Saramago

Bueno, papá. Aunque ya no estés en este plano, tú y yo seguimos teniendo un montón de conversaciones pendientes. Se que estás orgulloso de todo lo que he ido logrando; lo siento cada vez que doy un paso nuevo. Cuando me miro al espejo te veo entero, no solo los rasgos que compartimos, también en esa picardía que hacía reír a mamá, tu amabilidad y ese espíritu aventurero y despreocupado que te definía.

Nos quedaron tantas cosas por hacer… Me habría encantado contarte mis aventuras, sentarnos a hablar de ingeniería o ver juntos una corrida en Ventas. La vida se nos quedó corta, pero intento alargarla llevando tu voz conmigo.

Se que el gusto por escribir viene de ti; tenías esa facilidad para decir mucho con pocas palabras. Por eso esta tesis también es tuya. No es de ingeniería civil, como te habría gustado,

pero sí explora esa mecánica que tú llamabas más compleja e intrigante. Cada página late con tu curiosidad.

Te extraño, *tayta*. Gracias por todo lo que me dejaste y por empujarme todavía, desde donde estés.

"Tus acciones hablan tan fuerte que no puedo escuchar lo que dices"

Ralph Waldo Emerson

Desde que nuestros caminos se cruzaron, Andrés, agradecerte se ha vuelto el reto más grande. Ningún párrafo alcanza para condensar todo lo que has hecho por mí. Enseñas con hechos; tus silencios pesan más que cualquier discurso, y cada paso tuyo me deja una lección nueva.

Como el *beskar*, que se forja a golpe de fuego y martillo hasta volverse indestructible, así has templado mi carácter: con tu ejemplo firme, noble y resistente, recordándome que la verdadera fuerza nace de la integridad y del compromiso con los demás.

En nuestra rutina de trabajo, esa fortaleza toma forma de guitarra que nos pasamos sin hablarnos: cuando tú marcas el compás estratégico, yo armo los acordes tácticos; si improviso un solo, tú mantienes la armonía con la precisión de un metrónomo. De esa sinergia casi instintiva brota esta tesis doctoral, una melodía posible solo gracias a la confianza y al respeto mutuo.

Por todo lo que me has enseñado, aspiro a ser algún día tan buen ser humano, hijo, esposo, padre y maestro como tú, e impactar la vida de otros con la misma profundidad con que tú has marcado la mía. Sabes que me sobran ganas de estar ahí para lo que haga falta, lo digo de corazón.

Aun con todo, sé que esta gratitud es apenas el preludio, porque confío en que esto sea solo el comienzo de muchos proyectos que seguiremos construyendo mano a mano.

Gracias por todo Andrés.

"Solos podemos hacer poco; juntos podemos hacer mucho"

Helen Keller

Quiero agradecer a la División de Ingeniería de Máquinas, mi hogar académico desde 2021. Cada logro de esta tesis lleva impreso un trozo de la generosidad, la paciencia y el talento que comparten a diario. A Juanma, Javier y Enrique; sus lecciones durante el máster y sus consejos en el doctorado trazaron el rumbo de mi formación. Gracias por enseñar sin prisa, escuchar sin prejuicios y demostrar que la excelencia se cultiva en equipo. Soqui y Silvia, detrás de cada congreso hubo una coreografía logística que ustedes dirigieron con calma. Esos pre- y pos-viajes que a cualquiera habrían llevado al borde de la locura terminaron siendo experiencias gratificantes gracias a su temple. Pedro, sin ti, ni los prototipos ni el

banco de ensayos para la expansión de piel habrían pasado del papel a la realidad. Tu disposición para ayudar, sobre todo cuando el reloj apretaba, hace que este éxito también sea tuyo.

Javi, Gonzalo, Sonia, Adri y Álvaro; las charlas con café o cerveza, el queso manchego de las celebraciones improvisadas y las discusiones técnicas afinadas han dejado huella en más capítulos de los que imaginan. Muchas gracias.

Paco, fuiste mi primer amigo en la UPM y ha sido un verdadero lujo trabajar codo a codo contigo todos estos años. Confío en que seguiremos celebrando muchos éxitos, espero alguno de ellos por Perú. Adrián Martínez, tu pericia con nTop y las impresoras DLP convirtió en realidad la estructura de mimbre, y además me ayudaste con generosidad en el diseño de los bancos de ensayo para la craneosinostosis. Nuestra aventura en 3Dtive no solo marcó una etapa, sino que para mí simboliza lo que se puede lograr cuando la pasión y la curiosidad se ponen en común.

Carlos, admiro tu perseverancia y tu disposición para entregar siempre el máximo. Tus aportes con los expansores de piel y tu capacidad para aterrizar ideas han sido decisivos. Rodrigo, jefe y compañero de salsa, gracias por tomar las riendas cuando todo parecía difuso y por ser punto de apoyo cuando las ideas necesitaban suelo firme.

Mar, la DIM siempre será tu casa. Gracias por abrirme la puerta cuando llegué a Madrid en 2019, por enseñarme a domar *Origin* y por recordarme, y ahora yo intento recordárselo a mis propios tesistas, que mostrar lo aprendido es el primer paso para seguir aprendiendo.

A cada uno de ustedes, gracias por demostrarme cada día que la colaboración multiplica las posibilidades. Somos, sin duda, un gran equipo, y esta tesis es la prueba escrita de ello.

"El tesoro más grande de nuestro día reside en percibir cada paso, emoción y momento desde la hermosa gracia de un gracias vida mía"

Andy Assaël

Ha llegado el momento de abrazar con gratitud a quienes, contra viento y marea, permanecieron a mi lado cuando más los necesitaba.

Vanesa, mi etapa en IMDEA Materiales no habría sido la misma sin ti. Tu ayuda palpita en cada ensayo mecánico de esta tesis. Gracias por tu entrega sin reservas y por esa infinita paciencia que nos sostuvo cuando corríamos contra los plazos. Tienes un equipo maravilloso. Al *dream team;* José Luis, Mónica, Javier, Amalia, Miguel, Manuel, Sergio, Paco y Ter; mi gratitud por convertir el taller en un lugar tan acogedor. Entre cafés y tartas tejimos amistades y forjamos ideas que, confío, serán apenas el comienzo de muchos proyectos compartidos. Pedro, tu apoyo resultó decisivo para la caracterización biológica de los materiales. Incluso durante tu baja encontraste tiempo para revisar la parte biológica de la tesis. Gracias por esa generosidad que desborda los horarios, ojalá sigamos coleccionando aventuras juntos.

A Jon, Óscar, Muzi y Guillermo, vuestra labor en las primeras pruebas con metales fue clave. Jon, aquellas charlas en tu despacho iluminaron mis ideas; gracias por prestarme los equipos de IMDEA y escuchar mis planes, a veces auténticas locuras, con una sonrisa.

From the University of Galway, Ted and Conall, thank you for opening the doors of your team and making Galway a pivotal chapter in this journey. Conall, your finite element lessons beat on every page; we owe each other a pint of Guinness when the road brings us together again.

A Santiago del Hospital Gregorio Marañón, mi sincero agradecimiento. Sin tus imágenes médicas y tu guía, diseñar los actuadores para tratar la craneosinostosis habría sido imposible. Simon, from Meotec, thank you for every meeting in which you revealed to me the ins and outs of metal additive manufacturing and for your help with magnesium and zinc printing.

Álvaro, tus fotografías dignas de un estudio llenan este trabajo de belleza. Gracias por ese ojo milimétrico y, sobre todo, por aquel *Pad Thai* compartido cuando pensaba que todo estaba perdido. Llevar la aventura de 3Dtive contigo ha sido un auténtico privilegio.

A Rocío, que me guió con maestría durante la postulación al programa Erasmus Prácticas; sin ti, nunca lo habría conseguido. Y a Luis, por tus consejos certeros. Tus palabras me ayudaron a mirar mis problemas con madurez y a preguntarme si cada paso era realmente el adecuado.

"Tener un lugar al que ir es un hogar. Tener a alguien a quien amar es una familia. Tener ambas es una bendición"

Papa Francisco

Mi gratitud más entrañable es para mi familia, el motor y el sentido de este viaje. Nuestra reunión en Piura fue un chute de energía justo cuando la tesis amenazaba con agotarme. Su amor incondicional me recuerda, a cada paso, que lo esencial ocupa el centro de mi vida. Los quiero con todo el corazón y procuro honrar nuestros apellidos en cada logro.

Grecia, prima querida, llegaste a Madrid como un regalo inesperado; sin tu respaldo habría sido imposible culminar este trabajo. Has presenciado mis horas más oscuras, conoces cada obstáculo que hubo detrás de esta versión del manuscrito y, aun así, estuviste allí para sostenerme. Aprendo de tu perseverancia y de esas agallas que te llevan a abandonar la comodidad para lanzarte a lo incierto. Te mereces lo mejor, hoy y siempre.

Una mención especial para Nelly y Eric, mi familia escogida en Madrid. Nelly, gracias por tu intuición para descubrir mis desvelos, por tus consejos certeros y por esos potajes que, más de una vez, fueron auténtico consuelo. Eric, hermano menor, tu alegría es el pulso de

la casa. Recién comienzas tu camino y sé que te aguarda un futuro brillante; ánimo, seguiré con ilusión cada paso que des.

"La amistad es innecesaria, como la filosofía, como el arte… No tiene valor de supervivencia; sino que es una de esas cosas que le dan valor a la supervivencia"

C.S. Lewis

Carlos, mi primer maestro, gracias por embarcarte en cada locura que se me ocurre, por domar mis impulsos y darles rumbo. Esta travesía madrileña empezó porque confiaste en mí sin reservas y me apoyaste a capa y espada. Los proyectos que hemos compartido hoy se traducen en profesionales que sirven al Perú e impactan su entorno. Lo dijiste bien: conmigo tienes siempre un pie dondequiera que esté. Gracias, de corazón.

Alex, tartita, tu apoyo, sobre todo en la recta final de la tesis, fue decisivo. Siempre preguntabas si necesitaba algo, aun sabiendo que suelo resistirme a pedir ayuda. Gracias por hacerme uno más en tu grupo y por ser clave en mi regreso a Madrid. No lo dudes, tienes un corazón de oro y celebraré tus logros como propios. Jamás olvidaré aquella madrugada lluviosa en Atocha, cuando llegaste con los prototipos cual escena de James Cameron jaja. Que sigan los viajes y las anécdotas; donde yo vaya, tendrás un hogar esperándote. ¡Gracias por todo, causita!

Cristian, mi rolo de confianza, gracias por aguantarme todo este tiempo. Eres el amigo que cualquiera querría, siempre listo para ir por una cerveza y diluir las penas jeje. Más en serio, gracias por escucharme, por escribirme cuando me pierdo y por compartir alegrías y derrotas. Te mereces lo mejor.

Jesús, gracias por cada caña tras el trabajo, por las charlas profundas con patatas con pimentón y por aquella visita a Irlanda en la que trajiste, milagrosamente, una semana entera de sol. Aquí tienes un hermano peruano para lo que haga falta, sé que te aguarda un gran porvenir.

Daniel, gracias por aquellas escapadas improvisadas de sushi cada vez que pasabas por Madrid. También por abrirme las puertas de tu casa en Ciudad Real, guiándome entre sabores manchegos y noches de fiesta que todavía recuerdo con una sonrisa. Ojalá muy pronto pueda devolverte tanta hospitalidad y recibirte en mi país.

Evelyn, has sido mi apoyo desde el primer día. Más que nadie sabes lo duro que fue migrar y cómo, paso a paso, todo fue mejorando. Gracias por ser mi *coach* en la edición de videos, muchas de las imágenes de esta tesis llevan tu sello, y por ese viaje loco a Ámsterdam que aún tenemos pendiente. Siempre te lo he dicho, eres una crack.

Estephany y Alberto, no hay palabras para el cariño que les tengo. He sido testigo de su compromiso, de su boda y ahora del hermoso hogar que construyen juntos. Sus peques siempre contarán con el tío chisma. Los quiero, familia.

Fátima y Elías. Como dices, Fati, soy el punto medio entre ustedes: comparto contigo la estructura y también la locura y la pasión cervecera de Eli. Haber hablado en su boda fue un honor que guardo en el corazón. Los espero pronto en Perú para mostrarles sus maravillas.

Miguel, Daniela, Santiago, Jacobo y David; gracias por el buen ánimo y las conversaciones profundas, ojalá podamos reunirnos pronto para revivir los días locos del máster. David, Alejandro, Lara y Peio; aunque nos veamos a menudo, la amistad forjada en el aula sigue intacta, gracias por soportar mis manías de compañero pesado.

Blanca y Josué, siempre me rescatan cuando alguien llega a Madrid; su hospitalidad se refleja en los trabajos de Javier, Isabel e Isaac. Mil gracias, Blanca, por estar siempre pendiente. Marilucy, me tendiste la mano desde que pisé Madrid y así pude volver para hacer esta tesis. Gracias por tu hospitalidad; tu familia es entrañable y los espero en Tarapoto.

Carlos, Javi y Belén; amigos que me apropié. Gracias por su cariño, brindo por más cenas en el Duero y más viajes juntos. María y Lennin, verlos siempre es un placer; la amistad nacida en Piura sigue tan viva como el primer día. Son de lo mejor que me regaló la universidad.

Karla, Alexandra y Alonso; los mejores amigos que uno puede tener en Lima. Gracias por la hospitalidad y el cariño pese a la distancia. Nos vemos en breve para celebrar la boda de Ale y Alonso ¡vayan afinando el baile!

Querido Enrique, Kikin para los amigos, cómplice de mil locuras desde aquellos días en que tramitaba mi viaje a España. Tu constancia es un faro que me llena de orgullo, y llevo en el corazón la gratitud infinita hacia tu familia por la calidez y generosa hospitalidad con que me cobijaron. Tarapoto, Piura o Madrid serán siempre tu hogar, del mismo modo que tú y los tuyos son parte del mío. Ya celebraremos este logro con un buen chicharrón en el Chinito, nuestro lugar de confianza. Gracias por todo amigo.

Ana, Julio y Yazmín; su conexión con Perú me renueva. Ana, tu alegría por mis logros se multiplica ahora que tienes a un gran compañero a tu lado. Carolina, gracias por estar, desearme lo mejor y soportar mis altibajos. Eres maravillosa; pronto te veré volar alto y yo seré testigo de tus logros. Lamento mis torpezas y te agradezco la paciencia.

Keerthy, you were the best thing about 2024. We met at a bad time and shared our sorrows; it was short, but it changed everything. Now I will be your guide in Barcelona and hopefully make you fall in love with Madrid. Thank you for everything.

Jaqueline, Andrea y Miguel, los mejores embajadores de México. Gracias por esos tacos, por las lágrimas provocadas por el picante y por la amistad. Nos veremos pronto.

No podía dejar de agradecer a mis compañeros de CrossFit, en especial a Laura, mi entrenadora. Coincidir cada mañana en el box despejaba la mente y ponía el cuerpo en marcha antes de sentarme a escribir. Laura, tus correcciones de técnica y la dosis justa de

presión fueron el contrapeso perfecto a las horas de escritorio. Gracias por compartir disciplina, bromas y buena música.

A todos ustedes, gracias por demostrar que la amistad no es requisito para vivir, sino el milagro que convierte la vida en algo digno de ser celebrado.

“Nadie puede silbar una sinfonía. Se necesita una orquesta para tocarla”

Halford Luccock

Javier, Isabel, Diego, Víctor, Gabriel, Isaac, Stephen y Pepe, gracias por ser esa orquesta que da forma y volumen a mis melodías más disparatadas. Lo verdaderamente hermoso de lo que hemos creado es que lo hemos aprendido al unísono, yo de ustedes y ustedes de mí; compartiendo dudas, hallazgos y risas a partes iguales. Aceptaron mis ideas, en ocasiones sin pies ni cabeza, y las convirtieron en resultados que hablan de su talento y de su entrega. Me enorgullece ver hasta dónde han llegado y, sobre todo, imaginar todo lo que les queda por conquistar. Este pasaje no es el final, apenas es el primer movimiento de una sinfonía extraordinaria que todavía está por estrenarse.

“Lo que nada cuesta nada vale: y así lo que mucho vale, mucho es lo que nos ha de costar”

Luis de Granada

Esta sección final es, ante todo, una introspección. La tesis no ha sido un camino de rosas, sino una pendiente tan pronunciada que, por momentos, su cima desaparecía entre la niebla. Aún recuerdo el primer mecanismo que ensayé, visible en la Figura B.51, y el vértigo de comprender que lo realmente difícil no era conseguir que aquel artefacto cambiara de forma, sino aceptar que debía moldearme y vencer la angustia de idear cincuenta diseños.

En esta travesía, el aliento de cada uno de ustedes me sostuvo cuando las fuerzas flaqueaban; por eso, aunque la portada lleve mi nombre, cada página guarda la huella de quienes me acompañaron. Sí, este trabajo arrastra un leve matiz amargo: renuncias, desvelos, ausencias. Pero justamente ese sabor confirma la enseñanza de fray Luis: solo lo que cuesta de verdad acaba valiendo la pena.

Durante mi estancia en Madrid se ha fortalecido aún más el afecto y el orgullo que siento por el país que me vio nacer y formarme. Después de todo, quien ha concebido estos dispositivos es un ingeniero peruano, y ese guiño se deja ver en los actuadores de la librería, donde los tonos evocan los colores de mi bandera, recordatorio de que en esta tesis ningún detalle quedó al azar. Confieso, sin embargo, que gracias a ustedes considero a España mi segunda casa; me ha regalado tantas alegrías, me ha permitido crecer personal e intelectualmente y, sobre todo, nos ha posibilitado encontrarnos en este camino llamado vida.

Gracias por acompañarme, aligerar mis cargas y convertir este reto en algo valioso.

Abstract

This thesis focuses on the development and validation of a methodology for the design and fabrication of 4D printed degradable actuators, capable of transforming through selective material degradation. The idea is to apply this concept to medical devices that can evolve with the patient, allowing certain parts of the structure to degrade programmatically while others remain functional. This would reduce the need for additional surgery, minimize post-operative risks and improve patient experience.

The work is part of the European Commission-funded BIOMET4D project, which aims to develop a new generation of biodegradable implants with programmed activation for dynamic tissue repair. In this context, research has led to the development of resorbable actuators for reconstructive surgery, with specific applications in the treatment of craniosynostosis and skin expansion.

A multidisciplinary approach combining mechanical engineering, materials science, additive manufacturing, and biomedicine has been adopted to achieve these goals. One of the main advances of the thesis has been the development of an ontology and a universal coding system for 4D actuators, which allows the classification and description of morphodynamic structures in a standardized way. A library of degradable actuators has also been designed and manufactured using polymers such as polyvinyl alcohol (PVA) and polyethylene terephthalate modified with glycol (PETG). In addition, multi-material additive manufacturing has been implemented through fused filament printing technologies, enabling the creation of devices with controlled degradation.

Validation of these developments has required computational modelling to predict the mechanical response of the devices, complemented by mechanical and dissolution testing in the laboratory. As a result of these studies, functional medical applications have been developed, including bone expanders for craniosynostosis and tissue expanders for reconstructive surgery.

The research outcomes demonstrate that it is possible to design degradable and evolvable medical devices that can programmatically transform based on the time and conditions of the patient's biological environment. It has been experimentally validated that degradation can be used as an activation mechanism in 4D printing, opening up new possibilities for the development of smart implants, controlled drug delivery systems and temporary devices in reconstructive surgery.

Resumen

Esta tesis doctoral se centra en el desarrollo y validación de una metodología para diseñar y fabricar actuadores degradables impresos en 4D, capaces de transformarse mediante la degradación selectiva de materiales. La idea es aplicar este concepto a dispositivos médicos que puedan evolucionar con el paciente, permitiendo que ciertas partes de la estructura se desintegren de manera programada mientras otras continúan funcionales. Esto reduciría la necesidad de cirugías adicionales, minimizando riesgos postoperatorios y mejorando la experiencia del paciente.

El trabajo se desarrolla en el marco del proyecto BIOMET4D, financiado por la Comisión Europea, que busca crear una nueva generación de implantes biodegradables con activación programada para la restauración dinámica de tejidos. Dentro de este contexto, la investigación ha dado lugar al desarrollo de actuadores absorbibles para cirugía reconstructiva, con aplicaciones específicas en tratamientos para la craneosinostosis y expansión de piel.

Para alcanzar estos objetivos, se ha adoptado un enfoque multidisciplinario que combina ingeniería mecánica, ciencia de materiales, fabricación aditiva y biomedicina. Uno de los principales avances de la tesis ha sido el desarrollo de una ontología y un sistema de codificación universal para actuadores 4D, lo que permite clasificar y describir estructuras morfodinámicas de manera estandarizada. También se ha diseñado y fabricado una librería de actuadores degradables utilizando polímeros como el alcohol polivinílico (PVA) y el tereftalato de polietileno modificado con glicol (PETG). Además, se ha implementado la fabricación aditiva multimaterial a través de tecnologías de impresión con filamento fundido, lo que ha permitido crear dispositivos con degradación programada.

La validación de estos desarrollos ha requerido modelado computacional para predecir la respuesta mecánica de los dispositivos, complementadas con ensayos mecánicos y pruebas de disolución en laboratorio. Como resultado de estos estudios, se han desarrollado aplicaciones médicas funcionales, entre ellas expansores óseos para craneosinostosis y expansores tisulares para cirugía reconstructiva.

Los hallazgos de la investigación demuestran que es posible diseñar dispositivos médicos degradables y evolutivos que puedan transformarse de manera programada en función del tiempo y de las condiciones del entorno biológico del paciente. Se ha validado experimentalmente que la degradación puede utilizarse como un mecanismo de activación en impresión 4D, lo que abre nuevas posibilidades para el desarrollo de implantes inteligentes, sistemas de liberación controlada de fármacos y dispositivos temporales en cirugía reconstructiva.

Table of Contents

List of Figures

List of Tables

Abbreviations and Acronyms

AI	Artificial intelligence
AM	Additive manufacturing
AMT	Additive manufacturing technologies
AR	Augmented reality
CAD	Computer-aided design
CT	Computed tomography
CTF	Cell traction force
DBSCAN	Density-based spatial clustering of applications with noise
DfAM	Design for additive manufacturing
DIW	Direct ink writing
DO	Distraction osteogenesis
DOF	Degree of freedom
DOX	Doxorubicin
DP	Degree of polymerization
FEA	Finite element analysis
FEM	Finite element modelling/method
FFF	Fused filament fabrication
FGMs	Functionally graded materials
hMSC	Human mesenchymal stromal cells
ICP	Intracranial pressure
LCD	Liquid crystal display
LPBF	Laser powder bed fusion
MEMS	Micro-electromechanical systems
NEMS	Nano-electromechanical systems
PDE	Partial differential equations
PETG	Polyethylene terephthalate glycol-modified

PLA	Poly(lactic acid)
PVA	Poly(vinyl alcohol)
PVAc	Poly(vinyl acetate)
ROI	Region of interest
SAC	Spring-assisted cranioplasty
SE	Skin expanders
SMP	Shape memory polymer
UPM	Universidad Politécnica de Madrid

Symbols

T_{net}	Amount of net energy transferred across the system boundary	J
M	Bending moment	$N \cdot mm$
x	Body's displacement	m
C	Complementary strain energy	J
L_a	Conical spring length	mm
$\{u\}$	Continuous displacement fields	mm
h	Cross-sectional height of the serpentine spring	mm
w	Cross-sectional width of the serpentine spring	mm
$[C]$	Damping matrix	$N \cdot s/m$
δ_f	Deflection of the free coils	mm
δ_s	Deflection of the stacked coils	mm
d	Diameter of circular cross-section or side of square cross-section	mm
$\{d\}$	Discrete nodal displacement	mm
δ	Displacement/deflection	m/mm
ε	Elasticity resilience coefficient	-
T	Energy transferred across the system boundary	J
k_{eq}	Equivalent stiffness	N/mm
$\{F\}$	External force vector	N
F	Force or axial force	N
g	Gravitational acceleration	m/s^2
α	Inclination angle with respect to the horizontal of the straight bars of the	rad

	serpentine spring or angular ratio of conical spring spiral	
I_z	Inertia of the serpentine spring cross-section	mm^4
K	Kinetic energy	J
R_2	Larger radius of the conical spring	mm
l_2	Length of straight beams of serpentine spring unit cell	mm
$[M]$	Mass matrix	kg
E, E_0	Material's modulus of elasticity	MPa or GPa
F_C	Maximum force of the conical spring	N
$\delta_{geom,max}$	Maximum geometric deflection	mm
$E_{mechanical}$	Mechanical energy	J
L_C	Minimum length of the conical spring	mm
W_{net}	Net work	N
$\{D\}$	Node displacement vector	m
N_a	Number of active coils	-
n	Number of cells units that compose the serpentine spring	-
N_f	Number of free coils	-
N	Number of turns of the conical spring spiral	-
P	Potential energy	J
R	Radius of the curved beams that compose the serpentine spring unit cell or mean radius of helical coil	mm
ε_i	Residual strain	%
θ	Rotational displacement	rad
J	Second polar moment of area	mm^4
$[N]$	Shape function matrix	-
S_r	Shape recovery ratio	%

V	Shear force	N
G	Shear modulus	MPa or GPa
R_1	Smaller radius of the conical spring	mm
F_{spring}	Spring force	N
k	Spring rate, stiffness or constant	N/m
$[K]$	Stiffness matrix	N/m
U	Strain energy	J
z	System's height	m
m	System's mass	kg
v	System's velocity	m/s
t	Time	s, min or hours
E_{system}	Total energy of the system	N
ε_t	Trained strain	%
F_T	Transition force of the conical spring	N
L_T	Transition length of the conical spring	mm
l_1	Unit cell length of the serpentine spring	mm
W	Work	J
$W_{conservative}$	Work done by conservative forces	N
$W_{non-conservative}$	Work done by non-conservative forces	N

1. Introduction

1.1. Background

Four-dimensional (4D) printing introduces a temporal component to conventional 3D printing, enabling printed objects to autonomously modify their shape, properties, or functionality in response to environmental stimuli such as temperature, light, humidity, magnetic/electric fields, mechanical stress, (bio)degradation, among others [1]. While many existing 4D printed materials systems and structures employ external triggers (temperature, light, electromagnetic signals, environmental cues, pH…) to induce shape shifts, recent studies are increasingly highlighting biodegradability as a promising, though underexplored triggering mechanism [2–4]. Biodegradable materials can gradually resorb or dissolve in physiological settings, potentially eliminating the need for surgical removal and allowing implants or devices to self-transform over time.

A notable example is the work of Parkinson et al. [4], who developed a resorbable actuator that dissolves its structural "locks" over time, thus triggering a catapult-like mechanism. This approach illustrates the fundamental and quite innovative use of degradation to drive shape morphing, with significant implications for temporary medical devices, surgical release systems, or single-use devices that autonomously self-destruct without external intervention [3,5]. In contrast, most other degradable solutions employ heat, moisture, or magnetic fields as the principal actuation triggers, with degradation merely ensuring eventual resorption [6,7].

Beyond structural morphing, biodegradable polymers have gained traction in smart packaging and biomedical applications, where they respond to environmental stimuli in real time. Smart biodegradable films can include natural dyes or pH-sensitive compounds to monitor product freshness or precisely manage degradation rates [8]. Similarly, polymeric hydrogels with dual-stimulus responsiveness (pH and temperature) are being explored for targeted drug delivery, wherein local physiological conditions initiate both drug release and hydrogel degradation [9]. Such advances in (bio)degradation-based actuation are particularly attractive for scenarios requiring autonomy, bioresorbability, and delayed release, and future work may focus on tailoring degradation kinetics and material compositions to precisely control the timing and nature of structural changes.

Biodegradable 4D concepts hold significant promise for craniosynostosis treatment. Recent initiatives have integrated bioresorbable plates and screws into cranial fixation systems, improving surgical outcomes by aligning with natural bone healing processes and reducing interference with craniofacial growth. The eventual dissolution of these biodegradable devices diminishes the need for secondary removal surgery, a particularly valuable advantage in pediatric patients [10–13]. In parallel, superelastic alloys such as Nitinol, a family of Ni-Ti alloys with shape memory and superelastic properties depending on composition have revolutionized cranial remodeling by providing controlled, consistent expansion forces via springs [14]. These springs enable gradual skull reshaping, thereby optimizing outcomes in children requiring skull vault remodeling.

Additionally, 4D printing is also impacting soft-tissue expansion strategies. More recently, self-expanding tissue expanders triggered by osmosis have emerged, enabling continuous, autonomous enlargement without repeated clinic visits [15,16]. Incorporating biodegradable materials into these self-expanding systems could further streamline the process, with the expander remaining mechanically active only as long as necessary, then safely resorb, thus preventing additional procedures or complications.

The integration of advanced additive manufacturing technologies and biodegradable materials is rapidly reshaping the landscape of 4D printing in healthcare. Craniosynostosis interventions stand to benefit from bioresorbable fixation devices and controlled expansion mechanisms that adapt in tandem with a child’s natural growth, while soft-tissue expansion can leverage biodegradable 4D triggers for more comfortable, less invasive, and potentially autonomous procedures. As research continues to refine how and when biodegradable materials degrade, a new generation of intelligent, patient-centric medical devices will further transform surgical practice and postoperative care.

1.2. Motivation, objectives and outline

1.2.1. Motivation

Additive manufacturing technologies (AMTs) have reshaped product engineering in the last decades and completely transformed our engineering design approach. During the last two decades of the 20th Century and the early 2000s the main families of AMTs were conceived, developed and industrially established. These include, according to ASTM F2792 [17], vat photopolymerization, powder bed fusion, binder jetting, material jetting, sheet lamination, material extrusion and direct energy deposition, in many cases referred to as 3D printing technologies for generalization purposes. At the beginning, most of them were employed mainly for rapid prototyping tasks, linked to the manufacturing of conceptual models for screening and validation of ideas, for supporting interactions between designers and mass producers, for fostering communication between developers and end users, for analyzing aesthetics and ergonomics, for assembly analyses and for limited evaluation of devices, structures and materials’ performance, among others. Progressively, technologies improved in terms of printing speed, resolution, precision and processability of materials. The increasing portfolio of high-performance materials, including several families of alloys, ceramics and biomaterials, has importantly promoted a shift from mass production to massive customization and the application of AMTs to creating final products, not just as rapid prototyping technologies.

The additive processing of raw materials, usually based on layer-by-layer construction strategies, has enabled unprecedented geometrical complexity and promoted "solid freeform fabrication", which has proven very adequate for appliances and devices aimed at interacting with the complex geometries of the human body. Accordingly, the medical device industry and healthcare management has lived through important recent transformations, as a consequence of the manufacturing paradigm shift. Personalization and multi-functionality have been fostered in a wide set of medical devices, starting with biomimetic replicas for surgical training and planning, progressing with biomodels for supporting diagnostic tasks, advancing with surgical guides and appliances for enhanced surgeries, achieving personalized orthoses and prostheses, and even reaching biofabricated tissues and organs' portions to some extent. The final goal is the digital design and fabrication of bioinspired materials and devices, as perfect biomechanical, biochemical and biological matches of the patients' tissues and organs for optimal tissue engineering and regenerative medicine tasks.

In this transformative context, a fundamental feature of living tissues and biological structures, which is especially challenging to achieve, is dynamism. The term "4D printing" was coined in the mid-2010s, referring to the additive manufacturing of components capable of controlled geometrical transformations or metamorphoses, as a more market-oriented way of referring to the more classical 3D printing with "smart" or stimuli responsive materials. For healthcare purposes, the 4D printing of medical devices heralds a new generation of minimally invasive solutions capable of evolving with patients according to their healing and growth processes and, eventually, degrading once their mission has been fulfilled. However, degradation as triggering stimulus has been scarcely explored, despite its remarkable potential for shape-morphing medical devices. This will be the central topic of the PhD thesis, as further described in the following pages, while analyzing the context of the PhD thesis and its main scientifical and technological research objectives.

1.2.2. Context

In agreement with the presented motivation, the PhD has been carried out in the context of: 1) the PhD Programme in Mechanical Engineering at Universidad Politécnica de Madrid (UPM), 2) the Product Development Laboratory of the Machines Engineering Division at the ETSI Industriales of UPM, and 3) the "**BIOMET4D: Smart 4D BIOdegradable METallic Shape-shifting Implants for Dynamic Tissue Restoration**" funded by the European Union through the European Innovation Council (EIC) and the "EIC Pathfinder Open 2021 call" (grant agreement ID: 101047008).

Throughout this project, the research collaboration between UPM's Product Development Laboratory and the IMDEA Materials Institute has been consolidated, with Dr. Jennifer Patterson from IMDEA Materials Institute, as BIOMET4D principal researcher and coordinator; Prof. Dr. Jon Molina Aldareguia from IMDEA Materials Institute, as leader of fundamental characterization and testing tasks; and Prof. Dr. Andrés Díaz Lantada, as principal investigator of UPM within the project, in charge of design principles for shape-morphing metamaterials and PhD thesis director.

First of all, the PhD Program in Mechanical Engineering at Universidad Politécnica de Madrid has a research line focused on the frontiers between mechanical engineering and product development, in which the development of biomechanical and medical devices has been a key research topic for more than a decade.

Within the Mechanical Engineering Department at Universidad Politécnica de Madrid, the Machines Engineering Division has researched and lectured in these topics for more than 30 years. Starting with courses on biomechanics by professors Emilio Bautista, Pilar Lafont and Julio Muñoz, progressively the educational connections with biomedical engineering and medical technologies grew, in parallel to the establishment of the research lines of the Product Development Laboratory and the creation at UPM of bachelor's and master's degrees in biomedical engineering, mechanical engineering and industrial engineering adapted to the European Area of Higher Education. Different courses were implemented in these degrees by professors Lafont and Díaz Lantada, to which the rapid design and prototyping of medical devices was incorporated as a topic for project-based learning actions.

International collaboration and impact promotion in the field of medical devices and biomechanics has been a yardstick for the Product Development Laboratory. Among the most relevant and long-lasting collaborations in this field, it is necessary to highlight the Universidad de Piura and Prof. Dr. Carlos Ojeda, close collaborator of Prof. Dr. Andrés Díaz Lantada since the period of their PhD theses under the guidance of Prof. Dr. Pilar Lafont. For more than 15 years, the Biomechanics Laboratory at Universidad de Piura and the Product Development Laboratory of UPM have developed joint research tasks involving mobilities of researchers.

Along his Bachelor's and Master's Degree Theses, the candidate benefited from such collaboration and counted with different research mobility scholarships for researching in engineering design methodologies for medical devices, in the additive manufacturing of medical technology and in the biomechanical modeling of implants for bone replacement. During the 2019-2022 period, he contributed to the development of innovative medical devices, including short stem hip replacements for young patients, cardiovascular appliances based on shape-memory and superelastic alloys and hierarchically defined tissue engineering scaffolds, to cite a few, and contributed to reformulating the mentioned engineering design methodologies through the combined employment of computing-intense simulations, artificial intelligence algorithms and rapid prototyping.

This background led to a passion for engineering technologies for health, for promoting open innovation and science approaches in this challenging and socially impactful industry, and to the consequent application of the candidate for a research position within the European Commission-funded "**BIOMET4D**" project, which importantly contributed to framing the objectives of the PhD thesis.

As detailed below in the original project proposal:

"Reconstructive surgeries frequently require multiple, often complex, procedures at high social and economic costs. A shape-morphing implant that can be implanted using less invasive procedures and that then undergoes predesigned shape changes, leading to tissue expansion and allowing for complete degradation coupled with tissue regeneration, is a radically new treatment concept.

BIOMET4D aims to create a new generation of shape-shifting and load-bearing implants for dynamic tissue restoration and to introduce a revolutionary paradigm in how actuators can be implemented in biomedicine. Science-towards-technology breakthroughs will be demonstrated with new shape-morphing metamaterials, 4D smart metallic actuators, advanced multi-domain optimization tools, and finally proof-of-concept for two potential clinical applications. Technologically, this vision also goes beyond existing paradigms because of the step-by-step actuation mechanisms, enabled through the additive manufacturing of multi-material degradable metallic structures, that are targeted for an order of magnitude improvement compared to the state-of-the-art.

A futuristic long-term vision of this breakthrough technology is to dynamically regenerate entire tissues, such as a nose or an ear, and proof-of-concept will be demonstrated for craniosynostosis treatment and skin expansion. This long-term vision can only be achieved through an interdisciplinary approach and will likely have high social and economic impact as well as provide a new line of research for applications of smart metamaterials in medicine and engineering."

In addition:

"Shape-morphing materials that can be predesigned to change shape over time in response to specific cues such as a magnetic field are of great interest in healthcare and biomedical applications. Using such materials to fabricate implants means that they could exert a force on the surrounding tissue at a controlled rate and lead to tissue expansion.

The EIC-funded BIOMET4D project proposes to introduce actuators and novel metallic biodegradable materials towards a new generation of implants with dynamic tissue restoration properties. The BIOMET4D implants will find application in reconstructive surgeries for example of maxillofacial defects and in connection with aesthetic surgeries."

Within "**BIOMET4D**" the role of UPM is to investigate design for additive manufacturing (DfAM) methodologies for facilitating and leveraging the additive manufacturing of multi-material shape-morphing actuators for medical devices, in which the metamorphoses are triggered by degradation. While the final objective of the "**BIOMET4D**" project is to reach final applications based on multi-metallic additive manufacturing, enabling combinations of biodegradable Zn and Mg alloys, UPM explores a rapid prototyping route based on combinations of biodegradable polymers for concept screening and for systematizing 4D printing research.

Through DfAM strategies and the incorporation of mechanical metamaterials, UPM aims at enhancing the shape-morphing ability of multi-material printed components regardless of the raw materials employed. The concrete objectives of the PhD thesis derive from the presented context.

1.2.3. Objectives

Considering the challenging nature of additively manufacturing multi-material constructs for achieving shape-morphing smart actuators, with application to medical devices, capable of evolving with patients according to their healing and growth processes and enabling minimal invasion, this PhD thesis intends to provide innovative methods and solutions for obtaining such high-fidelity smart medical devices, made of combined polymers and eventually alloys with different degradation rates.

In consequence, the main objective of the PhD thesis is:

Investigate, develop and validate an engineering design methodology for leveraging the multi-material additive manufacturing of shape-morphing actuators and derived medical devices capable of experiencing multiple design-controlled metamorphoses, triggered by selective degradation, hence enabling progressive or stepped actuations.

To achieve the main goal of this PhD thesis, an additional set of specific objectives must be considered and methodically tackled, following the inspiring experiences of UPM Product Development Laboratory in the biomedical field, of IMDEA Materials Institute in high-performance metallic additive manufacturing and benefiting from the background of the candidate in engineering design and the application of additive manufacturing technologies:

1. Promote the systematization of 4D printing, especially as regards the incorporation of degradation as triggering stimulus, through the development of a universal ontology for additively manufactured smart materials systems and structures. Provide a user-friendly codification for such ontology, with application to the schematic description of actuators capable of undergoing through different shape transformations along their life cycle.

2. Demonstrate the usability of the mentioned ontology and codification, not only for descriptive purposes, but also for creativity promotion in the field of smart materials systems and structures. Analyze the synergic employment of ontology and codification with generative artificial intelligence algorithms to foster innovation and support conceptual design tasks in the 4D printing realm.
3. Create (design, simulate, prototype and characterize) the most comprehensive collection of 4D printable shape-morphing actuators triggered by degradation ever achieved, considering the mechanical and biological properties and degradation rates of the polymers employed.
4. Demonstrate through a rapid prototyping route, involving multi-material fused filament fabrication, the possibility of achieving design-controlled multi-stepped and progressive actuations triggered by degradation of different printable polymers. Analyze the transferability of generated knowledge to other combinations of biodegradable alloys for reaching a more versatile portfolio of usable materials and manufacturing technologies.
5. Apply lessons learned and technologies developed to the engineering of conceptual medical appliances, for which 4D printed solutions may constitute a technological breakthrough compared to the *statu quo* for the benefit of patients. Specifically, design and prototype solutions for bone distraction and skin expansion in connection with surgical interventions like craniosynostosis and aesthetic reconstructions after tumor resection.
6. Disseminate and communicate main advances of the PhD thesis and hence contribute to the creation of a worldwide community of researchers devoted to multi-material additive manufacturing and 4D printed medical devices.

Accordingly, the PhD thesis is structured as described in the following section.

1.2.4. Outline

The PhD thesis is structured as follows. Chapter 1 provides a brief introduction to the research topic, lists the thesis objectives, and presents its overall structure.

Chapter 2 describes the state of the art in three main sections. The first section discusses 4D printing, focusing on the triggering stimuli and applications in biomedical engineering. The second and third sections analyze the current status and technological developments in treatments for craniosynostosis and skin expansion, respectively.

Chapter 3 serves as the theoretical foundation of the thesis. It defines the energy methods used, describes the mechanics of serpentine and conical springs (which underpin most of the mechanisms developed in the library), offers a brief overview of the finite element method, and introduces degradable polymers, particularly focusing on PVA. The chapter concludes with basic concepts of artificial intelligence.

Chapter 4 details the global materials and methods employed along the doctoral research leading to the PhD thesis.

Chapters 5, 6, 7, and 8 present the technical work. Chapter 5 outlines the creation of an ontology that captures the various shape changes of a 4D actuator in a single line of code and explains how this coding scheme facilitates communication with a generative artificial intelligence to foster creativity. Chapter 6 provides the mechanical, biological, and degradation characterization of PETG and PVA, materials used to rapidly prototype diverse 4D actuators. Chapter 7 describes the development of a collection of mechanisms based on the characterized materials and an ontology-driven approach, enhancing creativity. These mechanisms undergo shape changes triggered by the degradation of one of their components. Finally, Chapter 8 applies selected concepts from the mechanism library to design medical devices for the treatment of craniosynostosis and for skin expansion, both of which require shape changes to either distract skull sutures or enlarge tissue, thus promoting new tissue growth through biological skin creep.

Lastly, Chapter 9 summarizes the conclusions of the PhD thesis, highlights its main scientific-technological contributions, and describes the future research directions that arise from its findings.

2. State of the art

2.1. 4D printing

2.1.1. Definition

4D printing extends beyond conventional 3D printing by incorporating time as a functional component. As a result, printed objects can undergo shape changes, property alterations, or functionality shifts over time, triggered by temperature, humidity, light, electric and magnetic fields, internal stresses, cell traction forces, or even (bio)degradation [1]. This dynamic behavior is derived from the use of stimuli-responsive smart materials, which react predictably to external or internal changes by undergoing physical, chemical, or biological modifications [18].

The concept of “4D printing” was coined by Skylar Tibbits in 2013, although several studies since the dawn of additive manufacturing had already dealt with the printing of shape-morphing materials and structures. He proposed creating printed structures capable of self-transformation, meaning they could autonomously reshape or adjust their properties based on predefined material responses [19,20]. A defining feature of 4D printing is thus its ability to generate self-assembling and self-actuating systems [1,21]. These structures can adapt *in situ* to specific environmental conditions, an aspect particularly valuable for applications that demand programmability, reparability, or shape-shifting capabilities.

Moreover, 4D printing is inherently interdisciplinary, bridging materials science, mechanical engineering, chemistry, biology, and computational design [22]. Through the strategic selection of responsive materials and careful design optimization, engineers can embed “shape memory” or other adaptive characteristics directly into printed parts. This synergy empowers a broad range of cutting-edge applications, from soft robotics to aerospace, consumer goods, and particularly biomedical engineering, where responsiveness is critical [21–23].

Another key development is the shift from single to multi-material approaches in 4D printing. Single-material systems rely on one type of stimuli-responsive polymer, alloy, ceramic, among others, for shape changes. By contrast, multi-material systems combine different materials elements, each tailored to respond to distinct triggers [24]. This versatility enables the design of complex, multifunctional devices that can react to multiple stimuli, either sequentially or simultaneously, broadening the scope of possible applications.

2.1.2. Triggering stimuli in 4D printing

A defining characteristic of 4D printing is the reliance on a chosen stimulus (or stimuli) to provoke shape changes or functional transformations in a printed structure. Stimuli-responsive materials "sense" these triggers, whether external or internal, and respond by folding, expanding, contracting, twisting, self-assembling, among others. Researchers typically group these triggers into external (temperature, humidity, magnetic/electric fields, degradation) and internal (cell traction, mechanical stress) categories. Across all stimuli-responsive systems, the ability to switch between "temporary" and "permanent" states remains a shared principle.

Crucially, multi-material 4D printing allows more than one trigger to be embedded in a single device. For instance, a biomedical implant might respond to both body temperature and shifts in local pH, thus optimizing its function and safety [9]. If a particular stimulus is slow, another can compensate for fine-tune shape changes, ensuring a robust overall response. The following section provides an overview of the primary stimuli investigated in 4D printing, followed by a dedicated focus on degradation as a particularly promising yet underexplored trigger.

Temperature as shape-morphing trigger

Temperature-sensitive materials, such as shape memory polymers or alloys, and certain hydrogels, constitute the most prevalent class of stimuli-responsive 4D printed materials [25]. Upon heating above a transition temperature (glass transition or melting point), these materials become malleable and can be shaped into "temporary" form, which is then set in place once cooled. Subsequent reheating restores the original (permanent) shape.

A classic example of this phenomenon can be found in the self-folding flower by Ge et al. [26], produced via microstereolithography on a methacrylate-based copolymer. At room temperature, the structure remained closed; once heated above 65°C, it "bloomed" (Figure 2.1A). In a medical context, Nizioł et al. [27] developed a thermoresponsive hydrogel dressing that collapses at physiological temperature (37°C), aiding wound closure and allowing localized delivery of antimicrobial agents. Although these temperature-induced transformations are highly versatile, the relatively low operating temperature range can constrain higher-temperature applications [28].

Moisture as shape-morphing trigger

Certain polymers and composites undergo shape morphing upon exposure to moisture or water through mechanisms like plasticization, hydrogen bond disruption, or swelling [29–31]. Hydrogels, for instance, have the capacity to absorb significant amounts of water, resulting in swelling and the exertion of mechanical forces that bend or fold the structure. In bilayer actuators, one layer may swell more than the other, resulting in predictable shape changes upon hydration [32].

Mulakkal et al. [33] demonstrated this approach using carboxymethyl cellulose-based hydrogel inks, which altered shape when submerged in water. Similarly, Zheng et al. [32] created bilayer films of poly(vinyl) alcohol and polydimethylsiloxane that wrinkled under moisture exposure, mimicking skin wrinkling after prolonged immersion (Figure 2.1B). Such responsive systems hold promise for tunable optical devices, smart windows, and soft robotic components.

Magnetism as shape-morphing trigger

By embedding magnetic nanoparticles within a polymer matrix, 4D-printed structures can respond to external magnetic fields [34]. This response can be attributed to two principal mechanisms: magnetic alignment, where nanoparticles orient along field lines and generate internal stresses that deform the host polymer; and magnetic heating, where an alternating magnetic field induces localized heat, activating shape memory [35,36].

Breger et al. [37] demonstrated magnetically responsive hydrogel micro-clamps containing Fe_2O_3 nanoparticles, which can open or close remotely, an approach suited for handling delicate tissues or controlling microfluidic flows (Figure 2.1C). Wei et al. [38] used direct ink writing (DIW) to fabricate PLA/Fe_3O_4 nanocomposite scaffolds that expand under an alternating magnetic field (~30 kHz), highlighting the potential for remote, on-demand actuation in biomedical devices.

Electricity as shape-morphing trigger

Electrical control of shape changes generally exploits Joule heating, dielectric polarization, or electroactive swelling. Joule heating raises the polymer temperature when current passes through it, triggering shape memory. In dielectric polarization, polar segments within the polymer align under an electric field, creating the mechanical stress necessary for actuation. Electroactive hydrogels undergo volume changes owing to ion migration and osmotic gradients under an applied voltage [39–41].

In a recent study, Han et al. [41] investigated electroactive hydrogel technology using 3D-printed acrylic acid (AA)-PEGDA actuators capable of bending when exposed to an electric field. They developed a soft robotic gripper and a walking robot, showcasing the remarkable potential of electrical signals in engineering sophisticated, controllable motions (Figure 2.1D).

Stress as shape-morphing trigger

Stress-induced shape transformation is a process that exploits pre-programmed residual stress within 4D-printed objects. Though the manipulation of stress distribution during or after printing, designers can engineer self-actuating, reconfigurable, load-bearing structures [42]. For instance, FFF naturally introduces residual strain as the extruded filament cools. When later activated (typically by heat), this strain is released, causing the structure to morph [43].

Multi-material designs can also embed layers with mismatched elastic properties, resulting in multilayer structures that bend, buckle, or twist under mechanical forces [42]. Ion gel-based structures printed via DIW demonstrate multidirectional shape-morphing upon stretching and release, attributable to their carefully engineered viscoelastic and plastic responses [42]. Furthermore, multistable constructs capable of switching between stable geometries once particular force thresholds are reached can be created by leveraging residual stress accumulation [44,45].

Cell traction force as shape-morphing trigger

Cell traction force (CTF) arises from cytoskeletal contraction and dynamic focal adhesions in living cells. In the context of 4D printing, cells adhere to and pull on a printed substrate, causing autonomous shape transformations over time [46]. As these processes do not require external input, they are of great interest for tissue engineering and bio-hybrid soft robotics [47,48]. However, CTF is relatively small and more difficult to control than physical or chemical stimuli, placing high demands on the material's biocompatibility and mechanical design [28].

One notable example involves embedding living cells in collagen-hyaluronic acid bioinks within granular support hydrogels. Over days to weeks, the printed constructs naturally contract, fold, or stretch as the cells exert traction forces on the surrounding matrix. This mirrors embryonic morphogenesis and highlights the potential of cell-driven shape transformations for next-generation tissue models (Figure 2.1E) [49].

Degradation as shape-morphing trigger

Degradation occupies a unique but underexplored space as a primary trigger for 4D printed shape changes, despite the widespread use of biodegradable polymers in clinical settings. Typically, these polymers (e.g., polylactic acid, polycaprolactone , poly(vinyl) alcohol) serve as bioresorbable scaffolds or drug carriers but do not actively reshape or confer mechanical transformations to surrounding tissues [50]. In contrast, a (bio)degradation-driven mechanism can autonomously alter a structure's form when exposed to physiological or aqueous environments, opening up new possibilities in medical implants, drug delivery, and tissue engineering [5].

Parkinson et al. [4] illustrated this concept with a resorbable system in which structural "locks" dissolved over time, triggering a catapult-like mechanism (Figure 2.1F). This design strategy could avoid the need for removal surgery by undergoing controlled transformations or "self-destruction" after fulfilling implant's function [5]. However, for most other biodegradable solutions, the focus remains on facilitating resorption once other stimuli (heat, magnetic fields, etc.) have driven the device's initial shape change. For instance, Grosjean et al. [6] employed water-induced swelling in self-rolling bilayer tubes, while Lin et al. [7] used Fe_3O_4 nanoparticles within a biodegradable PLA matrix to achieve magnetically mediated shape changes alongside gradual degradation. In broader applications, biodegradable materials have seen extensive use in "smart" packaging and drug delivery systems due to their inherent environmental reactive effects on surrounding tissues, and remain a frontier area in 4D printing research [8,51].

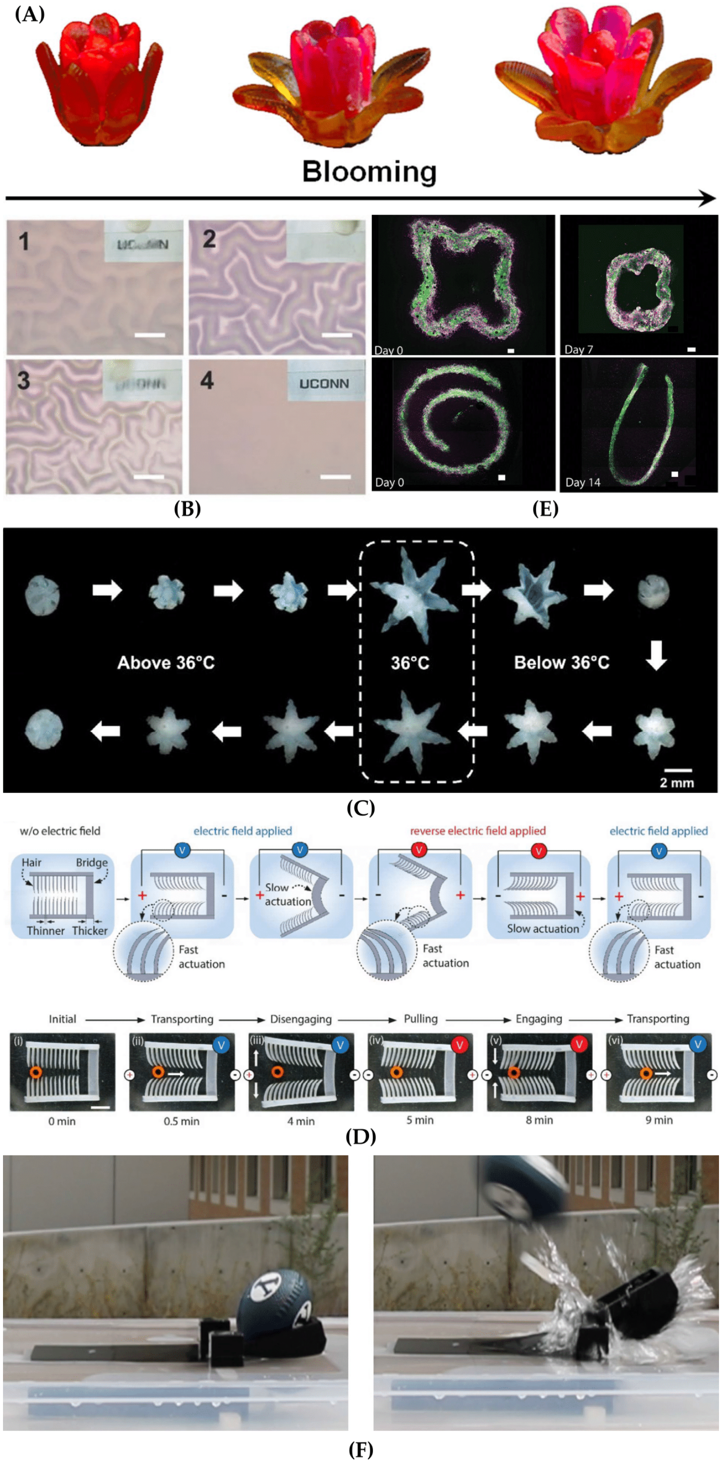

Figure 2.1: Examples of 4D printing activated by multiple stimuli. (A) Thermoresponsive multimaterial flower [26]. (B) Self-wrinkling surfaces revealing the "UCONN" logo [32]. (C) Reversible thermomagnetic gripper [37]. (D) Electrically actuated gripper [41]. (E) 4D bioprinting of shape-morphing tissues [49]. (F) Resorbable catapult-like actuator [4].

2.1.3. 4D printing in healthcare

Medical devices that can be implanted in one configuration and later morph inside the body demonstrate the transformative potential of 4D printing for healthcare. Such adaptability overcomes many of the limitations of static implants, which often fail to adapt to dynamic biological environments. As a result, 4D printed healthcare products including stents, drug delivery systems, and tissue scaffolds rely on various external or internal stimuli to achieve tailored shape changes [23,52].

Tracheal-bronchial stents exemplify how shape-morphing medical devices can enhance patient outcomes. Unlike conventional stents, which remain static under constantly changing airway dynamics, 4D-printed stents adapt in real time to respiratory motion, potentially reducing patient discomfort and minimizing secondary interventions [53]. To illustrate this, Zarek et al. [54] created a biodegradable polycaprolactone-based shape memory stent via stereolithography, which adjusted to the airway's microenvironment *in vivo* (Figure 2.2A). Similarly, Zhang et al. [55] incorporated Fe_3O_4 nanoparticles into PLA-based tracheal stents, using magnetic and UV triggers to facilitate remote shape transformation. In addition, Cabrera et al. [56] reinforced this approach with flexible thermoplastic copolyester elastomers in a FFF-printed heart valve stent. While the polyester component was bioabsorbable due to hydrolysable ester bonds, the device's primary shape transformation was thermally induced rather than solely driven by biodegradation.

Beyond tracheal applications, 4D printed implants also extend to orthopedics. Deployable meta-implants designed for vertebral compression fractures, for instance, utilize kirigami and origami-inspired architectures to expand minimally invasively and restore vertebral height without relying on bone cement [57,58]. Manufactured from PLA or aluminum, these implants can be folded flat for insertion and then self-expand to stabilize the spine (Figure 2.2B) [58].

In parallel, 4D printing has brought significant advances to drug delivery by enabling stimuli-responsive, biodegradable carriers. These include transdermal patches, orodispersible films, nanosuspensions, and injectable hydrogels [59–61]. Through external (e.g., temperature, magnetic fields) or internal triggers (e.g., pH), these systems can fine-tune drug release profiles to optimize therapeutic efficacy and reduce adverse effects [62–64]. In addition, the incorporation of biodegradable polymers allows these carriers to dissolve naturally after treatment, reducing the need for removal procedures [65].

Within this realm, pH-sensitive "smart" bandages equipped with embedded sensors detect infections and release antibiotics only when necessary, speeding up wound healing and reducing antimicrobial resistance [66]. Another notable development from Gupta et al. [67] is a 4D printed hydrogel capsule for on-demand drug release. The capsule features a biodegradable poly(lactic-co-glycolic acid) shell embedded with photo-responsive gold nanorods that rupture upon targeted laser stimulation to discharge anticancer agents precisely where they are needed. Similarly, Xin et al. [68] introduced shape-morphing microrobots composed of a pH-responsive biodegradable hydrogel encapsulating doxorubicin (DOX). These microfish-like devices navigate artificial vasculature and release DOX selectively in acidic tumor microenvironments (Figure 2.2C).

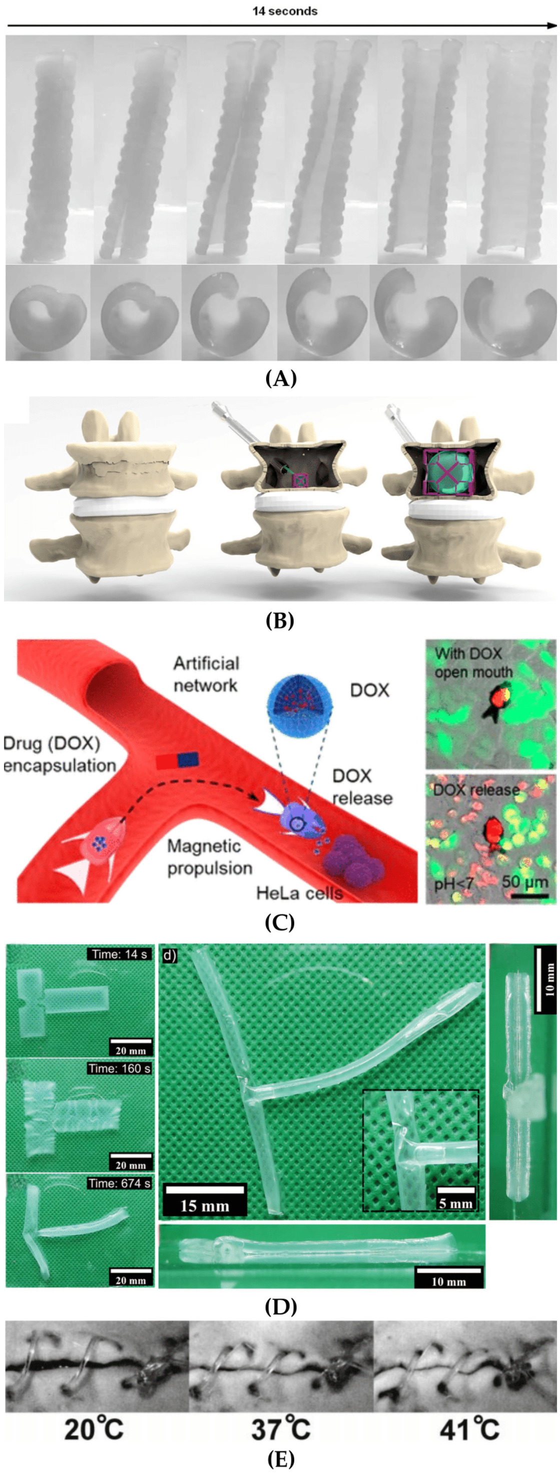

Figure 2.2: Examples of 4D medical devices for personalized treatments and smart drug delivery. (A) Personalized shape-memory airway stent [54]. (B) Deployable implants for vertebral fracture repair [58]. (C) pH-responsive microrobots for targeted DOX release [68]. (D) Self-folding 3D printed hydrogel structures [69]. (E) Degradable shape-memory suture for wound closure [70].

Additionally, 4D-printed tissue scaffolds that reshape over time can better emulate natural organ contours and facilitate tissue development. In vascular graft applications, planar hydrogel sheets have been programmed to self-fold into tubes as small as 20 µm in diameter upon hydration or temperature changes [69,71]. Advanced manufacturing processes even support branching (Y- and T-shaped) architectures, vital for replicating the hierarchical complexity of blood vessel networks (Figure 2.2D) [69].

Finally, outside of large-scale implants, biodegradable shape memory polymer (SMP) sutures have been designing to self-tighten at physiological temperatures, thereby improving wound closure and minimizing scarring (Figure 2.2E) [70]. When further integrated with biofunctional coatings or patterns, these sutures can promote targeted cell growth, enhance tissue healing and reduce the risk of infection.

2.2. Craniosynostosis

2.2.1. Fundamentals of craniofacial development and craniosynostosis

The development and growth of craniofacial structures is central to understanding craniosynostosis. The cranial sutures of the skull vault, which are fibrous joints, connect the bones of the skull and serve essential functions [72]. They not only coordinate the growth of the skull and brain, but also allow for small movements, act as shock absorbers, and function as growth centers that facilitate rapid brain expansion during infancy and early childhood [72,73].

Craniosynostosis, a major congenital craniofacial disorder affecting approximately 5 in 10,000 live births in Europe, occurs due to premature fusion of one or more cranial sutures [73]. This phenomenon can be explained by Virchow’s law, which states that cranial growth occurs perpendicular to open sutures and is restricted at fused sutures. This principle provides a theoretical basis for predicting cranial deformities based on the sutures affected and their impact on cranial morphology [72].

Craniosynostosis is primarily diagnosed by physical examination, with imaging techniques playing an important role in confirming the diagnosis and planning treatment [74]. Ultrasound, as a non-radiating tool, provides detailed visualization of suture fusion and allows classification of ultrastructural details [75]. Advanced imaging modalities, including magnetic resonance imaging and computed tomography, are particularly valuable for diagnosis, providing a comprehensive view of the condition before or after birth [76]. Accurate and early diagnosis is essential for timely referral and intervention to prevent complications associated with untreated craniosynostosis.

Cranial bone growth is driven by the interaction between osteogenic activity and mechanical forces generated by the developing brain, which reinforces the model of suture dynamics as a key determinant of cranial morphology under normal and pathological conditions [72,77]. As the brain grows, it exerts pressure on bony plates, promoting suture expansion and stimulating the generation of new bone through osteogenesis. This process depends on osteogenic fronts, composed of differentiating fibroblast-like cells, which play a crucial role in bone formation (see Figure 2.3) [78].

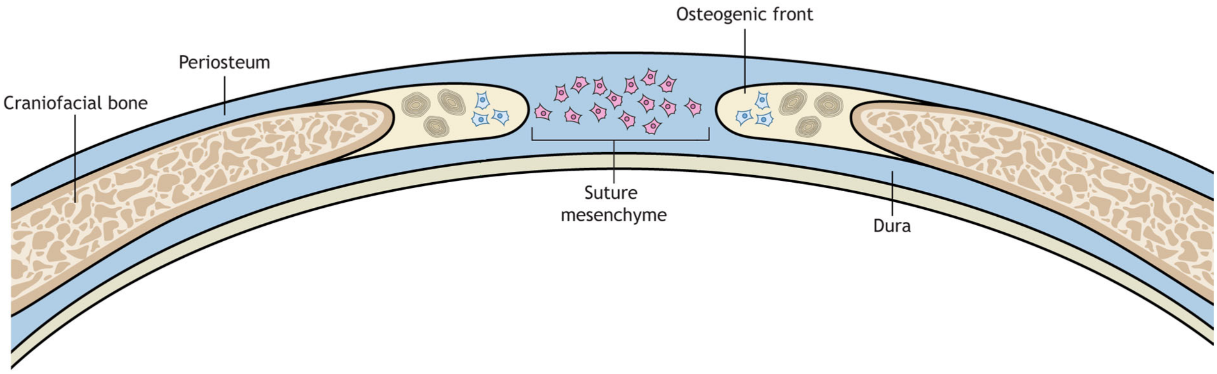

Figure 2.3: Suture development [77].

When this balance is disturbed in craniosynostosis, unfused sutures compensate for growth, which can lead to abnormal growth patterns, cranial deformities and functional alterations. This conceptual framework is fundamental to clinical assessments, which include head shape analysis, imaging studies and differentiation between craniosynostosis and positional plagiocephaly[1] [72,78].

Membranous bone formation is regulated by complex genetic processes. In craniosynostosis, common mechanisms include excessive osteoblastic activity and reduced osteoclastic activity, resulting in excessive bone growth and premature fusion at the cranial sutures. This phenomenon occurs at times when cell apoptosis[2] should have occurred to preserve the integrity of the sutures [82].

Craniosynostosis can occur in both *syndromic* and *non-syndromic* forms. The syndromic form, often associated with genetic syndromes, involves multiple sutures and is associated with systemic abnormalities, whereas the non-syndromic form is usually limited to isolated suture fusion without additional abnormalities [73,78]. Differentiating between these forms is critical for diagnosis, prognosis and treatment planning.

[1] Plagiocephaly, that results from extrinsic forces (rather than craniosynostosis), is defined as an abnormal shape of the skull that may persist or worsen over time, characterized by a parallelogram-shaped head with prominence in one quarter and flattening on the same side. It can be present at birth or develop after birth, often in association with abnormal uterine position or complications during labor [79,80].

[2] Apoptosis is the process of programmed cell death. It is used during early development to eliminate unwanted cell [81].

Syndromic craniosynostosis follows an autosomal dominant inheritance[3] pattern, accompanied by incomplete penetrance and variable expressivity, reflecting the genetic complexity of this condition. Understanding these differences is essential to investigate clinical trajectories and develop case-specific management strategies [78].

Defects in major sutures (metopic, sagittal, coronal and lambdoid) result in distinct clinical phenotypes that often require surgical intervention [77]. Studies on molecular pathways regulating suture fusion, such as upregulated osteoblastic activity, provide a basis for exploring therapeutic interventions and genetic predispositions [72].

2.2.2. Functional and neurocognitive implications

Craniosynostosis is associated with several functional complications that extend beyond cranial deformities, significantly affecting neurological, visual, and cognitive outcomes. This section discusses the mechanisms underlying these issues, their clinical manifestations, and broader implications for patient care and research.

One of the most critical complications is increased intracranial pressure (ICP), which arises from a mismatch between brain size and cranial vault volume. Elevated ICP manifests with symptoms such as headaches, irritability, and sleep difficulties, especially in severe cases, and has been linked to both syndromic and non-syndromic craniosynostosis. Premature fusion of sutures restricts cranial volume, compressing the growing brain and leading to elevated ICP, which contributes to neurocognitive deficits and visual impairments [73,77].

Visual disturbances are another critical issue, often resulting from mechanisms such as exorbitism, abnormal orbital development, and impaired vascular perfusion[4] to the retina. Exorbitism, caused by underdeveloped or abnormally shaped orbits, can lead to corneal exposure, keratitis[5], and even blindness if untreated, while developmental anomalies in orbital muscles contribute to ocular dysmotility[6], such as strabismus[7]. Elevated ICP further exacerbates these issues by reducing retinal perfusion, causing optic atrophy and visual loss. These complications, particularly common in syndromic cases, require early identification and intervention to prevent long-term morbidity [72,73].

Hydrocephalus is another potential complication, developing from increased venous pressure in the sagittal sinus caused by craniosynostosis. This disrupts venous outflow, leading to communicating or, less commonly, noncommunicating hydrocephalus. The interdependence

[3] Autosomal dominant is a way of passing genetic traits from a parent to their child. If a trait is autosomal dominant, only one parent needs to have a altered gene to pass it on. Half of the children of a parent with an autosomal trait will get that trait. Only changes in the DNA of the sperm or egg can be passed on from parent to child [83].
[4] Bathing an organ or tissue with a fluid [84].
[5] Keratitis is basically an inflammation of the cornea, which is the clear, dome-shaped tissue on the front of your eye that covers the pupil and iris. Keratitis can be linked to an infection, but it doesn't always have to be [85].
[6] Disorder presenting alterations in eye movements [86].
[7] This condition disrupts the normal alignment of the eyes, causing them to point in different directions [87].

between cranial sutures and intracranial fluid dynamics highlights the need for close monitoring in affected individuals [73].

Neurocognitive and neuropsychiatric disturbances in craniosynostosis range from mild behavioral issues to severe intellectual disabilities. ICP is a significant contributing factor; however, cases of single suture craniosynostosis often exhibit less pronounced impairments, which are more likely attributable to primary abnormalities in brain development rather than cranial restriction. In contrast, syndromic craniosynostosis involves more complex interactions between genetic mutations, brain malformations, and cranial constraints. Regardless of the cause, children with craniosynostosis have a higher prevalence of cognitive impairment than the general population, and the psychological discomfort associated with craniofacial deformities exacerbates these challenges [73,77].

The broader impact of craniosynostosis includes cosmetic deformities, which, while not directly affect physiological function, carry significant psychosocial implications. Advances in surgical interventions aim to correct these deformities while mitigating functional complications. Early surgical intervention has been associated with potential improvements in neurocognitive outcomes; however, genetic and developmental abnormalities are considered key factors in determining cognitive function [72].

2.2.3. Types of craniosynostosis

Craniosynostosis is categorized based on the specific cranial suture(s) affected, each presenting with distinct deformities (see Figure 2.4), incidences, and clinical features. Understanding these types is essential for accurate diagnosis and effective management. Below is a comprehensive summary of the major types of craniosynostosis, their associated characteristics, and treatment approaches.

Sagittal synostosis

Sagittal synostosis is the most common type of non-syndromic craniosynostosis, occurring in approximately 1 in 2,000 live births and accounting for 40% of all non-syndromic cases. It is more prevalent in males, with a male-to-female ratio of 4:1 [72,73]. The premature fusion of the sagittal suture results in an elongated, narrow skull, known as *scaphocephaly* or *dolichocephaly*. Characteristic features include frontal and occipital bossing, narrowing of the biparietal region, and a bullet-shaped occiput [78].

Treatment involves endoscopic linear craniectomy with postoperative helmet therapy for infants presenting early with mild to moderate deformities. For severe deformities or late presentation, open cranial vault remodeling is performed, often involving radial and wedge osteotomies to correct the narrow skull and prominent regions [73].

Metopic synostosis

Metopic synostosis, affecting the metopic suture, results in *trigonocephaly*, a triangular-shaped forehead with a pointed appearance and narrowed bitemporal region. It accounts for 10–20% of non-syndromic craniosynostosis, though recent studies report an increase to as much as 40% in some populations. It is more common in males, with a male-to-female ratio of 3:1 [72,73].

Surgical treatment typically involves open cranial vault remodeling with front-orbital advancement, performed between 6 to 9 months of age because it is thought that this age represents the optimal balance between bone malleability and reduced surgical risk. The aim is to expand the bitemporal region and advance the supraorbital bar, which in severe cases may be associated with hypotelorism[8] [73].

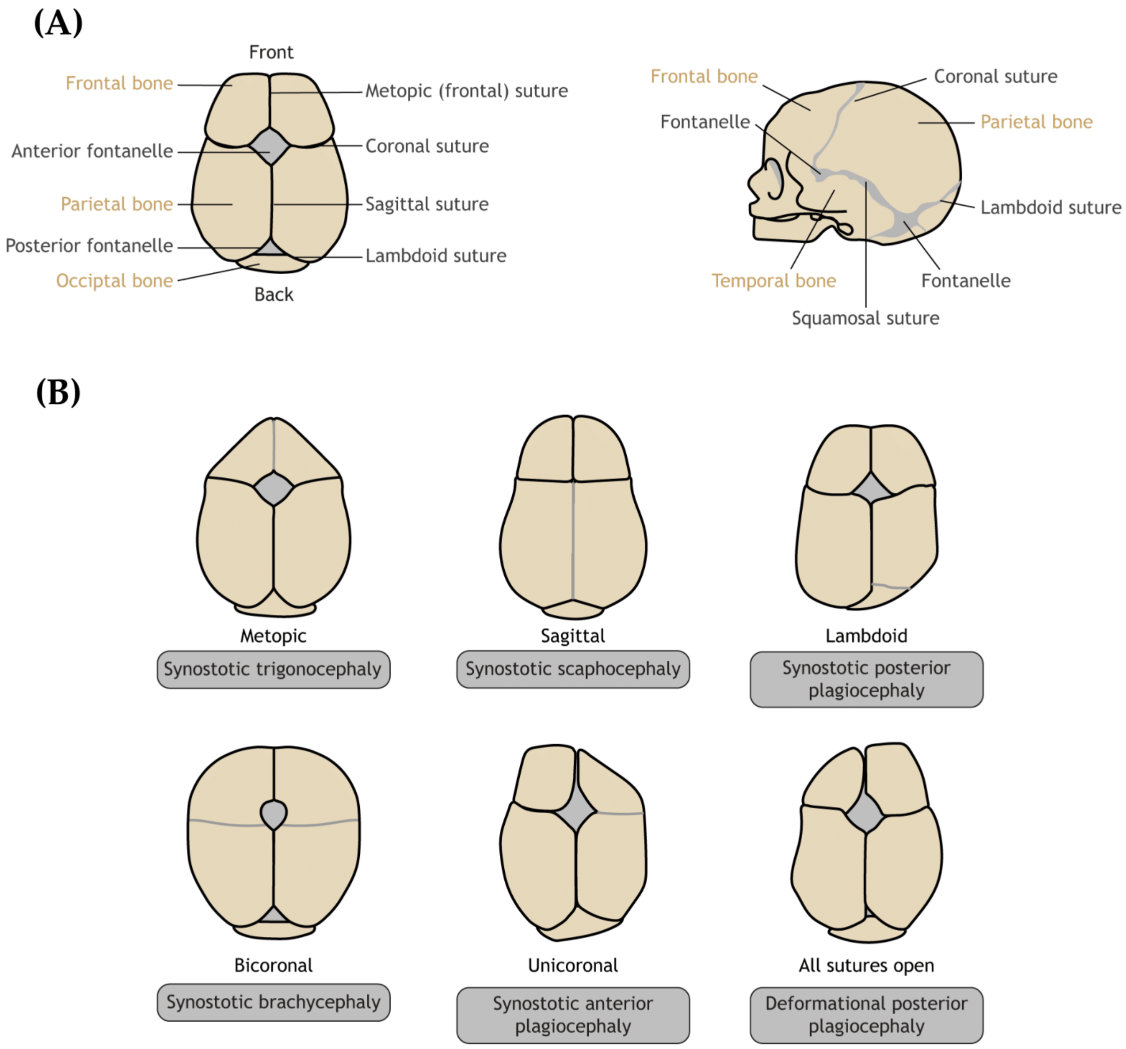

Figure 2.4: Cranial sutures and craniosynostosis in humans. (A) Normal infant skull anatomy and (B) skull deformities from different craniosynostosis types [77].

[8] Hypotelorism is when the eyes are abnormally close together, resulting in a reduced interocular diameter and binocular diameter [88].

Unicoronal synostosis

Unicoronal synostosis, occurring in 1 in 10,000 births, 20% of all non-syndromic cases, involves the premature fusion of one coronal suture [72,73]. It is more common in females (female-to-male ratio of 3:2) and results in *anterior plagiocephaly*, characterized by ipsilateral forehead flattening, elevation of the ipsilateral sphenoid wing, and contralateral displacement of the anterior fontanel. A hallmark feature is the Harlequin eye deformity, seen on frontal X-rays as an asymmetrical orbital roof resembling a masquerade mask [78].

Management includes open cranial vault remodeling with front-orbital advancement, ideally performed between 6 to 9 months of age. Surgery focuses on remodeling the affected forehead and advancing of the retraced supraorbital bar [73].

Bicoronal synostosis

Bicoronal synostosis affects both coronal sutures and results in *turribrachycephaly*, a short and wide skull with restricted anterior-posterior growth and compensatory temporal expansion. This type is often syndromic, with many cases linked to genetic mutations such as FGFR[9]-related syndromes. It occurs in 1 in 10,000 births with equal incidence in males and females [72,73].

Surgical treatment involves open cranial vault remodeling with front-orbital advancement and forehead vertical reduction, typically performed between 6 and 9 months of age [73].

Lambdoid synostosis

Lambdoid synostosis is rare, accounting for less than 3% of non-syndromic craniosynostosis, and is more common in males (male-to-female ratio of 2:1). The premature fusion of the lambdoid suture causes posterior *plagiocephaly*, with ipsilateral occipital flattening, mastoid elongation, and posterior displacement of the ear. Unlike deformational plagiocephaly, lambdoid synostosis involves asymmetry of the cranial base and inferior displacement of the ear [77,78]. Treatment involves open cranial vault remodeling at 6 to 9 months of age, focusing on expanding the affected posterior bone and restoring cranial symmetry [73].

2.2.4. Surgical techniques and complications

Craniosynostosis is a condition that requires surgical intervention to correct cranial deformities, restore normal cranial growth dynamics, and address functional complications such as increased ICP and neurocognitive deficits [73]. Surgical approaches have evolved

[9] FGFR stands for fibroblast growth factor receptor. FGFR helps cells to grow, survive and multiply. In certain cancers, such as some cases of bladder cancer, the gene that controls FGFR can change or mutate (known as FGFR alterations) [89].

significantly, integrating technological advances and minimally invasive techniques to improve outcomes while minimizing complications.

The decision-making process for surgical intervention in craniosynostosis is influenced by factors such as patient age, severity of deformity, type of craniosynostosis, presence of syndromic conditions and the child's overall health. Age is particularly important, younger patients (under six months) with single suture synostosis are often treated with minimally invasive techniques, such as endoscopic strip craniectomy with postoperative helmet therapy. These approaches use the natural growth of the brain to reshape the skull while avoiding the invasiveness of traditional procedures. In contrast, older children or those with complex or syndromic craniosynostosis typically require open cranial vault remodeling [72,73,78].

Depending on patient characteristics, surgeons can choose from minimally invasive techniques, open cranial vault remodeling or distraction osteogenesis. Each method has its own advantages and limitations, but all share the common goal of optimizing patient outcomes while minimizing risks. The selection of the appropriate surgical approach is tailored to ensure the best possible outcome for each individual case.

Among minimally invasive approaches, ***spring-assisted cranioplasty*** (SAC) has emerged as a transformative technique in the treatment of sagittal craniosynostosis, offering a less invasive but highly effective cranial remodeling approach. The procedure begins with a minimally invasive suturectomy, which removes the fused cranial sutures to allow the skull bones to move freely. Stainless steel springs are then implanted over the suturectomy site to apply a continuous outward force that gradually expands the cranial vault (Figure 2.6A). This process takes advantage of the natural growth and biomechanical properties of the infant's skull, allowing progressive reshaping over several months [90]. Once the desired cranial shape is achieved, the springs are removed in a straightforward secondary procedure, completing the treatment [90,91].

The biomechanical principles behind SAC are based on the unique properties of the infant skull, in particular its viscoelasticity and compliance. Infant cranial tissues are remarkably adaptable, allowing significant deformation under sustained mechanical force [92,93]. The collagen-rich cranial sutures stretch to accommodate this force, while the thinner and more flexible cranial bones contribute to the remodeling process [94]. The elasticity of the sutural junctions allows significant cranial expansion without the risk of trauma, making SAC most effective in infants under six months, when these properties are at their peak [90,91].

One of the major advantages of SAC is its minimally invasive nature, which reduces operative morbidity compared to traditional open cranial vault remodeling. The smaller incisions limited soft tissue dissection and shorter operative times associated with SAC result in less blood loss, reduced transfusion requirements and faster recovery [90]. In addition, the gradual remodeling process avoids abrupt volume changes that might otherwise stress the dura or soft tissues, allowing for more natural skull shapes. Long-term studies confirm the durability of SAC results, with sustained improvements in cephalic index[10] metrics [96,97].

The springs used in the SAC are carefully designed to provide consistent and controlled mechanical force. These omega-shaped springs are custom-bent by the surgeon to match the patient's cranial anatomy and reduce protrusion[11] (Figure 2.5A), securely anchored through burr holes and sometimes stabilized with absorbable sutures to prevent dislocation during the expansion process [92,93]. Initially, the springs exert a force of 7 to 12 N, which is carefully adjusted to the patient's specific cranial characteristics. Over time, this force decreases predictably, following an inverse exponential decay pattern [94,99].

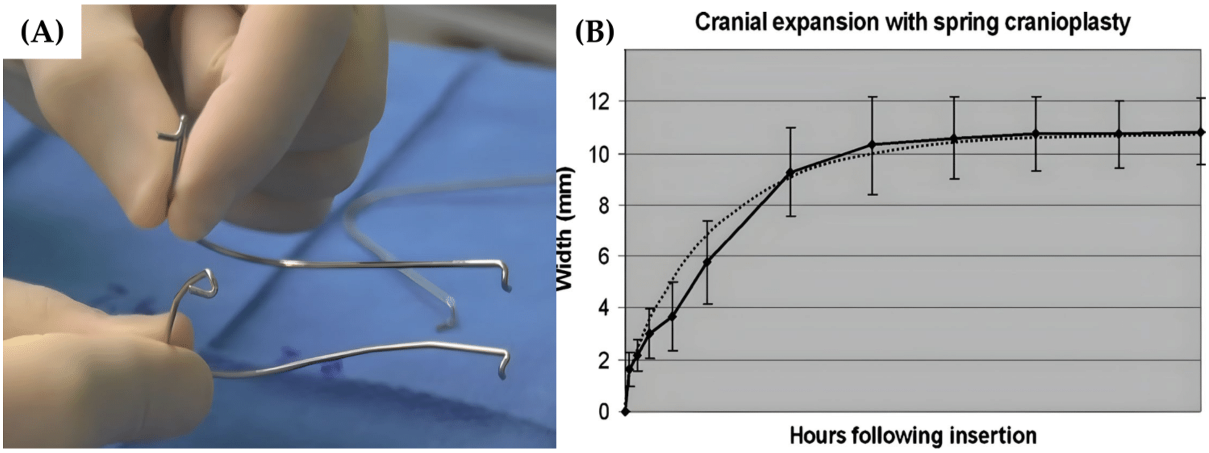

Figure 2.5: (A) Omega-shaped spring before and after being bent by the surgeon [100]. (B) Graph of spring expansion over time with dashed line indicating predicted expansion in a uniform mechanical environment [94].

The expansion dynamics of the springs progress in well-defined phases. Research [94] shows that significant skull expansion occurs immediately after spring insertion, with approximately 15% of the total expansion occurring within the first eight hours (see Figure 2.5B). This initial phase reflects the dissipation of force through the surrounding skull bone and suture complex until tissue resistance is equal to the applied spring force. By the second week, 80% of the expansion is complete and by the third week, 90% is achieved, after which the process plateaus. At the time of removal, a residual spring force of approximately 28% of the initial force is measured. This force ensures that the skull vault remains in its expanded configuration and clinical observations suggest that there is no immediate relapse when the spring is removed.

In particular, the expansion curve (Figure 2.5B) shows an unexpected slowdown between the second and fourth postoperative days, followed by a resumption of rapid expansion. This slowdown is thought to be due to structural changes within the suture, such as collagen fiber

[10] The cephalic index is a measurement used to classify the size of the skull, and the information needed to calculate it is the length and width of the skull [95].
[11] In medicine, a protrusion is something that sticks out or bulges [98].

failure, disinsertion of Sharpey fibers from the suture margins, or localized resorption of cranial bone under continuous compression [94]. These findings highlight the intricate biomechanical interactions between the springs and cranial tissues, and emphasize the precision and complexity required for successful application of this technique.

The success of SAC depends significantly on careful surgical planning and execution. Accurate spring selection and placement is critical to ensure symmetrical cranial expansion. Factors such as skull thickness, suture length and the severity of the cranial deformity guide the choice of spring design and placement. Advances in surgical planning tools, including 3D imaging and numerical simulation, have greatly improved the precision of these steps [101–104]. However, the inability to adjust the expansion process post-implantation further limits its versatility and can lead to under- or overcorrection if the initial spring selection or placement is suboptimal. Future innovations such as adjustable or self-regulating springs offer potential solutions to these limitations, improving outcomes and flexibility [91,105].

Despite its many advantages, SAC is not without challenges. The need for a secondary procedure to remove the springs increases the treatment burden, although this step is generally simple [90]. Additionally, SAC is most effective in early infancy, limiting its use in older children or those with delayed diagnosis. It is also less suitable for syndromic craniosynostosis or cases with multiple fused sutures, which often require more extensive interventions [90,91].

Alongside SAC, other minimally invasive techniques such as ***endoscopic strip craniectomy*** are frequently used. Endoscopic strip craniectomy involves the removal of the fused suture through small incisions, followed by postoperative helmet therapy to guide skull reshaping (Figure 2.6B). Like SAC, this approach is most effective in young infants and offers advantages such as reduced surgical trauma, shorter recovery times and excellent cosmetic results [72,73].

However, the success of helmet therapy depends on strict adherence, as it requires almost constant wear for several months, which can be a challenge for families [72,73]. It also requires frequent clinical visits for adjustment and replacement, with many patients requiring two to three helmets over the course of treatment to address skull growth [92].

Meanwhile, ***open cranial vault remodeling*** remains the gold standard for complex or severe cases, particularly syndromic craniosynostosis or when patients are diagnosed beyond infancy. This technique involves extensive remodeling and repositioning of the cranial bones to correct deformities and restore symmetry [72,73]. The procedure typically involves three steps: removal of the affected bones, remodeling of the bones to achieve the most appropriate shape for the patient, and precise placement and fixation of the remodeled bones (see Figure 2.6C) [106].

In sagittal synostosis, open remodeling focuses on widening the biparietal region and correcting the characteristic scaphocephalic deformity. In metopic or unicoronal synostosis, techniques such as front-orbital advancement are used to reshape the forehead and orbital region, effectively addressing trigonocephaly and anterior plagiocephaly, respectively [72,73]. Although open remodeling provides a comprehensive correction, it is associated with greater surgical trauma, longer recovery times and an increased risk of complications such as infection, bleeding and cerebrospinal fluid leakage. However, advances in 3D surgical planning and the use of bioabsorbable fixation materials have significantly improved the precision, safety and outcomes of this procedure [10,72].

Distraction osteogenesis (DO) is another innovative approach, particularly for syndromic or complex craniosynostosis requiring significant cranial volume expansion. It involves the creation of bone segments by precise osteotomies and their progressive separation using distraction devices (Figure 2.6D). These devices, consisting of screws, fixation pins and extension arms, allow incremental adjustments of 0.5-1 mm per day to stimulate osteogenesis at the distraction site, enabling customized cranial reshaping and increased intracranial volume [10,107,108]. DO is particularly beneficial in syndromic cases with elevated ICP, providing a gradual and controlled solution to severe deformities. However, challenges include prolonged treatment duration, the need for device removal, and potential mechanical complications such as hardware dislodgement, which require careful monitoring [108]. Despite these limitations, DO allows precise control of expansion vectors and rates, achieving significant volume gains with minimal disruption to the dura and surrounding tissues [10,108].

Each surgical technique, whether minimally invasive or traditional, plays an important role in the treatment of craniosynostosis. The chosen approach is influenced by patient-specific factors. SAC stands out as a particularly innovative and effective technique, combining the benefits of minimally invasive surgery with durable morphological results. While challenges remain, such as the need for secondary procedures and limited flexibility, ongoing advances in surgical technology and planning promise to further improve its efficacy. Together with complementary approaches such as endoscopic strip craniectomy, open cranial vault remodeling and distraction osteogenesis, they offer a comprehensive toolkit for optimizing outcomes in patients with craniosynostosis.

Despite advances, surgical treatment of craniosynostosis carries inherent risks. Complications include bleeding, infection, cerebrospinal fluid leakage and recurrent suture fusion. Syndromic cases in particular are prone to higher complication rates and often require multiple interventions. Persistent deformity, functional problems or ICP elevation may require repeat surgery, including monobloc procedures for significant midface retrusion and supraorbital deficiency in older children [72,78].

The risk of recurrence or regression remains a challenge, particularly in syndromic cases with underlying genetic factors. To address this, newer approaches, such as SAC and distraction techniques, aim to provide gradual and controlled cranial expansion to reduce the likelihood of re-fusion and relapse [10,90].

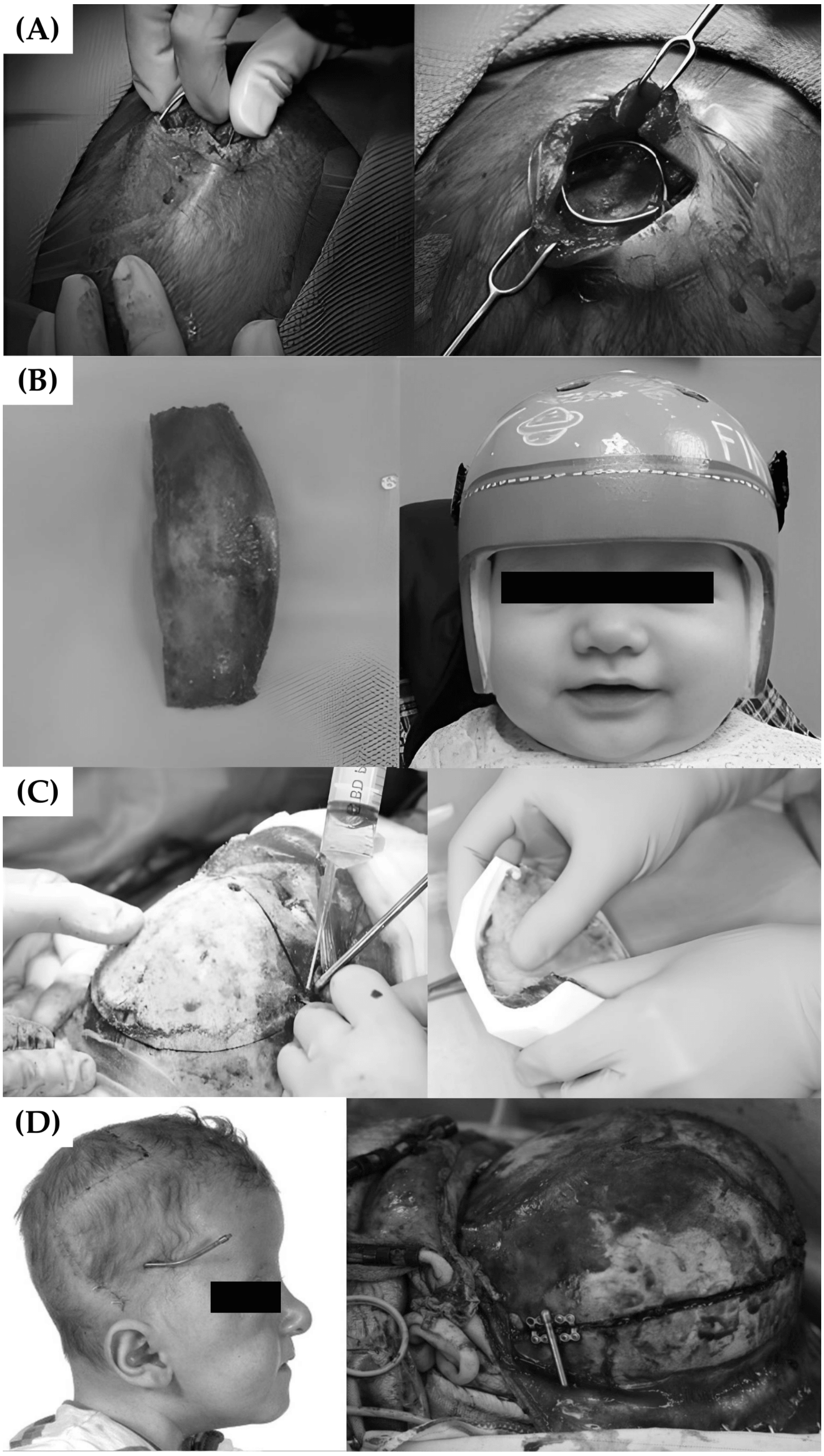

Figure 2.6: Surgical procedures for the treatment of craniosynostosis. (A) Spring-assisted cranioplasty [93]. (B) Endoscopic strip craniectomy [93]. (C) Open cranial vault remodeling [109]. (D) Distraction osteogenesis [110].

2.2.5. Innovations and challenges in craniosynostosis treatment

The integration of biodegradable materials, emerging technologies and innovative training tools is transforming the treatment of craniosynostosis. These advances are not only refining surgical procedures and post-operative outcomes but also rethinking how surgeons are trained, and procedures are planned. Among these developments, biodegradable fixation systems, such as bioresorbable plates and screws, play a central role by aligning with natural bone healing processes. These materials reduce the need for secondary removal surgery and minimize interference with craniofacial growth, offering clear advantages over traditional devices (Figure 2.7A) [10–13].

In addition to biodegradable materials, superelastic alloys such as Nitinol have provided a significant innovation in cranial expansion procedures. Nitinol has been used to create springs that facilitate controlled and gradual cranial remodeling. Studies investigating nitinol springs in the correction of craniosynostosis have highlighted their ability to deliver consistent and controlled forces, allowing effective cranial expansion in pediatric patients (Figure 2.7B) [14].

Building on these material innovations, advanced computing and simulation technologies have revolutionized surgical precision and training. Artificial intelligence (AI) facilitates personalized surgical planning, as exemplified by algorithms such as XGBoost that predict changes in cephalic index following SAC. These predictive capabilities streamline decision-making and enable tailored approaches to complex cases [101]. Complementing AI, augmented reality (AR) enhances intraoperative guidance by overlaying virtual models on the surgical field, allowing precise execution of osteotomies and fixation, particularly in syndromic or multisuture craniosynostosis (Figure 2.7C) [10,104].

To further improve preoperative planning and training, three-dimensional (3D) printing (Figure 2.7D) and mixed reality simulators (Figure 2.7E) have become invaluable tools. Patient-specific 3D printed models allow surgeons to visualize and simulate procedures, reducing intra-operative risks and improving outcomes. Meanwhile, mixed reality simulators provide immersive training environments where surgeons can practice different procedures. These simulators combine virtual and physical components to replicate realistic surgical scenarios, promoting both cognitive and psychomotor skill acquisition without patient risk. The utility of these models is underscored by studies demonstrating their effectiveness in improving technical proficiency and reducing surgical errors during neurosurgical training [111].

Finite element modelling (FEM) has become an important tool for optimizing surgical outcomes in SAC for sagittal craniosynostosis. By simulating the biomechanical and geometric factors that influence cranial expansion, FEM allows surgeons to analyze parameters such as cranial bone thickness, elastic modulus, spring stiffness and osteotomy size. This allows surgical procedures to be customized to each patient’s unique anatomy, improving precision and minimizing complications (Figure 2.7F) [102].

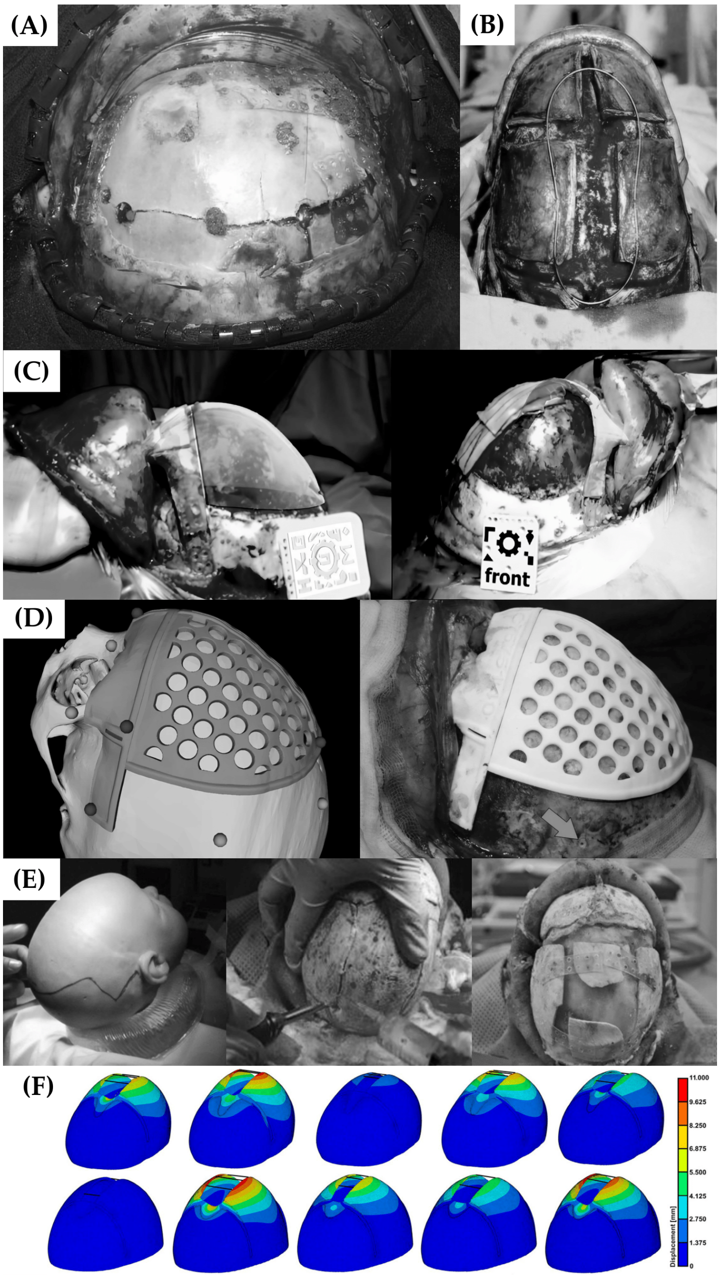

Figure 2.7: (A) Resorbable osteosynthesis plate employed in open skull remodeling [13] . (B) Superelastic nitinol spring in use [14]. (C) Augmented reality guiding intraoperative osteotomy [104]. (D) 3D printed surgical guides for osteotomy planning [103]. (E) Mixed reality simulator for open cranial vault surgery [111]. (F) Patient-specific finite element model of sagittal craniosynostosis [102].

Nevertheless, challenges remain to the large-scale adoption and validation of these advances. The high cost of AI, AR and simulation technologies, coupled with the need for specialized training, limits their accessibility, particularly in resource-constrained settings. Biodegradable materials, while promising, require further optimization to ensure consistent mechanical properties and predictable degradation rates. Moreover, FEM models require continuous refinement to improve their predictive accuracy and applicability in clinical settings.

In summary, the integration of materials science, AI, AR, 3D printing and simulation technologies has redefined craniosynostosis treatment and training. These advances improve precision, safety, and efficacy, and form a multidisciplinary approach that addresses both clinical and educational needs. However, addressing the challenges of accessibility, cost, and validation is essential to fully realize the potential of these innovations and ensure that they translate into improved outcomes for all patients.

2.3. Skin expansion

The skin, the largest mechanoreceptive interface of the human body, acts as a vital protective barrier, shielding muscles, bones, ligaments, and internal organs from chemical, biological, thermal, and mechanical environmental influences [112].

Structurally, it is a composite microstructural material composed of three distinct layers: the epidermis, dermis, and hypodermis (see Figure 2.8A). The epidermis, a 0.1-1 mm-thick, waterproof, outer layer, is primarily composed of keratinocytes[12], which constitute 95% of its cellular structure. Beneath the epidermis lies the dermis, a 1-4 mm-thick, load-bearing inner layer that is largely acellular and consists of 60% water. Its dry weight is primarily made up of loosely interwoven, wavy, and randomly oriented collagen fibers (80-85%), along with 2-4% elastin. Finally, the hypodermis, located below the dermis, is predominantly composed of adipose cells responsible for fat storage. While it plays a supportive role, the hypodermis is generally not classified as part of the skin tissue [114].

Skin expansion is a physiological process characterized by the ability of skin to increase its surface area in response to stress or deformation. This process is facilitated through the use of skin expanders. Due to the inherent properties of skin, stress decreases over time following an imposed deformation, enabling the formation of an additional flap of skin with the desired characteristics [115].

This method is strategically implemented near the area requiring skin reconstruction, ensuring that the expanded skin closely matches the original in terms of color, texture, sensation, and structure [115]. As a result, skin expansion emerges as an ideal strategy to generate skin that is consistent in appearance and function with surrounding healthy tissue, while minimizing scarring and the risk of rejection [116].

[12] Keratinocytes are the principal cells of the epidermis, the outermost layer of the skin, which produce keratin [113].

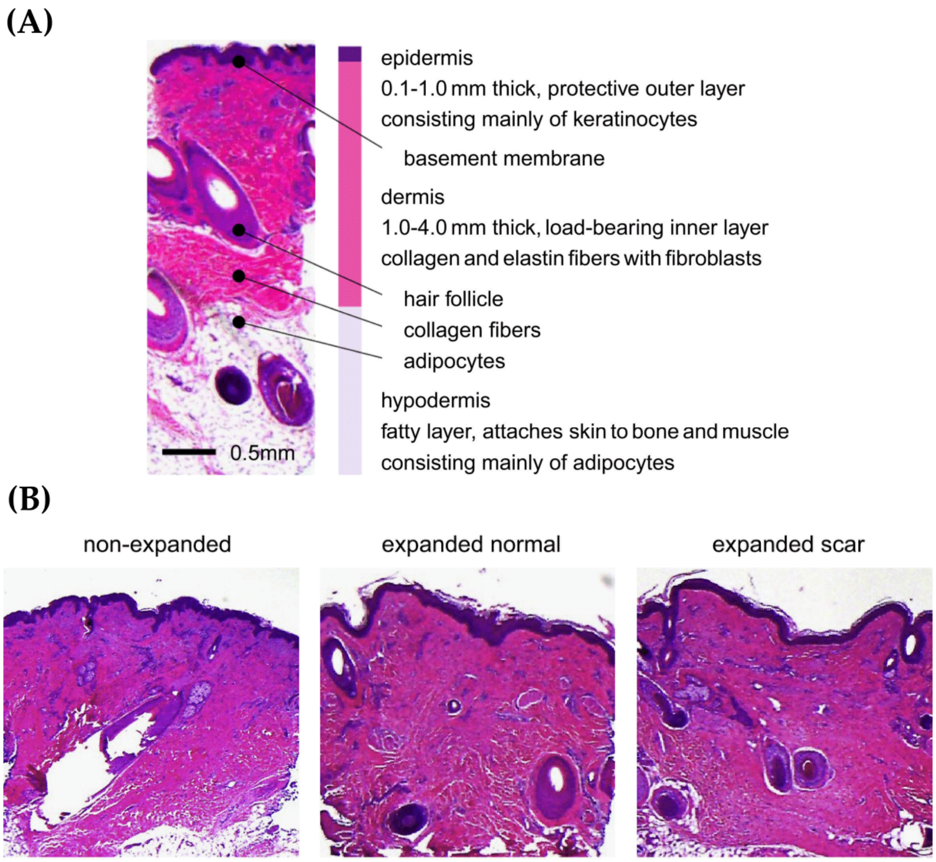

Figure 2.8: (A) Histological cross-section of human skin. (B) Comparative histological sections of non-expanded control, expanded normal skin, and expanded scar from pediatric scalp [112].

2.3.1. Biomechanical properties of skin

Human skin has complex biomechanical properties that are critical for skin expansion. Its viscoelasticity allows it to dynamically adapt to mechanical forces, providing the elasticity and plasticity necessary for controlled stretching and growth. Two key phenomena, creep and stress relaxation, facilitate this process. *Creep* involves the gradual stretching of the skin under a constant load, allowing progressive tissue elongation. *Stress relaxation*, on the other hand, describes the reduction in force required to maintain a fixed stretch as the tissue adapts to deformation [115,117,118].

The stress-strain behavior of the skin is characterized by three distinct phases, corresponding to its structural composition and its response to stress (see Figure 2.9). In the first phase, dominated by elastin fibers that provide elasticity, the skin stretches easily with minimal resistance. As a result, the collagen fibers, which provide tensile strength, begin to align and bear the load. In the second phase, the alignment of the collagen fibers leads to a high resistance to load, which makes the skin tissue behave like a stiffer material. Finally, in the third stage, excessive loading can lead to structural failure as the skin reaches its ultimate tensile strength [118–120].

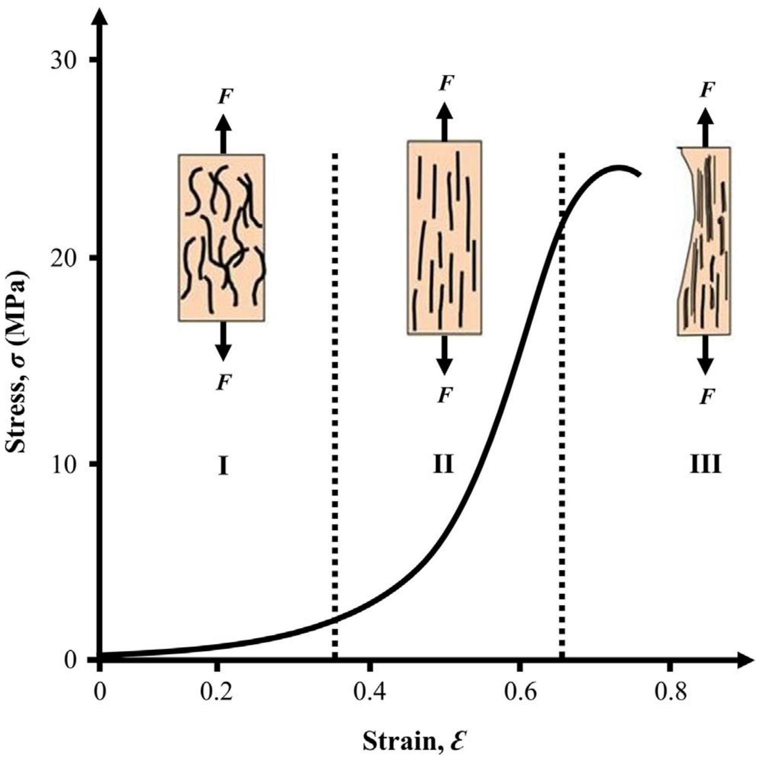

Figure 2.9: Stress-strain curve for skin tissue under uniaxial tension [118].

These properties are determined by the complex interplay of the skin's structural components, including collagen, elastin and ground substance. Collagen fibers, which are arranged in a crimped configuration at rest, straighten and align during stretching, providing resistance to deformation. Elastin fibers contribute to the skin's ability to return to its original shape after deformation, while ground substance facilitates movement and lubrication within the extracellular matrix[13] [118,119].

Skin is also anisotropic, with mechanical properties that vary depending on the direction of the applied force. Along Langer's lines, where collagen fibers are more aligned, stiffness is greater. These natural lines of tension are important for surgical planning and tissue expansion, as aligning procedures with them improves both functional and aesthetic outcomes [118,122].

The viscoelastic properties of skin, coupled with its anisotropic behavior, influences the design and use of tissue expanders. When an expander is inflated, the internal pressure stretches the skin, initially causing discomfort. Over time, viscoelastic relaxation reduces pressure, alleviating the pain. Within a week, the internal pressure is usually negligible (Figure 2.10B) [115].

[13] A large network of proteins and other molecules that surround, support and give structure to cells and tissues in the body. The extracellular matrix helps cells attach to and communicate with nearby cells and plays an important role in cell growth, movement and other cell functions. The extracellular matrix is also involved in the repair of damaged tissue. Abnormal changes in the extracellular matrix can lead to the development of certain diseases, such as cancer. The extracellular matrix of cancer cells can affect how they grow and spread [121].

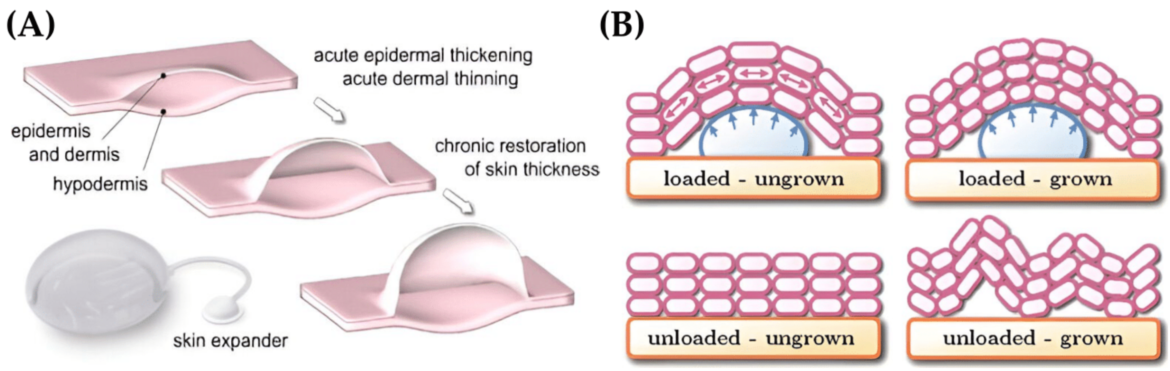

Figure 2.10: (A) Biomechanics of growing skin [116]. (B) Schematic of tissue expander inflation sequence [123].

Skin expansion involves reversible and irreversible deformations known as mechanical and biological creep. *Mechanical creep* occurs as collagen fibers stretch and may partially recoil when the expander is removed. *Biological creep* involves cellular activation and increase in tissue mass, resulting in permanent tissue growth [112]. Mechanical creep supports temporary elongation, whereas biological creep ensures permanent tissue generation, which is essential for effective expansion [124].

The thickness of the skin affects the biomechanical properties of skin. When comparing skin on the forehead with skin on the ventral forearm, forehead skin is thicker, stiffer, less tense, and less elastic. Older skin is typically thinner than younger skin because less collagen and ground substance are synthesized in the dermis [119].

2.3.2. Mechanobiology and histological changes in expanded skin

Tissue expansion uses the skin's innate ability to grow in response to mechanical stimuli through the process of mechanotransduction. This complex biological mechanism converts mechanical forces applied during stretching into biochemical signals that stimulate cellular and molecular activities leading to new tissue formation. Key components of mechanotransduction include the activation of stretch-sensitive ion channels, cytoskeletal rearrangements and the release of growth factors [112,116,123].

At cellular level, mechanical forces applied by skin (tissue) expanders initiate a cascade of events. Stretch-induced activation of ion channels in keratinocytes and fibroblasts[14] triggers intracellular signaling pathways that regulate cell proliferation, migration and extracellular matrix remodeling. The cytoskeleton, a dynamic network of actin filaments[15] and microtubules, plays a central role in sensing and responding to mechanical stress by

[14] A fibroblast is a type of cell that contributes to the formation of connective tissue, a fibrous cellular material that supports and connects other tissues or organs in the body. Fibroblasts secrete collagen proteins that help maintain the structural framework of tissues. They also play an important role in wound healing [125].

[15] Actin filaments are polar structures composed of globular actin molecules arranged in a helix [126]. Actin is a globular protein that has the unique ability to polymerize into filaments [127].

transmitting forces to the nucleus and activating gene expression related to growth and repair [116].

One of the most important outcomes of mechanotransduction is the increased synthesis of collagen and other extracellular matrix components by fibroblasts. These molecules contribute to the structural integrity and strength of the newly stretched skin. Furthermore, mechanical stretching promotes angiogenesis[16] to support the metabolic demands of growing tissue [116,123].

At the tissue level, mechanotransduction facilitates stress relaxation and restores homeostatic tension within the skin (Figure 2.10B). This balance is achieved through cycles of expansion, stretching, growth and relaxation [122]. Importantly, the skin's response to mechanical forces is not uniform across its layers. In the epidermis, keratinocyte mitosis is stimulated, resulting in increased surface area while maintaining normal thickness and histological architecture. Studies [112,116] suggest that the expanded epidermis does not show significant necrosis or inflammation, thus preserving its protective function and structural integrity.

In the dermis, fibroblast proliferation and increased collagen synthesis drive significant remodeling. Collagen fibers realign along the direction of mechanical stretch, increasing tensile strength and durability, allowing the stretched skin to withstand further mechanical forces [112,116]. Similarly, vascularization plays a critical role in tissue expansion. Mechanical stretching facilitates angiogenesis and the formation of new capillaries. This enhanced vascularization supports the metabolic demands of the tissue and ensures its viability throughout the expansion process [112].

The dermis also undergoes significant changes. Although initial expansion may thin this layer, long-term results generally show a return to baseline thickness [112,129]. In addition, expanded skin has viscoelastic properties comparable to native tissue, allowing it to adapt to external stresses without compromising its integrity. Moreover, the tensile strength of expanded skin is comparable to that of unexpanded skin, underscoring its suitability for reconstructive applications [112,116].

Experimental studies have shown that the biological response to mechanical stimuli depends on the magnitude, frequency and duration of the forces applied. Moderate and progressive stretching protocols are particularly more effective in stimulating cell proliferation and minimizing complications such as necrosis, in contrast to aggressive or rapid stretching [112,122].

Histological analysis shows that expanded skin closely resembles native tissue in terms of thickness, microstructure and mechanical properties (Figure 2.8). Expanded skin exhibits viscoelastic properties comparable to native tissue, enabling it to adapt to external stresses

[16] Angiogenesis is the growth of blood vessels from the existing vasculature [128].

without compromising its integrity. Studies confirm that the tensile strength of expanded skin is equivalent to that of unexpanded skin, reinforcing its suitability for reconstructive purposes [112,116]. Newly formed skin has aligned collagen fibers, increased fibroblast density and robust vascularization, ensuring its viability and functionality for reconstructive applications [112].

It is important to note that as skin is extended, such as with expanders or in other procedures that tighten the skin, the collagen fibers are also extended and cause stiffening in the skin, which results in it being more and more resistant to further stretching [115].

The integration of mechanotransduction principles into tissue expansion protocols has transformed the field of reconstructive surgery by harnessing the skin's natural growth potential. The histological and functional outcomes of tissue expansion highlight its efficacy as a reconstructive technique, as the expanded skin closely replicates native tissue. This ensures successful integration into surgical sites, solidifying tissue expansion as an indispensable procedure in modern reconstructive surgery [115].

2.3.3. Skin expanders

Skin expanders (SE) are essential medical devices in reconstructive surgery, designed to promote controlled skin growth through the application of prolonged mechanical tension. Their design has evolved significantly over the decades, from early models such as the rubber balloon used by Neumann in 1957 [130], to modern devices with biocompatible silicone shells, integrated or remote filling ports and specific geometries tailored to particular clinical needs. These advances have made it possible to address a wide range of skin defects and aesthetic reconstructions, optimizing both surgical outcomes and patient experience [117,122,131].

A typical SE consists of a bag made of refined silicone elastomer, a biocompatible, durable and flexible material. This cap acts as a structure containing the expansion medium, usually a saline solution. Inside is a one-way valve system that allows precise injection of the fluid without the risk of leakage. These valves, together with an integral or remote filling port, are critical elements in ensuring the device's functionality. Remote ports are connected to the expander via flexible tubing, allowing placement away from the expander site to reduce the risk of accidental puncture during inflation [117,131].

The geometry and texture of SE play a crucial role in their effectiveness [122]. Common shapes include circular, rectangular, cylindrical and crescent-shaped (croissant) expanders and are usually made in commonly required volumes from 50 to 1000 cc [120] (see Figure 2.11A). Circular expanders are ideal for creating a maximum increase in skin surface area, while rectangular and crescent-shaped ones are more suitable for linear or curvilinear defects. The choice of shape is closely related to the anatomical location of the defect and the orientation of Langer's lines [115,118].

The surface of the expander also has a significant effect on its performance. Expanders with smooth surfaces tend to have a lower risk of capsular contracture[17], but a higher probability of displacement. In contrast, textured expanders promote tissue attachment and reduce the risk of migration. Recent advances have introduced nanotextured surfaces that optimize the balance between adhesion and reduced foreign body reaction, thus improving reconstructive outcomes and minimizing complications [122,131].

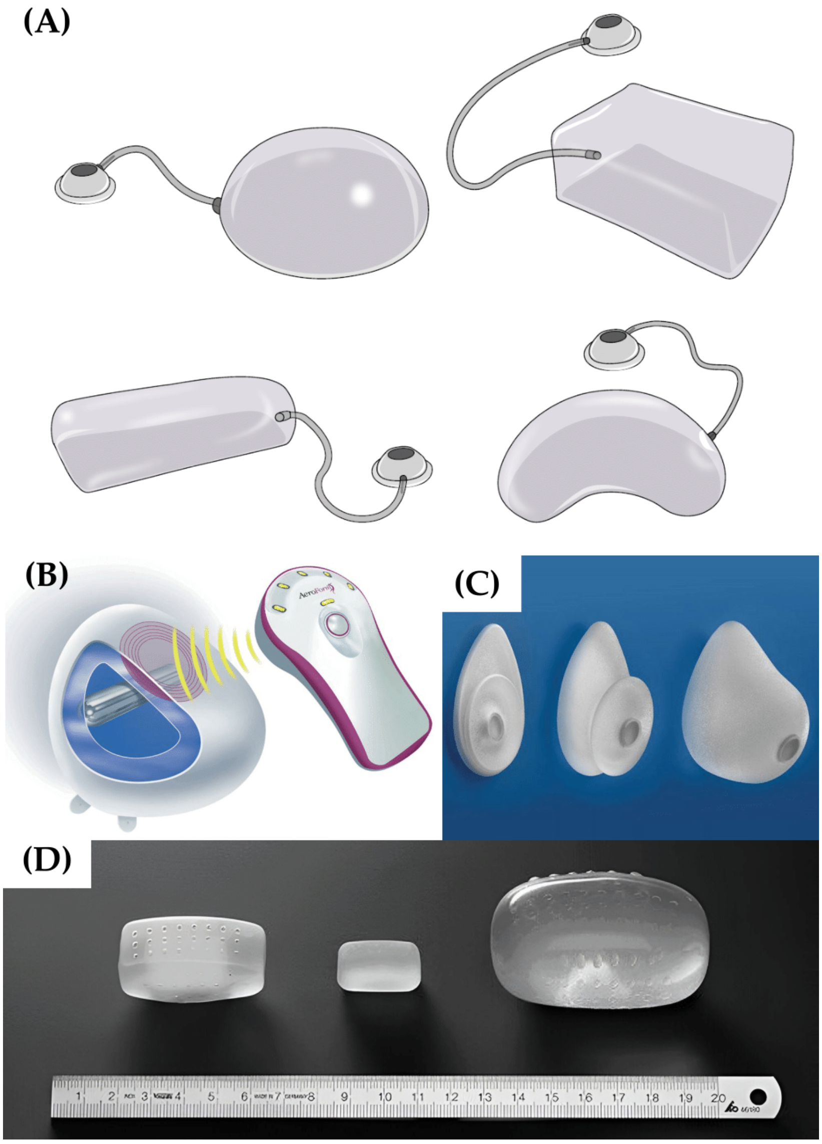

Figure 2.11: (A) Different shapes of skin expanders: circular, rectangular, cylindrical and crescent-shaped [132]. (B) AeroForm tissue expander design [133]. (C) Anatomical skin expander [134]. (D) Self-expanding expander activated by osmosis [135].

[17] Capsular contracture is a condition that can occur after breast reconstruction surgery with implants. It involves the formation of a capsule of fibrous tissue, which is a normal reaction of the body to protect itself against a foreign object such as the implant. Under normal conditions, this capsule is soft or slightly firm, is not noticeable, and helps to hold the implant in place. However, in some cases, this capsule becomes abnormally hard and dense, squeezing the implant excessively. This contraction and hardening of the capsule is called capsular contracture. It is a possible complication of surgery that can affect both the functionality and appearance of the implant [83].

In terms of expansion mechanism, traditional expanders use a saline solution that is gradually injected over several weeks. This process allows progressive stretching of the skin tissue and stimulates cell proliferation. More recently, carbon dioxide expanders have been developed, such as the *AeroForm* system (Figure 2.11B), which allows the patient to control the expansion via a remote device [136]. This method eliminates the need for frequent injections, although its availability and acceptance in clinical practice is still limited due to operational and regulatory concerns [131,137].

A critical aspect of SE design is the ability to adapt to the patient's needs and the defect being reconstructed. For example, differential expanders have regions of varying stiffness, allowing for more expansion in certain areas. On the other hand, anatomical expanders, designed specifically for breast reconstruction, mimic the natural proportions of the breast contour and provide aesthetically satisfactory results (see Figure 2.11C) [117,122].

Successful use of SE also depends on careful surgical planning. The choice of expander size, shape and volume must consider factors such as the size of the defect, the amount of donor tissue available and the elasticity of the surrounding skin [120]. Studies [138,139] have shown that rectangular expanders tend to provide the greatest increase in surface area, making them ideal for large defects. The phenomenon known as *tissue recoil* must also be taken into account when choosing an expander size, as the expanded skin may contract slightly after removal of the expander as a consequence of the mechanical creep [124,131].

In terms of innovation, modern expanders are equipped with dual-port systems that allow both expansion and aspiration of periprosthetic fluids, a feature that is particularly useful in the control of seroma[18] formation, a common complication [120]. In addition, the introduction of endoscopically placed expanders has allowed the use of smaller incisions in more discreet areas, thereby improving cosmetic outcomes [141,142]. However, this technique is associated with longer operative times, higher costs, and a requirement for specialized expertise [137]. Innovations in 4D self-expanding tissue expanders triggered by osmosis have further revolutionized the field, introducing the potential for autonomous and continuous expansion without the need for repeated clinical visits (Figure 2.11D). These devices simplify the expansion process, reduce patient discomfort and improve overall efficiency [15,16].

2.3.4. Surgical procedure and clinical applications

The surgical procedure to place an SE begins with meticulous pre-operative planning. The surgeon measures the length and width of the normal skin to determine the appropriate size and type of expander. It is recommended that the SE is placed under normal skin rather than scar tissue to reduce the risk of complications such as skin necrosis, SE exposure or extrusion.

[18] A mass or lump caused by a build-up of clear fluid in a tissue, organ or body cavity. It usually goes away on its own but may need to be drained with a needle. It often happens after breast surgery [140].

The incision is planned tangentially at the border between normal skin and scar. Typically, an incision length equal to half the SE length is sufficient to create the pocket [137].

Once the incision is made, the SE is temporarily inserted to ensure that the pocket is the correct size. The SE is then removed and disinfected. A tunnel is then created to position the port, ensuring that it is at least five centimeters away from the SE site. This eliminates the need for a second incision to place the port [137]. The SE is reinserted between the dermis and hypodermis, taking care to position all tubes and drains underneath [116].

The SE is deflated and connected to the port with a secure connector. The system is tested with a small saline injection to confirm that it is watertight and properly secured. The incision is then closed, and a vacuum drain is connected and activated to assist with fluid removal. Post-operatively, the wound is allowed to heal for three weeks before saline injections into the SE are started. This three-week period corresponds to the weakest phase of wound healing. Weekly injections are given for approximately four to six months until the desired tissue expansion is achieved [137].

During the second operation, the SE is removed through the same incision. The type of flap to be used is planned during the first operation based on the location of the scar, the availability of normal tissue and its flexibility. This detailed and methodical approach helps to ensure a successful outcome with minimal complications [137].

SE have become indispensable tools in reconstructive surgery for a wide range of conditions including birth defects, burn injuries, alopecia and post-mastectomy breast reconstruction [115,122]. The ability to grow skin that matches the color, texture and characteristics of the surrounding area offers unique advantages in achieving functional and aesthetic results. The skin created by tissue expansion can be used as a flap or, in some cases, as a skin graft for other parts of the body [137]. Consequently, the use of tissue expanders seems to be limited only by imagination [117]. Some examples of their use are as follows:

- Breast reconstruction: tissue expanders are widely used in post-mastectomy reconstruction. Advances in expander design, such as anatomically shaped devices and dual-port systems, have improved outcomes by reducing complications like capsular contracture and enhancing the final breast contour (Figure 2.12A) [131].
- Pediatric applications: while the use of tissue expanders in children has been controversial due to concerns about trauma and complications, studies have demonstrated their safety and efficacy in carefully selected cases. The unique properties of pediatric skin, including its greater elasticity and regenerative capacity, often lead to excellent results (Figure 2.12B) [117,122].
- Facial and scalp reconstruction: the versatility of expanders makes them invaluable in reconstructing complex areas such as the face and scalp. For example, crescent-shaped

expanders are often used for curvilinear defects, allowing for precise restoration of hair-bearing regions with minimal scarring (Figure 2.12C) [124].

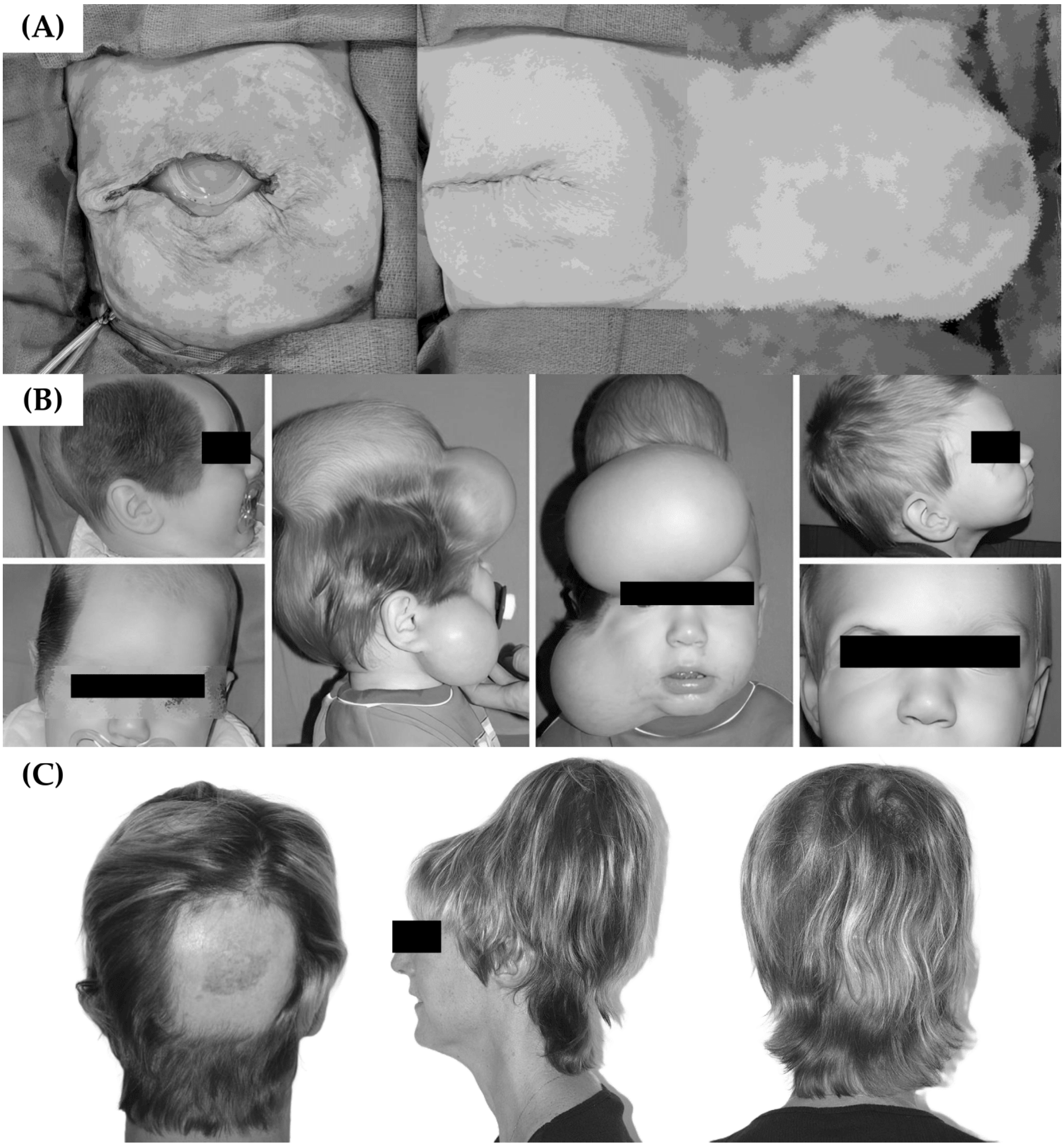

Figure 2.12: Application of skin expanders for (A) breast reconstruction [131], (B) pediatric cases [123] and (C) scalp reconstruction [124].

Skin expansion has several disadvantages and risk factors that can lead to complications. The procedure often requires multiple visits and prolonged treatment over several months, which can be psychologically challenging for patients due to the temporary disfigurement caused by the expander. Major complications include infection, implant exposure, seroma formation, tissue necrosis and device failure. These issues can require additional interventions and potentially compromise the success of the procedure. Patients may also experience pain during expansion, particularly in sensitive areas such as the forehead and distal extremities and may experience permanent atrophy or thinning of the underlying tissue. In severe cases, complications can interrupt treatment and compromise the final result [132].

These problems are influenced by several specific risk factors that are important to consider during the planning and execution of the procedure. Risk factors contributing to these complications include improper surgical technique, excessively tight dressings, lying on the tissue expander (especially at night), excessive fluid injection per session, non-cooperative patients, a history of radiation therapy in the area, incorrect measurement of expander volume and size, placement of a large expander in a small pocket, and positioning the expander below a scar [137].

Given the impact of these complications and contributing factors, planning tissue expansion requires careful attention to various technical parameters. Significant challenges arise from the lack of clear guidelines on essential aspects such as the amount of fluid to be injected, the intervals between inflations, and the exact degree of expansion required to obtain sufficient skin for procedures such as flaps or grafts.

While the practical limit in each session is often determined by the patient's perceived pain, it is crucial to continually assess the vascularity of the tissue. Monitoring includes observing capillary refill and adjusting fluid volumes according to clinical response. Although advanced techniques such as transcutaneous oximetry or intraluminal pressure measurement have been proposed to refine monitoring, clinical observation remains the primary standard to ensure a safe and effective procedure [124].

In addition, the mechanical creep of the expanded skin necessitates overstretching during the procedure. This approach mitigates potential complications, addresses excess tissue by allowing its removal if necessary, and ensures complete elimination of residual scarring [2,27,3]. However, the extent to which the skin should be overstretched remains non-standardized. Various strategies have been proposed, including stretching the tissue by 20 to 30% [124], using a more conservative range of 30-50% of the estimated size required [143], or adding a minimum physical margin of 2 cm [137].

Together, these techniques highlight the importance of careful planning and ongoing clinical supervision. This is particularly critical given the absence of uniform standards and the inherent complexity of controlling vascularity and fill volumes, factors that still limit the optimization of clinical outcomes in tissue expansion.

2.3.5. Innovations and challenges in skin expansion

Recent advancements in computational modeling have revolutionized our understanding of skin expansion. Personalized simulations allow surgeons to predict the outcomes of various expansion protocols, optimize expander placement, and minimize risks of over-expansion or tissue necrosis. These models incorporate the viscoelastic and growth properties of skin, enabling precise control over clinical parameters including the timing of each inflation, the exact volume of saline solution required per session, expander geometry, and maximum allowable stress on the tissue (Figure 2.12A) [112,122].

Computational approaches have also provided insights into the comparative performance of different expander shapes and designs, guiding the selection of devices that maximize tissue gain while minimizing complications. For instance, rectangular expanders aligned with Langer's lines have been shown to produce optimal results in specific anatomical regions [120,122].

Despite its widespread use, tissue expansion is not without challenges. Complications such as infection, device failure, and patient discomfort remain concerns, particularly in high-motion areas [122]. Emerging technologies, such as endoscopic insertion techniques and bioengineered expanders, hold promise in addressing these limitations (Figure 2.12B) [141,142,144]. Additionally, further research into the molecular pathways of mechanotransduction may unlock new strategies for enhancing tissue growth and reducing complications [122].

The development of self-inflating expanders (Figure 2.11D) and biodegradable devices represents a promising direction for future innovation, these technologies aim to reduce the need for repeated clinical interventions and improve patient comfort [5,15,16]. Moreover, integrating tissue engineering approaches, such as combining expanders with growth factor delivery systems or bioactive scaffolds, could enhance the quality and functionality of expanded skin (Figure 2.12C) [145–147].

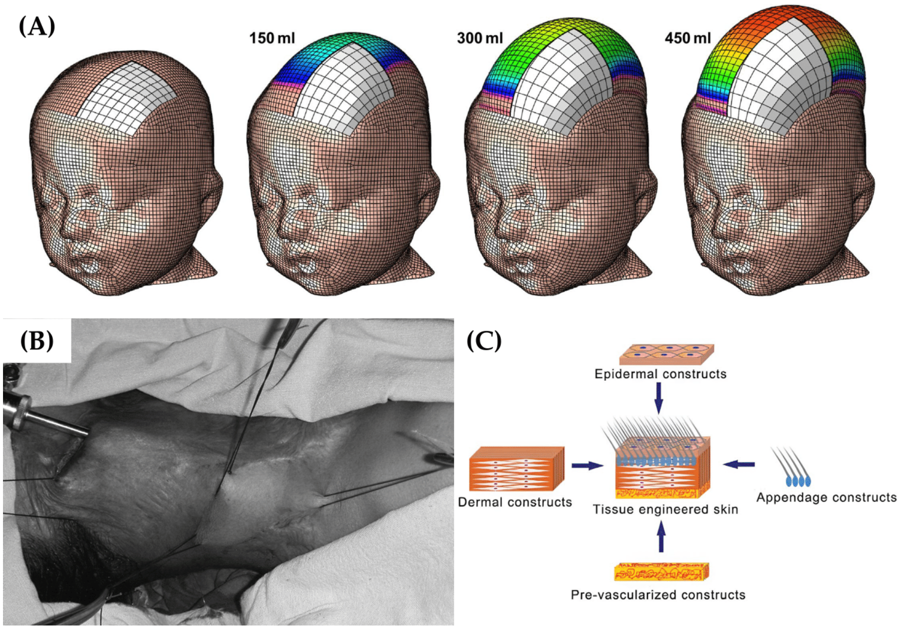

Figure 2.13: (A) Simulation of skin growth during expansion in pediatric scalp reconstruction [112]. (B) Neck reconstruction using an endoscopic tissue expander placement technique [141]. (C) Schematic representation of an ideal skin tissue engineering scaffold [147].

3. Theory

3.1. Energy methods

3.1.1. Basic concepts

In engineering, a *system* is defined as a particular portion of the universe selected for analysis. A valid system can be a single object or particle, a collection of objects or particles, or a region of space that may vary in size and shape [148]. Regardless of the type of system, it is always delimited by a boundary, which may be real or imaginary, that separates the system from its surroundings. This boundary does not necessarily coincide with a physical surface and can be fixed or movable depending on the case [148,149].

There are two types of systems. A *closed system* is characterized by the fact that it contains a fixed amount of mass, which means that mass cannot cross its boundary, although energy can. In addition, the volume of a closed system can change. The system is said to be *isolated* if neither mass nor energy can cross the boundary [148,149]. In contrast, an *open system*, also known as a control volume, is a specific region of space in which both mass and energy can cross its boundary. This type of system is often used to analyze mass flow devices such as compressors, turbines or nozzles [149].

A system in equilibrium has measurable properties that fully describe its *state*. If one of these properties changes, the system moves to a different state. The change from one equilibrium state to another is called *process*, and the sequence of states through which it passes is called the *path* of the process. To describe a process, it is essential to specify the initial state, the final state, the path followed and the interactions with the surroundings [149].

A process is quasi-static or quasi-equilibrium if it occurs so slowly that the system always remains virtually in equilibrium. This type of process allows the system to adjust internally in a uniform manner, preventing properties in one part of the system from changing more rapidly than in another. However, once a process is initiated, it cannot be spontaneously reversed to return the system to the initial conditions, which classifies it as *irreversible*.

In contrast, a *reversible* process is one in which the system can return to their initial state with no net change. However, reversible processes are merely idealizations that do not occur in nature, although they represent the theoretical limits of the corresponding irreversible ones [149].

The causes that make a process irreversible are called *irreversibilities*. These include factors such as friction, unrestrained expansion, inelastic deformation of materials and chemical reactions. These irreversibilities are responsible for the fact that all natural processes are inherently irreversible [149].

3.1.2. Classification and transfer of energy

Energy can exist in various forms such as internal, thermal, kinetic, potential, electrical, magnetic, chemical, nuclear and others. The sum of all these forms is the total energy of a system. It is fundamental to understand that energy is a property, and the value of a property does not change unless the state of the system also changes. Therefore, any change in the total energy of a system during a process is equal to the sum of the changes in each of its individual forms [149].

Thermodynamics focuses not on the absolute value of total energy, which is generally indeterminate, but on measurable changes in energy as processes occur [149,150]. This approach is essential for solving engineering problems. To simplify energy analysis, the different forms of energy are divided into two main categories: *macroscopic* and *microscopic* energy [149].

Macroscopic energy relates to the motion of the system and the influence of external factors such as gravity, magnetism, electricity and surface tension. A prominent example of macroscopic energy is *kinetic energy*, which is associated with the motion of the system relative to a fixed frame of reference. If all parts of the system are moving at the same speed, kinetic energy (K) can be expressed mathematically as a function of the system's mass (m) and velocity (v), representing the energy it possesses due to its motion [148,149].

$$K = \frac{mv^2}{2} \tag{1}$$

Another component of macroscopic energy is *potential energy*, and it is useful to employ an example to define it. Suppose an object is at the highest point of its trajectory. In this state, the system has the ability to convert its energy into kinetic energy, but it does not do so until the object begins to fall. Therefore, potential energy is the energy storage mechanism prior to the initiation of motion. In general, this energy can only be associated with specific forces acting between the components of the system [148]. A special case is gravitational potential energy (P), which depends on the height of a system in a gravitational field. It is calculated as a function of mass (m), gravitational acceleration (g) and the height (z) of the centre of gravity relative to an arbitrary reference plane [149].

$$P = mgz \tag{2}$$

Mechanical energy, which includes both kinetic and potential energy, is defined as the form of energy that can be completely converted into mechanical work by an ideal device. These two forms of energy are essential for the analysis of physical systems [149].

Microscopic energy, on the other hand, is associated with the molecular structure and activity of molecules within the system, independent of any external frame of reference. This category includes molecular kinetic energy, derived from the random motion of molecules; vibrational potential energy, associated with the forces between atoms within molecules; and electrical potential energy, resulting from intermolecular interactions [148]. An important part of microscopic energy is chemical energy, which is associated with the atomic bonds in molecules. During chemical reactions, the breaking and forming of these bonds produces changes in the internal energy of the system [149].

The above-mentioned forms of energy can be stored within the system and are therefore classified as static forms of energy. In contrast, forms of energy that are not stored within the system are considered dynamic forms of energy or energy interactions. These dynamic forms are observed at system boundaries as they cross them and represent the energy exchanged, either gained or lost, by the system during a process [149]. Dynamic forms of energy transfer include work, where energy is transferred by the application of force and displacement; mechanical waves, where energy is transferred by a disturbance in a medium, such as sound; heat, which is transferred by a temperature difference between two regions; and matter transfer, where matter physically crosses a system boundary, carrying energy with it [148].

3.1.3. Work, conservative and non-conservative forces

Work is a form of energy transfer associated with the action of a force over a distance. For work interaction to exist between a system and its surroundings, two conditions must be fulfilled: there must be a force acting on the boundary of the system, and the boundary must be displaced. Mechanical work is the only form of work involved in this context and is related to the movement of the system boundary or the system as a whole [149].

Work (W) is a directional quantity, which means that its full definition requires specification of both its magnitude and its direction. From a thermodynamic perspective, if W is the work done on a system and its value is positive, energy is being transferred into the system; if it is negative, energy is being transferred out of the system [148].

As an energy transfer mechanism, work has several important properties. First, work is detected at the boundaries of the system as it crosses those boundaries, which classifies it as a boundary phenomenon. Second, a system does not possess work as an intrinsic property; work is only manifested during a process. Moreover, it is associated with processes, not states, which means that it has no meaning in any particular state of the system. Finally, work is a path function, since its magnitude depends both on the path followed during the process and on the initial and final states. In contrast, the properties of the system are point functions, i.e. they depend only on the state of the system and not on the path taken to reach it [149].

Work can be expressed in various ways, all of which relate to a force acting over a distance. In elementary mechanics, the work done by a constant force F on a body displaced a distance x in the direction of the force is calculated as [148,149]:

$$W = Fx \tag{3}$$

However, when the force varies with position ($F(x)$), the work is calculated as the integral of the product of the force and the displacement along the path. In this case, the work done by a varying force can be represented geometrically as the area under the force-displacement curve (Figure 3.1) [148]:

$$W = \int F(x)\, dx \tag{4}$$

A special case of mechanical work is the work done by a spring. When a force is applied to a spring, its length changes depending on the magnitude of the force (F_{spring}). If the spring is stretched or compressed a small distance from its equilibrium configuration, the force exerted by the linear spring can be mathematically modelled as [148]:

$$F_{spring} = kx \tag{5}$$

Where k is the elastic constant of the spring and x is the displacement relative to the equilibrium position. The work done by the spring is calculated from equation (4), as the area under the curve F_{spring} (Figure 3.1), which, for a displacement from x_i to x_f, is given by the integral [148]:

$$W = -\int_{x_i}^{x_f} F_{spring}\, dx = -\int_{x_i}^{x_f} kx\, dx = \frac{1}{2}k{x_i}^2 - \frac{1}{2}k{x_f}^2 \tag{6}$$

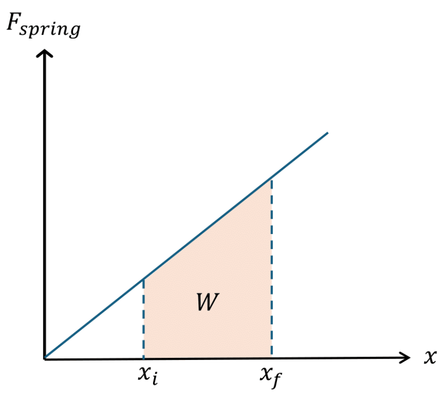

Figure 3.1: Force-displacement curve of a linear spring. The area under the curve represents the mechanical work done by the spring. Special thanks to M. Eng. Alex De Blas for his support and help with this illustration.

Forces acting on a system can be classified as *conservative* or *non-conservative* depending on how the work done varies with the path followed. Conservative forces have two basic properties. First, the work done by a conservative force on a particle moving between any two points is independent of the path taken. This means that only the initial and final positions of the system matter, not the path taken. Secondly, the work done by a conservative force on a particle following a closed path (i.e. returning to its starting point) is zero.

One of the main implications of conservative forces is that they determine the variation of the potential energy associated with the system on which they act. In this context, the work done by a conservative force ($W_{conservative}$) on an object as it moves from one position to another is equal to the difference between the initial and the final value of the system's potential energy (ΔP). This relationship applies to any conservative force, such as gravity or the elastic force of a spring.

$$W_{conservative} = -\Delta P \tag{7}$$

This indicates that the work done by a conservative force is translated into changes in the potential energy of the system, keeping the total mechanical energy constant [148,149]. On the other hand, non-conservative forces do not have the properties of conservative forces. The work done by a non-conservative force depends on the path of the system and is not zero for closed trajectories. Common examples of non-conservative forces are friction and air resistance. These forces cause a dissipation of the mechanical energy of the system, converting it into other forms of energy such as thermal or internal energy. Non-conservative forces are therefore associated with losses of mechanical energy that cannot be fully recovered to perform mechanical work [148].

In a system where both conservative and non-conservative forces act, the net work (W_{net}) can be expressed as the sum of the work done by conservative forces ($W_{conservative}$), which is associated with changes in potential energy, and the work done by non-conservative forces ($W_{non-conservative}$), which represents the dissipation or transfer of energy to other non-mechanical forms [148].

$$W_{net} = W_{conservative} + W_{non-conservative} \tag{8}$$

Understanding work, especially that done by conservative and non-conservative forces, is fundamental to analyzing how the total energy of a system is conserved, which is addressed in the next section.

3.1.4. Principle of energy conservation

The first law of thermodynamics, also known as the conservation of energy, states that energy cannot be created or destroyed, it can only be transformed. This principle is fundamental to understanding energy interactions and the relationships between different forms of energy in a system [149].

If the total energy of a system changes, it is only because energy has crossed the boundaries of the system through a transfer mechanism. This principle is described mathematically by the conservation of energy equation [148,149]:

$$\Delta E_{system} = T_{net} \tag{9}$$

Where ΔE_{system} is the total energy of the system, including all forms of energy storage (kinetic, potential and internal), while T_{net} is the amount of net energy transferred across the system boundary. The extended form of this equation is [149]:

$$\Delta K + \Delta P + \Delta E_{int} = T_{in} - T_{out} \tag{10}$$

The net energy transfer is calculated as the difference between the amounts entering (T_{in}) and leaving (T_{out}) the system. In an isolated system, there is no energy transfer, and the total energy of the system remains constant. One way of understanding this principle is to compare it to an accounting system where energy inputs and outputs must balance [148].

In systems where only conservative forces act, the sum of the changes in kinetic and potential energy remains constant. This result is known as the conservation of mechanical energy. However, when non-conservative forces are present, some of the mechanical energy of the system is dissipated. To analyze the effect of non-conservative forces, the theorem of work and kinetic energy is used. This states: *"when work is done on a system and the only change is in its velocity, the net work done is equal to the change in the kinetic energy of the system"* [148].

$$W_{net} = \Delta K \tag{11}$$

Thus, by combining equations (7) and (11) and substituting the terms in equation (8), it can be seen that the work done by non-conservative forces is directly related to the total change in the mechanical energy of the system [148]. This relationship will be very useful when studying systems where conservative and non-conservative forces coexist.

$$W_{non-conservative} = \Delta K + \Delta P = \Delta E_{mechanical} \tag{12}$$

3.1.5. Strain energy

Strain energy is a key concept in applied mechanics and is widely used to analyze the response of machines and structures subjected to static and dynamic loads [151]. It represents a form of potential energy associated with the internal deformations of a material or structure under load. Unlike gravitational potential energy, strain energy depends on the relative positions of the particles that constitute the material [150].

To illustrate this concept, consider a bar of length L subjected to a tensile force $F(x)$. If this force is applied gradually from zero to its maximum value, the bar will undergo progressive elongation up to a maximum elongation x. During this process, the external force performs work as the bar deforms. According to the principle of conservation of energy (equation (9)), the work done by the external force is converted into potential energy, known as strain energy (ΔU), assuming that there are no other forms of energy transfer. Mathematically, this relationship is expressed as [150,151]:

$$\Delta U = W = \int F(x)\, dx \tag{13}$$

From a geometrical point of view, for both linear and non-linear elastic materials, the area under the force-elongation curve represents the stored strain energy (Figure 3.2) [150]. Initially, when there is no deformation, the stored energy is zero. U therefore, corresponds to the energy stored in the bar during the loading process.

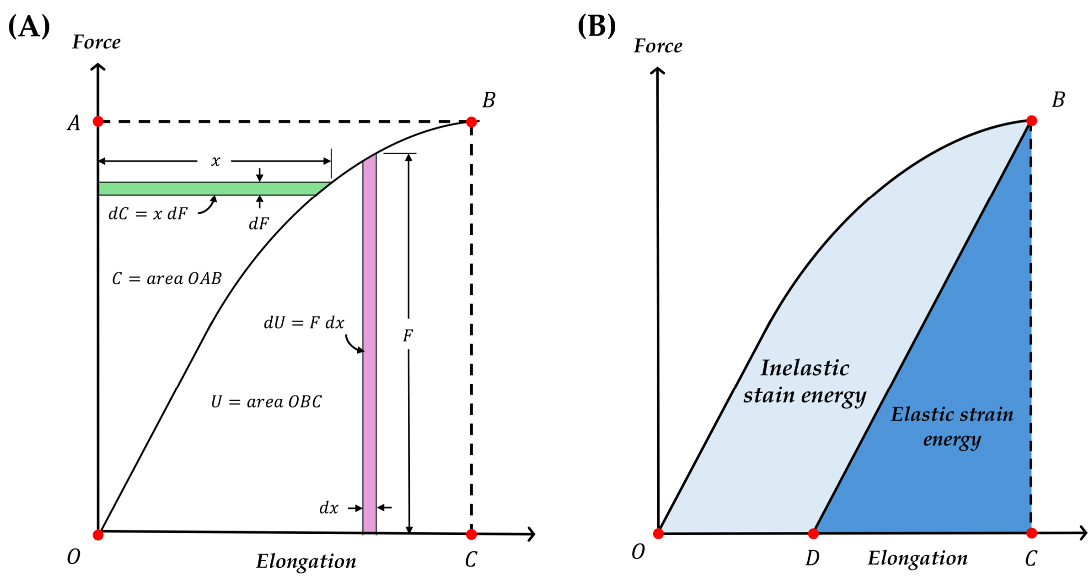

Figure 3.2: (A) Nonlinear elastic force-elongation curve. (B) Elastic and inelastic strain energy. Adapted from [150,151]. Special thanks to M. Eng. Alex De Blas for his support and help with this illustration.

In certain cases, for example when the tensile force is replaced by a force generated by a linear spring (equation (5)), this strain energy is also called *elastic potential energy* [150]. However, this term is less precise as strain energy can include both elastic and inelastic components. *Elastic* *strain energy* is the part of the energy that is reversibly stored and can be fully recovered as work. In contrast, *inelastic strain energy* is associated with permanent deformations that cannot be recovered once the material has exceeded its elastic limit [151].

In the force-elongation diagram shown in Figure 3.2B, the total area under the curve OBCDO represents the work done by the external load. If the force exceeds the yield strength of the material, the curve will follow a different path (path BD) during unloading, resulting in permanent deformation of the structure. The elastic strain energy recovered during unloading corresponds to the area under line BD, represented by the shaded triangle BCDB. On the other hand, the inelastic strain energy is calculated as the difference between the total area under the load curve OBCDO and the area of the triangle BCDB [151].

The total strain energy in a structure is calculated as the sum of the strain energies of its individual components. For specific loads, such as torsion and bending, the strain energy values are listed in Table 3.1. It is essential to note that this energy is not linearly related to the applied loads, even for materials with linearly elastic behavior. For this reason, the total energy cannot be obtained by simply adding up the energies associated with each individual load considered separately [150,151].

Table 3.1: Strain energy expressions [150,152]. For further details see reference [152].

Strain energy expression	Geometric interpretation	Equation
Axial loading (tensile and compression)	Area under the force-displacement curve	$U = \int \frac{F}{2EA} dz \quad (14)$
Bending for straight beams	Area under the moment-bend angle curve	$U = \int \frac{M^2}{2EI} dz \quad (15)$
Bending for curved beams[19]		$U \approx \int \frac{M^2}{2EI} R d\theta \quad (16)$
Torsion	Area under the torque-twist deformation curve	$U = \int \frac{T^2}{2GJ} dz \quad (17)$

3.1.6. Theorem of Castigliano

Castigliano's theorem is a fundamental energy-based method for the analysis of elastic systems, both linear and non-linear, especially in the study of displacements and rotations in stressed structures. Formulated by Carlo Alberto Castigliano in the 19th century, this method is based on the concept of complementary strain energy and its relationship to the forces or moments applied to a system [150]. It is particularly useful in the analysis of statically

[19] For curved sections where the radius is significantly larger than the thickness, typically when the ratio exceeds 10, the effect of eccentricity can be considered negligible. In such cases the strain energies can be approximated by directly replacing dx by $Rd\theta$ [152].

indeterminate structures where traditional equilibrium methods are insufficient to solve the system [152].

The *complementary strain energy* (C) is defined as the area over the force-elongation curve (Figure 3.2A), while the strain energy is the area under the curve. For linear materials the two energies are equivalent. In the derivation of the theorem, C is considered as a function of the generalized forces ($C(F_i)$). The theorem can be expressed in general terms as follows: in an elastic system in which rigid displacements of the body are prevented and concentrated forces are applied, plus distributed loads or thermal deformations, the displacement δ_i at the point of application of a force F_i is given by [150]:

$$\delta_i = \frac{\partial C}{\partial F_i} \tag{18}$$

This result assumes small displacements[20], so the theorem is limited to structures with small deformations [150]. For rotational displacements, the theorem takes the form:

$$\theta_i = \frac{\partial C}{\partial M_i} \tag{19}$$

Equation (19) determines the angular displacement θ_i in the arm of a moment M_i applied to the elastic structure. Although equations (18) and (19) are restricted to small displacements, they can be applied to materials with non-linear elastic behavior.

For linear elastic materials, the expressions provided below are valid under specific conditions. In this case, the force-elongation relationship of a member or structure is linear, the energies U and C are equal and the superposition principle applies [150]. Consequently, in equations (18) and (19), C can be replaced by U. The strain energy used in the theorem depends on the type of stress present in the structure. The most common cases are tension, compression, bending and torsion [151,152]:

$$\delta_i = \frac{\partial U}{\partial F_i} \qquad \text{tension and compression} \tag{20}$$

$$\theta_i = \frac{\partial U}{\partial M_i} \qquad \text{bending} \tag{21}$$

$$\phi_i = \frac{\partial U}{\partial T_i} \qquad \text{torsion} \tag{22}$$

When the calculation of strain energy involves multiple terms or extensive integrations, a modified version of the theorem can be used, which allows differentiation within the integral

[20] Small-displacement theory is a concept used mainly in the mechanics of solids, structures and vibrations, in which it is assumed that the displacements and deformations of a system are sufficiently small that the equations of equilibrium can be formulated in terms of the undeformed configuration [150].

sign. This simplifies the mathematical process by avoiding the need to explicitly calculate energy prior to derivation. For a bending load, the expression takes the form [152]:

$$\delta_i = \frac{\partial U}{\partial F_i} = \frac{\partial}{\partial F_i}\left(\int \frac{M^2}{2EI} dx\right) = \int \frac{M}{EI}\left(\frac{\partial M}{\partial F_i}\right) dx \tag{23}$$

This simplified version is particularly useful for problems that require the introduction of "dummy loads", which allow the evaluation of displacements or rotations at specific points where no load is applied to the original structure [151].

Castigliano's theorem has important applications in structural and mechanical engineering. It allows the calculation of deflections and rotations in beams, members and other elements under load, and is particularly valuable in statically indeterminate structures [151,152]. It is also used in the design of mechanical components to evaluate loads and deflections and optimize their performance.

3.2. Spring mechanics

Elasticity is an inherent property of materials that allows them to return to their original shape after deformation, as long as their elastic limit is not exceeded. In the case of springs, this property is characterized by the relationship between the applied force (F) and the resulting deflection (x). Stiffness, also known as spring constant (k), is a key parameter in describing this relationship and is mathematically defined as the derivative of the force with respect to the deflection [152].

$$k = \frac{dF}{dx} \tag{24}$$

This definition implies that stiffness quantifies how much force is required to produce a unit of deflection and its value can vary depending on the type of spring. In a *linear spring*, the relationship between force and deflection is directly proportional. This means that within the elastic range, the applied force increases uniformly with deflection (equation (5)). In this case, stiffness remains constant, resulting in a perfectly linear force-deflection curve (Figure 3.3).

In non-linear springs, the relationship between force and deflection changes according to the specific characteristics of the system. In a *stiffening spring*, the stiffness increases with increasing deflection. This is reflected in a force-deflection curve that becomes more pronounced as the load increases, indicating that the spring requires greater forces to deform further (Figure 3.3) [152,153].

In contrast, a *softening spring* exhibits different behavior. In this case, the force-deflection curve shows an initial increase in the force required to deform, followed by a decrease as the spring approaches a certain configuration state (Figure 3.3). This indicates that there is a reduction in stiffness at certain ranges of deflection, which makes the spring easier to deform at later stages [152,153].

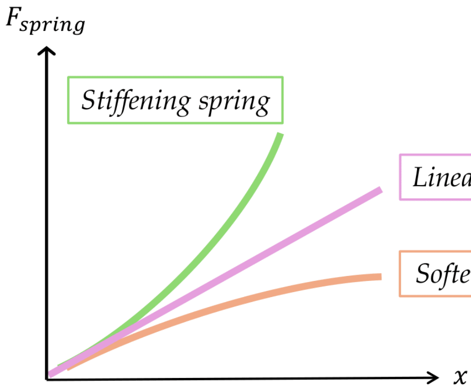

Figure 3.3: Force-deflection curves of linear, non-linear stiffening and softening springs. Based on [152]. Special thanks to M. Eng. Alex De Blas for his support and help with this illustration.

Stiffness plays a central role in defining the relationship between force and deflection, which is crucial for understanding the mechanical behavior of spring-based systems under various loading conditions. To explore this further, the following sections will analyze the mechanical performance and unique characteristics of two spring types: serpentine and conical.

3.2.1. Serpentine spring mechanics

Serpentine springs, characterized by their undulating, snake-like geometry, are integral components in various micro-electromechanical systems (MEMS). Their design, which incorporates repeated meanders, allows for low stiffness within limited design spaces, making them particularly effective in applications requiring precise in-plane and out-of-plane displacements, as well as angular deflections [154,155].

Because of their zigzag shape, serpentine springs can be divided into basic repeating entities called unit cells (see Figure 3.4A) [156]. These unit cells are fundamental to their mechanical analysis. Geometrically, a unit cell consists of straight beams of length l_2, inclined at an angle α to the horizontal, and curved beams of radius R. The cross section of the beam is rectangular with width w and height h (Figure 3.4B) [156]. With these six design parameters (l_2, R, α, w, h and the number of unit cells (n) the geometry of the spring is fully described and the length (l_1) of a unit cell is given by the equation:

$$l_1 = 4l_2 \cos(\alpha) + 4R\cos\left(\frac{\pi}{2} - \alpha\right) \tag{25}$$

The calculation of deflections in the spring is performed using Castigliano's theorem, which states that deflections in a given direction can be obtained by deriving the total strain energy with respect to the force or moment applied in that direction.

To determine the spring constant (k), the dummy load strategy described in the section on the Theorem of Castigliano is applied. It is assumed that the spring is subjected to an axial force F, a shear force V and a bending moment M at the right end, as shown in Figure 3.4A. In each *i-th* unit cell, the axial and shear forces remain constant, but the moment varies and is given by:

$$M_i = M + Vl_1(n - i) \tag{26}$$

Each unit cell is modelled as a connection of several elementary beams, considering that these are subjected to bending deformation only [154,157]. According to the free body diagram of the unit cell (Figure 3.5), the structure is decomposed into three straight beams and two curved beams [158]. The length of each beam is measured along its central axis, from the center of one corner to the center of the next. To simplify the analysis, it is assumed that the connections are ideal and transmit forces, moments and torques without significant deformation [154].

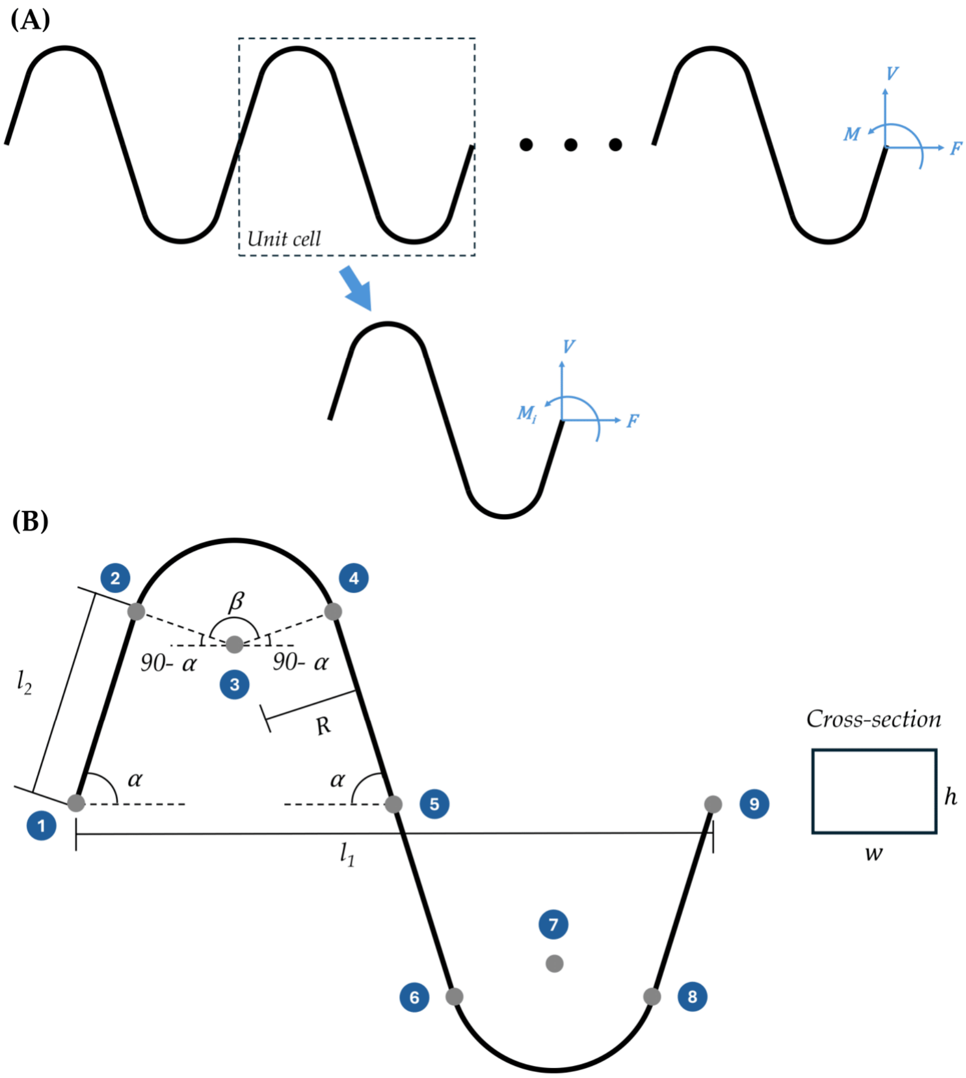

Figure 3.4: (A) Unit cell of the serpentine spring subjected to dummy loads and (B) its geometrical parameters. Special thanks to M. Eng. Alex De Blas for his support and help with this illustration.

In order to calculate the strain energy of each beam of the unit cell, it is essential to first determine the bending moment acting on them. These moments, which are linear functions of the forces and moments applied at the ends of the structure, are determined from the free body diagram shown in Figure 3.5. From this analysis, the moments corresponding to the different sections of the unit cell are obtained.

$$M_1 = M_i + V \cdot \varepsilon \cos(\alpha) - F \cdot \varepsilon \sin(\alpha) \tag{27}$$

$$M_2 = M_i + V \cdot (R \sin(\alpha) - R \sin(\alpha - \theta) + l_2 \cos(\alpha)) - F \cdot (R \cos(\alpha - \theta) - R \cos(\alpha) + l_2 \sin(\alpha)) \tag{28}$$

$$M_3 = M_i + V \cdot (\varepsilon \cos(\alpha) + 2R \sin(\alpha) + l_2 \cos(\alpha)) + F \cdot (\varepsilon \sin(\alpha) - l_2 \sin(\alpha)) \tag{29}$$

$$M_4 = M_i + V \cdot (l_2 \cos(\alpha) + 2R \sin(\alpha) + 2l_2 \cos(\alpha) + R \sin(\alpha) - R \sin(\alpha - \theta)) - F \cdot (l_2 \sin(\alpha) + R \cos(\alpha - \theta) - R \cos(\alpha)) \tag{30}$$

$$M_5 = M_i + V \cdot (l_2 \cos(\alpha) + 4R \sin(\alpha) + 2l_2 \cos(\alpha) + \varepsilon \cos(\alpha)) + F \cdot (l_2 \sin(\alpha) - \varepsilon \sin(\alpha)) \tag{31}$$

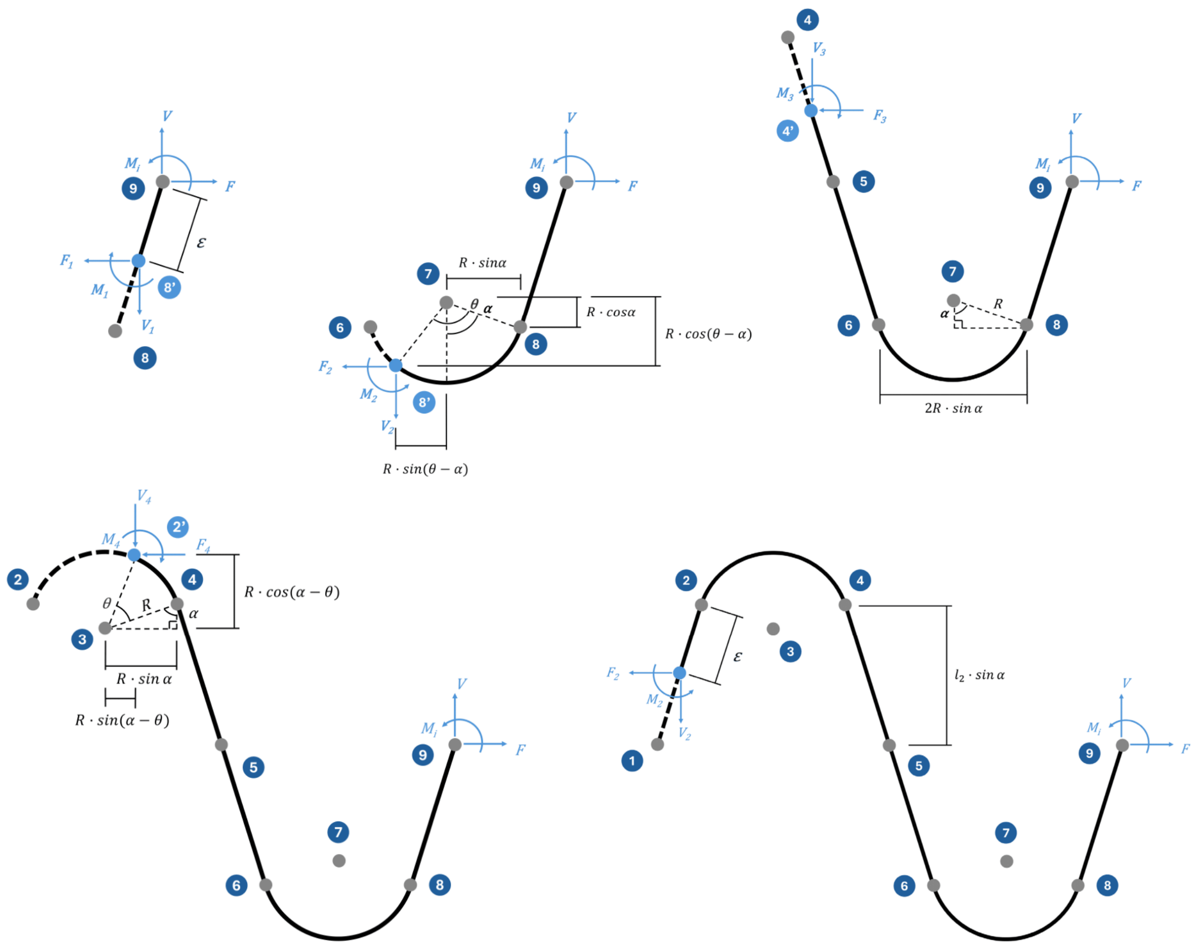

Figure 3.5: Free-body diagram of serpentine spring unit cell. Special thanks to M. Eng. Alex De Blas for his support and help with this illustration.

These moments are then substituted into equations (15) and (16) to calculate the bending strain energy. As a result, the total strain energy of the unit cell ($U_{(i)}$) is obtained by summing the individual contributions of all the beams that compose it, which is expressed by the following equation [156]:

$$U_{(i)} = \int_0^{l_2} \frac{{M_1}^2}{2EI_z} d\varepsilon + \int_0^{2\alpha} \frac{R{M_2}^2}{2EI_z} d\theta + \int_0^{2l_2} \frac{{M_3}^2}{2EI_z} d\varepsilon + \int_0^{2\alpha} \frac{R{M_4}^2}{2EI_z} d\theta + \int_0^{l_2} \frac{{M_5}^2}{2EI_z} d\varepsilon \tag{32}$$

Substituting the moments (27)-(31) into equation (32), it can be seen that the strain energy of the unit cell is a quadratic function of F, V and M. The total energy of the spring (U) is obtained by summing the contributions of all the unit cells (n):

$$U = \sum_{i=1}^{n} U_{(i)} \tag{33}$$

In order to calculate the spring constant in the axial axis (k_X), the boundary conditions are considered, which specify the absence of displacement in the Y-axis and rotation [156].

$$y = \frac{\partial U}{\partial V} = 0 \tag{34}$$

$$\theta = \frac{\partial U}{\partial M} = 0 \tag{35}$$

Mathematically, the above equations allow V and M to be expressed as functions of F. From the same theorem, the displacement in the X-axis can be calculated, resulting in:

$$x = \frac{\partial U}{\partial F} \tag{36}$$

Spring constant is obtained from the general relationship between force and displacement. In this case, equation (5) is used, solving for k_X and substituting x from equation (36) [159].

$$k_X = \frac{F}{\partial U / \partial F} \tag{37}$$

The result depends only on the design variables of the spring (l_2, R, α, n, w and h) and the Young's modulus of the material from which it is produced. Manually solving all the equations required to determine spring stiffness can be a complex task. However, symbolic calculus offers an efficient solution by allowing mathematical expressions to be manipulated in a precise manner using algorithms that work directly with symbols and equations rather than numerical values [160]. This computational tool allows performing derivatives, integrals and solve equations, and is particularly useful for dealing with the integrals and partial derivatives involved in the analytical model of the serpentine spring.

In this context, the analytical model was implemented in Python using the *Sympy* library [161], with the aim of evaluating how each variable affects the spring rate. This was done by varying each variable individually, while keeping the others constant ($w = 1mm, h = 1mm, R = 5mm, l_2 = 10mm, n = 1, \alpha = 90º$ and $E = 10GPa$), in order to analyze their specific effect. Force-deflection curves were generated from the Python code (Figure 3.6A), from which the spring rate values were extracted and plotted to see how this parameter varies as a function of each design variable (Figure 3.6B).

The analysis in Figure 3.6A shows a linear relationship between force and deflection, confirming that the serpentine spring is a linear spring. Although these curves allow the spring rate to be assessed, Figure 3.6B provides a clearer understanding of how each design parameter affects it. Following a suggestion by [156], a dimensionless parameter called the cross-section aspect ratio (w/h) has been introduced and is shown to be relevant in the analysis.

From Figure 3.6B it can be seen that most of the parameters have a decreasing non-linear relationship with stiffness, except for the material modulus of elasticity and the cross-section aspect ratio. It is interesting to note that a higher number of unit cells in the structure reduces its stiffness, which is explained by referring to the behavior of series springs, whose equivalent stiffness (k_{eq}) is calculated as:

$$k_{eq} = \frac{1}{\sum_{i=1}^{n} \frac{1}{k_{(i)}}} \tag{38}$$

If the springs in series have the same stiffness (k), the equation is simplified to:

$$k_{eq} = \frac{k}{n} \tag{39}$$

It is therefore confirmed that as the number of cells increases, the stiffness of the system decreases in a non-linear manner, as observed in the analytical model of the serpentine spring.

For linearly varying parameters, one way to increase stiffness is to select a material with a higher Young's modulus. However, this increase will be proportional to the change made. On the other hand, although the relationship between w/h and spring rate is linear, increasing the section height (h) has a more significant effect on stiffness due to its non-linear relationship.

Since the thickness of the spring is considerably less than its overall length (nl_1), there is a risk of buckling when subjected to compression. To deal with this phenomenon, it is essential to analyze the critical loads that cause structural instability [162]. Although the analytical method allows exact solutions to be obtained, its complexity makes it unsuitable for most practical engineering problems. For this reason, approximate or semi-empirical methods are often used [156,162]. However, the latter are often based on results obtained from finite element simulations, suggesting that it is more efficient to use this approach directly. Finite element simulations not only allow the critical loads to be accurately determined but also allow the different buckling modes to be visualized. Furthermore, following Euler's theory for columns, it is observed that an increase in the length of the structure causes a non-linear increase in the critical load [150–152], which is crucial for predicting the structural behavior of the design.

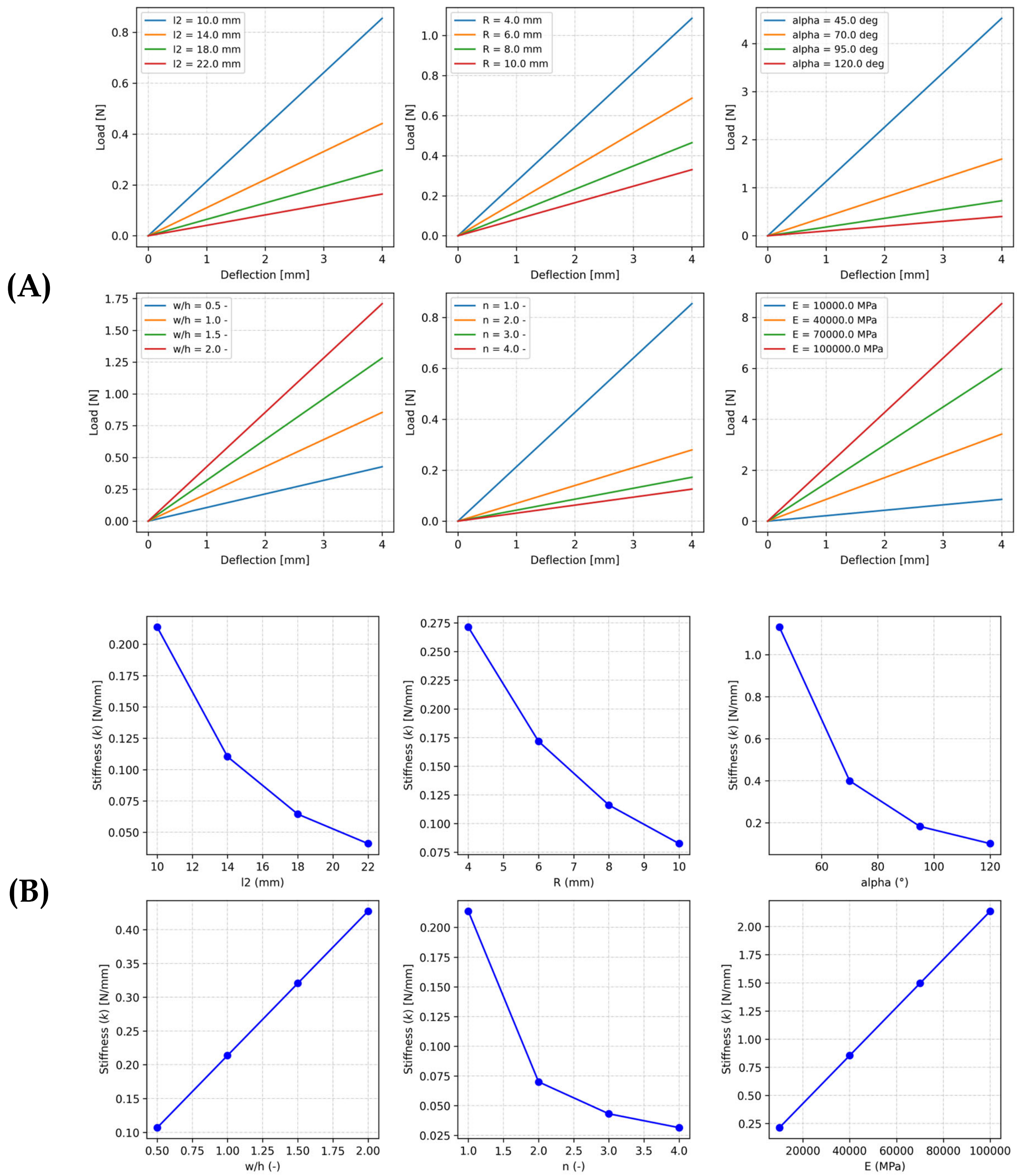

Figure 3.6: (A) Force-deflection curves and (B) serpentine spring rate behavior varying one parameter at a time ($w = 1mm, h = 1mm, R = 5mm, l_2 = 10mm, n = 1, \alpha = 90º$ and $E = 10GPa$).

In addition to the mechanical analysis performed with Python, this tool is also used for the geometric visualization of a unit cell of the spring. Using the *Plotly* library, the curved and straight beams of the design are represented by parametric equations and trigonometric relationships. Key geometric parameters such as the length of the straight beams (l_2), the radius of the curves (R) and the angle of inclination (α) are entered as user input, generating a two-dimensional representation of the serpentine spring, as shown in Figure 3.7. This approach provides a preliminary tool that allows the geometric parameters to be adjusted and visualized prior to implementing the design in CAD software, facilitating real-time exploration of the spring characteristics.

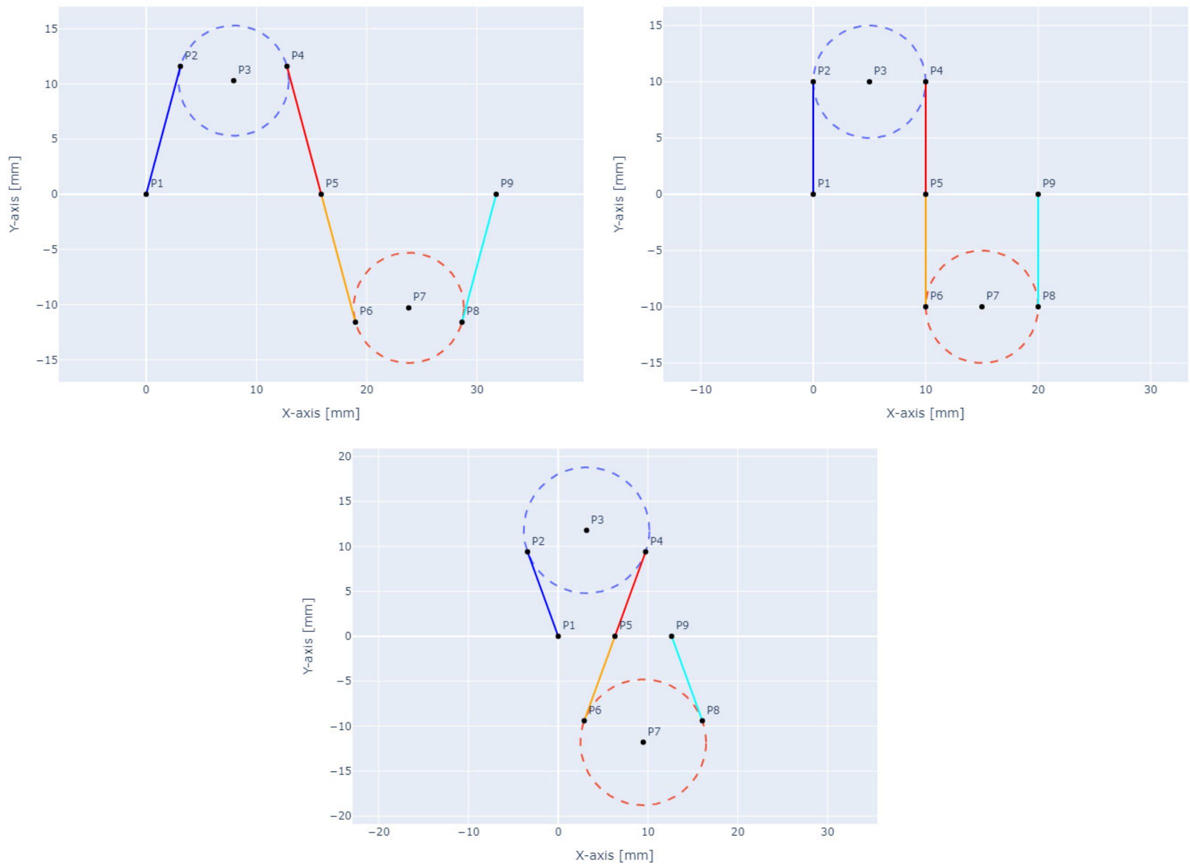

Figure 3.7: 2D representation of a serpentine springs with different geometrical parameters.

3.2.2. Conical spring mechanics

The conical spring formulation, based on [150,152,163], begins with the derivation of the force-deflection relationships of a helical spring. This spring, subjected to an axial load F, is analyzed by considering R as the mean radius of the coil and d as the diameter of the wire (Figure 3.8A). To calculate the deflection caused by F, the effect of coil twist is generally prioritized, as this component represents the largest energy contribution. However, the total strain energy of the spring includes both torsional and shear components. By analyzing an infinitesimal segment $mnm'n'$ (Figure 3.8B), it is possible to determine the torsion angle of the element between two adjacent cross sections and thus obtaining:

$$d\phi = \frac{F \cdot R \cdot R d\alpha}{JG} \tag{40}$$

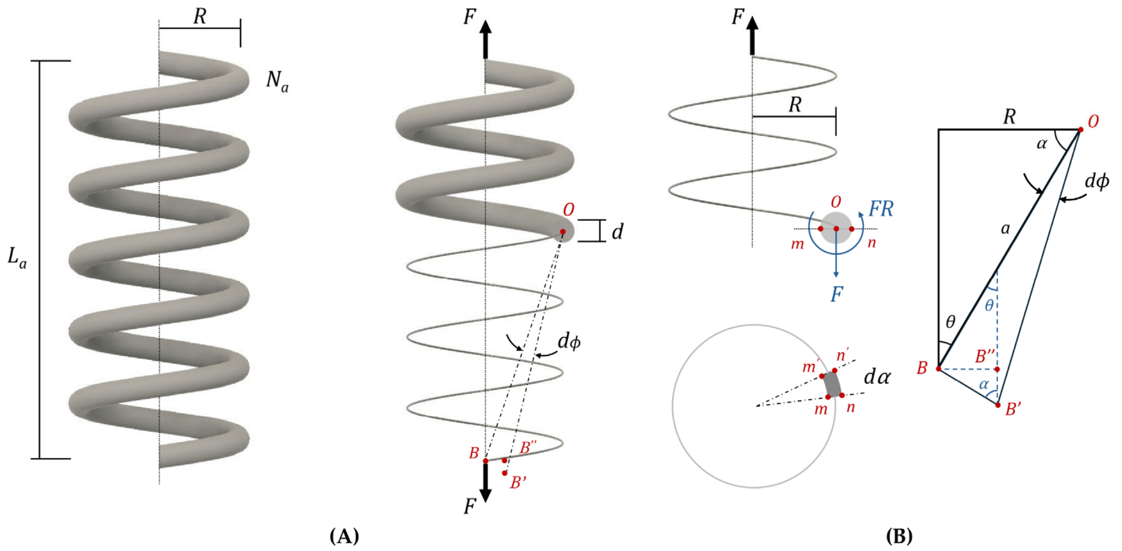

Figure 3.8: (A) Helical spring subjected to a force F. (B) Analysis of the torsion caused by force F on an infinitesimal element $mnm'n'$. Special thanks to M. Eng. Alex De Blas for his support and help with this illustration.

Where J is the second polar moment of area and G is the material shear modulus. The torsion causes the lower part of the spring to rotate relative to point O, resulting in the force application point B tracing a small arc $BB' = a \cdot d\phi$ (Figure 3.8B). This movement of B can be visualized by considering the spring as rigid except for the element $mnm'n'$. The vertical component of this displacement is:

$$d\delta = BB'' = BB'\frac{R}{a} = Rd\phi = \frac{F \cdot R^3}{JG}d\alpha \tag{41}$$

Therefore, the total deflection of the spring (δ) is calculated by adding the deflections BB'' produced by each infinitesimal element $mnm'n'$ along its entire length. This gives an integral expression describing the behavior of the system.

$$\delta = \int_0^{2\pi N_a} \frac{F \cdot R^3}{JG} d\alpha = \frac{F \cdot R^3 \cdot 2\pi N_a}{JG} \tag{42}$$

In this equation, N_a represents the number of active coils. Considering a circular cross-section, substituting the expressions $J = \pi d^4/32$ and $A = \pi d^2/4$ gives a final expression. This allows the total deformation to be determined from the geometric and material properties of the spring.

$$\delta = \frac{64N_aFR^3}{Gd^4} \tag{43}$$

The ratio F/δ for a given spring is called the *"spring stiffness or constant"*, represented by k. From equation (43) this relationship can be calculated as:

$$k = \frac{F}{\delta} = \frac{Gd^4}{64N_aR^3} \tag{44}$$

Spring stiffness can be modified by varying factors such as material, wire diameter, coil radius or number of coils. If instead of a circular cross-section a square of side d were used, equation (44) would become:

$$k = \frac{Gd^4}{\frac{32\pi}{2.25} N_a R^3} \tag{45}$$

The difference between equations (44) and (45) lies in the elasticity resilience coefficient (ε), the value of which depends on the geometry of the cross-section. This coefficient has a value of 64 for a circular section of diameter d and $32\pi/2.25$ for a square section of side d. The general equation is therefore expressed as:

$$k = \frac{Gd^4}{\varepsilon N_a R^3} \tag{46}$$

Having analyzed the helical spring, it is easy to move on to studying the conical spring. Unlike the helical spring, the conical spring does not have a constant radius. Instead, its radius varies mathematically from a larger radius (R_2) at the base to a smaller radius (R_1) at the top. This variation follows the projection of the spring in the plant plane, forming a spiral (Figure 3.9A). The equation of this spiral can be expressed in terms of the angular ratio (α) or the number of turns (N), allowing a precise mathematical modelling of its geometry.

$$R(\alpha) = R_1 + \left(\frac{R_2 - R_1}{2\pi N_a}\right)\alpha \tag{47}$$

$$R(N) = R_1 + \left(\frac{R_2 - R_1}{N_a}\right)N \tag{48}$$

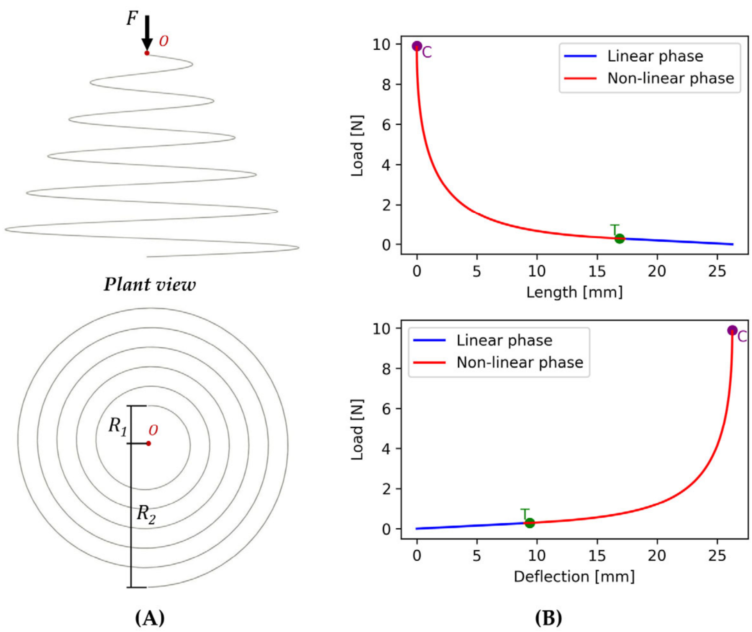

Figure 3.9: (A) Conical spring subjected to a force F. (B) Load-length and load-deflection curves of the conical spring. Special thanks to M. Eng. Alex De Blas for his support and help with this illustration.

To determine the deflection of a conical spring, equation (42) is used, adjusting the value of R according to the spring geometry. The results for the spring stiffness are defined in equations (49) and (50) depending on whether the cross section is circular or square.

$$k_{circular\ cross-section} = \frac{Gd^4}{16N_a(R_1 + R_2)({R_1}^2 + {R_2}^2)} \tag{49}$$

$$k_{square\ cross-section} = \frac{Gd^4}{\frac{8\pi}{2.25}N_a(R_1 + R_2)({R_1}^2 + {R_2}^2)} \tag{50}$$

The behavior of the conical spring during compression is characterized by two main phases. In the linear phase, all coils are active and contribute to deformation. The largest, completely free coil defines the behavior of the system, and the relationship between load and deflection is linear, as the spring rate remains constant. This linear section ends at the point T, when the largest coil reaches its maximum deflection and rests on the ground, ceasing to be an active element of the spring (Figure 3.9B).

In the non-linear phase, stiffness increases progressively due to the gradual stacking of the coils. During this stage, the number of free coils (N_f) decreases from N_a to 0, while the stacked coils ($N_a - N_f$) stop contributing to the deformation. This behavior generates a non-linear characteristic curve, which culminates at the point C when the last free coil, corresponding to the smallest radius (R_1), reaches its maximum deflection and defines the maximum load P_c (Figure 3.9B).

The maximum elementary deflection at the ground, corresponding to the maximum geometric deflection ($\delta_{geom,max}$), can be calculated directly for the conical spring. This deflection is key to describe the behavior in the transition and full compression phases.

$$\delta_{geom,max} = \frac{L_a}{N_a}N_f \tag{51}$$

In the load-length curve of the conical spring, the transition point T marks the boundary between the linear and non-linear phases. The point T is defined by two coordinates: the transition load (F_T) and length (L_T). F_T corresponds to the load at which the largest active coil (R_2) reaches its maximum geometric deflection. This is calculated by equating the elemental deflection (equation (43)), considering the spring as a helical spring with radius R_2, and the maximum geometrical deflection of the coil (equation (51)), allowing F_T to be determined.

$$\frac{\varepsilon F_T {R_2}^3}{Gd^4} = \frac{L_a}{N_a} \tag{52}$$

$$F_T = \frac{1}{\varepsilon} \cdot \frac{L_a}{N_a} \cdot \frac{Gd^4}{{R_2}^3} \tag{53}$$

Once this value is known, the length is derived directly.

$$L_T = L_a - \frac{F_T}{k} \tag{54}$$

In the final compression state, the point C defines the minimum length L_C associated with the maximum load F_C. F_C is the load for which the smallest active coil (R_1) reaches its maximum elementary deflection. Similar to the point T, the value F_C is obtained analytically, and L_C, being a telescopic spring, is taken to be zero.

$$F_C = \frac{1}{\varepsilon} \cdot \frac{L_a}{N_a} \cdot \frac{Gd^4}{{R_1}^3} \tag{55}$$

With these points (O, T and C) completely defined, the basis for analyzing and modelling the characteristics of the conical spring is established. To describe the load-length curve of the conical spring (Figure 3.9B), analytical expressions that capture both the linear and non-linear phase are used. In both phases, the spring length L is determined from the initial spring length (L_a) and the deflection caused by the applied load $\delta(F)$:

$$L(F) = L_a - \delta(F) \tag{56}$$

During the linear phase, the spring rate is constant, the deflection follows a direct relationship with the load:

$$\delta(F)_{linear\ phase} = \frac{F}{k} \tag{57}$$

In the non-linear phase, the total deflection of the spring for a given load is obtained by summing the individual deflections of each angular segment, treating them as if they were part of a helical spring (equation (43)). These individual deflections are limited by their maximum geometric values (equation (51)). In this case, the total deflection includes both the deflections of the free (δ_f) and stacked coils (δ_s):

$$\delta(F)_{non-linear\ phase} = \delta_f + \delta_s \tag{58}$$

$$\delta(F)_{non-linear\ phase} = \int_0^{N_f} \frac{\varepsilon F[R(N)]^3}{Gd^4} dN + \int_{N_f}^{N_a} \frac{L_a}{N_a} dN \tag{59}$$

At this stage, N_f, the number of current free coils, can be calculated as the value for which elementary deflection of free coils reaches the maximum geometrical deflection at ground, for any load value F between F_T and F_C:

$$\frac{F\left[R\left(N_f\right)\right]^3}{Gd^4} = \frac{L_a}{N_a} \tag{60}$$

$$N_f(F) = \left(\sqrt[3]{\frac{L_a}{N_a} \cdot \frac{Gd^4}{\varepsilon F}} - R_1\right) \cdot \frac{N_a}{R_2 - R_1} \tag{61}$$

As in the previous case, the analytical model is implemented in Python. The three-dimensional visualization of the conical spring is done with the *Plotly* library [164], using the spatial coordinates calculated for the spring helix. The radius is linearly interpolated from its maximum value to its minimum value along the Z-axis, with a defined length (L_a). Using parametric equations, find the Z coordinates as a function of the angle (α), considering the total number of active coils (N_a) according to equation (47). These coordinates allow the generation of a 3D graph that provides an orthographic view of the spring (Figure 3.10), which is essential for validating its geometry and analyzing its spatial characteristics in applications that require high precision.

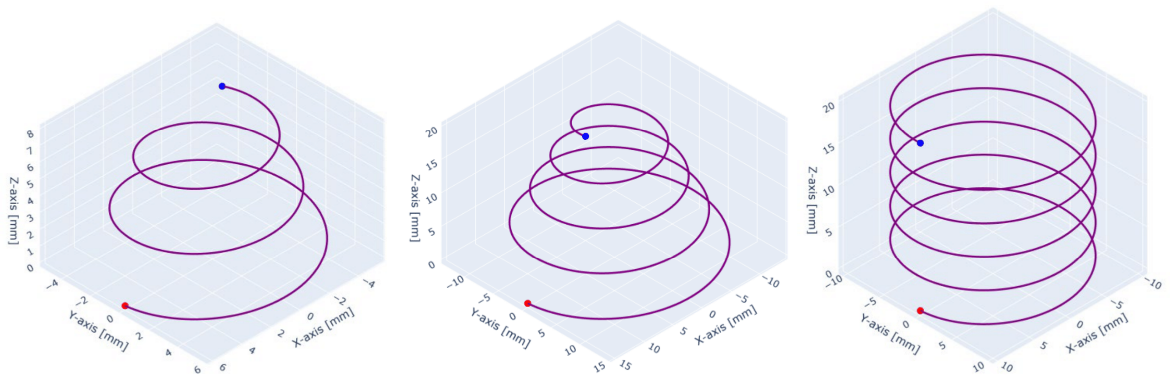

Figure 3.10: 3D representation of a conical springs with different geometrical parameters. Helical springs can be represented when the larger and smaller radii are equal.

In addition to the geometric representation, the implemented analytical model uses symbolic computation with the Python library *SymPy* [161] to evaluate the mechanical behavior of the conical spring. This approach allows the non-linear equations associated with its deformation under load to be solved. Symbolic computation is used to derive analytical expressions describing the force-deflection relationships, thus obtaining the characteristic curve of the spring. This allows the code to calculate equations as a function of variables and evaluate how these affect the curve when geometric parameters or material properties are changed. This tool is invaluable as it allows mechanical evaluation of the spring without the need to design it in CAD/CAE software or manufacture it using conventional or additive methods.

The code also generates the force-deflection curve by defining the spring parameters and calculates its stiffness in the linear region. In addition, it allows designers to analyze how the various parameters affect the conical spring's characteristic curve (Figure 3.11A). For key aspects of the design, variations in spring rate (k), transition (F_T) and maximum (F_C) force are also evaluated as a function of these variables. The graphs obtained, with all but one variable held constant ($R_1 = 10mm, R_2 = 30mm, L_a = 20mm, N_a = 3$ and $G = 10GPa$) and a circular cross-section ($d = 1mm$), clearly show the relationship between the geometric and material parameters and the mechanical spring behavior.

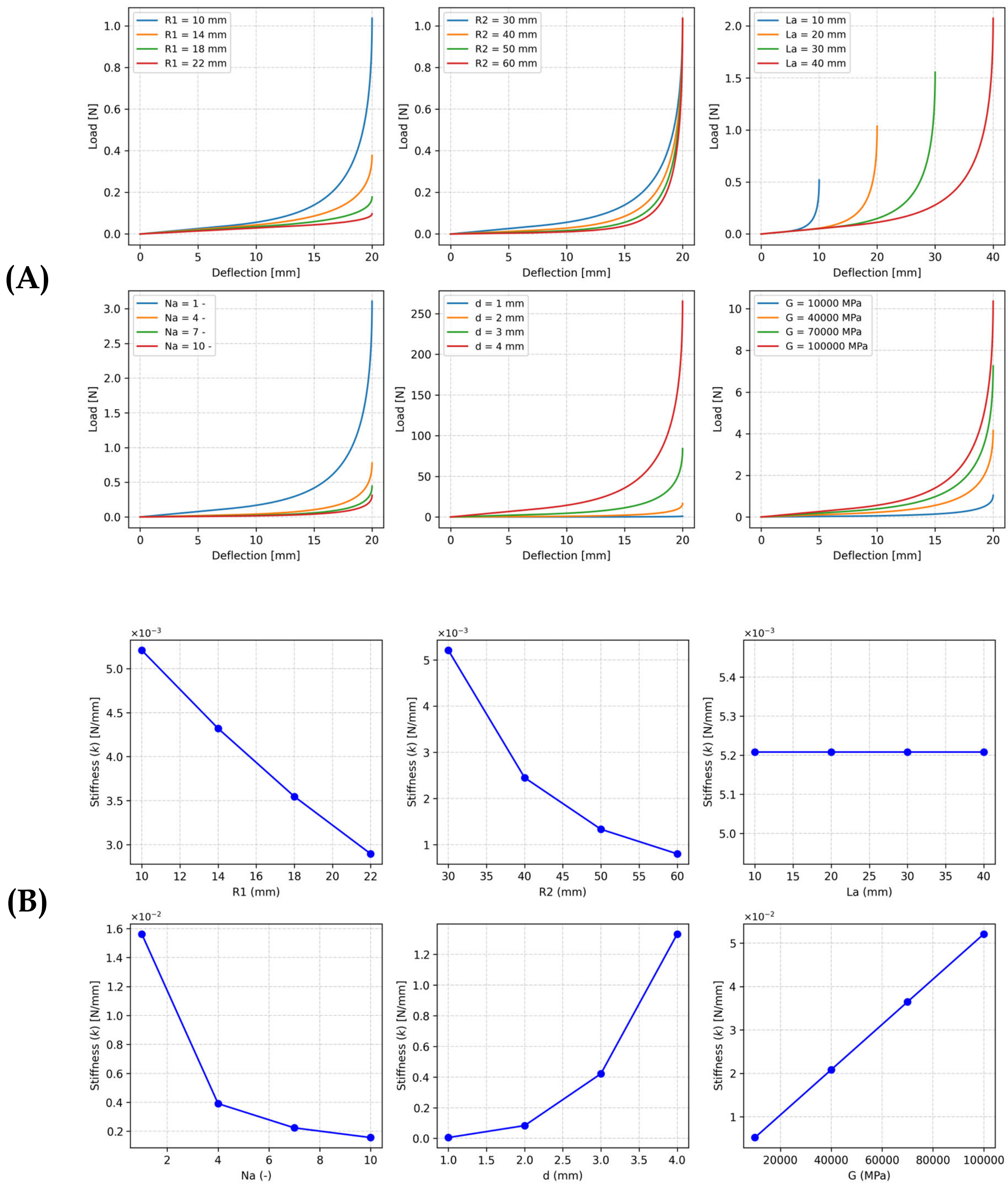

Figure 3.11: (A) Load-deflection curves and (B) conical spring rate behavior varying one parameter at a time ($R_1 = 10mm, R_2 = 30mm, L_a = 20mm, N_a = 3$, $G = 10GPa$ and $d = 1mm$).

Figure 3.11B shows that the spring rate (k) has a decreasing exponential relationship with the parameters R_2 and N_a, while it increases exponentially with d. On the other hand, there is a linear relationship between spring stiffness and the parameters R_1 and G: it increases with R_1 and decreases with G. The influence of L_a is not reflected in the analytical formulation, resulting in a constant stiffness value regardless of L_a, as this variable is not part of equation (49).

In the force analysis (Figure 3.12), all variables except R_1 and R_2 affect F_C and F_T in an equivalent way, but with different magnitude ($F_C > F_T$). There is a linear increasing relationship between these forces and the parameters L_a and G, while the relationship is exponentially increasing with d and decreasing with N_a. For radii, according to equations (53) and (55), R_1 influences F_C and R_2 influences F_T inversely. Therefore, R_1 and R_2 affect only one of the forces, as shown in the graphs, where F_C remains constant when R_2 is varied and the same is true for F_T when R_1 is varied. Although these conclusions have been derived for a spring with a circular cross-section, they would also apply to a spring with a square cross-section.

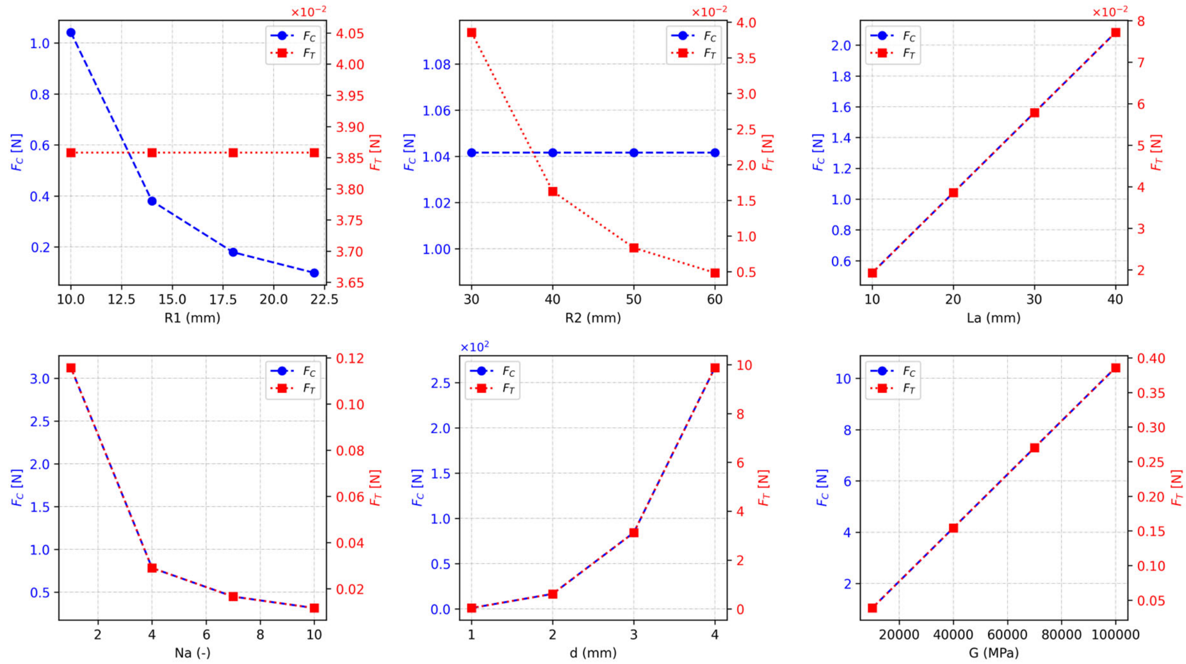

Figure 3.12: Transition (F_T) and maximum (F_C) load varying one parameter at a time.

By understanding how each design variable influences spring's behavior, it is possible to determine whether adjustments to geometric parameters (R_1, R_2, L_a, N_a and d) or material properties (G) are required to achieve the desired performance. In this context, metaheuristic algorithms provide a powerful tool for optimizing the design of conical springs to ensure appropriate mechanical behavior. For instance, the Bees algorithm has been successfully applied to optimize the parameters of torsion and compression springs in folding wing mechanisms [165]. Furthermore, a recent study introduced an automated inverse design method for spiral torsion springs using a non-linear constrained global optimization algorithm, this method ensures that the springs satisfy complex mechanical requirements while improving the efficiency and accuracy of the design process [166]. By using these approaches, the design space can be systematically explored, enabling the identification of optimal configurations that align with the desired force-deflection curve.

3.3. Finite element modelling

Finite element method (FEM) is a sophisticated numerical technique widely used in engineering to solve complex problems involving irregular geometries, non-linear material properties and varying boundary conditions. In the presence of nonlinearity and dynamic effects, analytical solutions become practically unreachable [167]. Formally introduced in the 1960s, FEM has become an essential tool in disciplines such as structural mechanics, heat transfer and fluid dynamics. Its strength lies in its ability to transform continuous problems governed by partial differential equations (PDE), which are difficult to solve analytically, into systems of algebraic equations that can be solved efficiently by computation [168].

At its core, FEM divides the problem domain into smaller subdomains, called *elements*, which are connected at specific points, called *nodes* (see Figure 3.13). This discretization process transforms a continuous problem into a discrete one, where each element is treated as an independent entity. The mathematical relationship between the elements is established by a global system of equations [169]. Instead of solving for unknown continuous functions (e.g. displacement fields), FEM focuses on solving for discrete node values (e.g. displacements at nodes). In three-dimensional problems, each nodal displacement is represented as a vector with three components, resulting in a total number of unknowns equal to three times the number of nodes [167].

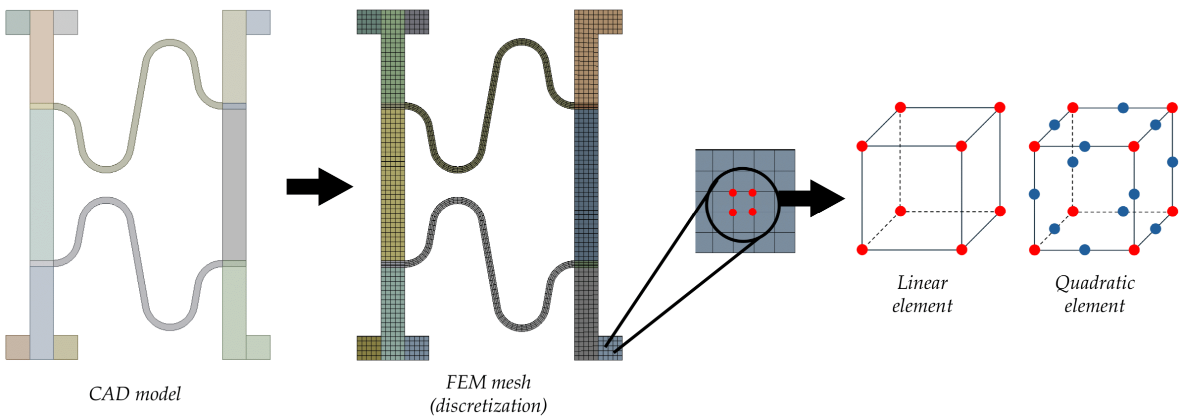

Figure 3.13: Discretization of a CAD object to create a mesh of elements connected by nodes. These elements may be linear or quadratic.

The FEM is based on robust mathematical principles which ensure that the approximate solution is a faithful representation of the system's physical behavior. The main foundations include the virtual work principle, the Galerkin method and the Rayleigh-Ritz theorem, each of which plays a key role in the formulation and solution of the problem.

The virtual work principle states that for a system in equilibrium, the work done by the internal forces is equal to the work done by the external forces. This principle is fundamental because it ensures that the system remains in equilibrium in its approximate representation. The Galerkin method, on the other hand, is a technique for obtaining approximate solutions to differential equations. In the context of FEM, it is used to project the original PDE into a space of "basis" functions, resulting in a system of algebraic equations that describe the approximate system's behavior. This method ensures that the error of the approximate solution is minimal, i.e. that the solution is the best possible within the chosen function space [170].

The discretization step involves dividing the domain into elements of predefined shapes (e.g. tetrahedron or hexahedron, Figure 3.13). Each element is characterized by shape functions, which are interpolation functions that describe how variables such as displacement vary within the element. These functions, typically polynomials, provide continuity between elements and numerical stability in the calculations [171].

Once the elements and their shape functions are defined, the local equations for each element are combined into a global system. The displacements at the nodes, called degrees of freedom (DOFs), fully define the behavior of the system. For static problems, the equilibrium equation is expressed as [167]:

$$[K]\{D\} = \{F\} \tag{62}$$

Where $[K]$ is the stiffness matrix, $\{D\}$ is the node displacement vector and $\{F\}$ is the external force vector derived from the boundary conditions. In linear problems, $[K]$ is constant, but in nonlinear cases it depends on $\{D\}$ [167].

After solving the discrete node displacements, the displacement fields $\{u\}$ are computed by interpolating these values using shape functions. For example, in a 2D 4-node quadrilateral element, the nodal displacement vector $\{d\}$ contains eight components [167]:

$$\{d\} = \{d_1 \quad d_2 \quad d_3 \quad d_4 \quad d_5 \quad d_6 \quad d_7 \quad d_8\} \tag{63}$$

The displacement fields are then calculated as [167]:

$$\{u\} = [N]\{d\} \tag{64}$$

Where $[N]$ is the shape function matrix that links the discrete nodal displacements $\{d\}$ with the continuous displacement fields $\{u\}$. Linear shape functions, used in first-order elements, interpolate displacements between nodes located only at the vertices of the element, providing a simpler but less accurate representation. In contrast, quadratic shape functions, used in second-order elements, add intermediate nodes along the edges, allowing more accurate interpolation by capturing more spatial detail, particularly in complex geometries or problems with high gradients (Figure 3.13) [167].

For dynamic cases, inertia and damping effects need to be added to equation (62) [167]:

$$[M]\{\ddot{D}\} + [C]\{\dot{D}\} + [K]\{D\} = \{F\} \tag{65}$$

Where $[M]$ is the mass matrix and $[C]$ is the damping matrix. The terms on the left-hand side represent inertia, damping and elastic forces respectively, while the terms on the right-hand side correspond to external forces. In FEM, the methods for solving the global system (equation (65)) can be classified as implicit and explicit [167].

3.3.1. Implicit finite element method

As mentioned, dynamic simulations involve solving the equation (65). Consider a typical time step at t_n. Let D_n, $\dot{D}_n$ and $\ddot{D}_n$ be the displacement, velocity and acceleration at t_n, and D_{n+1}, $\dot{D}_{n+1}$ and $\ddot{D}_{n+1}$ at t_{n+1}. Also, let $\Delta t = t_{n+1} - t_n$. Then, by Taylor series expansion at t_n [167]:

$$\dot{D}_{n+1} = \dot{D}_n + \Delta t \ddot{D}_n + \frac{\Delta t^2}{2} \dddot{D}_n \tag{66}$$

$$D_{n+1} = D_n + \Delta t \dot{D}_n + \frac{\Delta t^2}{2} \ddot{D}_n + \frac{\Delta t^3}{6} \dddot{D}_n \tag{67}$$

$\dddot{D}_n$ can be approximated by [167]:

$$\dddot{D}_n = \frac{\ddot{D}_{n+1} - \ddot{D}_n}{\Delta t} \tag{68}$$

Substitution of equation (68) into equation (66) and (67) respectively gives [167]:

$$\dot{D}_{n+1} = \dot{D}_n + \frac{\Delta t}{2} \left(\ddot{D}_{n+1} + \ddot{D}_n \right) \tag{69}$$

$$D_{n+1} = D_n + \Delta t \dot{D}_n + \ \Delta t^2 \left(\frac{1}{6} \ddot{D}_{n+1} + \frac{1}{3} \ddot{D}_n \right) \tag{70}$$

The method is called implicit because the calculation of $\dot{D}_{n+1}$ and D_{n+1} requires knowledge of $\ddot{D}_{n+1}$. This means that the response at the current time step depends not only on the historical information but also on the current information. Therefore, the solution of equations (69) and (70) involves an iterative process [167].

This feature increases the computational cost but ensures numerical stability, even at relatively large time steps. This is particularly beneficial when dealing with complex geometric or material nonlinearities, or in quasi-static analyses where inertial effects progressively decrease [169,170]. For implicit methods, the integration time step typically ranges from milliseconds, and a simulation lasting between 0.1 and 10 seconds usually requires hundreds to ten-thousands of integration time steps [167].

Implicit methods are effective for most dynamic structural simulations, especially when the problem involves moderate nonlinearities and stable dynamic conditions. However, in highly nonlinear problems, these methods often face convergence issues. Additionally, for high-speed impact problems, the integration time steps become so small that the required computational time becomes prohibitive. In these situations, explicit methods are more appropriate, as they can efficiently handle small time steps without the need for iterative processes [167].

3.3.2. Explicit finite element method

The explicit method is based on half-step central differences [167].

$$\dot{D}_{n+1} = \dot{D}_n + \frac{\Delta t}{2}\left(\ddot{D}_{n+1} + \ddot{D}_n\right) \tag{71}$$

$$D_{n+1} = D_n + \Delta t \dot{D}_n + \Delta t^2 \left(\frac{1}{6}\ddot{D}_{n+1} + \frac{1}{3}\ddot{D}_n\right) \tag{72}$$

Equations (71) and (72) are described as explicit methods because the calculation of $\dot{D}_{n+1}$ and D_{n+1} only involves knowledge of historical information. This means that the response at the current time can be calculated explicitly, no iterations within a time step are required. One of the peculiarities of the explicit method is that its integration time step must be very small to obtain a stable solution [167].

Explicit methods are particularly suitable for fast transient events, such as high-speed impacts, explosions or highly non-linear problems. Their efficiency lies in their ability to compute the system response directly, without the need for iterative processes. However, the stability of explicit methods depends on the choice of a sufficiently small-time step to satisfy the Courant-Friedrichs-Lewy condition. This requirement ensures numerical stability but imposes a significant limitation [172].

While explicit methods excel in simulations of fast, short-lived phenomena, they become impractical for slow or quasi-static problems with long durations. In such cases, the need for extremely small-time steps leads to prohibitive computational costs. Consequently, explicit methods are most effective for scenarios requiring high temporal resolution over short intervals, as opposed to problems with slower dynamics or longer time frames [167].

As highlighted in the previous section, the FEM is a powerful tool that can optimize the design of different types of springs subjected to different loading conditions. This method allows the analysis of tension/compression, bending, torsion and combinations of these loading scenarios, providing a detailed evaluation of their mechanical behavior. It is also particularly useful for studying critical phenomena such as buckling and predicting possible catastrophic failures, thus ensuring a more reliable and efficient design of the component [156,173,174].

3.4. Degradable Polymers

Degradable polymers are defined by substantial structural modifications, primarily evidenced by a decline in molecular weight when exposed to specific environmental or biological conditions [175,176]. Factors that promote such transformations include humidity, ultraviolet radiation and the action of various microorganisms. In order to regulate and classify these "degradable plastics", the American Society for Testing and Materials (ASTM) formed in 1988 the Subcommittee D-20.96 (Committee on Plastics). This committee established standardization criteria, including those included in ASTM D883 [177], which describes the different degradation routes such as photodegradation, oxidation, hydrolysis and biodegradation, and defines specifications for the materials that present them [175–177]. Some basic degradability terms are summarized in Table 3.2.

Table 3.2: Polymeric degradation terminology [176–178].

Term	Definition
Bioassimilation	The conversion of a polymeric material into biomass
Biodegradable	Describes a polymeric material that is capable of biological degradation
Biodegradable plastic	A type of degradable plastic whose decomposition is driven by naturally occurring microorganisms (e.g. bacteria, fungi, algae)
Biodegradation	The degradation of polymeric material by cell-mediated processes
Bulk degradation	A scenario in which the interior of a polymeric material degrades more rapidly than its surface
Degradable	Refers to a polymeric article that is capable of undergoing degradation
Degradable plastic	A plastic that is designed to undergo a significant structural change under certain environmental conditions, resulting in a measurable loss of certain properties within a time period that defines its classification
Degradation	Any deleterious change in the chemical composition, physical properties or appearance of a polymer, often involving scission of chemical bonds, regardless of the specific scission mechanism
Dissolution	The process by which the macromolecules that make up a polymeric item dissolve in a liquid medium
Hydrolytic degradation	Degradation specifically identified as resulting from hydrolytic scission of macromolecules
Hydrolytically degradable plastic	A type of degradable plastic that degrades primarily by hydrolysis
Surface degradation	A more pronounced alteration at the surface of a polymeric material than in its interior

From a chemical perspective, degradation leads to alterations in the polymer structure and properties, which can be observed through mechanical, optical or thermal characteristics. These alterations can occur in a sequential or concurrent manner, often catalyzed by integrated mechanisms, such as exposure to solar radiation and oxygen supply, or elevated humidity and the presence of microorganisms. The investigation of these processes is imperative to optimize the lifespan of materials according to the requirements of each application. In the environmental field, their use is directed towards the substitution of conventional plastics by products with a programmed degradation [175,176]. In the biomedical industry, these characteristics are exploited to engineer implants and devices that, upon fulfilling their function, undergo fragmentation, thereby averting potential complications associated with the accumulation of polymeric waste [179–181].

3.4.1. Water soluble polymers

Water-soluble polymers represent a group of these materials with the characteristic of dissolving or swelling in aqueous media, due to the presence of hydrophilic groups in their chemical structure. This class can be derived from natural sources, modified semi-synthetically or designed entirely by industrial synthesis routes. Water solubility, in all cases, is determined by a combination of molecular interactions between the polymer and the surrounding medium, as well as the material's internal morphology, which governs the diffusion of water molecules within the polymer matrix. When a soluble polymer is placed in contact with water, an erosion phenomenon can be observed, which typically manifests in two distinct forms: surface and bulk erosion [176].

Surface erosion occurs when the rate of decomposition or reaction, driven by hydrolysis or solubilization, exceeds the diffusion rate of water into the polymer. Under these conditions, the material gradually thins from the outer surface while maintaining its structural integrity in the inner regions, which preserve a relatively high molecular weight until the later stages of degradation. Bulk erosion, on the other hand, occurs when water penetration is rapid or comparable to the reaction rate, so that the polymer matrix undergoes uniform degradation throughout its thickness and experiences a progressive reduction in its mechanical properties. The distinction between the two processes is important because erosion control allows the tailoring of drug, nutrient or active ingredient release profiles and the determination of the temporary persistence of the polymer in the aqueous environment (Figure 3.14) [176,182].

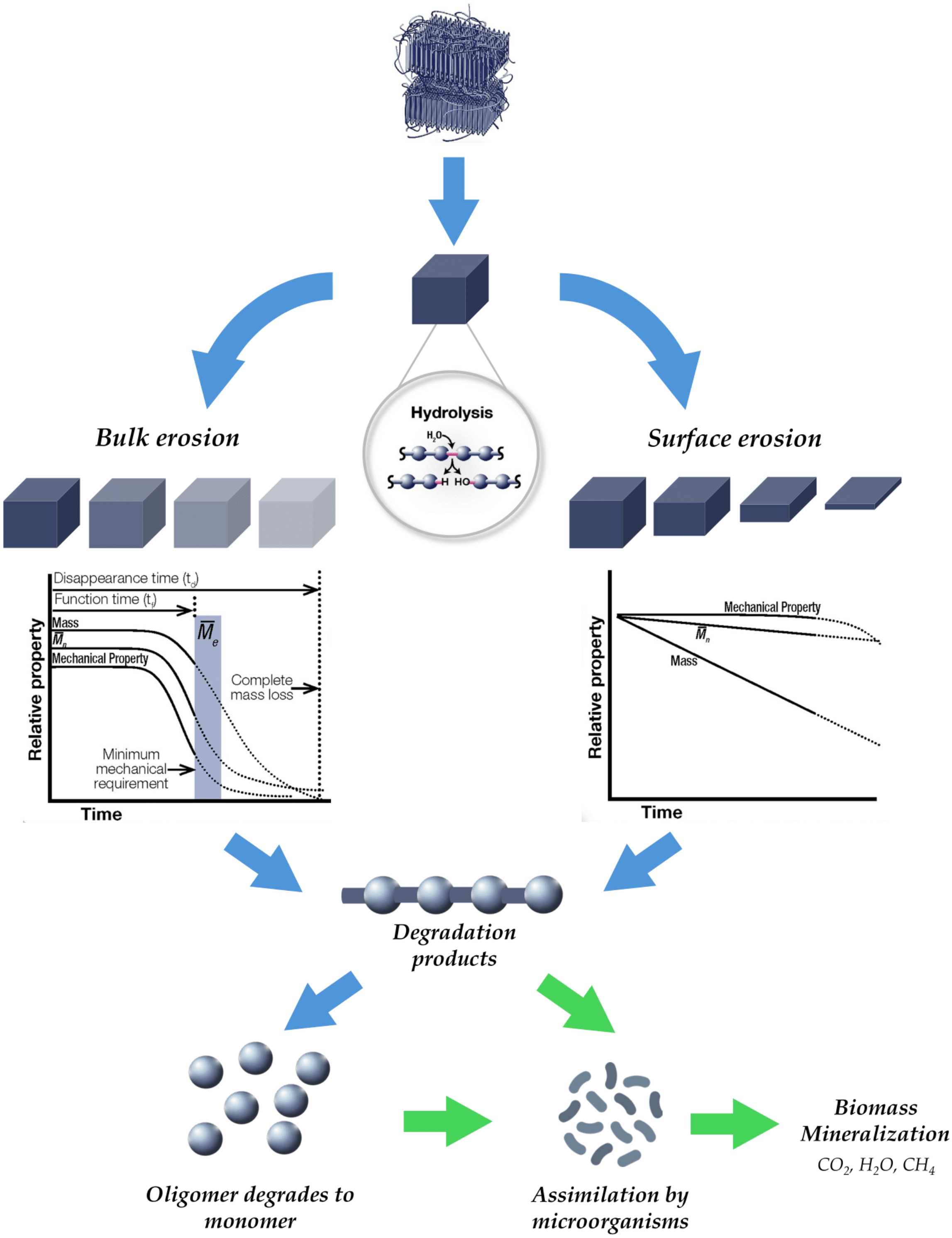

Figure 3.14: Polymer biodegradation through hydrolysis under surface and bulk erosion. Blue arrows represent the hydrolysis process, while green ones represent the biodegradation process. Adapted from [176]. Special thanks to M. Eng. Alex De Blas for his support and help with this illustration.

3.4.2. Biodegradable polymers

The biodegradability of polymers is defined as the ability of these materials to be assimilated, totally or partially, by microorganisms (bacteria, fungi, yeasts) under appropriate environmental or biological conditions, producing CO_2, H_2O and biomass under aerobic conditions, or CH_4 and H_2O in anaerobic environments [183–185].

Structurally, biodegradability is strongly influenced by factors such as crystallinity, the presence of functional groups susceptible to hydrolysis, molecular weight and the incorporation of additives (e.g. plasticizers or degradation catalysts) [183,186]. Morphological properties (porosity, size, part geometry) and processing conditions are also determinants of the degradation rate and mechanism [176]. In practice, the biodegradation of a polymer goes through several stages [185–188]:

1. Biodeterioration: initial fragmentation of the polymer matrix, facilitated by the combined action of enzymes, mechanical and chemical means.
2. Depolymerization: breaking polymer chains into oligomers and monomers.
3. Assimilation: incorporation of the resulting products into microbial metabolism for biomass and energy synthesis.
4. Mineralization: complete oxidation leading to the formation of CO_2, H_2O, CH_4 and salts.

In the biomedical field, biodegradable polymers have gained prominence in the manufacture of temporary implants, tissue engineering scaffolds and controlled drug delivery systems [176]. In such contexts, degradation must not only ensure the elimination of the material once its function has been fulfilled but also avoid the accumulation of toxic by-products in the body. This dual requirement, predetermined service time and biocompatibility of degradation products, represents one of the major challenges in the engineering and design of new polymers for biomedical applications [176,185].

3.5. Poly(vinyl) alcohol

Poly(vinyl alcohol) (PVA) is considered one of the most commercially and scientifically relevant water-soluble polymers due to its wide range of applications and advantageous physicochemical properties [189]. Although the term "poly(vinyl alcohol)" refers to a polymer derived directly from vinyl alcohol, this monomeric species is unstable and tends to tautomerize[21] to acetaldehyde [191,192]. Therefore, the synthetic route to PVA is via poly(vinyl acetate) (PVAc). Its general structure consists of a main chain of carbon atoms with hydroxyl groups on alternating carbons [193].

PVA is a semicrystalline material with a predominantly amorphous phase [185]. Due to the abundance of hydroxyl groups in its structure, it has a high affinity for water and exhibits water solubility, resulting in excellent film-forming, emulsifying and adhesive properties. It

[21] Addition of a hydrogen atom at one molecular site and its removal from another [190].

also has high tensile strength and good flexibility and acts as a barrier to oxygen and aromas [194–196]. However, its melting point is very close to its decomposition temperature, which is why plasticizers are required for processing by extrusion or injection molding [185].

On the other hand, modifications with natural fibers and fillers can improve the mechanical properties of PVA without affecting its degradability [43]. In the PVA matrix, the incorporation of nanomaterials increases the interaction between the chains, resulting in higher mechanical strength and new functionalities such as increased water resistance and improved barrier properties [197]. PVA is considered a biodegradable polymer under aerobic and anaerobic conditions, mainly due to the presence of hydroxyl groups that promote hydrolysis and chain scission[22] [199]. Importantly, PVA can maintain its stability over a wide pH range, which contributes to its versatility in different environments [200].

These properties have made PVA a material of choice for a wide range of industrial applications: from textile sizing and paper coatings to water-soluble flexible packaging, dialysis membranes, controlled drug release systems and wound dressings, among others [194]. In addition, its high biocompatibility allows it to be used in the biomedical field, for example in the production of artificial skin [201]. Its relatively low cost, combined with its ease of processing and biodegradability, has significantly boosted its adoption in the field of 3D printing [185].

3.5.1. Synthesis

PVA was first synthesized by Hermann and Haehnel in 1924 [202]. Unlike many polymers, it is not obtained by polymerization of its monomer, vinyl alcohol, as this monomer does not exist in a stable free state due to its spontaneous conversion to the enol form of acetaldehyde, driven by thermodynamic considerations [194,203]. Instead, PVA is derived from the parent homopolymer PVAc by a process involving polymerization and subsequent hydrolysis [182].

First, vinyl acetate is polymerized to PVAc using conventional methods such as bulk, solution or emulsion polymerization [193]. The resulting PVAc is then dissolved in an organic solvent, often methanol due to its superior penetration and effectiveness in facilitating the ester exchange reaction. During this process, the PVAc is hydrolyzed, catalyzed by sodium hydroxide (NaOH) or occasionally hydrochloric acid (HCl), to produce PVA. The reaction is endothermic and involves the replacement of acetate groups with hydroxyl groups, forming a mixed polymer containing both hydroxyl and acetyl groups [192,204]. Methanol is a by-product, forming methyl acetate during the reaction [204]. A schematic representation of the PVA synthesis process is shown in Figure 3.15.

[22] The term chain scission refers to the process of breaking of chemical bonds within a polymer chain, resulting in a reduction of its molecular weight and degradation of the polymer [198].

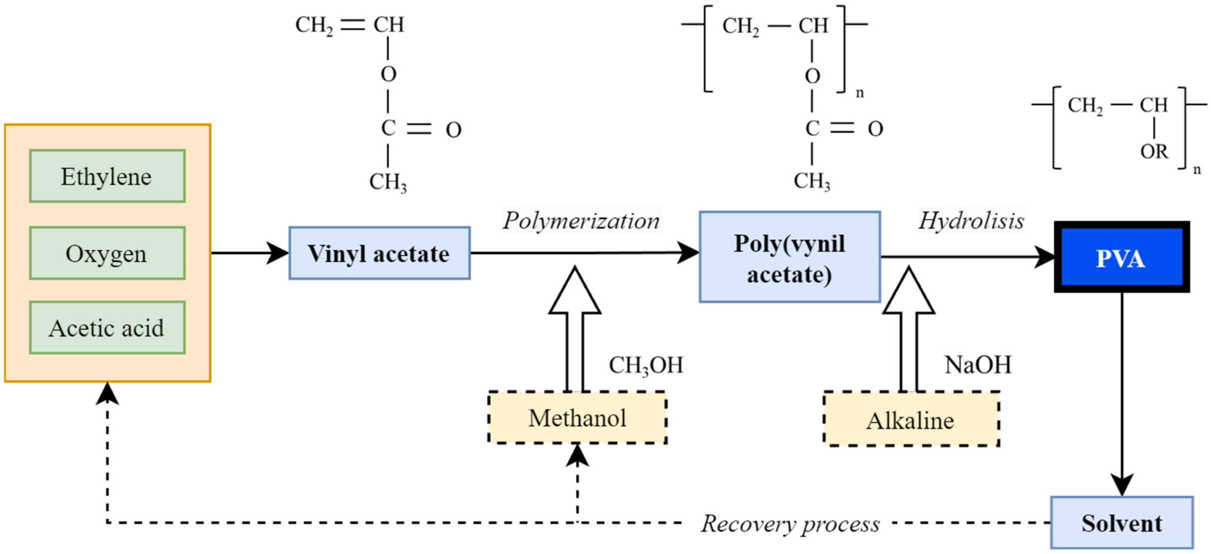

Figure 3.15: Production outline of PVA. "R" represents either H or $COCH_3$. Based on [194,196,205,206]. Special thanks to M. Eng. Alex De Blas for his support and help with this illustration.

The water solubility of PVA is largely influenced by the increased hydroxyl group content, which is directly related to the degree of hydrolysis (the ratio of hydroxyl to acetyl groups) [207]. As a result, PVA is classified into two classes: fully and partially hydrolyzed. Fully hydrolyzed PVA (90-99.5%mol) is highly soluble in water and almost insoluble in organic solvents, while partially hydrolyzed PVA contains both hydrophilic and hydrophobic regions, making it a copolymer of vinyl alcohol and vinyl acetate (Figure 3.15) [191,204,208]. The degree of hydrolysis, which is a critical parameter in determining PVA properties, can be controlled by catalyst concentration and hydrolysis temperature [185].

The hydrolysis reaction removes acetate groups without altering the long-chain polymer structure of PVAc. If the reaction is incomplete, the resulting polymer will have reduced water solubility and increased solubility in certain organic solvents [182,207]. The degree of hydrolysis is commonly measured by titration[23], where the remaining acetate groups are quantified [210].

The physical and chemical properties of PVA, including crystallinity, molecular weight and degree of hydrolysis, play an important role in its functional applications [197,205]. In addition, factors such as the production process of the precursor PVAc, water content and additives such as plasticizers further influence the PVA properties [203]. Commercially, PVA grades with degrees of hydrolysis ranging from 70% to 99% are available to meet specific application requirements [182].

[23] A method of accurately determining the amount of a substance in a solution by gradually adding measured amounts of another substance that reacts in a known way (e.g. by causing a color change) [209].

3.5.2. Solubility

PVA is a hydrophilic polymer whose solubility in water and other polar solvents depends on structural and physicochemical factors such as its chemical composition, crystallinity, degree of hydrolysis, molecular weight and processing conditions. These aspects determine the interaction of the polymer with the solvent molecules and are fundamental to understanding its behavior in industrial and scientific applications [193,210].

The degree of hydrolysis, an indicator of the percentage of acetate groups converted to hydroxyl groups during the conversion of PVAc to PVA, is a critical factor influencing its solubility. Partially hydrolyzed PVA contains residual acetate groups which reduce the formation of hydrogen bonds between polymer chains and favor interaction with water molecules. This increases solubility, particularly at low temperatures. For example, a PVA with a degree of hydrolysis of 87-89% is soluble in both cold and hot water, while fully hydrolyzed grades require higher temperatures due to increased intramolecular hydrogen bond formation [193,210,211].

The molecular weight of PVA, which is closely related to its degree of polymerization (DP), also influences its solubility. As the molecular weight increases, the density of intermolecular bonds increases, making it more difficult for water to access the polymer chains and reduce solubility. This decrease in solubility is reflected in a higher solution viscosity and a reduction in the diffusion coefficient of water in the polymer matrix, which in turn increases the resistance to swelling and dissolution [204,212].

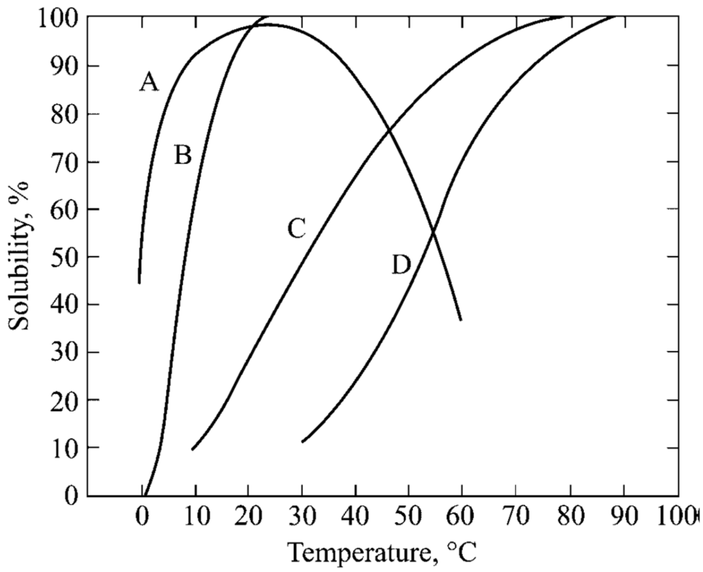

Figure 3.16: Solubility of PVA across molecular weights and degrees of hydrolysis: A, 78-81 mol% hydrolyzed, DP = 2000-2100; B, 87-89 mol% hydrolyzed, DP = 500-600; C, 98-99 mol% hydrolyzed, DP = 500-600 and D, 98-99 mol% hydrolyzed, DP = 1700-1800 [210].

The semi-crystalline structure of PVA, marked by the presence of both crystalline and amorphous regions, plays a crucial role in determining its behavior in solution. Crystalline regions, stabilized by strong hydrogen bonds and an ordered arrangement of chains, are less accessible to water, reducing solubility. In contrast, the amorphous, less structured regions interact more rapidly with water, facilitating the dissolution process [185].

Compared to its precursor, PVAc, PVA crystallizes because the hydroxyl groups are smaller and more flexible than the acetate ones. The larger acetate groups make it difficult to align the chains, which prevents polyvinyl acetate from crystallizing. In PVA, hydrogen bonds play a key role in facilitating the formation of an ordered structure that contributes to its high crystallinity. These bonds also stabilize its layered structure, allowing it to maintain a high degree of organization, even with the apparently random arrangement of OH groups [213].

Thermal processing of PVA significantly affects the arrangement of its molecular chains, which in turn influences its solubility. At elevated temperatures, these chains can reorganize into more crystalline regions, lowering solubility. This phenomenon is more pronounced in fully hydrolyzed grades, whereas partially hydrolyzed ones maintain higher solubility due to residual acetate groups that hinder the formation of such ordered structures [211,214].

PVA can be degraded by methods such as acoustic and hydrodynamic cavitation, which alter its crystallinity and fragment the polymer chains into lower molecular weight oligomers. These techniques not only facilitate its dissolution, but also increase its biodegradability, expanding the possibilities for sustainable applications [215]. Due to its hydrophilic nature and ease of processing, PVA readily forms blends with natural and synthetic polymers, enhancing its versatility in composite systems and advanced applications [193,210]. In addition, its solubility facilitates its biodegradation (Figure 3.14), as the process starts with water diffusion into the polymer matrix, followed by swelling, fragmentation and dissolution [193].

The hydrophilic nature of PVA, derived from its hydroxyl groups, and its ability to form both intra- and intermolecular hydrogen bonds are essential for its solubility and structural stability. However, these same properties can limit its interaction with water molecules under certain conditions. The interplay between factors such as degree of hydrolysis, molecular weight, crystallinity and processing conditions allows the properties of PVA to be tailored to meet the needs of different industries. In addition, its ability to form viscous solutions, biodegrade and blend with other polymers positions it as a key material in applications such as coatings, adhesives and biodegradable systems [193,210,211].

3.5.3. Biodegradability

PVA is a synthetic polymer of interest due to its ability to biodegrade under certain environmental conditions. However, it has also been identified as a relevant contaminant in industrial wastewater, particularly in the textile industry [216]. This problem has led to the investigation of the microorganisms responsible for its biodegradation and the factors influencing the process [199].

Biodegradation of PVA occurs through a sequential process starting with polymer chain scission by hydrolysis, which can be abiotic or enzymatically mediated [176]. This first step produces water-soluble oligomers and monomers. These products are then assimilated by microorganisms and converted to carbon dioxide (CO_2), water (H_2O) and metabolic products [176,185]. The biodegradation mechanism proceeds in two main stages: in the first, hydroxyl groups are randomly oxidized to ketones by the action of a secondary alcohol oxidase, resulting in the formation of β-diketones[24]. In the second stage, these β-diketones are cleaved by an extracellular hydrolase, producing terminal compounds such as carboxylic acid and methyl ketone groups. Finally, degradation proceeds to the formation of acetic acid, which is converted to CO_2 and H_2O [210].

Its biodegradability depends on several factors, both structural and environmental. The presence of hydroxyl groups in its structure facilitates processes such as oxidation and enzymatic hydrolysis, while environmental conditions such as temperature, pH and relative humidity also significantly influence its degradation. Furthermore, interaction with specific microorganisms can optimize this process, highlighting the crucial role of the microbiological and physical environment in polymer biodegradation [185,199].

PVA is unique among vinyl polymers in that it can be used as a carbon and energy source by certain microorganisms. Up to 55 different species, including bacteria, molds, yeasts and fungi, have been shown to degrade this polymer. These microorganisms are found in a variety of environments including activated sludge, compost, aquatic systems, soils and landfills [210].

Research has shown that blending PVA with natural polymers can be a promising strategy to increase its biodegradation rate in challenging environments. Polymers such as starch and cellulose not only improve the process but can also expand the range of applications of this material in environmental and industrial contexts [185,199].

In addition to its biodegradability, PVA is characterized by its bioinertness, biocompatibility and low cytotoxicity, properties that make it ideal for advanced applications in the biomedical field [218]. Over the last decade, its use as a drug carrier in controlled release systems, tissue engineering and implantable medical devices [51,219,220]. Its combination of biocompatibility and degradability has established PVA as a biomaterial of major importance in biomaterials research, significantly expanding its potential in the pharmaceutical and medical sciences [199].

[24] A molecule containing two ketones separated by one carbon [217].

3.6. Artificial intelligence

Artificial Intelligence (AI) is an interdisciplinary field of computer science that seeks to develop systems capable of performing tasks that traditionally require human intelligence, such as reasoning, sensory perception, learning, and decision-making. AI uses advanced mathematical models and algorithms to process large amounts of data, identify complex patterns and make predictions with high accuracy. This ability to adapt and improve on data is what distinguishes AI from traditional approaches to computing, which rely on explicitly programmed rules [221].

Since it was first conceptualized in the 1950s by Alan Turing and John McCarthy, AI has evolved significantly [222]. Initially limited to solving well-defined problems using symbolic approaches, it has moved on to methods based on machine and deep learning, which harness the power of large-scale data processing and modern computing capabilities [221].

The development of AI is divided into several subfields, each with specific approaches and goals. These subfields are machine learning, deep learning, and generative artificial intelligence.

- Machine learning: this subfield focuses on the development of algorithms and statistical models that allow machines to learn patterns from data. Through supervised, unsupervised and reinforcement learning, machine learning is applied to tasks such as classification, regression and prediction [221]. For example, recommendation systems used by streaming platforms are based on machine learning algorithms [223].
- Deep learning: an extension of machine learning, deep learning uses deep neural networks to model complex, non-linear data. These networks, made up of multiple layers of artificial neurons, are particularly effective at tasks such as image recognition, machine translation and natural language processing [224]. The success of deep learning is largely due to the availability of large data sets and advances in computing power [225].
- Generative artificial intelligence: this subfield, an advanced branch of deep learning, specializes in the creation of original content such as text, images, music and video from patterns learned from existing data. Using architectures such as generative adversarial networks and transformers, generative AI has revolutionized areas such as graphic design, synthetic data simulation and virtual assistant generation [226,227].

These subfields are not only complementary, but also overlap in their application, allowing complex problems to be addressed from different perspectives [228]. Their ongoing development is transforming many disciplines, from medicine to engineering, and will continue to be a key driver of innovation in the years to come [229,230]

3.6.1. Clustering algorithms

Clustering is a fundamental machine learning technique, in unsupervised learning, that allows datasets to be organized into clusters based on inherent similarities. Unlike supervised algorithms, clustering does not require prior labelling, making it ideal for exploring unknown or unstructured data. This ability to discover underlying patterns makes it an essential tool in a wide range of disciplines [221].

One of the most widely used clustering algorithms is K-Means, known for its simplicity and effectiveness. This algorithm tries to divide a dataset into a predefined number of clusters by minimizing the sum of the squared distances between the data points and the cluster centroids. The iterative process of K-Means begins with the initial selection of random centroids, continues with the assignment of each point to the nearest cluster, and ends with the recalibration of the centroids until either they converge, or a stopping criterion is met [231].

Image processing is an interdisciplinary field that uses computational techniques to analyze and manipulate images. A common first step is to represent the image in a processable format, such as a color space (RGB, HSV) where each pixel is represented by intensity vectors. Segmentation, a central task in this field, attempts to divide an image into meaningful regions, facilitating tasks such as edge detection, feature extraction, and classification [232].

The K-Means algorithm is often used for image segmentation because of its ability to group pixels into clusters based on features such as color or intensity. This approach starts by converting each pixel into a data point in a multidimensional space, where each dimension represents a feature of the pixel (e.g. its RGB components). K-Means groups these points into clusters, assigning each pixel a cluster label corresponding to its similarity to the others. This results in a segmentation where each region of the image corresponds to a cluster, simplifying further analysis [233].

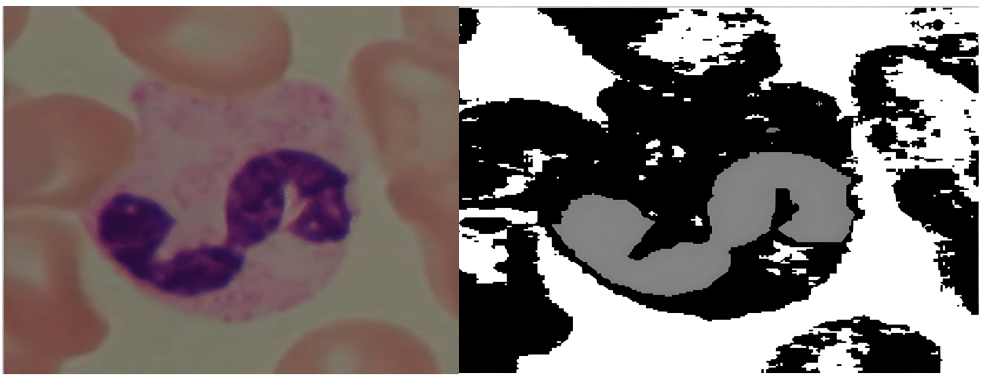

(A) **(B)**

Figure 3.17: (A) Original image of leukemic cells and (B) its segmentation using the K-Means algorithm [234]. The colors white, black and grey represent an image cluster.

Although effective in many contexts, K-Means has limitations, such as sensitivity to centroid initialization and the need to predefine the number of clusters. Alternatively, algorithms such as Density-Based Spatial Clustering of Applications with Noise (DBSCAN) and Hierarchical clustering offer more robust approaches to these challenges [221]. DBSCAN, for example, identifies clusters based on local data densities, allowing it to detect non-linear shapes and handle noisy data more effectively [235].

3.6.2. Generative artificial intelligence

Generative AI is one of the most innovative developments in AI, characterized by its ability to create original content from patterns learned from pre-existing data. This technology is based on advanced models, such as deep neural networks, that have been trained to generate text, images, music, video and other forms of content. Generative models use architectures such as generative adversarial networks (GANs), transformers and diffusion models, which have proven to be highly effective in creating realistic and useful content [226].

Two outstanding developments in this area are ChatGPT and DALL-E, both developed by OpenAI . ChatGPT is a transformer-based language model designed to generate coherent and relevant text [236]. This model uses large amounts of text data to learn linguistic and contextual patterns, enabling it to answer questions, write articles and perform virtual assistance tasks with high accuracy. On the other hand, DALL-E specializes in generating images from text descriptions, combining visual and conceptual elements in an innovative way. This model has revolutionized fields such as graphic design, advertising and artistic creation, facilitating the materialization of complex ideas in visual forms [227].

The impact of generative AI goes beyond content creation. In fields such as medicine, these models make it possible to simulate clinical scenarios and generate synthetic medical images to train diagnostic algorithms [237]. In education, they contribute to the design of adaptive learning materials that respond to the individual needs of students [238]. However, the implementation of these technologies also faces ethical and technical challenges, such as control over the generated content, intellectual property and mitigation of inherent biases in the training data [239].

3.6.3. Prompt engineering

Prompt engineering is an emerging technique in generative AI that focuses on optimizing the inputs provided to AI models, such as ChatGPT, in order to maximize the quality, relevance and utility of the outputs generated. As these models are highly dependent on the way in which the initial instructions or questions are formulated, the design of effective prompts has become an essential component to ensure successful outcomes in practical applications [240].

The concept of prompt engineering is based on fundamental principles such as clarity, context and iteration. Clarity involves writing prompts in a precise way, avoiding ambiguities that may generate undesired outputs. Context plays a crucial role in providing additional information or specific details that guide the model towards more useful responses. Finally, iteration allows the prompts to be continuously refined based on the results obtained, progressively improving the interaction with the model [227,240].

In the case of ChatGPT, its ability to generate coherent and contextual text was key to demonstrating the impact of good prompt design. For example, well-structured prompts allow ChatGPT to generate technical documents, answer complex queries, or emulate specific styles, while ambiguous instructions may lead to less accurate or unexpected results [241].

Prompt engineering is a powerful approach to interacting with AI models, but it also presents challenges, such as the need to thoroughly understand how models interpret instructions and to recognize their inherent limitations. Research suggests that small changes in prompt structure can lead to significant differences in model performance [242]. Furthermore, linguistic properties have been identified as critical factors in determining the success of a prompt [243].

As AI models evolve, this technique is likely to evolve further, promoting more intuitive and efficient human-machine interactions. Breaking complex tasks into simpler subtasks has been shown to enhance model performance in reasoning-intensive scenarios [244]. Reviews of prompt engineering techniques highlight its role in expanding the potential applications of AI across multiple domains [245].

For instance, design engineering has used ChatGPT through constructive dialogue to transform CAD models into innovative designs ranging from futuristic medical prostheses to buildings inspired by biological and artistic structures. These iterative dialogues have demonstrated how a methodological approach can lead to creative and practical proposals across disciplines, including bioengineering and architecture [246]. Additionally, the creation of knowledge graphs using generative techniques has enabled the identification of unexpected connections between seemingly disparate scientific concepts. In one case, structural parallels between biological materials and musical compositions were revealed, highlighting the potential of prompt engineering to foster interdisciplinary innovation by discovering new material designs and behavioral predictions [247].

4. Materials and methods

This chapter provides a detailed description of the materials, methods, and procedures used throughout this doctoral thesis, highlighting the chapters where each technical and scientific aspect is further detailed. It covers the conceptualization of shape-morphing actuators and implants and their computational design, the additive manufacturing of prototypes, and their mechanical, biological, and degradation validation. Additionally, it includes considerations regarding the implementation of anatomical test benches and the integration of artificial intelligence tools to optimize and conceive 4D devices.

4.1. Materials

The main materials used in this study were polyethylene terephthalate glycol-modified (PETG) and poly(vinyl alcohol) (PVA) thermoplastic filaments (1.75 mm diameter, Smart Materials 3D, Alcalá la Real, Jaén, Spain). PETG provides robustness and some flexibility that enables it to store elastic energy during its deformation, whereas PVA, being water-soluble, serves as the degradable component essential for generating shape changes in the 4D actuators through the controlled release of PETG's energy in a variety of temporal patterns, ranging from instantaneous to progressive or gradual.

Chapter 6 details the mechanical properties of both polymers and their behavior in contact with water. Chapter 7 justifies their selection through the creation of a PETG-PVA bimaterial actuator collection, following a rapid prototyping route, capable of shape morphing due to the damage PVA undergoes upon contact with water, which results in an exponential loss of mechanical properties.

For manufacturing test benches that evaluate the metamorphosis of proof-of-concept shape-morphing implants for the craniosynostosis treatment and skin expansion (chapter 8), poly(lactic acid) (PLA) and FLEX 93A were used (1.75 mm diameter, Smart Materials 3D, Alcalá la Real, Jaén, Spain). In instances where the creation of more complex structures was required, but Fused Filament Fabrication was not an option, such as the wicker-based mechanism (described in the same chapter), photopolymerization printing was employed using Phrozen Aqua Gray 4K resin (Phrozen 3D Tech Co, Ltd, Hsinchu City, Taiwan).

Furthermore, to create the membrane simulating the dermis and epidermis, PlatSil Gel-0030 (Feroca, Madrid, Spain) silicone was used. This membrane facilitates the analysis of how 4D skin expanders progressively stretch tissue once the internal stress in PETG is released, at the moment PVA loses its structural integrity (chapter 8).

In the context of biocompatibility studies of 3D printed PETG and PVA (chapter 6), human mesenchymal stromal cells (hMSC, #PCS-500-012, LGC ATCC, Spain) were cultured and the material samples were sterilized with 70% ethanol. This approach enabled the assessment of cell viability in direct contact with the materials studied.

4.2. Additive manufacturing processes

Chapter 6, 7, and 8 of this text describe the production of prototypes and samples using two main additive manufacturing technologies.

- *Fused Filament Fabrication (FFF)*. A Bambu Lab X1 Carbon Combo 3D printer (Bambu Lab, Austin, TX, USA) equipped with a hardened steel 0.4 mm nozzle and an Automatic Material System capable of handling up to four filaments simultaneously was employed. A layer thickness of 0.2 mm and a print speed of 50 mm/s were used, with a build plate heated to 70 °C. Extrusion temperatures were set to 220 °C for PVA and 240 °C for PETG. This equipment was crucial for the production of test specimens in chapter 6, which were used to characterize the materials' properties. In chapter 7, it was used to fabricate mono and multimaterial PETG-PVA mechanisms activated through PVA erosion. The use of the equipment in printing test benches for craniosynostosis and skin expansion, as well as proof-of-concept shape-morphing implants, is detailed in chapter 8.

  Most parts were printed without support, optimizing their orientation. When needed, purge towers were employed to switch between PETG and PVA. Various infill patterns (rectilinear, concentric, gyroid, and quasi-isotropic) were tested throughout the research. A summary of the printer's technical specifications can be found in Table 4.1.

- *Liquid Crystal Display (LCD).* Chapter 8 examines the fabrication of intricate structures through the employment of a Phrozen Sonic Mighty 4K printer (Phrozen 3D Tech Co, Ltd, Hsinchu City, Taiwan) and Phrozen Aqua Gray 4K resin, such as the wicker-based mechanism, which could not be produced via FFF. The following parameters were utilized: a layer height of 100 microns, an exposure time of 2.4 seconds, and a post-curing step of 3 minutes. This process has been shown to yield resolutions that are superior to those achieved by FFF, as well as surface finishes that are more refined, a property that is particularly important for intricate weave patterns and compact internal channels (Figure 4.1). The specifications of this printer are also detailed in Table 4.1.

Table 4.1: Specifications for the Bambu Lab X1 Carbon and Phrozen Sonic Mighty 4K printers [248,249].

Specifications	Bambu Lab X1 Carbon	Phrozen Sonic Mighty 4K
Technology	FFF	LCD
Build volume	256 x 256 x 256 mm3	200 x 125 x 220 mm3
Max. printing speed	500 mm/s	80 mm/h
Layer resolution (Z)	0.1 – 0.35 mm	0.01 – 0.3 mm
Lateral resolution (XY)	-	0.052 mm
Nozzle diameter / Light source	0.4 mm	405nm
Slicer	Bambu Studio	Chitubox

(A) **(B)**

Figure 4.1: Comparison of objects produced with two additive manufacturing technologies in the PhD thesis: (A) Minipig skull anatomical models via FFF and (B) wicker-based shape-morphing skin expanders via LCD technology (chapter 8). Pictures courtesy of Álvaro Troyano.

4.3. Software

Design and modeling played a key role in this work, conducted with various software tools described across multiple chapters:

- *Autodesk Fusion 360* (Autodesk Inc., San Rafael, CA, USA). It was used to create parametric geometries for specimens (chapter 6) and 4D devices based on springs and biodegradable anchors (chapter 7). In Chapter 8, the software was also used to generate modular test bench assemblies, which were later printed and combined with a silicone membrane.
- *NX 2206* (Siemens PLM Solutions; chapter 8). Utilized for virtual planning of minipig cranial osteotomies to develop craniosynostosis test set-up. Its advanced modelling

capabilities enabled the design of cutting guides and angled stops to simulate metopic and/or coronal suture expansion, reproducing the frontal bone rotation observed in spring-assisted cranioplasty [250].

- *nTop* (nTopology Inc., New York, NY, USA; chapter 8). Used to create complex structures, such as the wicker-inspired mechanism where the degradable part is woven through the flexible structure. nTop's lattice generation capabilities allow customized cell patterns and precise control over thickness, cell frequency and other variables.
- *Meshmixer 3.5* (Autodesk Inc., Mill Valley, CA, USA; chapter 8). After anatomical segmentation of the minipig skull and export to STL format, it was used to repair gaps, simplify the mesh and smooth the surface prior to creating the craniosynostosis test set-up.
- *3D Slicer 5.6.2* (https://www.slicer.org; chapter 8). This program was applied to obtain anatomical models from a six-week-old minipig CT scan, using thresholding, seed growth and manual editing to isolate the skull bone with sufficient accuracy for subsequent osteotomies and the design of the craniosynostosis test bench.
- *Ansys Workbench 2022 R2* (chapter 8). Used to simulate the 3D printed devices, generating hexahedral meshes with partitions to minimize distortion. An elastoplastic behavior was defined for PETG (modulus of 1790 MPa, Poisson' ratio of 0.38, density of 1.27 g/cm^3), together with large displacements in compression due to the significant deformations of the flexible structures. These simulations allowed the prediction of force-displacement curves, which were later compared with experimental data from loading-unloading tests.
- *Python*. Chapter 3 presents the analytical models of serpentine and conical springs, where equations describe the spring stiffness as a function of geometric variables and the material Young's modulus. Python and the Sympy library [161] were used to solve these equations systems, and the Plotly library [164] was used to generate preliminary geometric visualization of the spring centerlines. In Chapter 6, Python was also employed to segment images of the degradation of 2D PVA samples, using OpenCV [251], Numpy [252], Matplotlib [253] and machine learning algorithms such as K-Means.
- *Bambu Studio* (Austin, TX, USA). Bambu Lab's slicer, which takes the STL files, sets the printing parameters for each material, and generates the G-code used to make the PETG-PVA parts tested in this research.
- *Chitubox* (Chitubox, Zhongcheng Future Industrial Park, Hangcheng Avenue, Baoan District, Shenzhen, Guangdong, China 518128). Similar to Bambu Studio but tailored

to photopolymerization. It creates the masks for the production of the wicker-based mechanism described in chapter 8 using the Phrozen Sonic Mighty 4K printer.

- *ImageJ* [254]. Used to measure geometric changes from images taken during the degradation tests of the shape-morphing actuators (chapter 7) and the proof-of-concept implants for craniosynostosis and skin expansion (chapter 8).
- *ChatGPT and DALL-E* (chapter 5). Generative AI techniques were explored to support the design process of 4D printed actuators using different materials, additive manufacturing processes and triggering stimuli. ChatGPT was employed to structure prompts incorporating the actuator ontology defined in this PhD thesis, enabling recommendations on geometry, materials and manufacturing processes. Meanwhile, DALL-E generated basic visual representations of the actuators, providing a conceptual guide for designers and engineers prior to CAD implementation.

4.4. Mechanical testing

Tensile, flexural, and compressive tests were conducted on the same universal testing machine, Instron 5966 (Instron, Norwood, Massachusetts, USA), but with different load cells according to the expected force range. In all cases, the crosshead speed was set at 2 mm/min. Except for the wicker-based mechanism (chapter 8), most specimens were manufactured with the Bambu Lab X1 Carbon Combo printer. The particular features of each test are described below:

- *Tensile tests* (chapter 6, Figure 4.2A). Performed according to ASTM D638-03 [177] with deformation monitored by digital image correlation (VIC-2D, VIC, Correlated Solutions, USA). To analyze the degradation of PVA and the structural stability of PETG in water, a test set-up was used that allowed immersion at 25°C with laminar flow. Different immersion times (0, 10, 20, 40 and 80 minutes) were studied for PVA, while PETG was subjected to stress relaxation tests at 1% strain to assess possible changes in its modulus of elasticity.
- *Three-point flexural tests* (chapter 6, Figure 4.2B). Performed according to ISO 178 [255]. Specimens measured 80 × 10 × 4 mm^3 and were printed on edge to investigate fiber orientation along the neutral axis, which is relevant for degradation-sensitive 4D mechanisms. A solid infill with a 90° rectilinear pattern was used, with a support span of 64 mm and 10 mm diameter rollers in both the supports and the load applicator.
- *Compression tests* (Figure 4.2C). Conducted to validate the behavior of the flexible structures that make up the shape-morphing implants (chapter 8). A 100N load cell and LVDT sensor (50mm maximum travel) provided accurate deformation tracking. Two specimens of each configuration were tested through a load-unload cycle to

quantify the stored elastic energy, which is critical in determining the ability of the structure to release energy and achieve the intended shape transformations.

Table 4.2: Technical specifications for Instron 5966 universal testing machine [256].

Specifications	Instron 5966
Load capacity	10 kN
Column type	Dual column
Speed range	0.001 – 3000 mm/min
Load measurement accuracy	± 0.5% of reading down to 1/1000 of load cell capacity option
Data acquisition rate	Up to 2.5 kHz

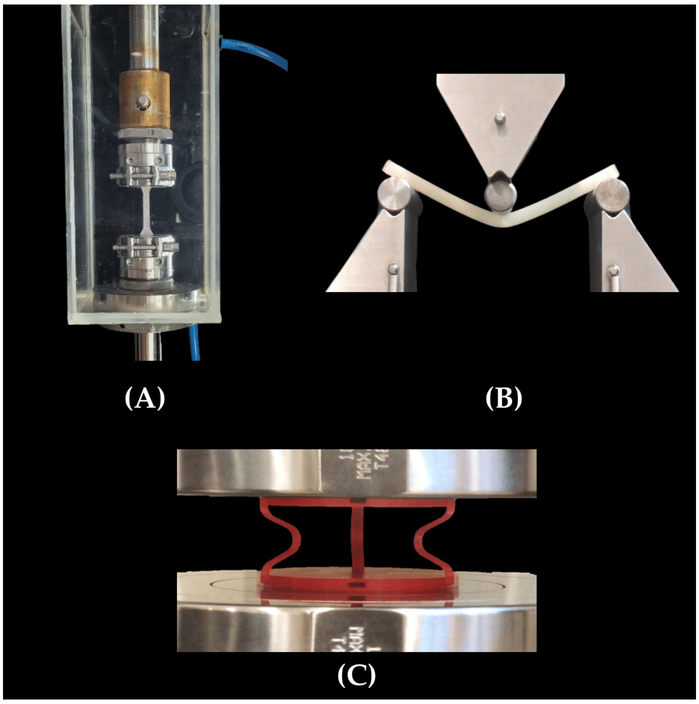

Figure 4.2: Experimental setup for mechanical testing, including (A) underwater tensile, (B) flexural, and (C) compression testing. Special thanks to Dr. Vanesa Martínez and José Luis Jiménez for their invaluable support and expertise in the mechanical characterization of the materials and actuators developed in this doctoral thesis. Their guidance and contributions were instrumental throughout the process.

4.5. Degradation tests

The degradation tests described in Chapters 6, 7, and 8 share several common features. They were carried out by immersing the specimens in 800 mL of water at 25 °C (in a 200 × 150 × 50 mm³ container), which prevented the thermal activation of PETG's shape memory [257,258], ensured uniform PVA exposure, and avoided saturation of the medium due to PVA dissolution. High-resolution optical sensors (12 megapixels, f/1.5, optical stabilizer) captured images at intervals appropriate for the PVA degradation rate. These images were then analyzed using software such as ImageJ (chapters 7 and 8) and computer vision/machine learning algorithms (chapter 6) to quantify erosion and distinguish degraded regions from artifacts like air bubbles.

In chapter 6, tests were designed to investigate the bidimensional degradation of 3D printed PVA and how infill patterns and surface area-to-volume ratio affect erosion (Figure 4.3A). Chapter 7 focuses on the metamorphosis induced by degradation, using image capture to measure geometrical changes over time and verify any residual deformation. Depending on the expected dimensional change, the camera was placed above or to the side to record the shape morphing performance in detail (Figure 4.3B).

Finally, chapter 8 aimed to validate "smart" shape-morphing implants for applications such as craniosynostosis and skin expansion. Two cameras were strategically positioned (top and side views) with image capture intervals of one or ten seconds, depending on the degradation rate of the degradable anchor. This dual perspective provided a more comprehensive record of implant metamorphosis (Figure 4.3B).

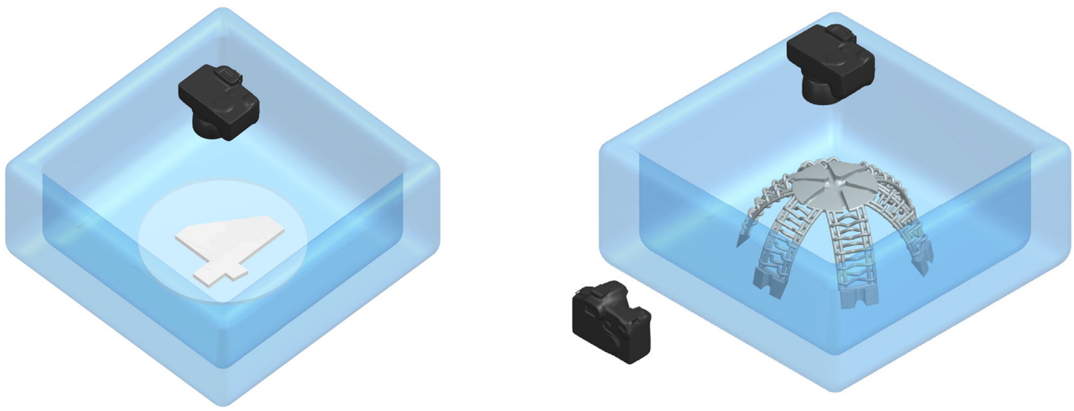

(A) **(B)**

Figure 4.3: Experimental setup for (A) 2D degradation analysis and (B) degradation test with single- or dual- view recording.

4.6. Biocompatibility tests

To determine the suitability of PETG and PVA for biomedical applications, chapter 6 details the use of hMSC, cultured up to passage 6 in αMEM supplemented with antibiotic/antimycotic, FBS, ascorbic acid, and FGF-2. Printed samples with concentric infill at various sizes were sterilized in 70% ethanol before direct cell contact.

The PrestoBlue assay measured the metabolic activity of hMSC at 24, 72, and 144 hours, comparing the experimental group (PETG or PVA samples) with positive control (cells without material) and a negative control (medium without cells). Additional bright-field and confocal microscopy evaluated cell viability and density. These results confirmed the compatibility of PETG and PVA for potential medical applications.

5. Ontology for smart 4D printed material systems and structures synergically applied with a generative artificial intelligence for creativity promotion

A preliminary version of this chapter has been published as "*Ontology for smart 4D printed material systems and structures synergically applied with generative artificial intelligence for creativity promotion*". Smart Materials and Structures, 34(1), 015045. https://doi.org/10.1088/1361-665X/ad9dca, under Creative Commons License (CC 4.0 BY).

5.1. Introduction

Shape-morphing materials and structures enable the creation of smart devices and systems with metamorphic abilities, which are capable of improved interactions with the environment by adapting their geometry, in some cases with reversible operation [259–262]. Shape-morphing regions within complex devices can serve also as actuators for performing extremely varied functions. These shape-shifting structures and devices are already making an impact in several industrial fields, from robotics to medicine, from architecture to inner design, from vehicles to space technology. Deployable satellite structures, adaptative furniture, environmentally responsive façades, minimally invasive surgical tools, tissue engineering scaffolds and implants, to cite just a few, benefit from an implementation involving shape-morphing structures or shape-shifting components. In terms of size, applications range from large-scale systems for buildings, vehicles and machines, to micro-/nano-manipulators and micro-/nano-electro-mechanical-systems (MEMS/NEMS) [263–267].

Numerous design and manufacturing strategies allow for the development of shape-morphing systems. Smart or multifunctional materials, capable of responding in a controlled way to external stimuli, can be arranged as the active elements within shape-morphing structures [261–263]. Functionally graded materials (FGMs) or structures [264,265] and metamaterials [266] may also have shape-shifting properties and can be used as driving elements for shape-morphing structures. Conventional hydraulic, pneumatic and electromagnetic actuators can be active elements within transformable structures and machines' subsystems [264,268]. Special designs for creating structures that transform into mechanisms and vice versa can be also employed.

Many of the previously mentioned materials and geometrical configurations, leading to shape-morphing structures and devices, can be materialized employing additive manufacturing (AM) technologies. AM technologies, usually working following a layer-by-layer approach, enable the creation of complex-shaped objects, functionally graded materials and structures, multi-material and multi-scale objects, and have helped to reinvent product development in many ways. Some AM technologies (and careful design procedures) can help to directly manufacture mechanisms (kinematic chains made of interconnected links, as basic units for mechanical systems and machines), mechanical metamaterials, functionally graded geometries, and even micro/nanomechanisms (and MEMS/NEMS), starting from a computer-aided design (CAD) file and avoiding a variety of time-consuming and demanding post-processes and assembly operations [269–271].

All these innovations synergize for empowering the field of shape-morphing (meta)materials, structures, devices and engineering systems in general. In fact, the AM of shape-shifting systems has been a research topic for almost two decades now. 3D printing with shape-memory materials, 3D printing of structures with inner mechanisms and 3D printing of graded structures and materials have also been reported. These alternative or complementary routes, for achieving metamorphic structures and devices employing AM technologies, have been more recently integrated under the term four-dimensional printing or "4D printing" [52,259,261,267,272–279]. The fact is that 4D printing is an emergent and rapidly evolving field, which still needs to be defined and structured, for increased industrial impacts.

In general, 4D printing uses the materials and techniques common from 3D printing, sometimes with slight adaptations, and generates components and devices that perform controlled geometrical changes over time. The transformation is usually enabled by special design features, by the use of digital or stimuli-responsive materials, by multi-material printing or even by actively producing deformation upon the part structure in a controlled way [52,259,261,267,272–279]. Bioinspired design principles are employed in many cases [280–282], as well as graded materials and composites [283–285].

More recently, the creation of biohybrid systems [47,286,287], in which living cells perform as active elements, driving the motion of MEMS and micromachines, is also becoming a relevant R&D trend. In many ways, smart and living materials share several features, including the possibility of responding to external stimuli in a controlled way through morphological changes.

To better understand the field of 4D printing and analyze its potentials for the development of smart shape-morphing (meta)materials, structures, devices and systems, systematically describing and presenting the field, while exploring its boundaries can be a successful strategy connected to creativity promotion. In this creative exercise, it is relevant to start with an ontology or classification and codification scheme for the 4D printing field. Ontologies are schemes for classification, typically defining categories, properties and relationships between concepts data and entities, which help organize and index knowledge and research fields. Apart from classifying what already exists, ontologies and taxonomies (special hierarchical ontologies) can be used to foresee and organize what may still be developed or created, especially in the cases of ontologies and taxonomies dealing with novel research fields.

Different ontologies are being constructed for varied areas of materials science and engineering, including 4D printing, for which already a taxonomy and an ontology have been recently proposed [259,273]. Other nascent areas in materials science and engineering, like the field of engineered living materials, whose dynamic properties have direct connections with 4D printed devices and shape-morphing structures, are also benefiting from the organizational impact of ontologies and taxonomies [47,286]. Soft-robotics actuators, obtained by AM procedures in many cases, are also being classified [287]. Despite the above-mentioned pioneering studies, 4D printing still lacks a complete ontology capable of considering geometries, shapes, shape-morphing principles, triggering stimuli, applicable manufacturing technologies and usable raw materials. Some of the referred schemes mainly focus on soft materials, shape-memory polymers and alloys and single-step actuators, which are too limited considering the vast potential of 4D printing. Furthermore, existing codification schemes for 4D printing do not usually consider shape-morphing actuators, which benefit from several actuation metamorphoses. Additionally, novel generative artificial intelligence (AI) resources combined with ontological frameworks and codification schemes may support radical innovation and automated discoveries in the field, which constitutes an unexplored synergy presented for the first time in this work.

Consequently, this study aims at exploring the concept of 4D printing in depth and introducing the most versatile and useful ontology to provide a codification scheme. This ontology has already demonstrated its usefulness in facilitating the identification and classification of functional principles and fundamental concepts for the development of smart devices in various projects. Through this process of abstraction, creativity has been enhanced by an exploratory cycle linked to the development of the ontology and the codification scheme. This was followed by a contraction cycle, through which the ontology and codification have been applied to different particular use cases.

The next section presents the proposed ontology and classification scheme, for which relevant pioneering studies have served of inspiration [47,259–261,267,272–275,286–289], before illustrating its utility through the classification of 54 examples of 4D printed shape-morphing actuators responding to a wide set of stimuli. Besides, the usability of the ontology and related codification by a generative AI for supporting engineering design tasks is explored and validated through a comprehensive set of examples and thanks to the development of a complete industrial use case: the design of a 4D printed shape-memory cardiovascular stent. Finally, a discussion on current challenges and future research proposals is provided.

Throughout the study, reference is made to the tables in Appendix A, which provide a detailed glossary of the ontology together with a description of the proposed codification scheme.

5.2. Ontology and codification scheme for 4D printed material systems and structures

Detailed below, the different categories for the proposed ontological framework for 4D printed material systems and structures, and the rationale for the codification scheme are presented. Compared to existing related studies, to the authors' best understanding, present ontology and codification scheme for 4D printing and their application for creativity promotion stand out for the following reasons:

- The presented ontology provides one of the most comprehensive collection of geometries, shapes, shape-morphing principles and triggering stimuli considered in any of the existing examples of classifications dealing with 4D printing as a field of study and with 4D printed actuators as the direct result of such research field.
- Breakthroughs derived from the European BIOMET4D project, which is funding this PhD thesis, have been incorporated into both the ontology and the proposed coding scheme. In particular, innovations such as multimaterial printing and the use of (bio)degradation as a stimulus to trigger shape transformation have been integrated. This incorporation gives the proposal a distinctive character, as it addresses pioneering aspects in the field of 4D printing and its application in the development of intelligent systems for biomedical engineering.
- The conceived codification scheme includes a unique set of codes that can present, in a single code line, the whole life cycle (the different actuation steps) of a 4D printed material or component or shape-morphing actuator, detailing and codifying all its shape changes with their respective triggering stimuli along the actuator's life.
- Both ontology and the codification consider 4D printed materials or components or shape-morphing actuators capable of performing multiple actuation steps, as compared to existing reference that deal typically with single step actuators.
- Above all, according to our best knowledge, for the first time the employment of an ontology and codification scheme for 4D printed materials and shape-morphing components is employed for training a generative AI and for taking benefit from such innovative resources as creativity promotion tool. The understanding of the ontology and codification scheme by the generative AI is illustrated, its applicability for generating ideas about geometries (even with visual representations), materials and printing technologies along the development of new actuators is exemplified, and a

complete industrial design use case involving a set of constructive dialogues with the generative AI is provided.

5.2.1. Ontology

The main categories employed for constructing this 4D printing ontology are detailed below, before presenting the codification scheme. The glossary, summarized in Table A.1 to Table A.5, acts as an essential companion to this section.

Geometries and shapes: Geometrical dimensions and shapes are fundamental features required for classifying 4D printing as a field and for categorizing 4D printed actuators as research outcomes. In the proposed ontology, 0D, 1D, 2D, 3D and 4D geometrical dimensions are considered, following the usual engineering concept for one-, two- and three-dimensional objects. For example, a 1D object has two dimensions c.a. one order of magnitude smaller than the other one, while a 2D planar object has one dimension c.a. one order of magnitude smaller than the other two. 4D objects evolve with time, while 0D objects have all dimensions one order of magnitude smaller than a conventional 3D body (e.g., particles). As regards shapes, the glossary of the Annex presents, in Table A.1, the common shapes (cubes, domes, spheres, plates, bars, springs…) that 4D printed objects or shape-morphing actuators can adopt in their different actuation steps. The change from one shape to another is connected to the shape-morphing principles detailed below, which constitute another essential taxonomic group for the proposed classification scheme.

Shape-morphing principles (geometrical evolutions): Shape-morphing principles in 4D printing are related with the geometrical evolutions that the actual printed shape-morphing actuators undergo during the shape-shifting/morphing stages. The way in which an actuator evolves from one geometrical dimension and shape to another is illustrated by terms such as: folding, bending, rolling, buckling, shrinking, expanding, to cite a few. Other more complex shape-morphing principles/strategies, like those based on origami/kirigami/kusadama or those relying on bistable and multistable structures or kinematic chains and mechanisms, are also noteworthy, as they help to empower the shape-morphing abilities of the 4D printed actuators. In many cases such principles are reversible, which is also considered in the proposed scheme. Table 5.1 below summarizes such shape-morphing principles, trying to provide the most comprehensive set existing in the literature for this field of research. Table A.2 lists them comprehensively with the codes associated with the codification scheme.

Triggering stimuli: The stimuli that trigger and help to control the shape-morphing ability of 4D printed mechanisms are also fundamental in a classification or organizational scheme for the field. It is a common practice to classify actuators by means of their driving principles. Common stimuli for sparking the geometrical evolutions of smart 4D printed devices include changes in environmental conditions, like temperature or humidity; external mechanical actions upon the devices' structures, like force, pressure, vibration or acoustic actions; electromagnetic stimuli, chemical and biological actions, among many others. Table A.3 enumerates all the triggering principles that the authors have been able to review in the literature and provides a coding scheme. As already advanced, special relevance is the triggering by biodegradation, which is not usually considered in 4D printing reviews, and opens new horizons in fields including biomedical practice, as it may contribute to minimal invasion, improved ergonomics and enhanced healing processes based on biodegradable smart devices.

Materials: As happens with available technologies for 4D printing, the portfolio of materials capable of being additively processed and applicable to the development of shape-morphing actuators is continuously increasing. Most studies and reviews dealing with the field of 4D printing concentrate on the printing of shape-memory polymers and alloys, which lead to actuators triggered by temperature changes. However, other relevant materials like biomedical alloys, carbon-based materials, ceramics and composites, which can lead to other kinds of shape-morphing actuators triggered by a wide set of stimuli, are often neglected. These need to be considered for the proposed 4D printing ontology and are also listed in Table A.4.

Technologies: The family of AM technologies is continuously receiving more members, and the related achievable precision, resolution, repeatability and manufacturing volumes keep on increasing, as required for high-performance and impactful industrial applications. Table A.5 provides a comprehensive recapitulation of AM technologies following commonly accepted families and representative technologies. Such collection, which is also codified, even if not being totally complete and probably requiring periodic updates (for example new bioprinting and 4D bioprinting resources are currently under development), proves an adequate compromise for the purposes and timely nature of this study.

Table 5.1: Summary of gathered shape-morphing principles or geometrical evolutions. Different examples of shape-morphing principles, usually employed from promoting transformations across the considered geometrical dimensions, are gathered and presented in form of symmetric matrix.

	0D	**1D**	**2D**	**3D**
0D	Topographical change Expanding/ contracting Swelling/ deswelling	Mechanism Metamaterial Self-assembly	Mechanism Metamaterial	Swelling/deswelling Blossoming Origami Kirigami Self-assembly
1D	Mechanism Metamaterial Self-assembly	Stretching/compressing Topographical change Twisting/untwisting Helixing/unhelixing	Folding/unfolding Bending/straightening Rolling/unrolling Buckling/debuckling Bistable Multistable Mechanism Metamaterial Auxetic Textile	Expanding/contracting Stretching/compressing Swelling/deswelling Twisting/untwisting Helixing/unhelixing Origami Kirigami
2D	Mechanism Metamaterial	Folding/unfolding Bending/straightening Rolling/unrolling Buckling/debuckling Bistable Multistable Mechanism Metamaterial Auxetic Textile	Expanding/contracting Topographical change Twisting/untwisting Mechanism Metamaterial Auxetic Textile Self-assembly	Swelling/deswelling Folding/unfolding Bending/straightening Rolling/unrolling Curving/flattening Bistable Multistable Origami Kirigami Blossoming Mechanism Metamaterial Auxetic Textile
3D	Swelling/deswelling Blossoming Origami Kirigami Self-assembly	Expanding/contracting Stretching/compressing Swelling/deswelling Twisting/untwisting Helixing/unhelixing Origami Kirigami	Swelling/deswelling Folding/unfolding Bending/straightening Rolling/unrolling Curving/flattening Bistable Multistable Origami Kirigami Blossoming Mechanism Metamaterial Auxetic Textile	Swelling/deswelling Topographical change Twisting/untwisting Hierarchical Origami Kirigami Kusadama Mechanism Metamaterial Auxetic Textile Self-assembly

5.2.2. Codification scheme and practical examples

Now that the boundaries of 4D printing as a field of study are clearer, thanks to the implemented ontology, this section is devoted to providing a straightforward codification scheme for working with 4D printed actuators. Furthermore, it aims to systematically foster creativity through semantic combinations. The term actuator is employed here as a generalization of shape-morphing material, structure, device or system, although in most cases actuators are constitutive elements of even more complex engineering systems. It is necessary to point out that our codification tries to illustrate, in a single line of code, the whole metamorphoses of smart 4D printed actuators, in a way that contributes to organize the field of study. Groups of acronyms or symbols, each one representing a specific state of the actuator, are joined. Each of the groups includes an indication of the geometrical dimension and of the general shape of the actuator in a certain state. Between blocks, the shape-morphing principles and triggering stimuli are indicated. In this way, multiple actuation steps can be easily described, detailing the actuator' whole life cycle. Finally, the code line ends with an indication about the raw materials and technologies employed for manufacturing the actuators, as schematically presented in Figure 5.1.

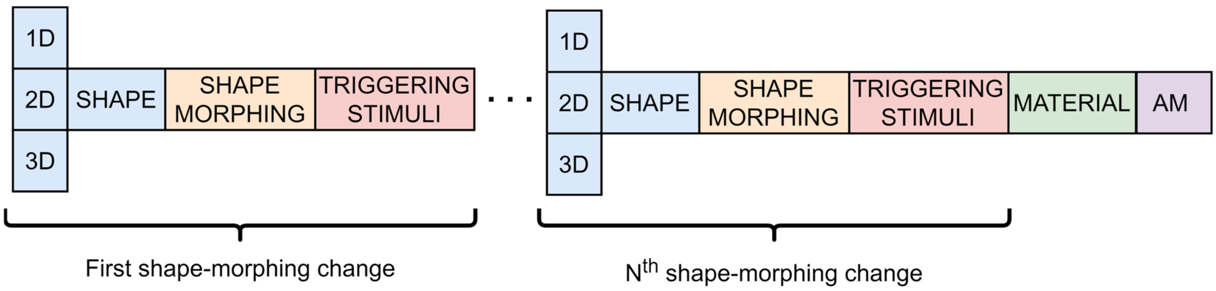

Figure 5.1: General codification scheme for 4D printed material systems and structures.

As advanced, the glossary of the Appendix A provides a list of geometries, shapes, shape-morphing principles (or geometrical evolutions), triggering stimuli, materials and technologies that constitute the key features for classifying smart shape-morphing actuators. Explanations and symbols are provided as an initial attempt to create a universal language for 4D printing. To illustrate the codification, three examples from very different types of smart printable structures are provided.

The first case (Figure 5.2) is linked to a linear actuator, with the shape of a planar spring (2D & LSP) and capable of stretching (STR), once the biodegradation (BIODEG as triggering principle) of an external framework takes place. It is manufactured using a polymer (P) by fused filament fabrication (FFF). It represents the first conceptual demonstrator for a distraction device, which will be transformed into solutions for craniosynostosis and skin expansion. Different combinations of codes and symbols can be employed to illustrate its life cycle and metamorphoses, as shown in the images of the figure.

The second case (Figure 5.3) deals with a stent for cardiovascular pathologies, a field in which smart materials and 4D printing can have a very relevant impact. In the specific case of the illustrative example, the stent is manufactured using a shape-memory alloy (SMA) by selective laser melting (SLM). The presented shape-shifting steps are connected to the shape-memory training, in which the initial stent with tubular shape (3D T) is compacted (INV-EXP) by means of a radially applied force (MS-F) to reach a unidimensional temporary shape (1D T) with cross-section diameter c.a. one order of magnitude lower than its length. Subsequently, radial expansion (EXP) is achieved by heating (TS, as triggering principle). The three shapes are represented in the codification, with two shape-morphing steps in between with different triggering principles: mechanical and thermal stimuli respectively.

The third case (Figure 5.4) presents a 4D printed chassis, in which living cells can be cultured for reaching an innovative living material or living micromachine. In this case, cell traction force (CTF) is the triggering stimulus for producing a shape-shift from an initial unidimensional structure towards a final two-dimensional shape, thanks to the rotation of different parts of the chassis.

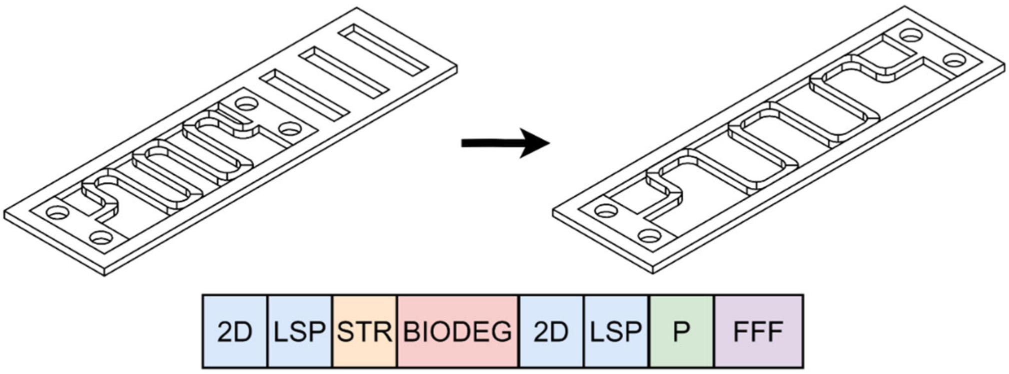

Figure 5.2: Codification scheme application example: linear spring with stepped actuations triggered by biodegradation of surrounding frameworks. Geometrical evolution and codifications are presented.

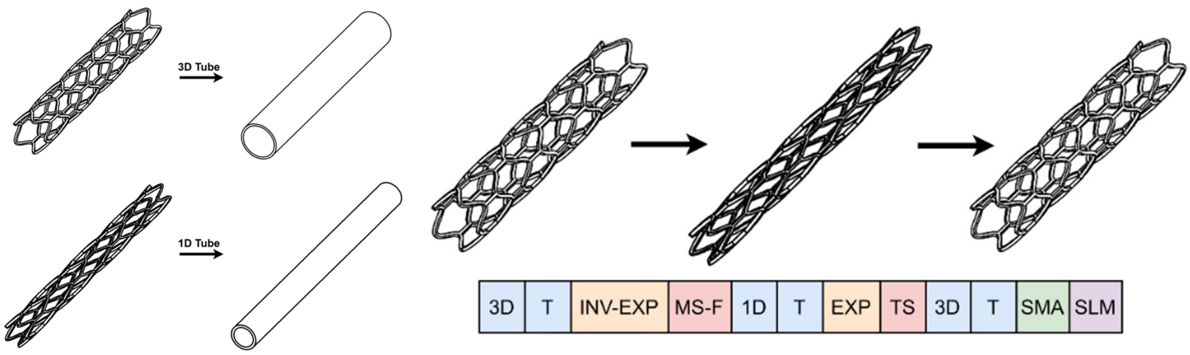

Figure 5.3: Codification scheme application example: shape-memory stent concept with geometrical changes triggered by mechanical and thermal stimuli. Geometrical evolution and codifications are presented.

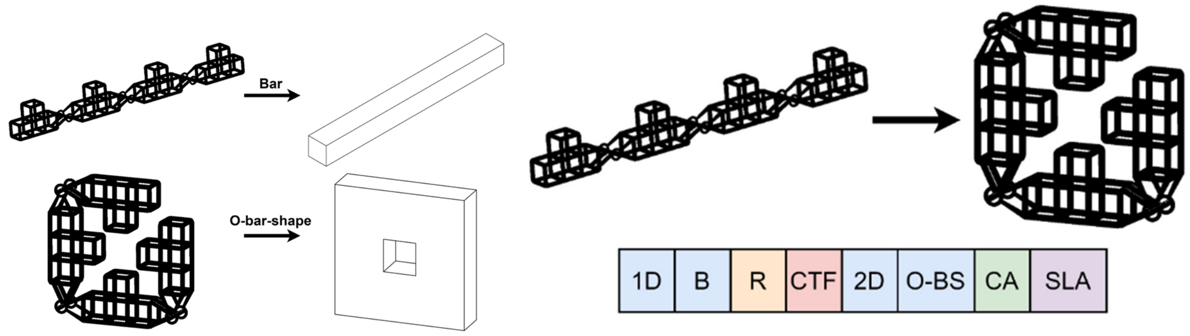

Figure 5.4: Codification scheme application example: 4D printed micromechanism actuated by cell traction force of cultured cells, as concept for living micromachine. Geometrical evolution and codifications are presented.

5.3. Application of the ontology to a collection of 4D printed material systems and structures

Once the ontology and related codification schemes have been described and illustrated through the examples of Figure 5.2 - Figure 5.4, it is important to analyze its versatility and, to some extent, its universality for univocally describing smart shape-morphing materials, structures, actuators, devices, systems in general, enabled thanks to the application of 4D printing principles. In a way, the ontology classifies these engineering systems, but also the whole 4D printing scientific-technological realm. It gives an idea, not only of what already exists, but of what could be developed through synergic research and co-creation methods, which will be illustrated in following sections by employing generative AI resources.

With this purpose, a brief review of recently published studies dealing with 4D printed shape-morphing actuators has been performed. Several scientific documents published along the last decade have been gathered and organized [38,268,290–317]. Most families of usable materials, such as polymers, ceramics, alloys and composites, both passive and with shape-morphing and shape-memory properties, have been represented in the gathered collection. Regarding AM technologies, capable of producing 4D printed geometries, relevant examples have been included, like fused filament fabrication, stereolithography, digital light processing, selective laser melting, direct ink jetting, binder jetting, drop on demand or laminated object manufacturing, to cite a few. Both very simple shapes, including bars, plates and springs, as well as complex flower-like structures, scaffolds and metamaterials, have been taken into account. In terms of shape-morphing triggers, a wide range of examples using mechanical, electromagnetic, chemical, and biological stimuli have been explored.

After gathering these relevant examples of 4D printed shape-morphing actuators, the ontology has been systematically applied to all of them, codifying their life cycle (metamorphoses) considering initial geometry and shape, shape-morphing, triggering principle, final geometry and shape, material and printing technology. Actuating life cycles involving more than one metamorphosis are also included. In those cases, different coding lines codify the different stages of actuation. The result is summarized in Table 5.2, which provides a brief description of the considered 4D printed actuators and classifies them providing a codification of their morphological lifecycle. The different references are also listed, to facilitate colleagues finding the original publications and checking the actual geometries, shapes and properties of the different actuators.

A remarkable feature of the ontology and codification is that, even without checking the photographs of the different classified actuators in the seminal publications, it is already possible to imagine the described metamorphoses just by reading a single text line. The abstraction power of this codification and its potential for creativity promotion should not be neglected. Arguably, in the future, it may be possible to combine these blocks of text to conceptually design complex shape-morphing systems, emulating the use of letters for representing verbal communication. This and other possibilities are discussed in the following sections, which also present current challenges and some ongoing research lines and directions of study.

Table 5.2: Application of the proposed ontology for 4D printed actuators with 54 examples of application demonstrating its utility and versatility. The codification should be read with the support of Table A.1 to Table A.5.

Description of 4D printed actuator	**Ontology application**								**Ref.**
	Geometry	**Shape**	**Shape-morphing principles**	**Triggering stimuli**	**Geometry**	**Shape**	**Material**	**AM technology**	
Ni-Ti gripper responsive to thermal stimuli	2D	U-BS	INV-BE	MGS	1D	B	SMA	SLM	[290]
Light-fueled rolling robot	2D	PL	KI	LS	3D	T	P	LOM	[291]
Multimaterial 4D printed homogeneous auxetic lattice	2D	PL	AUX	TS	2D	PL	MT(P+CO)	DIW	[292]
Multimaterial 4D printed heterogeneous auxetic lattice	2D	PL	CU	TS	3D	D	MT(P+CO)	DIW	[292]
Droplet network composed of two strips of droplets of different osmolarities	1D	B	BI	MO	2D	C-BS	MT(G+G)	DOD	[293]
Flower-shaped network folding spontaneously into a hollow sphere	2D	STAR-BS	INV-BLO	MO	3D	S	G	DOD	[293]
Hydrogel disk with 15% honeycomb filler that rolls into a tube	2D	DK	R	TS	3D	T	G	DIW	[294]
Self-folding string of letters “FBK”	1D	B	F	TS	2D	FBK-BS	SMMT(SMP+P)	FFF	[295]
Self-opening box	3D	C	O	TS	2D	PL	SMMT(SMP+P)	FFF	[295]
Helix formed by the gel sheet under the action of thermal stimuli	2D	PL	HE	TS	3D	T	G	DLP	[296]
Raster structure that changes shape after water absorption	2D	PL	SW	MO	3D	PL	P	DIW	[297]

Ring column that changes shape after water absorption	2D	RG	SW	MO	3D	T	P	DIW	
Herringbone tessellation origami*	3D	T	INV-STR	MS-F	2D	DK	SMP	FFF	[298]
	2D	DK	STR	TS	3D	T			
Full entubulation of 4D nerve guidance conduit via a "thermomechanical programming" shape transformation	2D	PL	R	TS	3D	T	SMP	SLA	[299]
Single cylindrical tube manufactured with a kirigami structure for a bifurcation stent*	3D	T	KI	MS-ST	3D	U-BS	SMP	FFF	[300]
	3D	U-BS	KI	TS	3D	T			
Self-folding of CLP (crossed layers of parallels) unit cell	2D	PL	O	MS-F	3D	C	P	FFF	[301]
Self-folding regular icosahedron under light stimuli	2D	PL	O	LS	3D	S	P	DLP	[302]
2D multi-stable metamaterials assembled by snapping segments	2D	PL	MTS	TS	2D	PL	MT(CO+P)	BJ+FFF	[303]
3D multi-stable metamaterials assembled by snapping segments	3D	C	MTS	MS-F	3D	C	MT(CO+P)	BJ+FFF	
3D microspiral capable of memorizing a 1D linear shape and recover its original form after the application of thermal stimuli*	3D	SP	UHE	MS-F	1D	CY	P	DIW	[38]
	1D	CY	HE	TS	3D	SP			
3D printed box that opens with a thermal or light stimulus*	3D	P-BS	F	MS-ST	3D	C	SMP	DLP	[304]
	3D	C	UF	TS or LS	3D	P-BS			
Self-folding box*	3D	C	O	MS-ST	2D	PL	SMCO	DIW	[305]
	2D	PL	O	TS	3D	C			

Horseshoe-shaped element that becomes linear when stimulated by heat*	1D	B	BE	MS-ST	2D	U-BS	SMCO	DIW	
	2D	U-BS	STRA	TS	1D	B			
The sequential drive of the multi-material Archimedean chord in a dome due to heating	2D	DK	CUR	TS	3D	D	MT(CO+CO)	DIW	[306]
Film which, when heated, turns into a twisting column	2D	PL	TW	TS	3D	CY	G	DIW	[307]
Porous structure composed of rectilinear printing paths alternating 90° with respect to the previous layer that contracts due to thermal stimuli	2D	PL	CONT	TS	2D	PL	G	DIW	
Complex flower morphology generated by 4D biomimetic printing	2D	STAR-BS	INV-BLO	MO	3D	S	P	DIW	[308]
4D printing of ceramics with the design of bending configuration	2D	B	BE	TS	3D	U-BS	CE	DIW	[309]
4D ceramic printing with shape-shifting design on a helical ribbon	2D	B	HE	TS	3D	T	CE	DIW	
4D ceramic printing with shape-shifting design on a saddle surface	2D	PL	CUR	TS	3D	PL	CE	DIW	
Auxetic structures exhibiting shrinkage in both length and width under applied magnetic fields	2D	PL	AUX	MGS	2D	PL	CO	DIW	[310]
Self-folding of a single strand into a three-dimensional cube.	1D	CY	F	MO	3D	C	MT(P+P)	JET	[311]
2D to 3D shape transformation of a flat flower-like structure	2D	DK	INV-BLO	TS	3D	S	SMP	FFF	[312]

Butterfly shape moves its wings under magnetic field actuation.	2D	PL	BE	MGS	3D	C-BS	CO	DIW	[268]
4D-printed electroactive smart gripper	2D	U-BS	BE	TS	2D	U-BS	SMCO	DIW	[313]
A ring that transforms into a wavy structure	2D	RG	CUR	TS	3D	T	SMMT(SMP+P)	BJ	[314]
4D printing of shape-memory scaffolds*	3D	CY	COMP	MS-ST	2D	DK	SMP	DLP	[315]
	2D	DK	STR	TS	3D	CY			
Shape-shifting specimen composed of an arrangement of out-of-plane bending elements	3D	T	STRA	TS	2D	PL	SMP	FFF	[316]
Flat structure that self-assembles with a mechanical stimulus to form a three-dimensional mechanism.	2D	PL	SFA	MS-ST	3D	D	MT(P+P)	JET	[317]
Water-responsive flower	2D	DK	INV-BLO	MO	3D	S	G	DLP	[318]
Tunable Octet lattice*	3D	C	COMP	TS + MS-ST	3D	C	SMP	FFF	[271]
	3D	C	STR	TS	3D	C			
4D printed Poly(l-lactide)/($FeCl_3$–TA/MgO) composite scaffolds	3D	C	STR	LS-NIR	3D	C	SMCO	DIW	[319]
Bistable shape-changing bar	1D	B	BS	TS	2D	U-BS	SMCO	FFF	[320]
Reprogrammable soft manipulator	3D	C	TW	MS-ST	3D	C	P	FFF	[321]
Asymmetrical flat composite sheet	2D	PL	BE	TS + MS-ST	3D	C-BS	SMCO	LAM	[322]
Micro-textured printed plate with shape-morphing pillars	2D	PL	TC	TS	2D	PL	P	SLA	[323]
DNA-like structure	2D	PL	HE	TS	3D	T	SMP	FFF	[324]

Reversible meta-sandwiches*	2D	PL	COMP	MS-ST	2D	PL	SMMT(SMP+P)	FFF	[325]
	2D	PL	STR	TS	2D	PL			
Reversible bistable actuator*	2D	Y-BS	BS	MS-ST	2D	M-BS	SMP	FFF	[326]
	2D	M-BS	BS	TS	2D	Y-BS			
Uniform honeycomb lattice structure*	3D	C-BS	COMP	MS-ST	3D	M-BS	SMP	FFF	[327]
	3D	M-BS	STR	TS	3D	C-BS			
Magneto-electroactive flat actuator	2D	PL	F	MGS	3D	C	SMCO	FFF	[328]
Self-bending gripper*	2D	U-BS	UB	TS + MS-ST	2D	V-BS	SMP	FFF	[329]
	2D	V-BS	B	TS	2D	M-BS			
	2D	M-BS	B	TS	2D	U-BS			
Self-morphing flower-shaped structure	2D	DK	INV-BLO	TS	3D	S	SMP	FFF	[330]
Self-rolling helix	2D	PL	HE	TS	3D	T	SMP	FFF	

* Two or more metamorphoses

5.4. Generative AI-driven coding and design of 4D printed material systems and structures

The integration of AI tools is driving a new era of ideation and prototyping, enabling designers to explore and iterate on design concepts more broadly and creatively. Generative AI technologies, such as ChatGPT, are starting to transform design and manufacturing processes. In AM, ChatGPT has streamlined G-code generation, which is essential for controlling 3D printers and ensuring high-quality results, by adjusting printing parameters in real time and significantly reducing the trial-and-error phase [331]. ChatGPT has also supported the design of 3D printed wrist-hand orthoses, suggesting procedures that include 3D scanning of the patient's anatomy and generating visual representations through DALL-E, demonstrating its versatility for specific design needs [332]. Additionally, ChatGPT has shown its ability to optimize design, planning and material selection in 4D printing, promoting more sustainable and efficient practices. In 4D printing, which uses materials that change properties over time, AI may enhance the process by aiding in the selection of materials that respond to specific stimuli, improving the adaptability and durability of printed structures [333].

This section presents an innovative approach for the coding and design of 4D printed material systems and structures using generative AI tools (i.e. ChatGPT). The ontology acts as a communication tool with ChatGPT, supporting the conceptual design phase and the selection of materials and manufacturing processes. The interaction with ChatGPT is carried out through "prompts", textual instructions that allow for constructive dialogues. The first prompt establishes the context and role for the AI, which is crucial for helping ChatGPT to understand the coding from an engineering perspective.

In our exploratory journey for establishing synergies between the ontology and codification and the generative AI technology, the initial prompt was as follows:

> *"You are an engineer specializing in coding shape-morphing actuators. To support your work, you have developed an ontology that outlines the entire life cycle of these actuators, including details on their shape, shape-morphing principles, triggering stimuli, materials, and technologies. Attached, you will find several Word documents, each serving a specific purpose:*
>
> *1. Ontology.docx: This document provides a comprehensive description of each component within the ontology.*
>
> *2. Tables A.1 to A.5: These tables offer detailed definitions for each component involved in the coding process.*
>
> *3. Codification of 4D printed actuators.docx: This document provides a list of examples of different 4D printed material systems and structures encoded with the ontology.*

Please review these documents thoroughly. After analyzing the provided information, could you confirm whether you understand the ontology and its coding?".

In response, the generative AI (ChatGPT) briefly described each component of the ontology and demonstrated an "understanding" of the coding and its applicability by looking at the table with the coded examples (Table 5.2). Furthermore, it encouraged questions related to the ontology or coding.

To validate its comprehension and ability to apply it, the next instruction was: *"Now, after analyzing all the information provided, could you use the ontology to code ten different 4D printed material systems and structures, ensuring they are distinct from the previously provided examples?"*. The answer is summarized in Table 5.3. These ten examples show that ChatGPT is capable of correctly coding shape-morphing actuators, after having been trained with the basic documents and tables that conform the ontology and codification.

Table 5.3: Application of the ontology for coding 4D printed material systems and structures by a generative AI (ChatGPT in our case).

Description of 4D printed actuator (input)	**Ontology code (output)**
Shape-memory polymer arch with temperature-responsive curving	2D / PL / CUR / TS / 3D / CY / SMP / SLA
Hydrogel strip that swells and folds with moisture	1D / B / SW/ MO / 2D / PL / G / DIW
Biodegradable scaffold with multi-stable folding mechanism	3D / SP / MTS / BIODEG / 3D / C / SMP / FFF
Magnetically actuated ring that twists into a helix	2D / RG / TW / MGS / 3D / HE / CO / SLM
Light-responsive composite disk that bends	2D / DK / BE / LS-V / 3D / CY / P / DLP
Thermo-mechanical shape-memory tube that expands	1D / T / EXP / TS / 3D / T / SMA / LENS
Humidity-responsive gel sphere that flattens	0D / S / FLAT / MO / 2D / PL / G / DIW
pH-responsive polymer plate that buckles	2D / PL / BU / pH / 3D / T / P / NPJ
Mechanical pressure activated multi-material spring	3D / SP / COMP / MS-F / 3D / SP / MT / CDLP
Biodegradable gel dome that collapses	3D / D / CONT / BIODEG / 2D / DK / G / DLP

However, the most interesting aspect of this section is the demonstration of how ChatGPT can be used as a tool to stimulate designers' creativity by exploring geometries that precisely change shape with the defined triggering stimuli, as discussed below. Once the ontology was provided to ChatGPT, the design process followed a structured approach guided by a series of prompts, which are presented in Table 5.4 in our wish to provide good practices for interacting with these resources in the fields of 4D printing and shape-morphing actuators. These prompts guided (or mentored) the generative AI to provide detailed recommendations on several critical aspects of 4D smart actuator design, including geometry, material selection and manufacturing processes. ChatGPT's ability to interpret coding and provide insightful design suggestions underlines its potential as an effective design tool for engineers and researchers.

Table 5.4: Prompts used in the conceptual design and optimization process of 4D printed material systems and structures and shape-morphing actuators in general.

	Prompt	Outcomes
Third prompt	*Thank you very much. As a 4D printing engineer, you are the best. Could you provide me with descriptions of how to design actuator(s) with the following encoding(s), including geometric and material aspects based on the selected additive manufacturing technology, ensuring that the actuator(s) are able to change shape as desired?*	Table 5.5
Fourth prompt	*Could you help me select the appropriate materials needed to achieve the desired shape change for each of the provided cases?*	Table 5.6
Fifth prompt	*Could you provide a separate visual representation for each designed actuator based on the coding provided above?*	Table 5.7

To illustrate this, ChatGPT was given four different codifications, each representing a different actuator design. Based on these code lines, ChatGPT was asked to generate specific design recommendations. The results, shown in Table 5.5, Table 5.6 and Table 5.7, demonstrate the capabilities of ChatGPT in several areas:

- Design recommendations (Table 5.5): ChatGPT provides detailed suggestions for the geometry and shape of each actuator based on the provided coding, addressing the specific requirements of shape-morphing actuators. It suggests features such as hinge-like structures or thin sections for smooth folding and unfolding, as well as embedded patterns or material gradients to induce controlled bending. These suggestions highlight ChatGPT's understanding of complex geometric requirements and its ability to offer feasible design solutions tailored to the intended behavior of each actuator.

  In addition, AI considers the interaction of the actuators with external stimuli such as temperature or magnetic fields. For example, it proposed the design of a cylindrical tube that unfolds into a flat plate when heated, demonstrating its ability to ensure smooth transitions between initial and final shapes in response to external triggering stimuli.

- Material selection (Table 5.6): ChatGPT provides valuable recommendations for materials that not only support the desired shape-morphing functionality but are also compatible with the proposed manufacturing techniques. For example, for heat-responsive actuators, it suggested shape-memory polymers with precise transition temperatures that allow shape change when heated. Similarly, for moisture-responsive actuators, it recommended hydrogels like polyacrylamide or chitosan, which swell when water is absorbed to achieve the desired folding effect.

  In the multimaterial case, ChatGPT is able to define optimal combinations, such as a rigid material that is a metal capable of withstanding cyclic loading, like nitinol, and a flexible polymer that complements the mechanical behavior under deformation, like TPU. In addition, it identifies synergies between these materials by proposing configurations that optimize both structural strength and flexibility at key application points. The use of metal-loaded filaments is also suggested, respecting the defined combination of materials.

What stands out is the personalized nature of ChatGPT's recommendations. It carefully considers key factors such as flexibility, strength and response to external stimuli to ensure that materials are well suited to the specific shape transformations required. It also considers the printability of the materials, suggesting those that are compatible with AM techniques such as Fused Filament Fabrication (FFF) or Direct Ink Writing (DIW), ensuring precise processing and high-quality results.

- Manufacturing process suggestions (Table 5.5 and Table 5.6): ChatGPT's design process goes beyond material selection, providing valuable insights into the manufacturing process and tailoring its recommendations to the capabilities of different 3D printing technologies. For the multimaterial actuator, it encourages the use of a dual extruder FFF printer to produce strategic infill patterns for accurate pre-programming of stress zones. In addition to recommending appropriate manufacturing techniques, ChatGPT considers post-processing steps to improve actuator performance. For example, it recommends reheating hinge-like features in certain designs to ensure proper functionality during shape-morphing. For magnetic materials, it suggests post-manufacturing magnetization to improve responsiveness to magnetic fields. This careful attention to the manufacturing process ensures that actuators meet design specifications and perform reliably in real-world applications.
- Visual representations (Table 5.7): In addition to its written outputs, ChatGPT's integration with DALL-E supports the design process by generating conceptual visual representations. While not as detailed as CAD models, these images may provide engineers with starting points for visualizing actuators and their shape-morphing behavior. By providing insight into the basic geometry and transformation processes, these visual sketches serve as a valuable tool for further refinement and inspiration. By combining both descriptive text and preliminary illustrations, ChatGPT supports a more holistic design approach. Designers can use these visualizations to better understand the physical form and function of their concepts, ensuring smoother progression from the initial idea towards a detailed CAD model and a fully realized prototype.
- Creative problem-solving and adaptability: One of ChatGPT's most notable contributions is its ability to offer creative alternatives when traditional approaches may not meet the design requirements. For example, in one design where shape-morphing through unfolding was required, ChatGPT suggested an innovative solution involving a helix-to-flat transition. This alternative not only met the design criteria, but

also introduced a novel approach that could inspire new engineering concepts. This highlights ChatGPT's ability to think beyond conventional solutions and propose inventive designs that stimulate new ideas.

Furthermore, ChatGPT's adaptability is demonstrated by its ability to suggest different stimuli to achieve similar results. In one case, it offered several material options based on the type of stimulus, suggesting that either magnetic or mechanical strain could trigger the desired shape change. This flexibility in its design approach allows AI to provide engineers with multiple pathways to achieve their goals, enhancing the overall creative process.

It is also interesting to highlight how the codification, which includes initial and final geometries based on primitives such as cubes, cylinders, rings, domes and springs, among others, can inspire even more complex geometries (as seen in the results from Table 5.7). These geometries meet the requirements of shape-shifting functionality based on the triggering stimuli and the selected manufacturing technologies.

Summarizing, the generative AI is able to operate with the ontology and codification provided, to codify textual descriptions of smart actuators, to describe codified shape-morphing systems, to support with materials selection tasks and to advise with manufacturing options for codified actuators and to generate conceptual design proposals, including inspirational images showing the actuation process on the basis of adequately codified smart materials systems and structures.

Table 5.5: From the codification to the description of 4D printed material systems and structures using a generative AI (ChatGPT). Remarkable proposals and advices given by the generative AI are highlighted in bold.

Ontology code (input)	Description (output)
3D/T/UF/TS/2D/PL/SMP/FFF	• Initial geometry and shape: Create a cylindrical tube with specific dimensions that allow for smooth unfolding. The tube should be hollow with uniform wall thickness for even heat distribution. • **Material selection: Select an SMP that has a transition temperature suitable for the application. Ensure the polymer has good flexibility and shape memory characteristics.** • Shape morphing principle: **Integrate hinge-like features or thin sections** along the length of the tube that facilitate controlled unfolding when heated. • Triggering stimuli: Ensure the SMP is responsive to a specific temperature range, which will trigger the unfolding mechanism. • Resulting geometry and shape: Upon heating, the tube unfolds into a flat plate. Design the **fold lines** to control the final shape accurately. • Manufacturing process: Use a 3D printer capable of FFF to print the tube. Ensure precise control over the extrusion process to maintain uniform wall thickness and hinge features. **Post-processing might include slight reheating to ensure the hinges function properly during actuation.**
2D/DK/CUR/MS-ST/3D/D/MT(A+P)/FFF	• Initial geometry and shape: Design the disk with a **thickness gradient** that promotes curving. Thicker regions should resist deformation more than thinner ones, enabling controlled curvature when stressed.

	Introduce **stress-relaxation zones in the disk structure (e.g., perforations or grooves)** to guide the curving process precisely • Material selection: Use a SMA like Nitinol for its excellent stress-strain response and ability to return to pre-defined shapes after deformation. Select flexible polymer such as thermoplastic polyurethane or a SMP that complements the alloy' behavior under mechanical strain. • Shape morphing principle: Curving implies a smooth deformation, such as rolling the disk edges upward or downward, depending on the stimuli. • Triggering stimuli: This means external forces, tension, or **programmed stress-relaxation properties** in the materials will initiate the curving process. • Resulting geometry and shape: The final dome shape is achieved through a combination of material strain recovery and geometric programming, where the alloys expand and polymers flex into the desired curvature. • Manufacturing process: Employ a **dual-extrusion FFF printer** to deposit the alloy-polymer combination. Print the **polymer as the outer layer and the alloy as an embedded mesh or skeleton within the disk**. Use precise **infill patterns to preprogram stress zones** that will guide the transition from disk to dome.
2D/U-BS/BS/MGS/1D/B/A/FFF	• Initial geometry and shape: Create a flat U-shaped bar with bistable properties, allowing it to snap between two stable states. • Material selection: Choose a magnetically responsive alloy that can maintain bistable behavior. • Shape morphing principle: Incorporate bistable elements in the U-shaped bar that allow it to transition to a straight bar under magnetic stimuli. • Triggering stimuli: **Embed magnetic particles or use a magnetically responsive alloy to facilitate shape change under magnetic fields.** • Resulting geometry and shape: The U-shaped bar snaps into a straight bar configuration when exposed to a magnetic field. • Manufacturing process: Use a 3D printer capable of FFF to print the U-shaped bar. Ensure precise control over the extrusion process to achieve the desired bistable properties. **Post-processing may include magnetization to enhance the magnetic response.**
2D/PL/O/MO/3D/C/G/DIW	• Initial geometry and shape: Create a flat plate with **predefined fold lines** to facilitate origami-like folding. • Material selection: Select a **gel that responds to moisture by swelling and becoming flexible, enabling folding.** • Shape morphing principle: Design the plate with precise fold lines and sections that fold into a cube upon moisture exposure. • Triggering stimuli: Ensure the gel material is sensitive to moisture and swells appropriately to initiate folding. • Resulting geometry and shape: The plate folds into a cube when exposed to moisture. • Manufacturing process: Use DIW to print the plate with precise fold lines and **ensure even distribution of the gel material.** Optimize the printing process to achieve the desired flexibility and folding behavior. Post-process to ensure the gel's moisture responsiveness is optimized for actuation.

Table 5.6: Generative AI (ChatGPT) proposals for innovative geometries, materials and manufacturing resources for the development of innovative codified actuators. Remarkable proposals and advices provided by the generative AI are highlighted in bold.

Ontology code (input)	Description (output)
3D/T/UF/TS/2D/PL/SMP/FFF	Material selection: • Polyurethane SMP: Known for its excellent shape memory properties and responsiveness to heat. • Polycaprolactone (PCL): Has a low transition temperature and good biocompatibility.

	• Polylactic Acid (PLA): Commonly used in FFF and has shape memory capabilities when blended or modified. Considerations: • Transition Temperature: **Ensure the SMP selected has a transition temperature suitable for the application.** • Flexibility and Strength: **The material should be flexible enough to fold and unfold without breaking.** • Printability: Must be compatible with FFF technology, ensuring smooth extrusion and layer adhesion.
2D/DK/CUR/MS-ST/3D/D/MT(A+P)/FFF	Material selection: • Nickel-Titanium (NiTi) Alloy: Known for its excellent shape memory properties. Provides **high fatigue resistance** and durability for repeated actuation cycles. • Alternative Alloys: **Stainless steel particles blended into a filament may be used if NiTi is unavailable.** • Thermoplastic Polyurethane (TPU): Offer flexibility and resilience, ideal for applications requiring durability and **wear resistance**. Considerations: • Material Compatibility: **Ensure NiTi and TPU/SMP bond well during printing** or assembly to avoid delamination during shape morphing. • Printability: **NiTi may need to be integrated post-printing or pre-treated for hybrid printing process.** • Flexibility and Strength: Materials must withstand mechanical stress without cracking or delaminating. TPU or SMPs with good elastic are essential.
2D/U-BS/BS/MGS/1D/B/A/FFF	Material selection: • Magneto-Responsive Alloys (e.g., Fe-Ga Alloy): Exhibits large magnetostriction and is responsive to magnetic fields. • Iron-Nickel (Fe-Ni) Alloy: Provides magnetic properties and bistable characteristics. • Terfenol-D (Terbium-Dysprosium-Iron Alloy): Known for its magneto strictive properties, though more challenging to print. Considerations: • Magnetic Responsiveness: The material must respond efficiently to magnetic fields. • Bistable Properties: Ensure the material can snap between stable states. • **Printability: Must be compatible with FFF, possibly requiring a filament with embedded magnetic particles.**
2D/PL/O/MO/3D/C/G/DIW	Material selection: • Hydrogel: Such as Polyacrylamide or Poly(N-isopropylacrylamide) (PNIPAM), which swell and change shape in response to water. • Alginate Gel: Biocompatible and responsive to moisture. • Chitosan Gel: Natural polymer gel that responds to moisture and has good mechanical properties. Considerations: • Moisture Responsiveness: **Ensure the gel swells adequately and uniformly**. • Mechanical Integrity: The gel should maintain structural integrity when folding. • Printability: Must be compatible with DIW, ensuring smooth extrusion and layer build-up.

Table 5.7: Visual representations of innovative coded actuators produced by ChatGPT and DALL-E as generative AIs.

Ontology code (input)	DALL-E representation (output)
3D/T/UF/TS/2D/PL/SMP/FFF	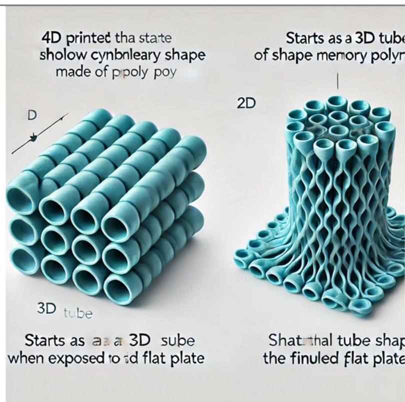
2D/DK/CUR/MS-ST/3D/D/MT(A+P)/FFF	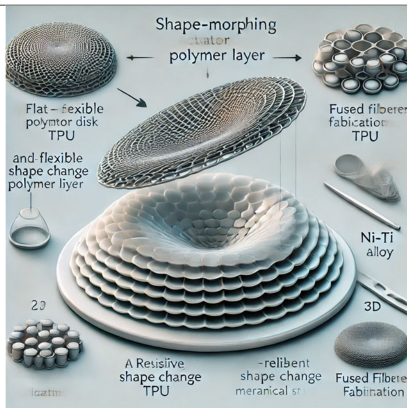
2D/U-BS/BS/MGS/1D/B/A/FFF	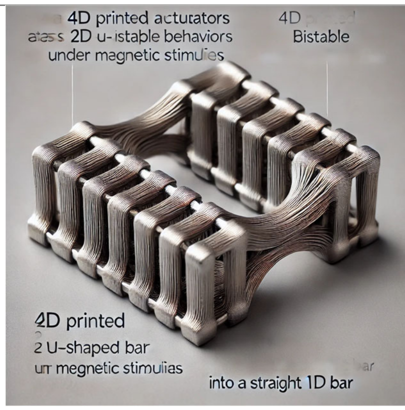
2D/PL/O/MO/3D/C/G/DIW	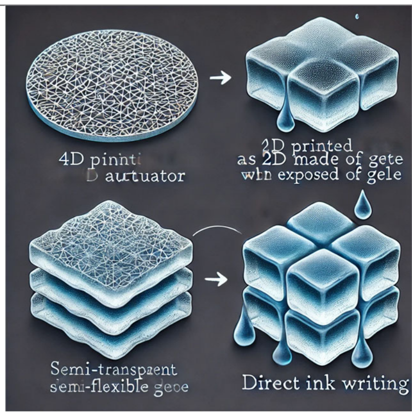

5.5. Application of generative AI to the design and manufacturing of a 4D cardiovascular stent

To further illustrate the potentials of synergically employing the codified ontology with generative AI resources an industrial use case linked to a shape-morphing cardiovascular medical device is presented here. Indeed, the designs and manufacturing of a coronary stent that changes shape in response to mechanical stimuli, following the life cycle *"3D/T/INV-EXP/MS/1D/T/EXP/MS/3D/T/A/SLM"*, represents an advanced case of 4D printing and demonstrates how generative AI can assist in the design process. The code line for this actuator describes the various transformations the coronary stent undergoes, starting as a three-dimensional tube (3D/T), which transitions to a one-dimensional shape (1D/T) due to radial compression (INV-EXP/MS). Upon releasing the stored energy (EXP/MS), the stent returns to its initial form (3D/T). The proposed device can be fabricated from an alloy (A) using the Selective Laser Melting (SLM) process.

ChatGPT was introduced to the first two prompts to re-explain the use of the ontology and validate its understanding. Subsequently, the ontology code was defined, which is attached after the third prompt. Finally, the other three prompts were then used to guide the design of the desired actuator (Table 5.4). To assess the consistency of ChatGPT's responses, the process was repeated three times as a proposed good practice, both to obtain a wider variety of ideas and to verify the variability of solutions provided by the generative AI.

The related key results are summarized in Table 5.8 and the whole design process is schematically illustrated in Figure 5.5.

Upon comparing the three iterations, authors observed similarities in the outcomes, such as the use of nitinol, the smart nickel titanium family of alloys, which is compatible with the defined manufacturing process, and the need for flexible or stretchable regions to allow the stent's radial contraction and expansion. In the second and third iterations, other materials, such as Co-Cr and titanium alloys, shape-memory and elastomeric polymers, and even hydrogels, were suggested to achieve the desired shape changes. Notably, in the case of hydrogels, ChatGPT recommended that DIW would be the most appropriate production process, demonstrating its ability to creatively and reliably bridge the gap between materials and manufacturing techniques.

In addition, the iterations defined certain geometric characteristics, such as varying wall thicknesses, creating internal channels, spiral designs, and correctly defining key parameters like wall thickness and the diameter of the tubular structure. Surprisingly, after the first iteration, the AI suggested potential industrial applications for the actuator in fields like medical device design or soft robotics mechanisms. Consequently, the information provided in each iteration complements the others, all following the same goal of designing the stent.

Based on the visual representations of the actuator provided in response to the fifth prompt, significant changes were observed between iterations. In the first image, intertwined helical fibers are visible, showing how these fibers close over time, resulting in the one-dimensional tube that enables the stent to be inserted into the corresponding artery via a catheter. In the second image, transverse strands are depicted, allowing the mechanism's dimensional change in height, meaning the expansion and contraction occur longitudinally rather than radially, in response to the triggering stimulus. In the third image, the intertwined strands of the stent are more explicitly visible, supporting the idea from the first image of designing a stent based on spiral intertwining, creating a flexible structure capable of shape-morphing when activated.

From these results, it was concluded that superelastic nitinol is the most suitable material for this application due to its biocompatibility, fatigue resistance, and ability to return to its original shape while withstanding the diameter variations the stent will undergo throughout its metamorphosis. Additionally, as ChatGPT suggested, post-processing the stent will be necessary to ensure a smooth and defect-free surface finish, a crucial aspect in medical devices. Regarding geometric design, the interwoven spirals that enhance the structure's flexibility were considered. As a result, the design is carried out in CAD software, allowing the STL file to be exported and imported into the corresponding slicer for manufacturing using the SLM process, which allows the precise creation of complex structures as conceptual preliminary prototypes.

Figure 5.5 summarizes the whole process, showing how, from the actuator's codification (in this case, the coronary stent), a series of textual and visual recommendations for its design, material selection, and manufacture are generated. These help to filter ideas, define requirements, design the actuator using CAD software, and fabricate it with the selected process and material. Other ideas provided by ChatGPT in different iterations may be useful for designing other related actuators or alternative solutions with various shape changes, triggering stimuli, materials, and manufacturing processes.

It is important to clarify that this is only a conceptual test, allowing designers to brainstorm using the ontology as a means of communication with the AI. In this case, an iterative brainstorming process is recommended since, as seen in this example, the information provided by ChatGPT is complementary across various iterations. To validate the AI-generated design, computational simulations, mechanical testing, and *in vivo* and *in vitro* tests can be conducted to confirm its biocompatibility and clinical efficacy, ensuring that the final product not only meets medical requirements but also provides a durable and safe solution for patients with cardiovascular diseases.

Indeed, with the current state of the art, according to our experience with the interactions with the generative AI, the combined employment of the ontology (and its codification) and generative AI tools are interesting from the point of view of creativity promotion, mainly for the conceptual design stage of the engineering design cycle. Once a codification for a possible 4D printed actuator is provided to the trained generative AI, it is possible to ask for materialization proposals, as exemplified in section 5.4 and summarized mainly in the outputs from Table 5.5 and Table 5.6. In those outputs, the generative AI makes specific references to aspects like strength, response to stimulus, and printability, providing concrete examples of usable materials, designs and manufacturing options, even without having been provided with materials properties.

In fact, those properties are already available to the AI, which searches for them within the general documentation already forming part of its "cultural background". However, at the current state of development of generative AI tools, even if vast information about materials properties may be available from the documentation employed for training (potentially the whole documentation from the world wide web), we still believe that the transition from the visual representations and conceptual descriptions provided as outputs by the AI towards the final reliable design of a functional shape-morphing device should be still carried out by experienced engineers, acting as quality control warrants.

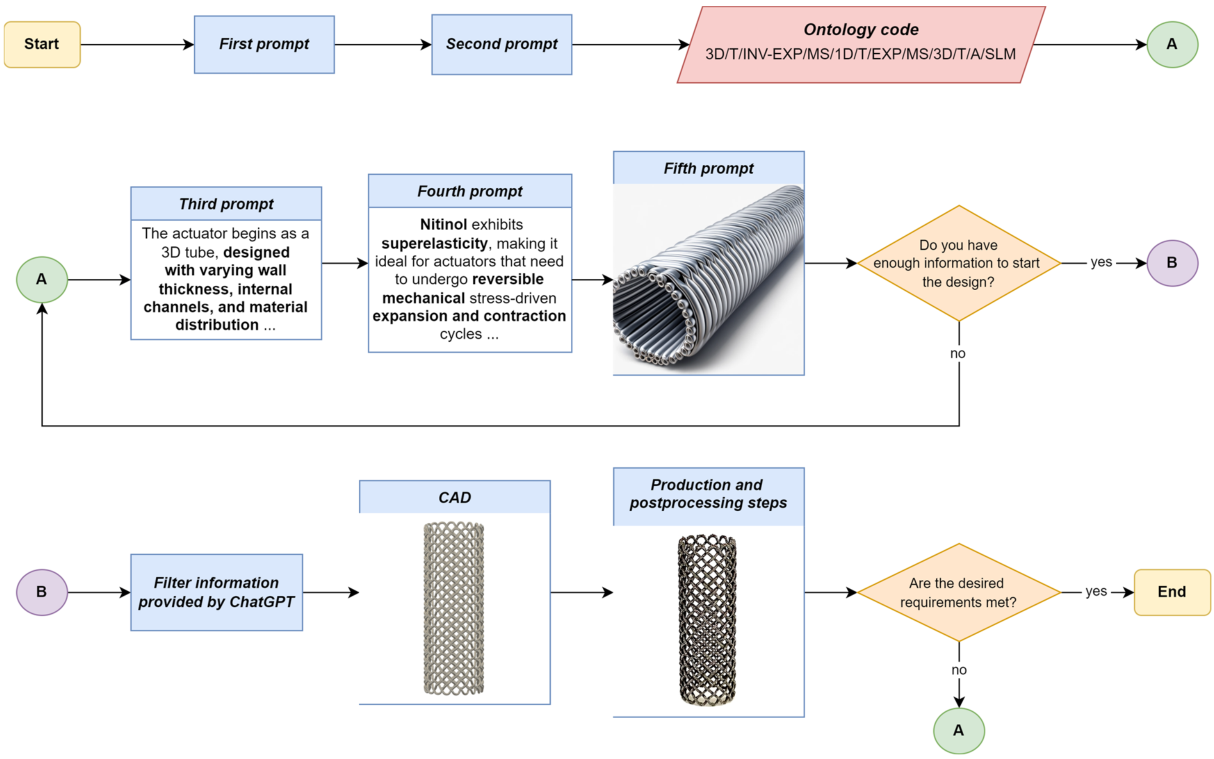

Figure 5.5: Generative AI-aided design and manufacturing process of a shape-morphing cardiovascular stent involving the interaction with ChatGPT and the employment and application of the developed ontology and codification. Printed nitinol prototype courtesy of IMDEA Materials Institute. Photographs courtesy of M. Eng. Carlos Aguilar Vega.

Table 5.8: Iterative outcomes of the generative AI during the design of a cardiovascular stent: three constructive dialogues are presented.

Input	Output 1	Output 2	Output 3
Third prompt	The actuator begins as a 3D tube, **designed with varying wall thickness, internal channels, and material distribution** to allow for inverted expansion. **Internal stress points or flexible regions** can be introduced to ensure morphing behavior, with **features like variable thicknesses or spiral designs** enabling contraction under external stress. **Selective Laser Melting** (SLM) provides precise control over the structure, **ensuring accurate internal features and mechanical properties**. **Surface finish and post-processing are critical**, especially for high-stress environments where smooth surfaces and precise tolerances are required.	This can be applied in situations where repeated expansion and contraction are required, such as in **pumps or soft robotics**. The shape change is triggered by mechanical forces like **stress, pressure, or external deformation**. This type of actuator is particularly useful in **medical devices**, where precise control of expansion and contraction is essential, or in **soft robotics**, where flexible and reversible actuators are needed.	The actuator begins as a 3D hollow tube with a **well-defined diameter and thickness** to withstand the mechanical forces it will encounter. Using SLM, the tube can be manufactured with precise dimensions and **complex internal structures, ensuring it remains lightweight yet strong enough to handle mechanical stress.** During actuation, the tube transitions into a 1D structure, likely through elongation or significant contraction, which may require **flexible or stretchable sections in its design.**
Fourth prompt	Mechanical Stress Responsiveness: **Nitinol exhibits superelasticity, making it ideal for actuators that need to undergo reversible mechanical stress-driven expansion and contraction cycles**. Compatibility with SLM: **Nitinol is suitable for SLM technology, as SLM can precisely fabricate intricate shapes and internal structures** from Nitinol powder. This ensures high-quality, detailed manufacturing of the 3D tubular structure.	Materials used for tubes in both 3D and 1D configurations must **offer flexibility** for deformation under stress and have **excellent recovery properties**. Mechanical forces trigger the shape changes, so the materials need to allow for deformation and recovery. **NiTi** is ideal for cyclical morphing due to **its ability to return to its original shape after stress**, making it suitable for **biomedical applications** like stents and grippers. **Elastomeric polymers**, such as TPU or silicone, provide softer, **more flexible deformations** with less force compared to metals. **Hydrogels, which can expand or contract with stress,** are suited for biocompatible applications but are usually used in Direct Ink Writing (DIW), not SLM.	**Shape-memory polymers** (SMPs) offer a **lighter, more flexible alternative to metals**, capable of contracting and returning to their original state when triggered by mechanical or thermal stimuli. **Ni-Ti** (Nitinol) is the preferred shape-memory alloy for its compatibility with SLM, providing **excellent shape recovery, fatigue resistance, and biocompatibility, ideal for medical applications**. Cobalt-chromium (**Co-Cr**) alloys are suitable for SLM when **corrosion resistance or biocompatibility** is needed, offering strength and durability in harsh environments. **Titanium alloys** are widely used in aerospace and medical devices due to their **lightweight, high strength, and biocompatibility.**
Fifth prompt	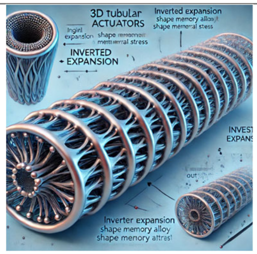	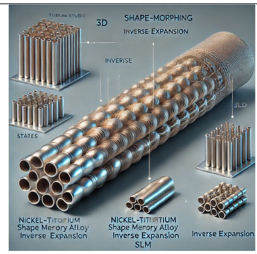	

5.6. Discussion, current challenges and future proposals

First, it is important to highlight the versatility and utility of the developed ontological framework and related codification scheme for classification and description purposes. It is true that most of the examples found in the brief review (and classified in Table 5.2) deal with a single metamorphosis: one initial shape and one final shape with a shape-morphing process in between. However, as illustrated in the example of Figure 5.3 and in 10 of the 54 examples of Table 5.2, the ontology and codification are perfectly adequate for dealing with 4D printed shape-morphing actuators capable of numerous shape-morphing steps or metamorphoses. A single line of code is enough to describe the whole actuation lifecycle, which includes all the geometrical transformations of the material, structure or device.

Regarding creativity promotion in the 4D printing arena, counting with this comprehensive ontology and codification can prove extremely rewarding, especially if combined with generative AI tools for fostering innovative solutions. Apart from the already presented synergies with generative AIs, by means of example, Figure 5.6 provides a general codification scheme applied to innovating 4D printed families of multi-stepped actuators triggered by biodegradation, manufactured using biodegradable alloys using powder-bed laser fusion. If the different boxes "shape" and "shape morphing" are methodically combined using the possibilities listed in Table A.1 and Table A.2 from the annexed glossary, an extremely varied set of potentially viable solutions should be obtained for biodegradation-triggered shape-morphing metallic actuators. To this end, generative algorithms may be also applied in the future.

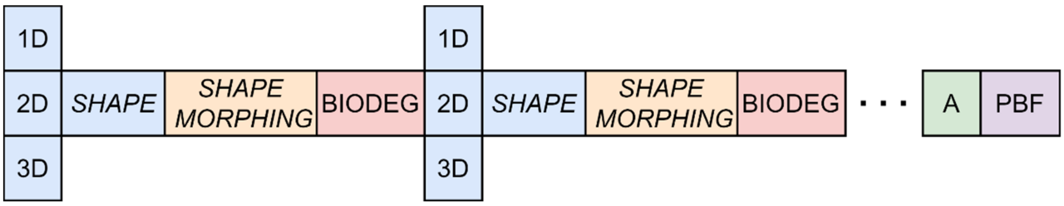

Figure 5.6: Codification scheme applied to innovating 4D printed families of multi-stepped actuators triggered by biodegradation, manufactured using biodegradable alloys employing powder-bed fusion.

Interestingly, the elements of the ontology can be employed as building blocks, to foster innovation in the 4D printing field, motivating researchers to search for potentially useful combinations of geometries, shapes, shape-morphing principles, triggering stimuli, materials and printing technologies, and, hence, additionally increase the already vast field of application for 4D printed shape-morphing devices. For this purpose, the progressive incorporation of the building blocks of this or similar ontologies, to the set of design operations within CAD modeling software, in connection with algorithmic design approaches, can constitute a relevant step forward. Counting on specific finite elements that adequately describe the shape-morphing of different printable materials, because of the applicable triggering stimuli, is hence essential. Linking these elements to the building blocks of the ontology can support the straightforward development of viable shape-morphing systems.

Considering other future research directions, an automated discovery of novel families and subfamilies of smart shape-morphing 4D printed actuators is envisioned. This process will be driven by the strategic combination of three types of self-organizing artificial systems: cellular automata, artificial intelligence (including generative adversarial networks and reinforcement learning), and genetic algorithms to emulate and amplify the designer' thinking and creativity [334].

With the proposed ontology and symbolic codification, the first step toward deciphering the genome of shape-morphing systems has already been taken [335]. The integration of both proposals, CAD/CAE modelling and artificial systems, is necessary for discovering new smart 4D printed structures. Therefore a generative cellular automaton could be employed, in which the lattice geometry would be univocally related to a control volume imported by the designer, which could be divided into voxels because they allow to arrange the material in any distribution and evaluate their behavior straightforwardly [336]. The information of the shape-morphing steps and their corresponding triggering stimuli would feed the automata, whose rules would be set by an artificial intelligence based on: 1) the laws of 4D printing [337], 2) the selected AM technology linked to the proposed materials and 3) their distribution. The result would be a CAD file built from the combination of the voxels in the final distribution, supplied by the automata, together with a simulation to verify if the result fits the desired metamorphoses. In addition, the designer could provide feedback to improve the model's performance based on previous experiences and experiments, for fine-tuning purposes. Eventually, the role of the designer will become that of a quality inspector evaluating if the proposed solutions meet the defined requirements (as schematically presented Figure 5.7). The additional integration of generative AI into the innovation cycle will also transform the role of the designer, including the need for training in ways of interacting with the AI (providing successful prompts) and an additional role as creativity promotion mentor and validator of artificially proposed solutions.

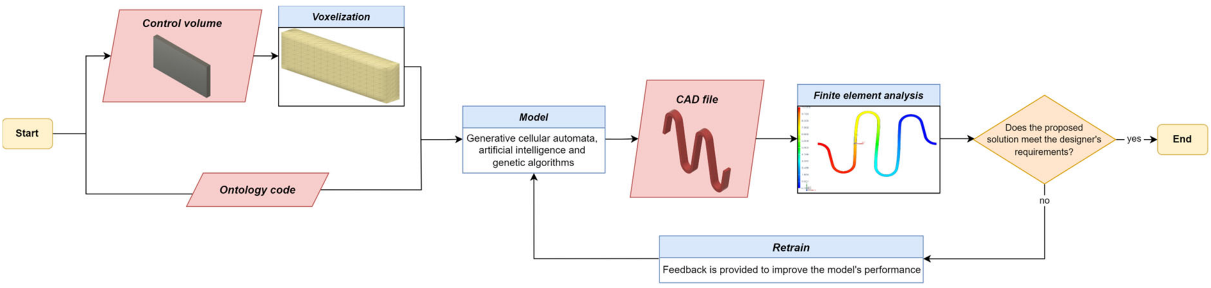

Figure 5.7: Codification scheme applied to innovating 4D printed families of multi-stepped 4D printed actuators.

5.7. Conclusions

A versatile and useful ontology, with universal ambition, for describing all kinds of smart 4D printed material systems and structures has been presented. The different components of the ontology, namely: initial geometry and shape, shape-morphing principle(s), triggering stimuli, intermediate/final geometry and shape, material and 4D printing or AM technology, have been described, and a codification scheme for accordingly describing the life cycle of 4D printed material systems and structures has been provided. The systematic application of the ontology to a set of 54 relevant examples has helped to illustrate its utility and adaptability to many different types of 4D printed devices.

The ontological framework and codification scheme developed represent one of the most comprehensive classification tools for the emerging field of 4D printing, thanks to incorporating several geometries, shapes, shape-morphing principles, triggering stimuli, materials and technologies not covered by previous examples of taxonomies and ontologies for smart and 4D printed materials and structures, as has been discussed and referred.

Besides, it is the first ontology capable of representing (in a single line of code) the whole lifecycle of complex 4D printed devices and actuators, in which several metamorphoses may be achievable, due to combinations of different shape-morphing principles and triggering stimuli. A glossary is provided as Appendix A, to support its implementation and application, and authors are available for fruitful discussions oriented to modifying, completing and improving the proposed ontology with the global aim of organizing this continuously evolving and fascinating field of study.

To the best of current knowledge, this is the first time in which an ontology of smart 4D-printed material systems and structures has been integrated with a generative artificial intelligence tool, with their synergistic utility validated. This combination has demonstrated exceptional potential as a powerful mechanism for fostering creativity in the engineering design of smart materials and structures.

6. Mechanical, biological, and degradation insights of PVA and PETG for 4D-printed actuator development

6.1. Introduction

Four-dimensional (4D) printing has emerged as an evolution of AM, integrating the ability of objects to change shape in response to internal or external stimuli [338,339]. This "fourth dimension" is based on design strategies with programmed internal stresses, the use of shape memory materials or the combination of different materials that respond to different stimuli such as temperature [340–342], voltage [343,344], light [345,346], humidity [347,348] or even (bio)degradation [4,349]. In the literature, promising applications have been reported in healthcare [267,350], robotics [351,352], architecture [353,354] and aerospace [355], where controlled geometric transformations are crucial for the development of "intelligent" structures and devices capable of adapting and evolving over time [338,339].

Within this spectrum of materials and technologies, polyethylene terephthalate glycol-modified (PETG) has proven to be particularly versatile due to its shape memory, amorphous nature and ability to easily induce molecular interactions for geometry recovery after programmed deformation [258,356]. By tuning the glass transition temperature during thermal programming, whether cold, warm or hot, mechanical properties can be modulated for specific applications, maximizing structural stability or energy efficiency as appropriate. Furthermore, the incorporation of Fe_3O_4 nanoparticles has improved the thermomagnetic response of PETG with significant recovery rates even at low concentrations [357]. Similarly, the combination of PETG with other polymers such as PLA or polybutylene adipate terephthalate (PBAT) has enabled complementary mechanical and memory properties. For example, the 75% PLA and 25% PETG blend shows 100% recovery as well as high tensile strength [358], while the addition of PBAT increases ductility and recovery speed, which is considered promising in soft robotics and biomedical devices [359].

On the other hand, poly (vinyl alcohol) (PVA) is a water-soluble material traditionally used as support in 3D printing with fused filament fabrication (FFF) technology, which facilitates the construction of complex geometries and the subsequent elimination of support structures by immersion in water [360,361]. This property has encouraged its use in the fabrication of anatomical scaffolds for tissue engineering [362] and in biomedical or pharmaceutical applications such as controlled drug delivery [65] and tablet printing [363]. However, its high affinity for moisture requires careful handling and storage to preserve its mechanical properties [361].

In this work, an approach is proposed that uses the degradation of PVA as a stimulus to trigger a programmed shape morphing, while PETG acts as a component capable of storing and releasing mechanical energy. The progressive dissolution of the PVA not only allows the strategic elimination of parts of the structure but can also be used to achieve a controlled metamorphosis when the design of the piece induces internal tensions in the PETG, which are gradually released until the shape is recovered. Although degradation has been little explored as a source of large or repeated geometric transformations, its inclusion in 4D printed devices opens up significant possibilities in fields where slow response can be an advantage, for example in medical applications where healing and growth processes require time [364,365]. Thus, the combination of these two polymers using FFF provides a rapid, affordable and scalable prototyping method for the development of programmable actuators which, with appropriate design, could be extrapolated to more advanced and robust configurations.

This study will characterize the mechanical properties, biological response and degradation of PETG and PVA, with a focus on the effect of water as a degradation medium. In addition, a proof-of-concept actuator will be presented to illustrate how the progressive dissolution of PVA triggers the shape change of PETG. This systematic approach to controlled degradation in 4D printing has the potential to lay the foundations for the design of sustainable, adaptive structures with high impact technological applications in areas such as regenerative medicine, soft robotics and advanced manufacturing.

6.2. Materials and methods

6.2.1. Mechanical tests

To determine the mechanical properties of the materials, uniaxial tensile and three-point flexural tests were carried out with the Instron 5966 mechanical testing machine (Instron, Norwood, Massachusetts, USA), equipped with a 500 N load cell. The tests were conducted at a constant crosshead speed of 2 mm/min. In the three-point bending test, a span of 64 mm and rollers (support and loading) with a diameter of 10 mm were used (Figure 6.1).

Deformation in the tensile test specimens was measured using digital image correlation (VIC, Correlated Solutions, USA). To do this, the test specimens were sprayed with a random pattern of black dots on a white background. This pattern was recorded by a high-resolution camera and subsequently analyzed with VIC-2D software to calculate the deformations.

In order to evaluate the effect of immersion in water on the mechanical properties, a system designed by Dr. Vanesa Martínez of IMDEA Materials Institute was employed (Figure 6.1A). This system allows the test pieces to be immersed in water at 25ºC with a controlled laminar flow during the tensile test. Temperature control avoids the shape memory effect in PETG [257,258] and reduces PVA erosion, as turbulent flows could accelerate its degradation [215].

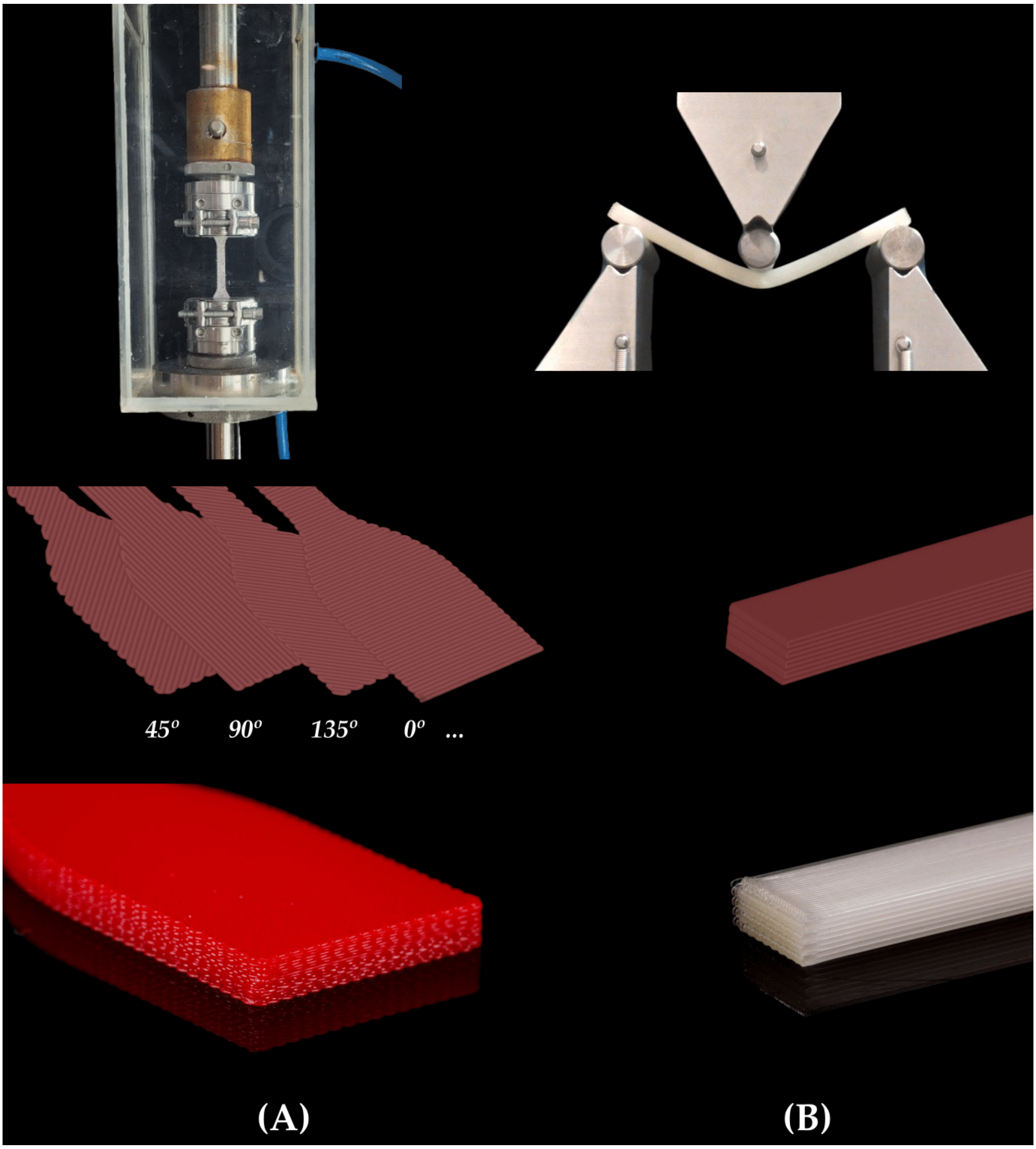

Figure 6.1: Mechanical testing setup, specimen slicing with infill patterns, and the 3D-printed part for (A) underwater tensile and (B) flexural tests. Courtesy of Dr. Vanesa Martínez and Álvaro Troyano.

In the case of PVA, the influence of immersion in water at different time intervals (0, 10, 20, 40 and 80 minutes) prior to the tensile test was investigated, given its high solubility. To prevent the specimens from slipping out of the holding grips, the grip area was made watertight, preventing local degradation. On the other hand, for PETG, its viscoelastic behavior was studied through stress relaxation tests, keeping the deformation constant at 1% (within the elastic zone) for 40 minutes and evaluating the variation of its elastic modulus before and after immersion.

The tensile test specimens were designed in accordance with ASTM D638-03 [177], using Type IV dogbone geometries and manufacturing them in build direction flat. To quantify the damage induced by immersion in water, a quasi-isotropic layup with the sequence [45º, 90º, 135º, 0º, 45º, 90º, 135º, 0º]$_s$ was used, which guarantees in-plane isotropy [366]. The design was made in Autodesk Fusion 360 (Autodesk Inc., San Rafael, CA, USA), dividing the total thickness of 3.2 mm into 16 layers of 0.2 mm each.

The resulting files were imported as assemblies into Bambu Studio software (Bambu Lab, Austin, TX, USA). During printing, a 100% rectilinear infill was applied, adjusting the orientation of each layer according to the corresponding angle. The final result is shown in Figure 6.1A.

The flexural test specimens were designed according to ISO 178 [255], with dimensions of 80 × 10 × 4 mm^3, and were manufactured on edge. A completely solid infill with a rectilinear pattern aligned at 90° was chosen, with the aim of evaluating the behavior of fibers oriented in the neutral axis, a particularly relevant arrangement for the development of 4D mechanisms triggered by (bio)degradation (Figure 6.1B).

All the test pieces in this section and the following ones were produced by the Bambu Lab X1 Carbon Combo printer (Bambu Lab, Austin, TX, USA), using PETG and PVA filaments with a diameter of 1.75 mm (Smart Materials 3D, Alcalá la Real, Jaén, Spain). The same printing parameters were applied to all samples: layer thickness of 0.2 mm, printing speed of 50 mm/s, bed temperature of 70 °C and nozzle temperatures of 220 °C and 240 °C for PVA and PETG, respectively. They were printed with the infill pattern defined in each configuration, omitting the addition of outer perimeters.

6.2.2. Degradation tests

In order to evaluate the solubility of PVA, one of the key factors inducing shape changes in 4D printed parts, experiments were designed with 30 × 30 × 1 mm^3 specimens. Due to the small size of their thickness compared to the other two dimensions, they were considered as two-dimensional samples. The tests were carried out in a glass container of 200 × 150 × 50 mm^3 containing 800 mL of water at 25 °C, giving an average volume to surface area ratio of the sample of 6.67 mL/mm^2. This was sufficient to prevent water saturation due to PVA dissolution. During the experiments, the test samples remained submerged and fixed on the bottom of the container; they were also covered with a transparent PETG plate, which restricted the direct penetration of water and allowed a controlled analysis of the two-dimensional erosion (Figure 6.2A).

Two main types of specimens were developed. The first group consisted of circular samples specifically designed to study the influence of the infill pattern on degradation. Two configurations were compared: a concentric pattern, where the fibers were aligned in the direction of erosion, and a rectilinear pattern with a layer sequence of [90°, 0°] (Figure 6.2B). The rectilinear configuration was selected as an alternative to emulate the quasi-isotropic pattern since the limited thickness of the specimens made it impossible to accurately replicate the quasi-isotropic distribution defined in the tensile specimens. The second group consisted of specimens with different shapes: triangles, squares, hexagons, and a figure shaped like a "4"; all produced employing the rectilinear pattern (Figure 6.2C). These samples were designed to assess how shape and exposed surface area influence the erosion of 3D printed PVA.

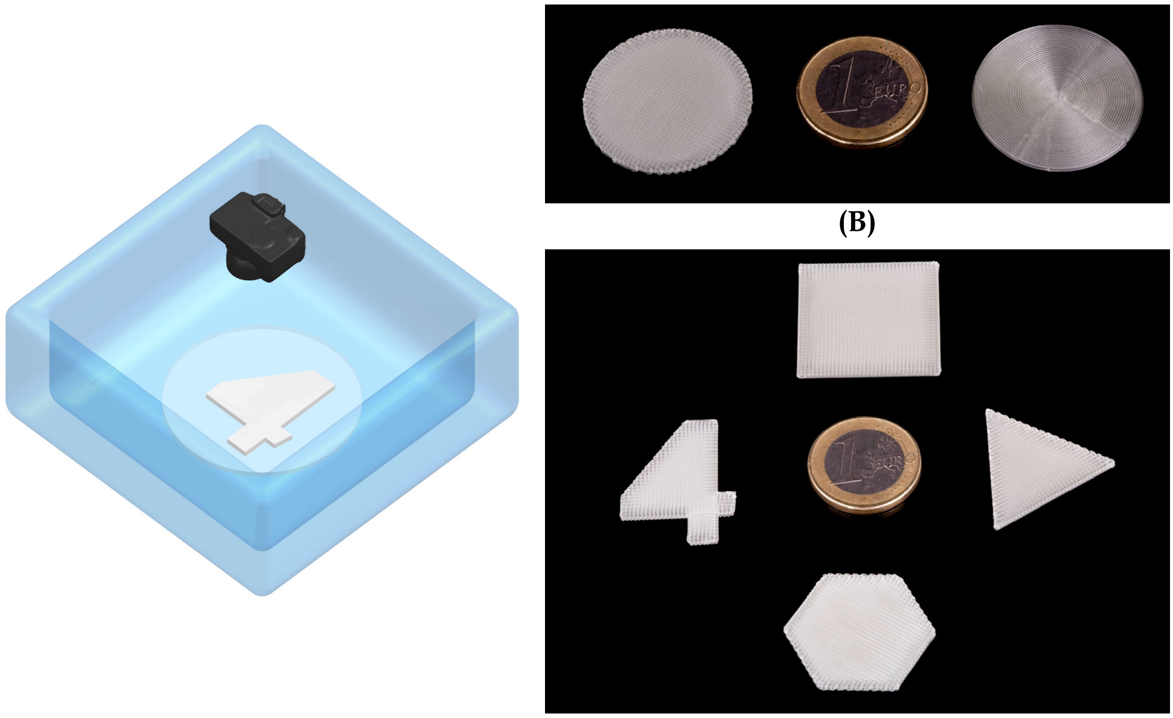

(A) **(C)**

Figure 6.2: (A) Test bench and samples for evaluating the erosion of 3D printed PVA, (B) influence of the infill pattern, and (C) exposed surface area-to-volume ratio. Photos courtesy of Álvaro Troyano.

To monitor the process, a high-resolution 12-megapixel optical sensor with f/1.5 aperture and optical stabilization was positioned at the top of the container to capture images of the degradation process every minute. It was observed that the erosion of the material started at the edges, where there was direct contact with the water. As the process progressed, bubbles appeared around the samples, complicating the interpretation of the images as these bubbles had intensity values similar to the degraded areas of PVA. To overcome this difficulty, an algorithm based on computer vision and machine learning was developed to accurately segment the degraded areas and distinguish them from the bubbles.

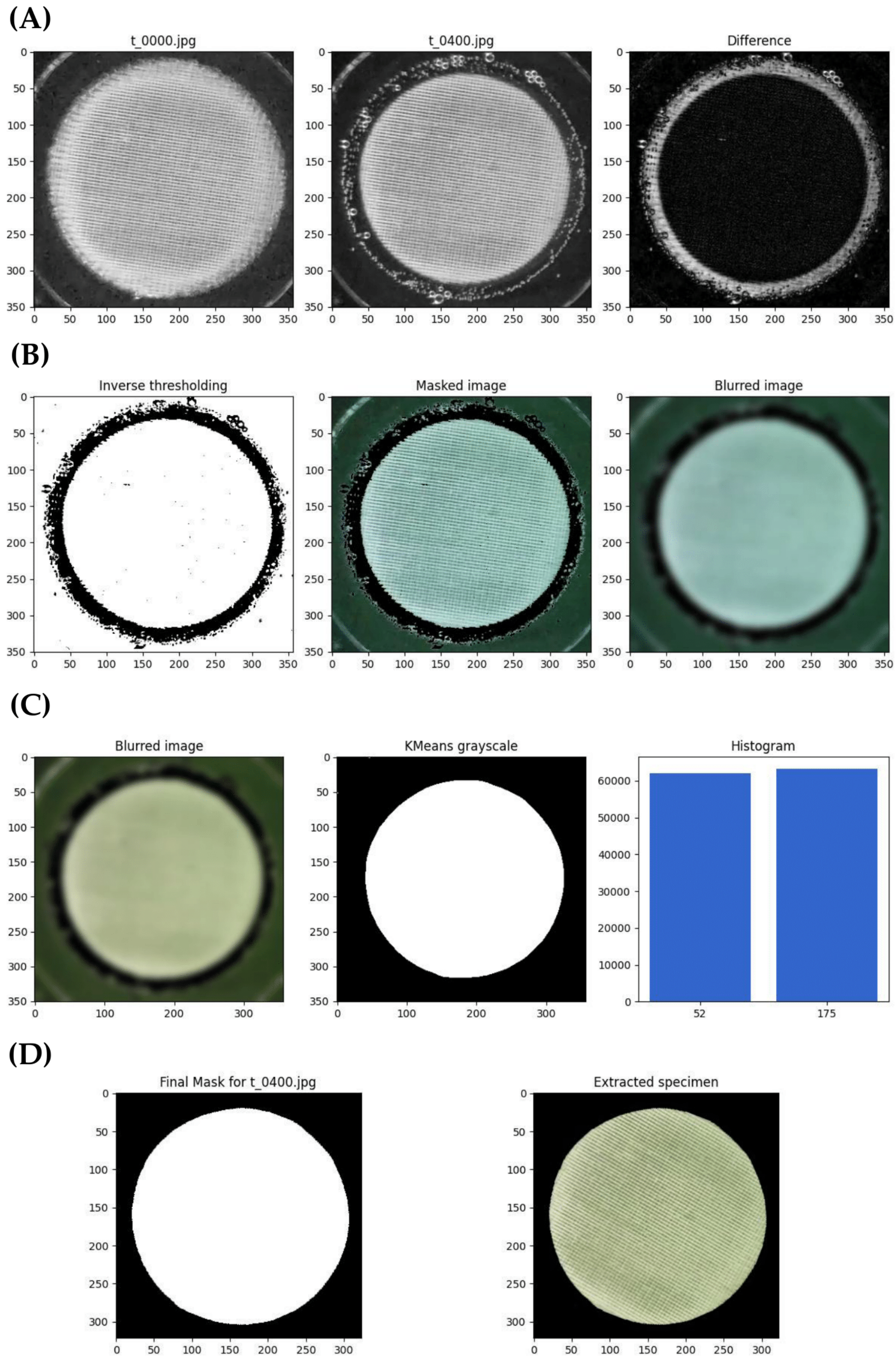

Figure 6.3: Automatic segmentation of PVA degraded specimens. (A) Comparison of consecutive images using the absolute difference, which highlights significant visual changes between them. (B) Refinement of the second image by inverse thresholding to generate a binary mask, followed by its application and smoothing with a Gaussian filter. (C) Segmentation of the smoothed image using K-means, accompanied by the histogram showing the distribution of intensity levels. (D) Extraction of the degraded sample by applying the final mask and perspective transformation to obtain the ROI.

The image processing was implemented in Python using the OpenCV [251], Numpy [252] and Matplotlib [253] libraries. First, the images stored in a ZIP file were extracted and sorted alphabetically to ensure sequential analysis. The initial image was then converted to greyscale, smoothed with a Gaussian filter and segmented using K-Means to separate the relevant areas from the background. This segmentation produced a binary mask that highlighted the region of interest (ROI). In addition, a perspective transformation was calculated based on the detected contours to fit the ROI into a uniform rectangular format, considering that each pixel represents 0.093 mm. The resulting mask, the segmented and transformed image (Figure 6.3D) and transformation matrix were stored for future use.

Analysis of subsequent images was performed recursively in successive pairs. For each couple, the absolute difference between the previous and current image was calculated to identify significant visual changes (Figure 6.3A). This difference was thresholded to produce a binary mask, which was then applied to the current image. This image was smoothed with a Gaussian filter to reduce noise, including any bubbles present (Figure 6.3B), and then segmented again with K-Means to produce a refined mask (Figure 6.3C). Finally, this mask was applied to the second image of the pair and transformed using the previously calculated perspective matrix (Figure 6.3D). Each time the processing of a pair was completed, the second image became the new reference. All results, masks, transformed images and intermediate visualizations were saved, together with a text file containing the greyscale masks, in order to analyze the progression of material degradation.

6.2.3. Cell culture testing

Bone marrow derived human mesenchymal stromal cells (hMSCs) were purchased at passage 1 (#PCS-500-012, LGC ATCC, Spain) and were cultured up to passage 6 in expansion medium: αMEM (#A1049001, Thermo Fisher, Spain), 1% antibiotic/antimycotic (#L0010-100, Biowest, Spain), 10% v/v FBS (#10270106, Thermo Fisher, Spain), 100 µm ascorbic acid (#A8960, Sigma, Spain), and 1 ng/mL fibroblast growth factor-2 (#Z03116, GenScript, Spain). The medium was refreshed twice a week. The cells were used at passage 6 for biocompatibility test.

Two different structures printed with the concentric pattern were used to test the materials biocompatibility: either 6 x 6 x 1 (S1) or 3 x 3 x 1 (S2) mm^3 samples . Samples were immersed in 70% ethanol for 30 minutes and then washed twice in sterile 1xPBS before use. hMSCs were seeded at a density of 5.3 x 10^3 cells/cm^2 onto a 48-well plate. Cells were cultured for 24 hours before adding the PVA or PETG samples on top of them. Then, the metabolic activity of the cells was measured 24, 72 and 144 hours post exposure to the samples. The same number of samples ($n = 3$) was used at all time points. Bright field microscope images were taken at each time point, from which quantitative analysis was performed to calculate experimental cell density over time. Live dead analysis was performed at day 6 and results were quantified from confocal images.

PrestoBlue assay was used to test the metabolic activity according to manufacturing instructions. Briefly, 10% of PrestoBlue™ Cell Viability Reagent (#A13261, Fisher Scientific, Spain) in expansion medium was incubated with the cells alone (positive control), cells containing PVA samples (experimental group), or the medium alone (negative control) for 30 minutes before reading the fluorescence using an excitation wavelength of 560 nm and an emission of 590 nm. Tukey test (two-way ANOVA) was used to calculate statistical significance.

6.3. Material characterization

6.3.1. PVA samples

The tensile curves of the PVA (Figure 6.4) show significant changes in its mechanical properties as the immersion time increases. In particular, a transition from brittle to more ductile behavior can be observed, as indicated by the progressive rise in strain at break, as shown in Figure 6.8. Similarly, the difference between the yield and tensile strength increases, indicating that the material acquires a greater capacity to deform plastically prior to failure (Figure 6.6 and Figure 6.7).

Detailed analysis shows that water causes significant damage to the polymeric structure, causing an exponential decrease in elastic modulus, yield and tensile stress as exposure progresses, an effect associated with the reduction in molecular weight [367,368]. Two models were fitted to describe this trend: a pure exponential and an offset exponential decay function. As can be seen in Figure 6.5B, Figure 6.6B and Figure 6.7B, the offset exponential decay function fitting gave the highest R-squared values (> 0.9). The pure exponential model was chosen as a baseline because it has been reported that hydrolytic damage follows the same trend as changes in the polymer molecular weight, which tracks this tendency [368]. However, studies on the erosion of water-soluble polymers indicate the existence of a critical value above which the polymer fails catastrophically (Figure 3.14). Consequently, the inclusion of a residual term in the model indicates that failure occurs when this value is approached [176,367].

After 80 minutes of immersion, the Young's modulus, yield and tensile stress decreased by 36.25%, 29.33% and 22.99% respectively, with an average damage approaching 30%. The elastic modulus was the most affected parameter. Examination of the fracture zone of the quasi-isotropic PVA specimens (Figure 6.9) shows that in the dry state each layer is clearly visible, with a pronounced brittle fracture. As the immersion time increases, the boundaries between the layers become blurred to the point where there is a homogeneous appearance with no obvious distinction of how each layer fails. It is also possible to see the formation of internal bubbles, probably due to air trapped during the printing process, which is concentrated in certain areas when water penetrates the structure.

Finally, the three-point flexural results (Figure 6.10A, Table 6.2) show a more ductile response of PVA when the infill pattern is oriented in the principal direction of the bending stress, in contrast to the brittle nature observed in the tensile test. Similarly, the material exhibits superior strength, reflected in higher values for its mechanical properties (Figure 6.10B). This ductile behavior is evident from the flattening of the layers without cracking in the region of the loading pin, as observed in Figure 6.10C.

Table 6.1: Tensile mechanical properties of PVA due to hydrolytic degradation over time.

Time (min)	Elastic modulus (MPa)	Yield strength (MPa)[25]	Tensile strength (MPa)	Strain at break (mm/mm)
0	4925.083 ± 575.651	48.439 ± 1.114	48.767 ± 0.653	0.011757 ± 0.000876
10	4119.668 ± 212.092	45.592 ± 1.205	46.27 ± 1.092	0.013128 ± 0.000569
20	3659.392 ± 61.45	40.885 ± 0.5	42.269 ± 0.75	0.014148 ± 0.000602
40	3261.026 ± 103.754	36.007 ± 0.198	39.118 ± 0.74	0.016121 ± 0.000069
80	3139.596 ± 9.647	34.228 ± 0.038	37.557 ± 0.415	0.016987 ± 0.000857

Table 6.2: Comparison of the tensile and flexural properties of PVA.

	Tensile specimens	Flexural specimens
Elastic modulus (MPa)	4925.083 ± 575.651	4304.768 ± 61.948
Yield strength (MPa)	48.439 ± 1.114	107.085 ± 3.095
Ultimate strength[26] (MPa)	48.767 ± 0.653	116.014 ± 3.486

[25] Defined as the stress corresponding to a strain of 0.2%.
[26] In the case of the tensile test, tensile strength.

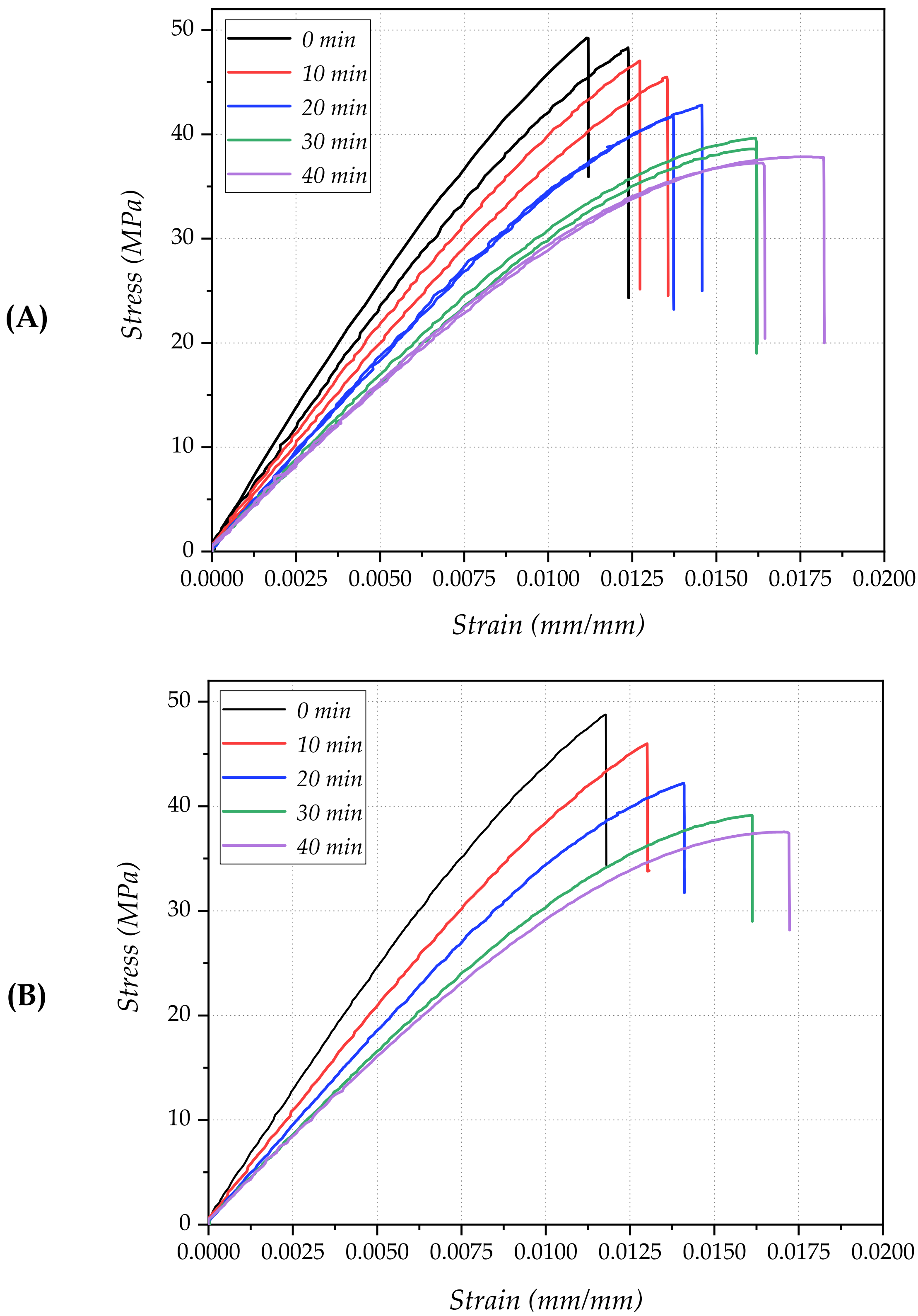

Figure 6.4: (A) Tensile curves of 3D printed PVA employing the quasi-isotropic pattern as a function of immersion time and (B) their average curves.

(A)

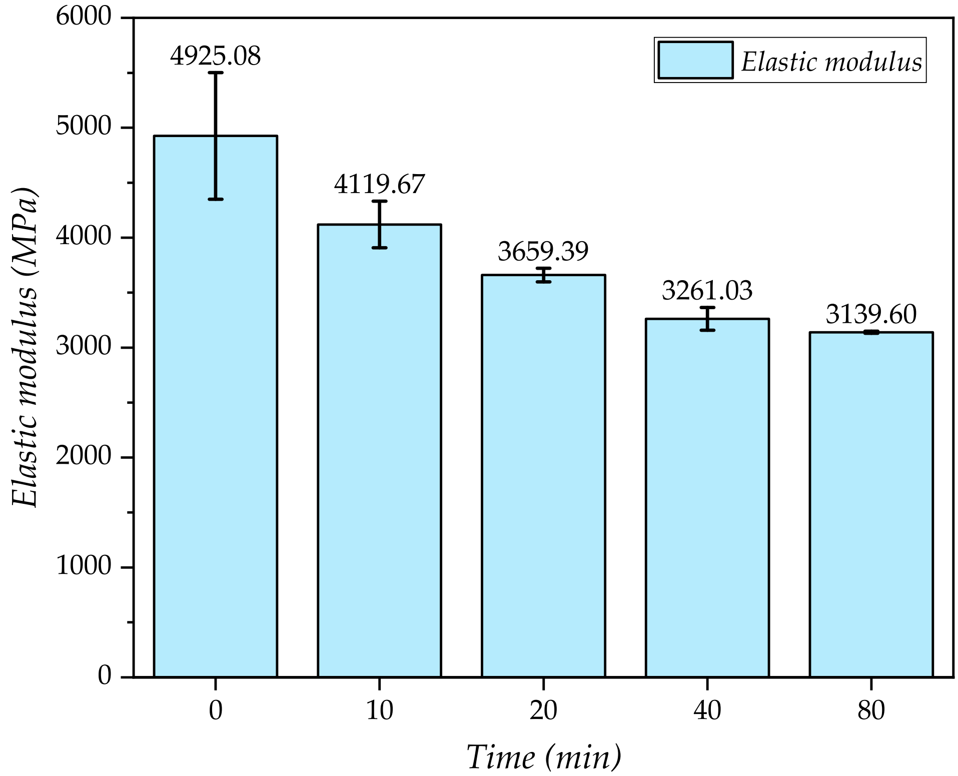

(B)

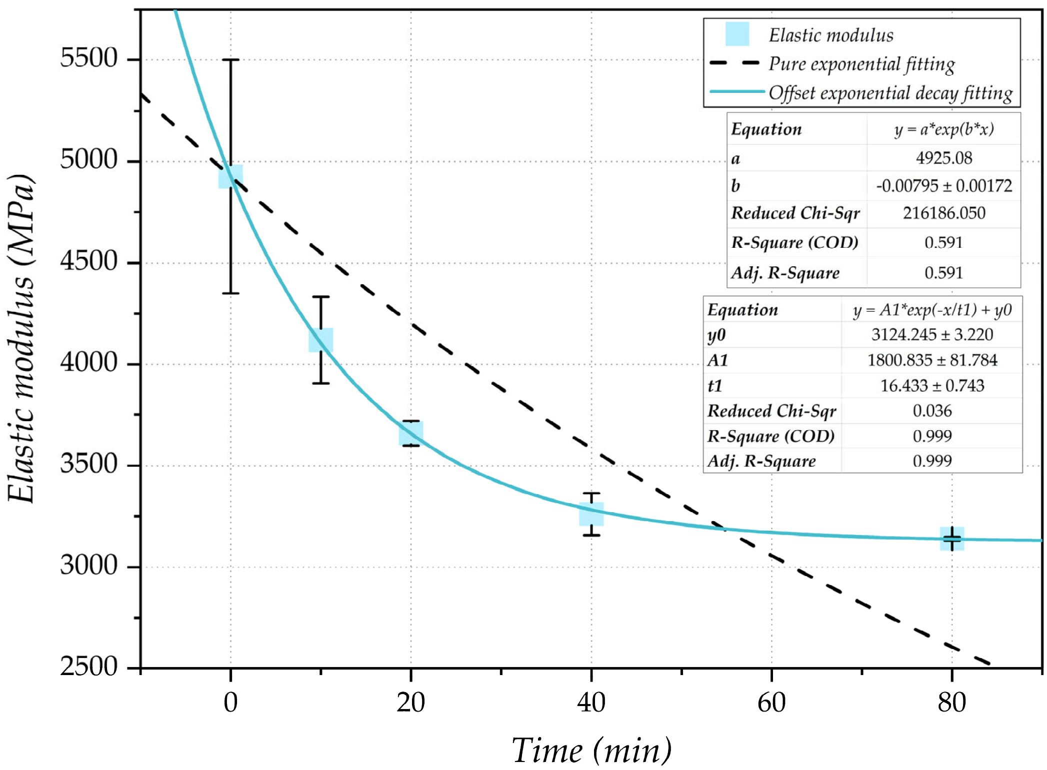

Figure 6.5: (A) Evolution of the elastic modulus from the tensile test of 3D printed PVA immersed in water and its (B) exponential fit analysis.

(A)

(B)

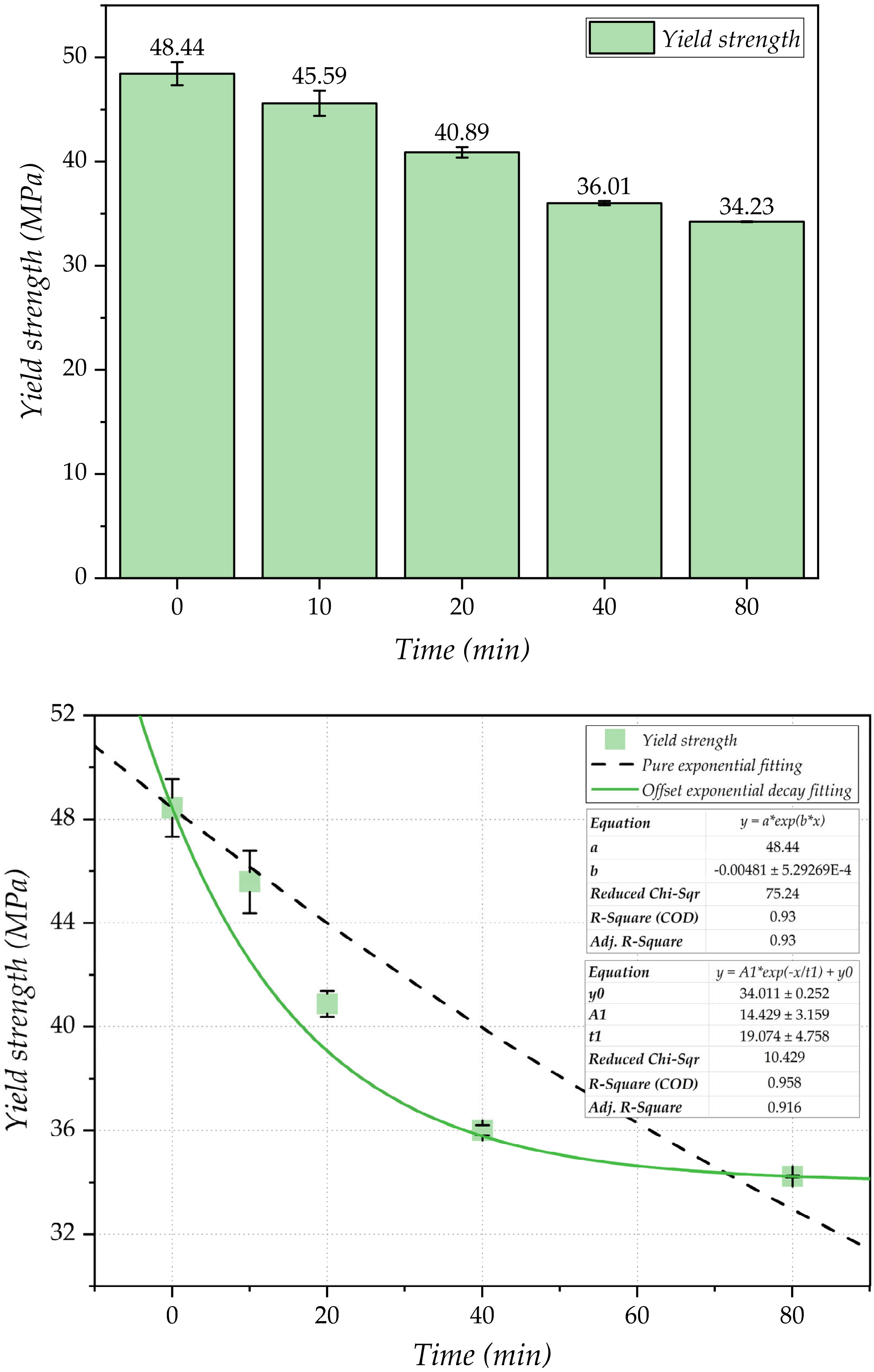

Figure 6.6: (A) Evolution of the yield strength from the tensile test of 3D printed PVA immersed in water and its (B) exponential fit analysis.

(A)

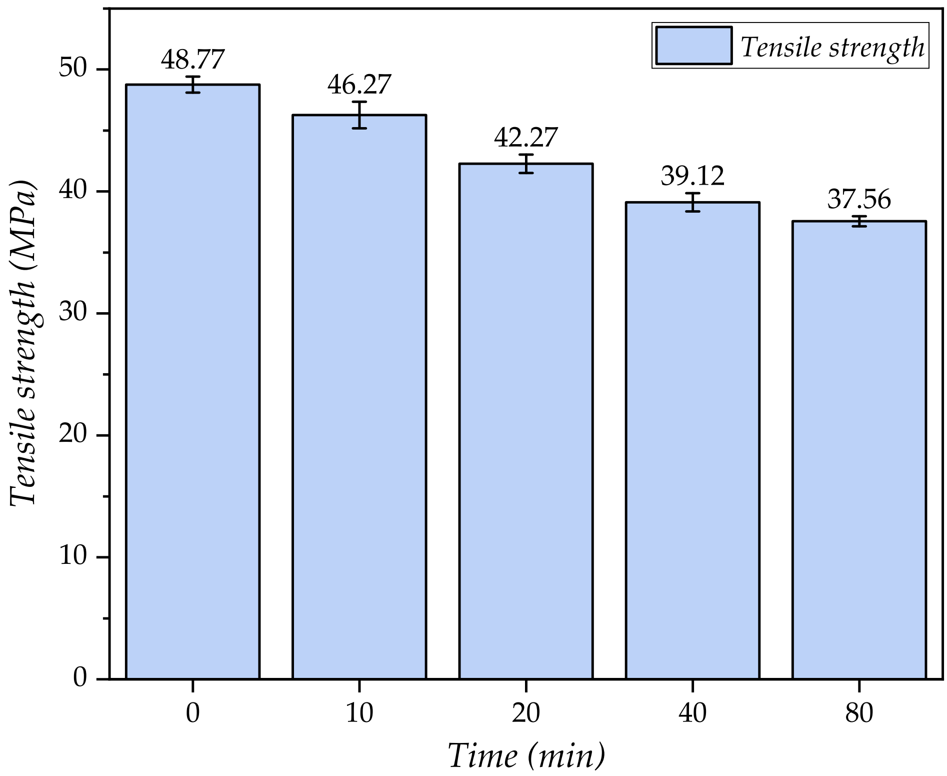

(B)

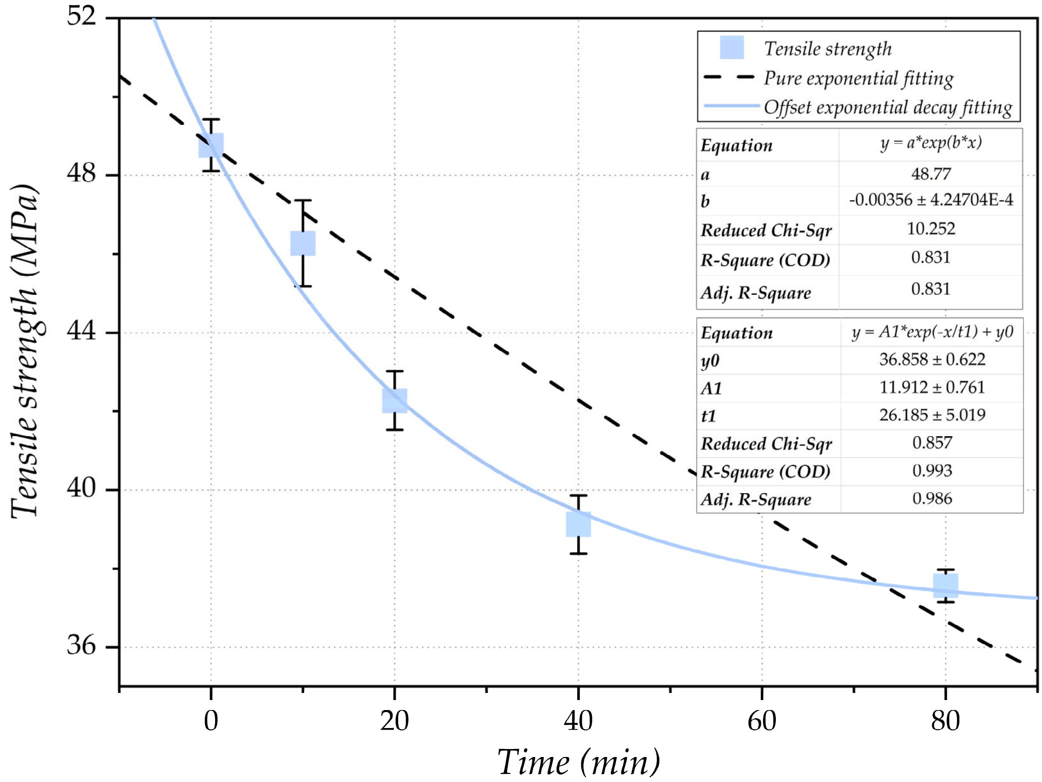

Figure 6.7: (A) Evolution of the tensile strength from the tensile test of 3D printed PVA immersed in water and its (B) exponential fit analysis.

(A)

(B)

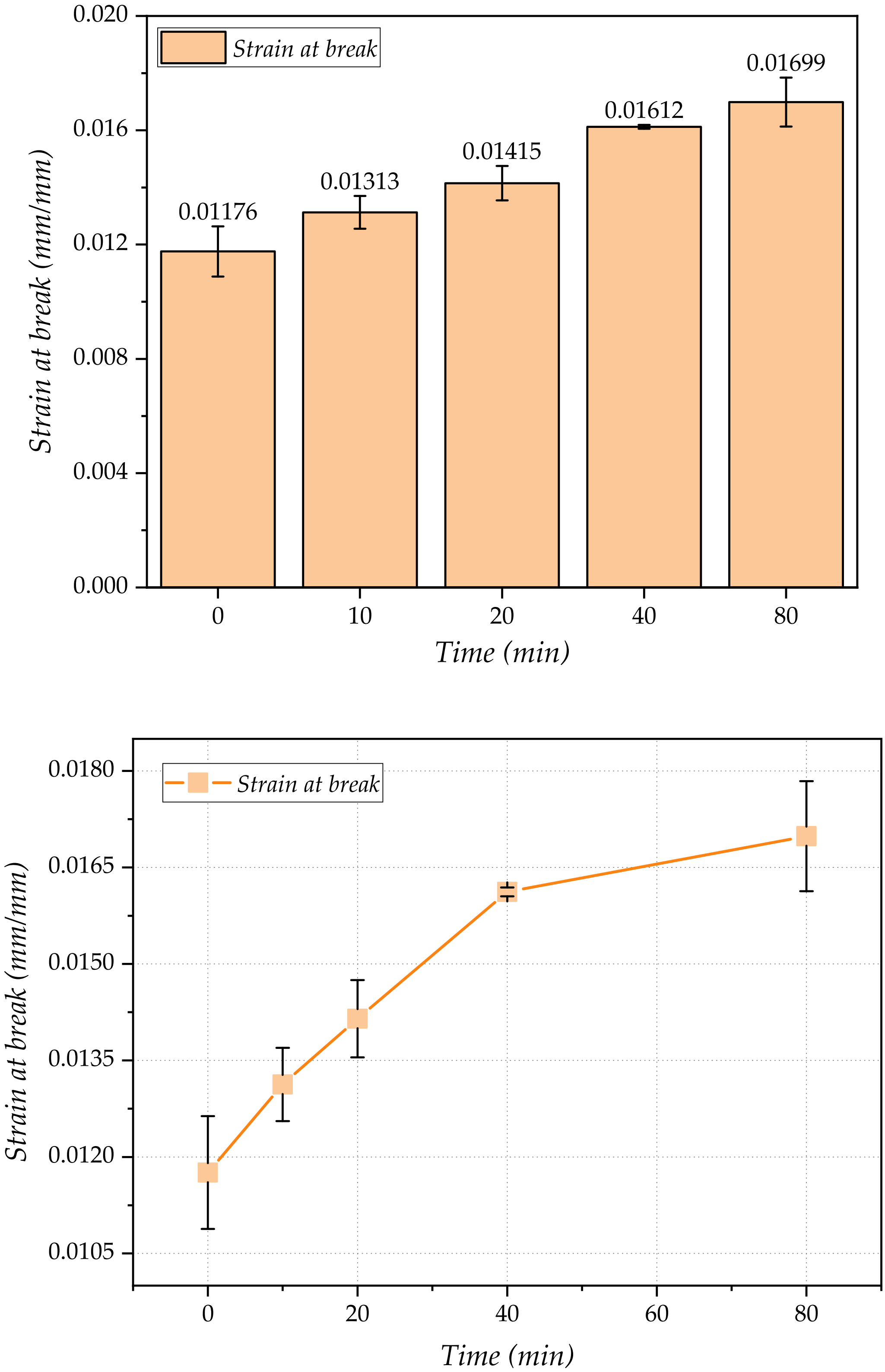

Figure 6.8: Evolution of the strain at break from the tensile test of 3D printed PVA immersed in water represented in (A) bar chart and (B) scatter plot.

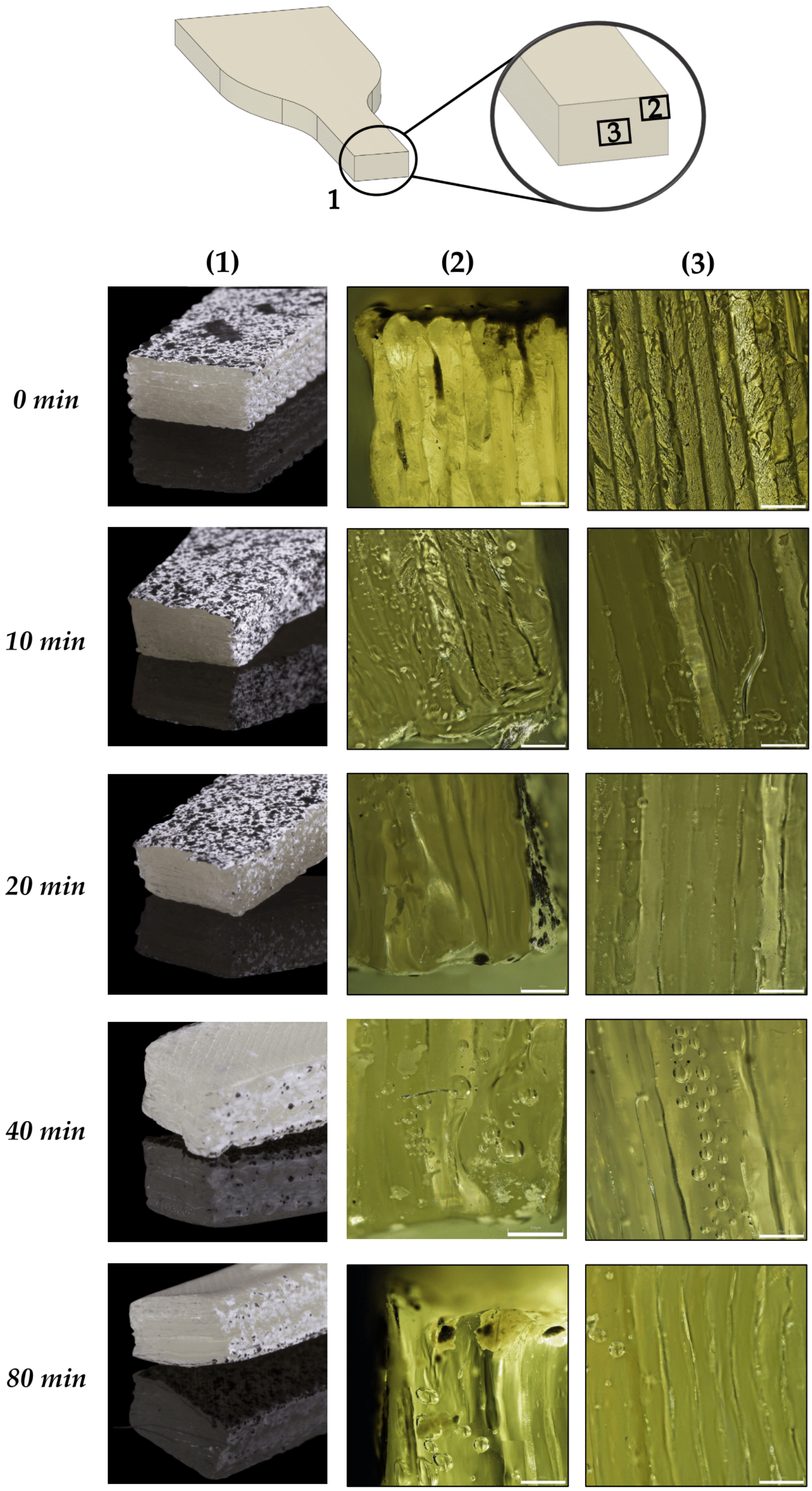

Figure 6.9: Macroscopic and microscopic images of the fracture sections of quasi-isotropic PVA test specimens after different immersion times, taken post-drying. The white scale bar in the microscopic images represents 400 microns. Pictures courtesy of Dr. Francisco Franco Martínez and Álvaro Troyano.

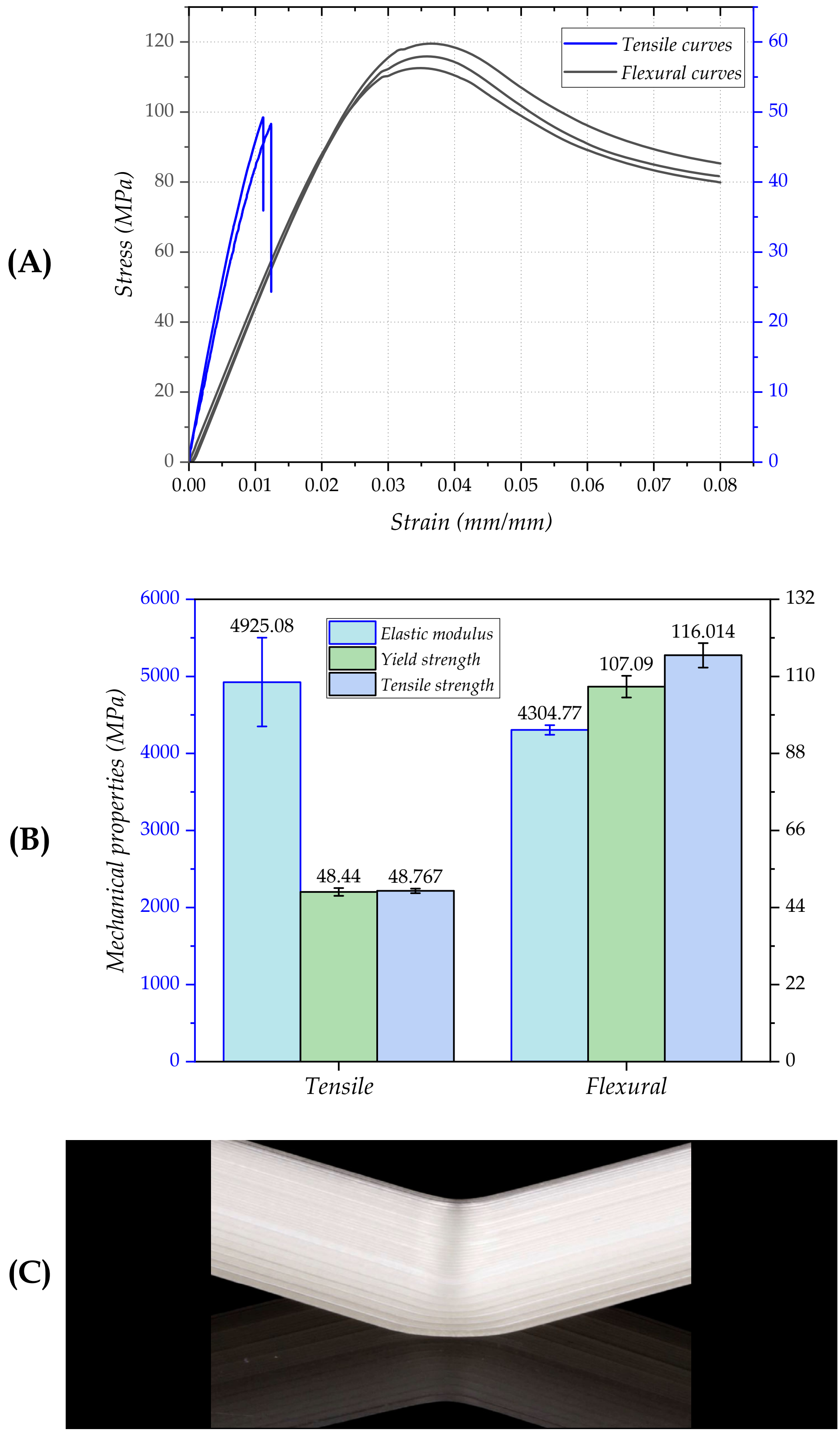

Figure 6.10: (A) Tensile and flexural curves of 3D-printed dry PVA. (B) Comparison of mechanical properties with the auxiliary axis representing strength. (C) Photograph of a sample tested in the region of the loading pin.

Based on the analysis of the tensile test specimens, the effect of water on PVA printed with a quasi-isotropic pattern was observed. However, in order to extrapolate the hydrolytic damage to other types of infill, it is necessary to verify whether or not the pattern influences the material degradation, taking into account that completely solid pieces are printed. For this reason, circular samples with concentric and rectilinear infill patterns were tested.

A qualitative comparison of the degradation of these different specimens (see Figure 6.11A) shows that the erosion between specimens and infill patterns shows poorly defined differences. Figure 6.11B, which shows how the number of pixels of degraded PVA decreases over time, confirms this general homogeneity. However, the samples with a concentric infill pattern show a greater dispersion, reflected in a higher standard deviation. This is because when printing with FFF technology, air is trapped between layers or perimeters, causing the variability observed in the graph. This hypothesis is confirmed when comparing the degraded samples with the concentric and rectilinear infill patterns, where the appearance of more surrounding bubbles can be seen in the concentric pattern, caused by the release of air confined during the manufacturing process (Figure 6.11C).

A one-way analysis of variance was performed to determine if there was a significant difference between the degradation of the concentric and rectilinear samples over time. The result of the study indicated that there was no statistically significant difference between the two groups (*p-value*=0.917). Consequently, the null hypothesis that the degradation patterns of the concentric and rectilinear samples are statistically equivalent cannot be rejected. This indicates that under the conditions evaluated, the infill pattern does not affect the erosion of the material.

Having established that the pattern did not affect erosion, tests were carried out on specimens of different geometries, each with a different exposed surface area-to-volume ratio. For these new tests, only the rectilinear pattern was used as these samples had fewer surrounding bubbles, making them easier to segment. Qualitatively, it was observed that the degradation was quite reproducible between samples and that the erosion was uniform (see Figure 6.12A). Quantitatively, this behavior was confirmed by showing that erosion in all cases follows an exponential decaying trend, analogous to that described for the change in mechanical properties of PVA under water (Figure 6.12B).

To analyze this trend in more detail, a normalized graph (see Figure 6.13A) was plotted showing the evolution of the number of PVA pixels in each sample as a function of time. Exponential behavior is observed, although each specimen has its own rate of degradation or erosion. To investigate this further, a Python script was developed to determine the radial dimensions of each sample every two degrees and how they change over time (see Figure 6.14), based on a previous work [369]. From this data the degradation ratios of the different geometries were obtained, and a positive relationship was found between the erosion rate of PVA and the exposed area-to-volume ratio (Figure 6.13B).

In summary, the results confirm that the type of infill pattern does not significantly affect the PVA degradation, but the exposed area-to-volume ratio does, which explains the different erosion rates observed according to the geometry of each rectilinear specimen.

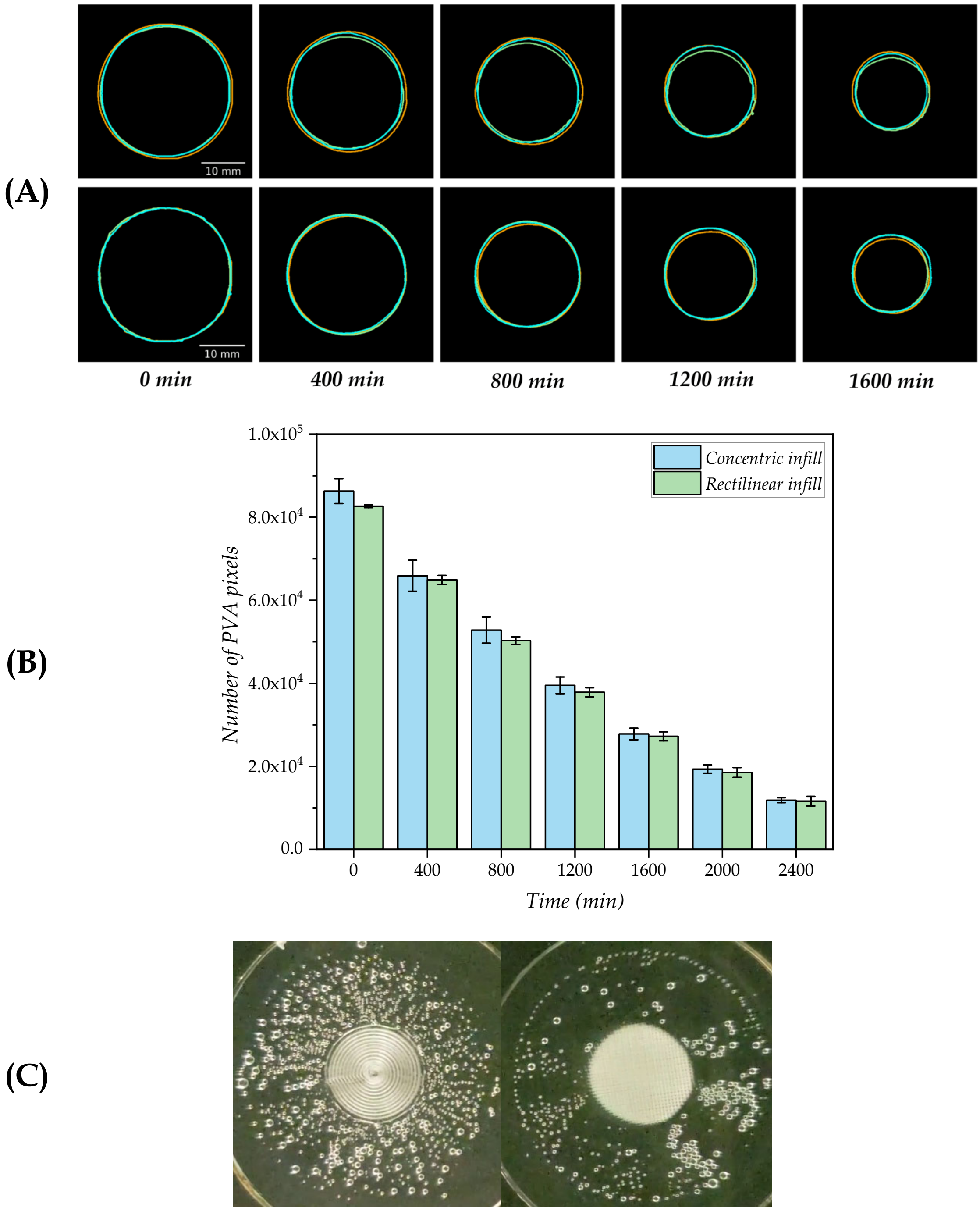

Figure 6.11: Evaluation of 2D erosion in circular specimens. (A) Geometric transformations in specimens with concentric (top) and rectilinear (bottom) infill patterns. (B) Evolution of the PVA pixel count extracted from frames captured every minute during the test, with changes highlighted every 400 minutes for greater significance. (C) Bubble formation observed during the degradation test in specimens with concentric (right) and rectilinear (left) infill patterns.

(A)

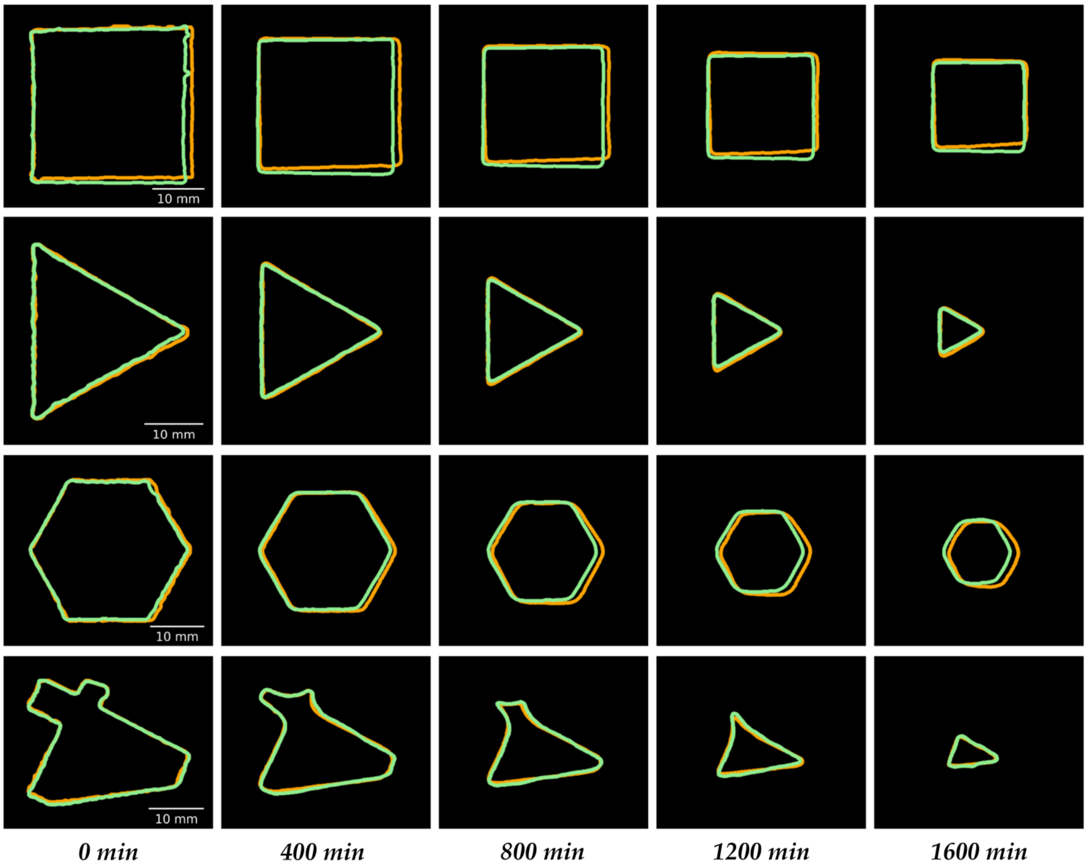

(B)

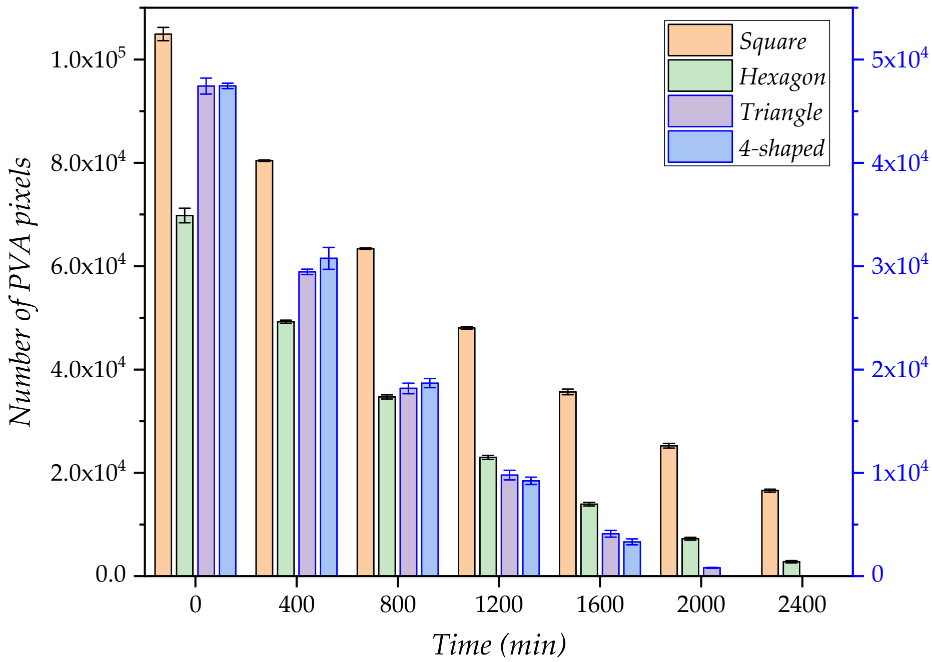

Figure 6.12:. (A) Geometric transformations in specimens with rectilinear infill patterns, featuring various shapes (triangles, squares, hexagons, and a 4-shaped). (B) Evolution of the PVA pixel count obtained from frames captured during the test. The auxiliary axis corresponds to the 4-shaped test specimens.

(A)

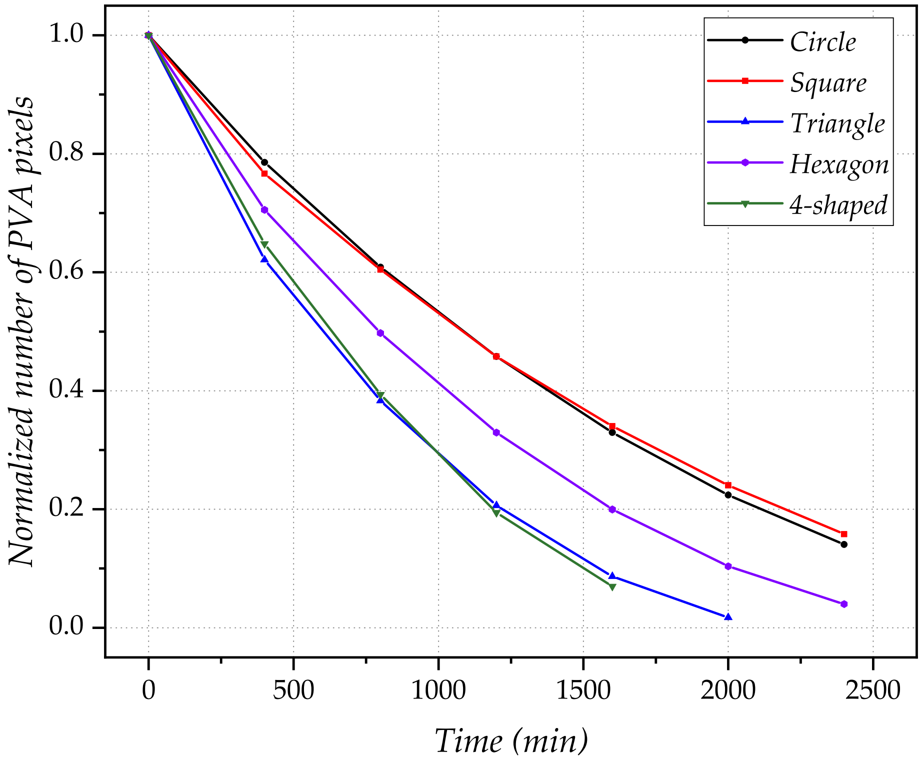

(B)

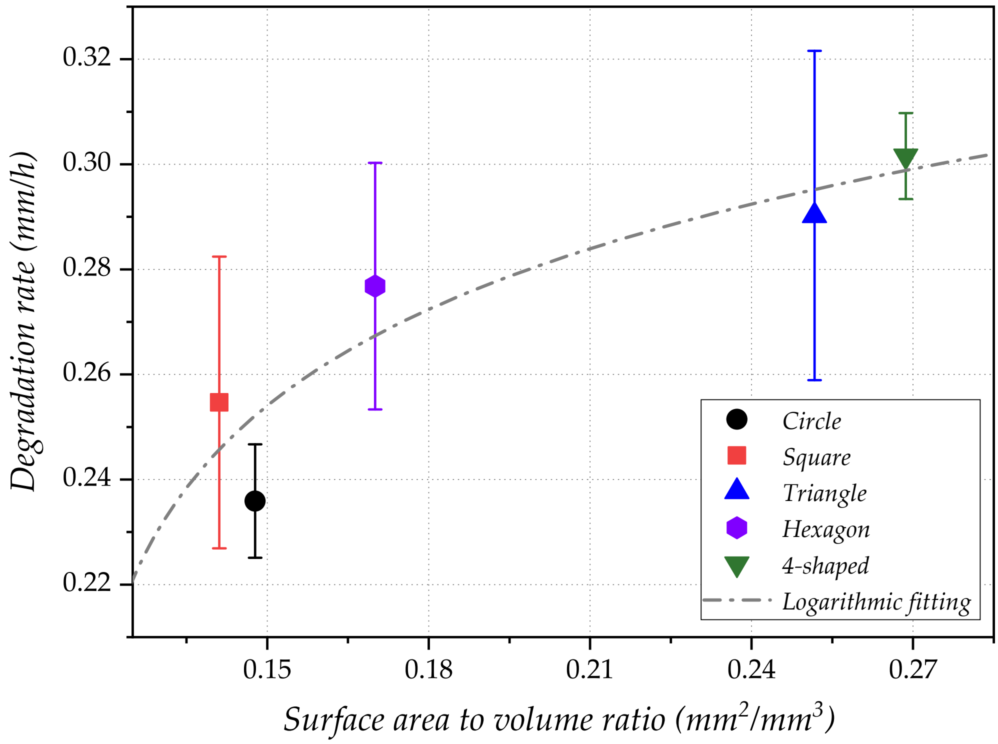

Figure 6.13: (A) Graph of normalized pixel count for each rectilinear test specimen. (B) Scatter plot illustrating the relationship between the degradation rate and the exposed surface area-to-volume ratio of the specimens.

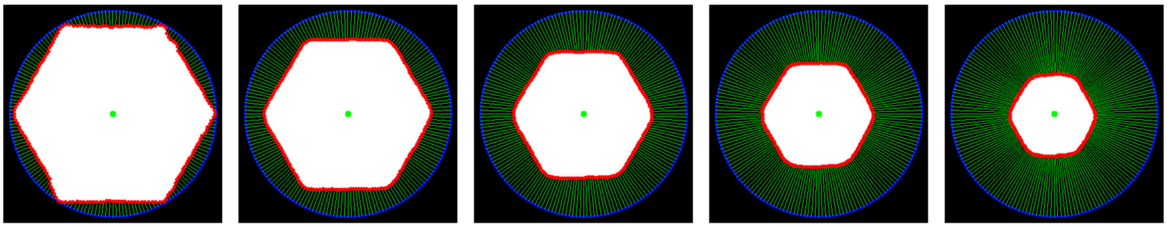

(A)

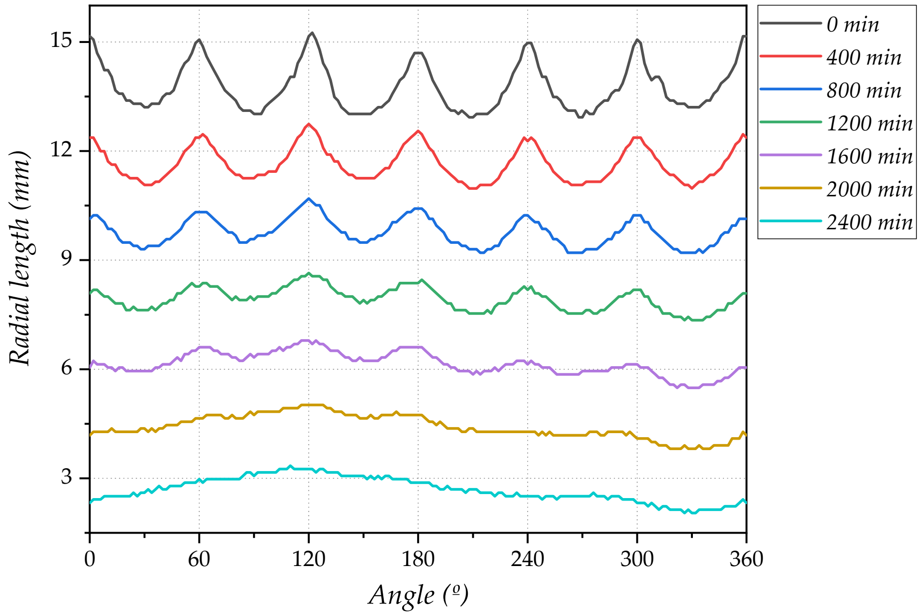

(B)

Figure 6.14: Analysis of the radial dimensions of PVA specimens over time. (A) The hexagonal-shaped sample is used as an example to demonstrate how dimensions are extracted every 2° and (B) how the data is plotted to evaluate surface erosion.

In the case of the biocompatibility test, the timeline of the experimental setup is illustrated in Figure 6.15A. Both PVA S1 and S2 structures (Figure 6.15B) were fully dissolved in the medium 24 h post exposure to the cells. After 24 and 48 h post exposure, no significant differences were observed in the metabolic activity of cells cultured alone or in the presence of either size of PVA samples (Figure 6.15C). After 48 h, positive control was significantly higher than after 24 h. After 144 h, a significant increase in the metabolic activity was found for all groups compared to previous time points. In addition, the positive control at 144 h had the highest metabolic activity of all groups. Cell density (Figure 6.15D) was quantified from bright field images (Figure 6.15E) and demonstrated that cell growth was observed in all groups overtime with the positive control having the highest cell number. Live dead assay (Figure 6.15F) indicated a high viability at day 6 in all groups. Quantification (Figure 6.15G) of live dead confocal images showed over 98% viability for all groups.

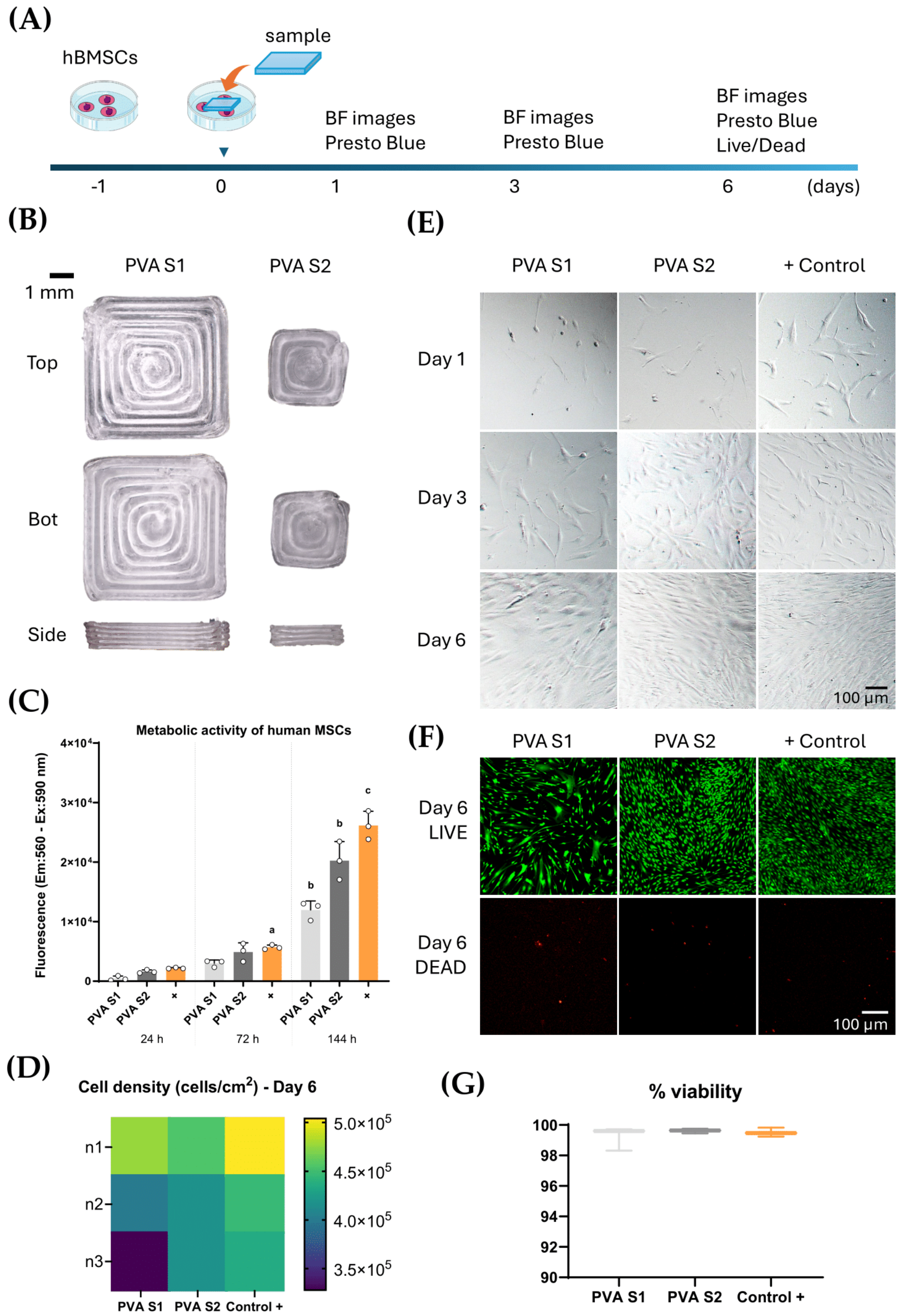

Figure 6.15: Metabolic activity of hMSCs in the presence of PVA. (A) Timeline of the experimental setup. (B) Representative macroscopic images of the two different 3D printed structures made of PVA showing the concentric pattern of the printing design (top view) and the number of layers per sample (side view). (C) Fluorescence readings of the metabolic activity after 30 min PrestoBlue assay incubation of the positive control (+), the 6 x 6 x 1 mm³ sample (PVA S1) and the 3 x 3 x 1 mm³ sample (PVA S2) for 24, 72 and 144 h post exposure to the PVA samples (a: p<0.002 Control + 24 vs 48 h; b: p<0.0001 PVA S1 or S2 at 144h vs 24 or 48 h; c: p<0.0001 Control + 144h vs all samples). Negative control (medium alone) values were subtracted from positive control and experimental groups. (D) Heatmap of the cell density across all samples from quantification of bright field images (E) with *n* of 3 for each sample and timepoint. (F) Confocal images from Live/Dead assay showing live in green and dead in red on day 6. (G) Quantification of the viability % based on the confocal images n of 3 per sample and n of 3 per replica. Special thanks to Dr. Pedro Díaz for his invaluable support in the biological characterization of the materials.

6.3.2. PETG samples

In the case of PETG, its mechanical properties were evaluated under tension and flexure without immersion. In both cases, the material exhibited ductile behavior (Figure 6.17) and the elastic modulus was observed to be very similar (Figure 6.16A, Table 6.3). However, the yield and ultimate strength were significantly higher in flexure than in tension (Figure 6.16B). Furthermore, when comparing its stress-strain curves with those of PVA, it can be seen that PETG can store a greater amount of elastic energy before undergoing permanent deformation.

Table 6.3: Comparison of the tensile and flexural properties of PETG.

	Tensile specimens	**Bending specimens**
Elastic modulus (MPa)	1790.884 ± 21.406	1463.598 ± 50.968
Yield strength (MPa)	33.2 ± 1.125	55.132 ± 1.171
Ultimate strength[27] (MPa)	42.098 ± 1.224	61.511 ± 1.454

Given that the 4D degradation-activated mechanisms will be composed of PVA and PETG, it is essential to understand the effect of water on structures or actuators made of PETG. Considering that PETG will remain in situations of constant deformation throughout the lifespan of these actuators and considering the viscoelastic nature of polymers, it is essential to study how water affects its stress relaxation.

As can be seen in Figure 6.18, the plot of the normalized elastic modulus against time, obtained from tensile tests on quasi-isotropic specimens under constant deformation in the elastic zone, shows that the polymer immersed in water undergoes a faster relaxation than that in dry conditions. The general equation of the Prony series is used to predict long-term stress relaxation [370]:

$$\frac{E(t)}{E_0} = y0 + \sum_{i=1}^{n} Ai \cdot e^{-(t/ti)} \tag{73}$$

Values of n equal to 1, 2 and 3 were tested. For the non-immersion test the best results were obtained with $n = 2$, while for the underwater test the outcomes were more accurate with $n = 3$. In both cases the adjusted R^2 was greater than 0.99. The original and adjusted curves are shown in Figure 6.18. Equations (74) and (75) describe the changes in Young's modulus ($E_0 = 1790.884\ MPa$) over time (in seconds), reflecting the stress relaxation of PETG in the absence and presence of an aqueous medium, respectively:

$$E_{non-immersion} = 1437.580 + 100.289 \cdot e^{-t/428.087} + 252.303 \cdot e^{-t/8538.246}\ [MPa] \tag{74}$$

[27] In the case of the tensile test, tensile strength.

$$E_{underwater} = 1334.509 + 34.206 \cdot e^{-t/_{34.246}} + 65.210 \cdot e^{-t/_{285.504}} + 356.638 \cdot e^{-t/_{3548.673}} \; [MPa] \quad (75)$$

On the biocompatibility of PETG, the timeline of the experimental setup is illustrated in Figure 6.19A. Both PETG S1 and S2 structures (Figure 6.19B) were placed bottom down on top of the cells. After 24 and 48 h post exposure, no significant differences were observed in the metabolic activity of cells cultured alone or in the presence of either size of PETG samples (Figure 6.19C). After 48 h, positive control was significantly higher than after 24 h. After 144 h, a significant increase in the metabolic activity was observed for all groups compared to previous time points. In addition, the positive control at 144 h had the highest metabolic activity of all groups. Cell density (Figure 6.19D) was quantified from bright field images (Figure 6.19E) and demonstrated that cell growth was observed in all groups overtime with the positive control having the highest cell number. Live dead assay (Figure 6.19F) demonstrated a high viability at day 6 in all groups without an obvious effect on the cells in direct contact with the material. Quantification (Figure 6.19G) of live dead confocal images showed over 89% viability for all groups.

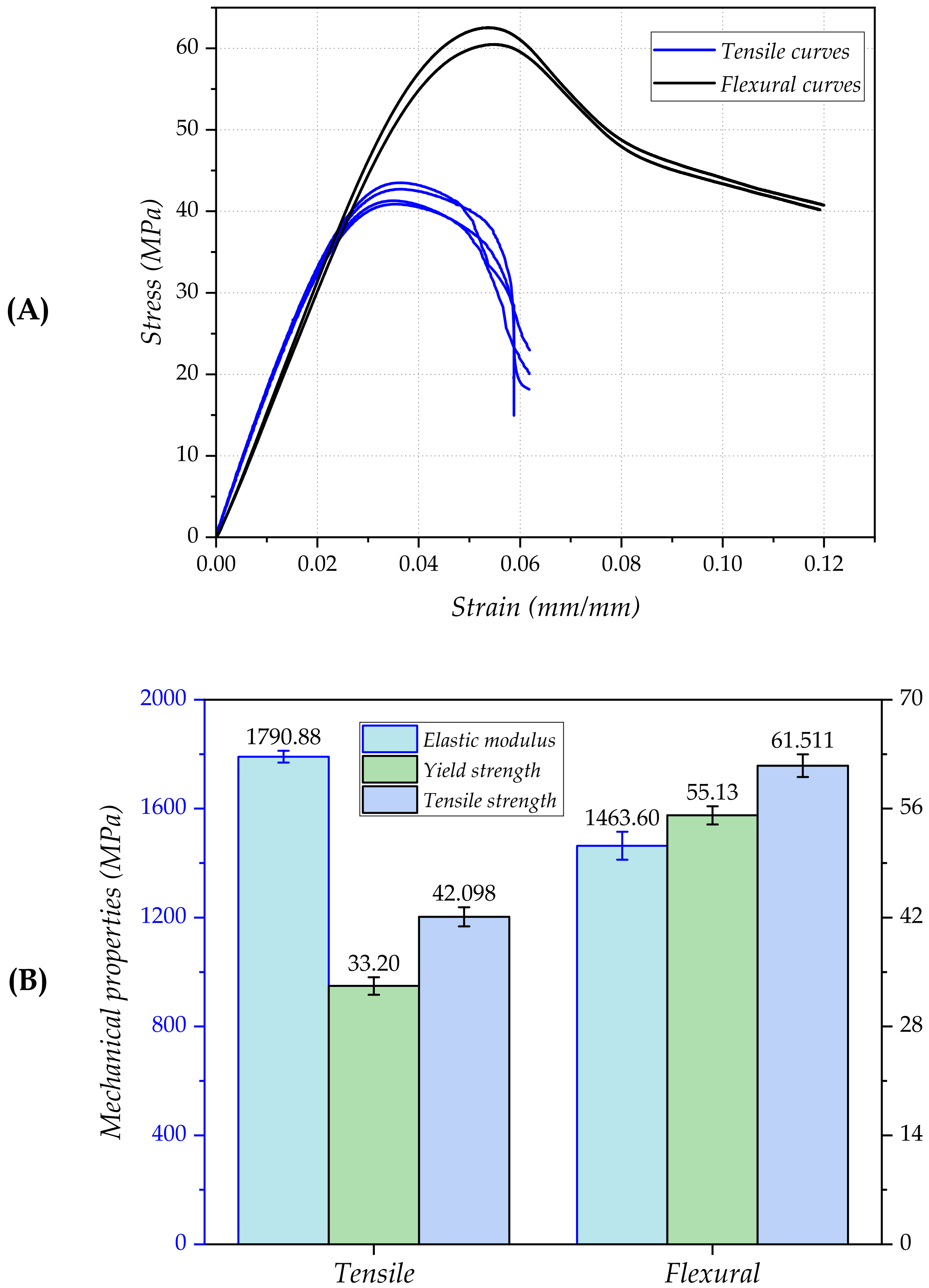

Figure 6.16: (A) Tensile and flexural curves of 3D-printed PETG. (B) Comparison of mechanical properties with the auxiliary axis representing strength.

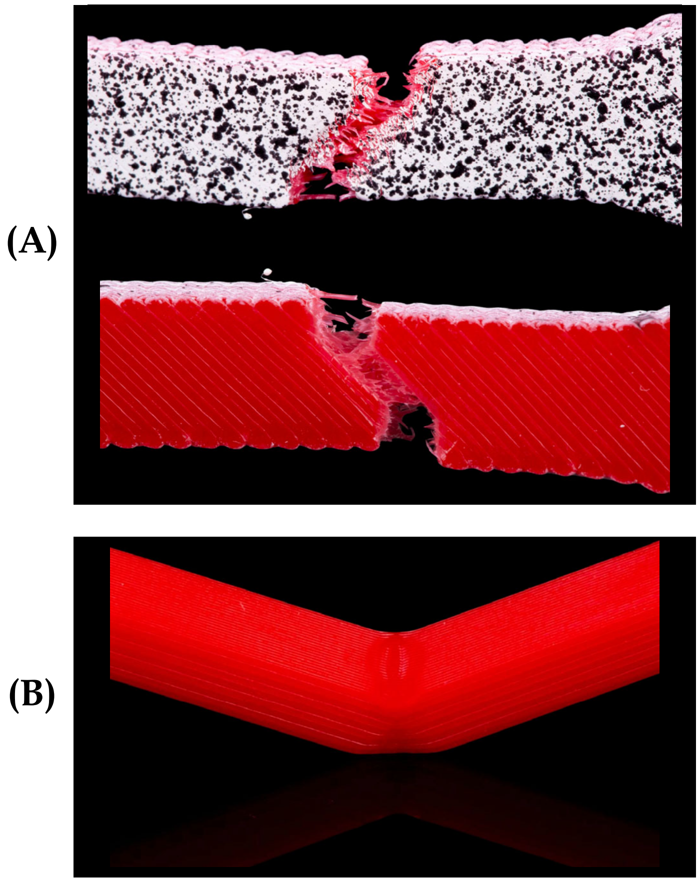

Figure 6.17: (A) Photograph of the failure in the quasi-isotropic PETG tensile specimen and (B) plastic deformation in the loading pin region of the rectilinear PETG sample from the flexural test. Images courtesy of Alvaro Troyano.

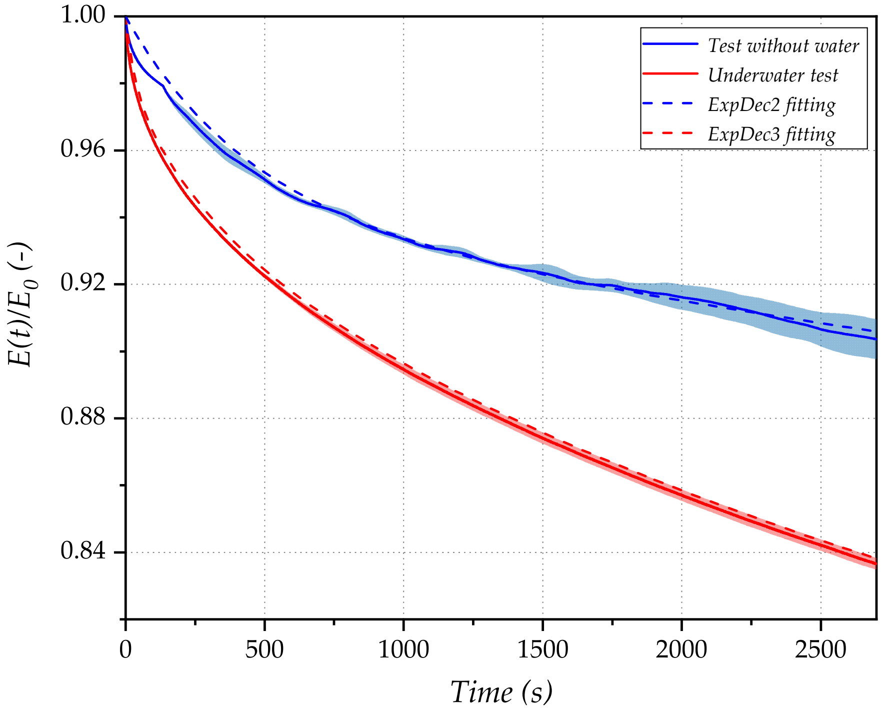

Model	ExpDec3
Equation	y = A1*exp(-x/t1) + A2*exp(-x/t2) + A3*exp(-x/t3) + y0
y0	0.745 ± 0.002
A1	0.0194 ± 2.8982E-04
t1	34.246 ± 0.961
A2	0.0364 ± 3.3136E-04
t2	285.804 ± 5.408
A3	0.1989 ± 0.0016
t3	3548.673 ± 65.082
Reduced Chi-Sqr	3.21083E-6
R-Square (COD)	0.998
Adj. R-Square	0.998

Model	ExpDec2
Equation	y = A1*exp(-x/t1) + A2*exp(-x/t2) + y0
y0	0.803 ± 0.062
A1	0.0560 ± 0.0025
t1	428.087 ± 16.767
A2	0.1409 ± 0.0596
t2	8538.246 ± 4883.469
Reduced Chi-Sqr	4.05967E-6
R-Square (COD)	0.991
Adj. R-Square	0.991

Figure 6.18: Time-dependent variation of elastic modulus during a 40-minute tensile test of quasi-isotropic PETG specimens in dry and underwater conditions.

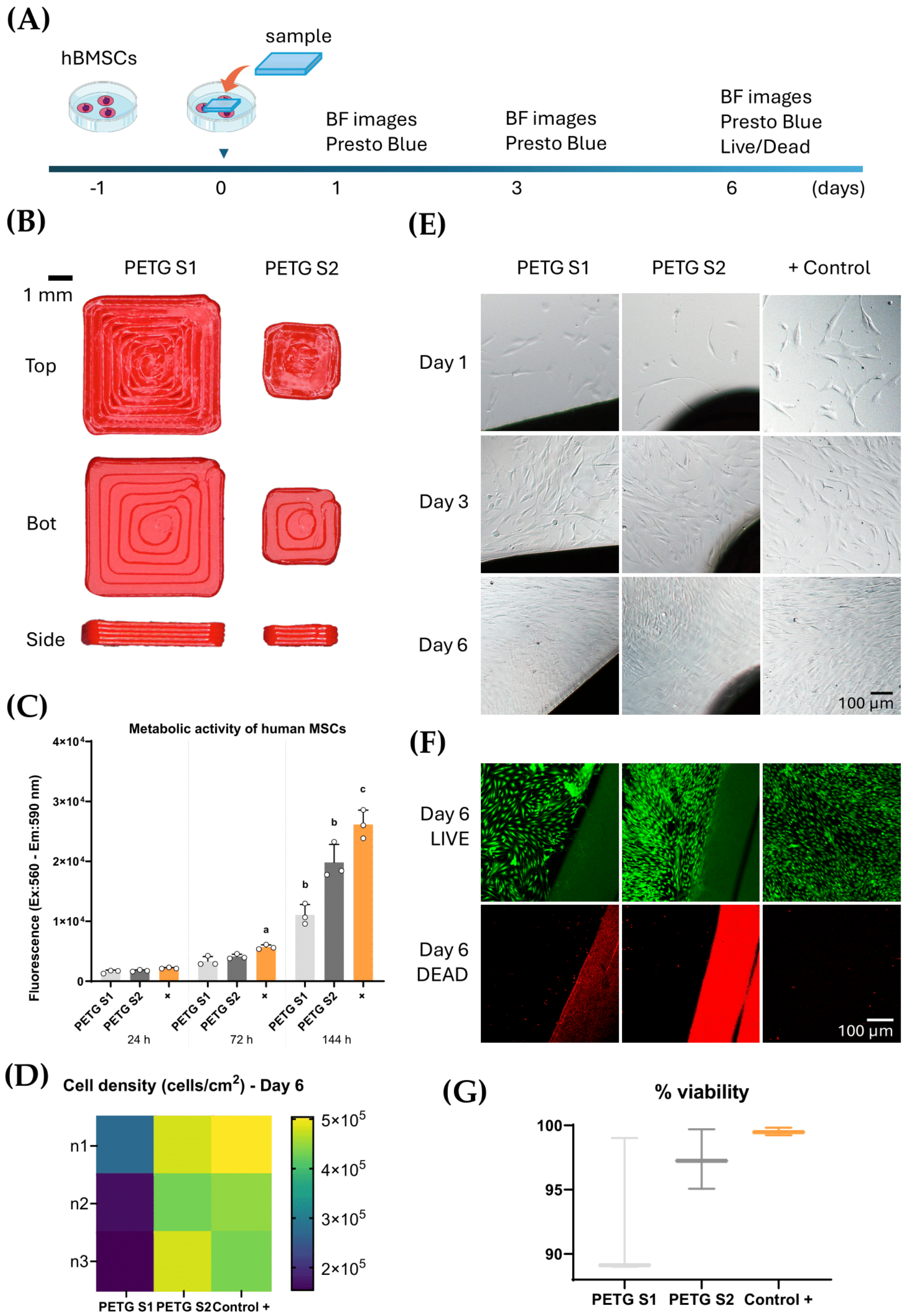

Figure 6.19: Metabolic activity of hMSCs in the presence of PETG. (A) Timeline of the experimental setup. (B) Representative macroscopic images of the two different 3D printed structures made of PETG showing the concentric pattern of the printing design (top view) and the number of layers per sample (side view). (C) Fluorescence readings of the metabolic activity after 30 min PrestoBlue assay incubation of the positive control (+), the 6 x 6 x 1 mm^3 sample (PETG S1) and the 3 x 3 x 1 mm^3 sample (PETG S2) for 24, 72 and 144 h post exposure to the PETG samples (a: $p<0.002$ Control + 24 vs 48 h; b: $p<0.0001$ PETG S1 or S2 at 144h vs 24 or 48 h; c: $p<0.0001$ Control + 144h vs all samples). Negative control (medium alone) values were subtracted from positive control and experimental groups. (D) Heatmap of the cell density across all samples from quantification of bright field images (E) with *n* of 3 for each sample and timepoint. (F) Confocal images from Live/Dead assay showing live in green and dead in red on day 6. (G) Quantification of the viability % based on the confocal images n of 3 per sample and n of 3 per replica. Special thanks to Dr. Pedro Díaz for his invaluable support in the biological characterization of the materials.

6.4. Proof of concept shape-morphing mechanism

Based on the results of the characterization of both materials, a shape-shifting mechanism was designed to be triggered by the PVA degradation underwater. Figure 6.20A shows this device, inspired by car shock absorber and designed in Autodesk Fusion 360 (Autodesk Inc., San Rafael, CA, USA). The design combines two types of springs: helical and serpentine.

The actuator consists of a PETG helical spring, which stores elastic potential energy, and a PVA serpentine spring, which limits its vertical movement. This design takes advantage of the PVA's stiffness, which is 2.75 times greater than that of PETG, allowing precise tuning of the spring rate (see Spring mechanics section). The PVA spring was printed with fibers aligned to withstand the axial load applied by the PETG coil, while the PETG component required support during printing. Both springs were assembled using a PETG cap and base, each with a hole to hold the PVA spring (Figure 6.20A). As the PVA structure is shorter than the PETG helix, it remains compressed during assembly, storing energy that is gradually released as the PVA degrades (Figure 6.20B). The entire mechanism is fully submerged in water, a key factor in the degradation-driven actuation process. Fabrication and testing followed the protocols detailed in the Materials and methods section.

Figure 6.20B shows the evolution of the actuator shape over time. It can be seen that the mechanism is progressively stretched due to the PVA hydrolytic damage, which causes an exponential reduction in its mechanical properties. By analyzing different frames that capture the metamorphoses of the mechanism, graphs of the evolution of its length and strain (Figure 6.20C) as a function of time are obtained. These data reveal the existence of two different behaviors: a predominantly linear one in the early stages and another with an exponential or logarithmic trend in the later ones.

This transition in dynamic behavior is directly related to the two types of erosion suffered by PVA. Initially, degradation occurs primarily on the surface, leading to a moderate and progressive reduction in material stiffness, which explains the linear tendency observed in the graphs. During this phase, the core of the material remains intact, allowing the mechanism to retain a certain level of structural stability. However, after 108 minutes, water begins to penetrate the interior of the specimen, triggering a process of bulk erosion that significantly accelerates the degradation rate, as reflected in the exponential nature of strain evolution. This shift in the degradation mechanism is visually confirmed by the increase in transparency of the PVA recorded in the images (Figure 6.20B), indicating a drastic loss of stiffness as the material erodes homogeneously throughout its structure until it ultimately transforms into a viscous and amorphous matter. These observations demonstrate that the two modes of erosion (surface and bulk) coexist during PVA degradation, with surface erosion dominating the initial phase and bulk erosion driving the later exponential softening. Understanding this duality is crucial for the design of 4D mechanisms, where the controlled degradation of the polymer can be leveraged to modulate the mechanical response of the device over time.

For PETG, the shape recovery ratio (S_r) was used to quantify the influence of stress relaxation in aqueous media. This metric assesses the material's ability to return to its original shape after being subjected to shape morphing. It is calculated by comparing the difference between the "trained" (deformed, ε_t) strain and the "irreversible" (residual, ε_i) strain after the structure is released [371]. The ratio is expressed and calculated as:

$$S_r = \frac{\varepsilon_t - \varepsilon_i}{\varepsilon_t} * 100 = \frac{30.35 - 5.53}{30.35} * 100 = 81.78\% \tag{76}$$

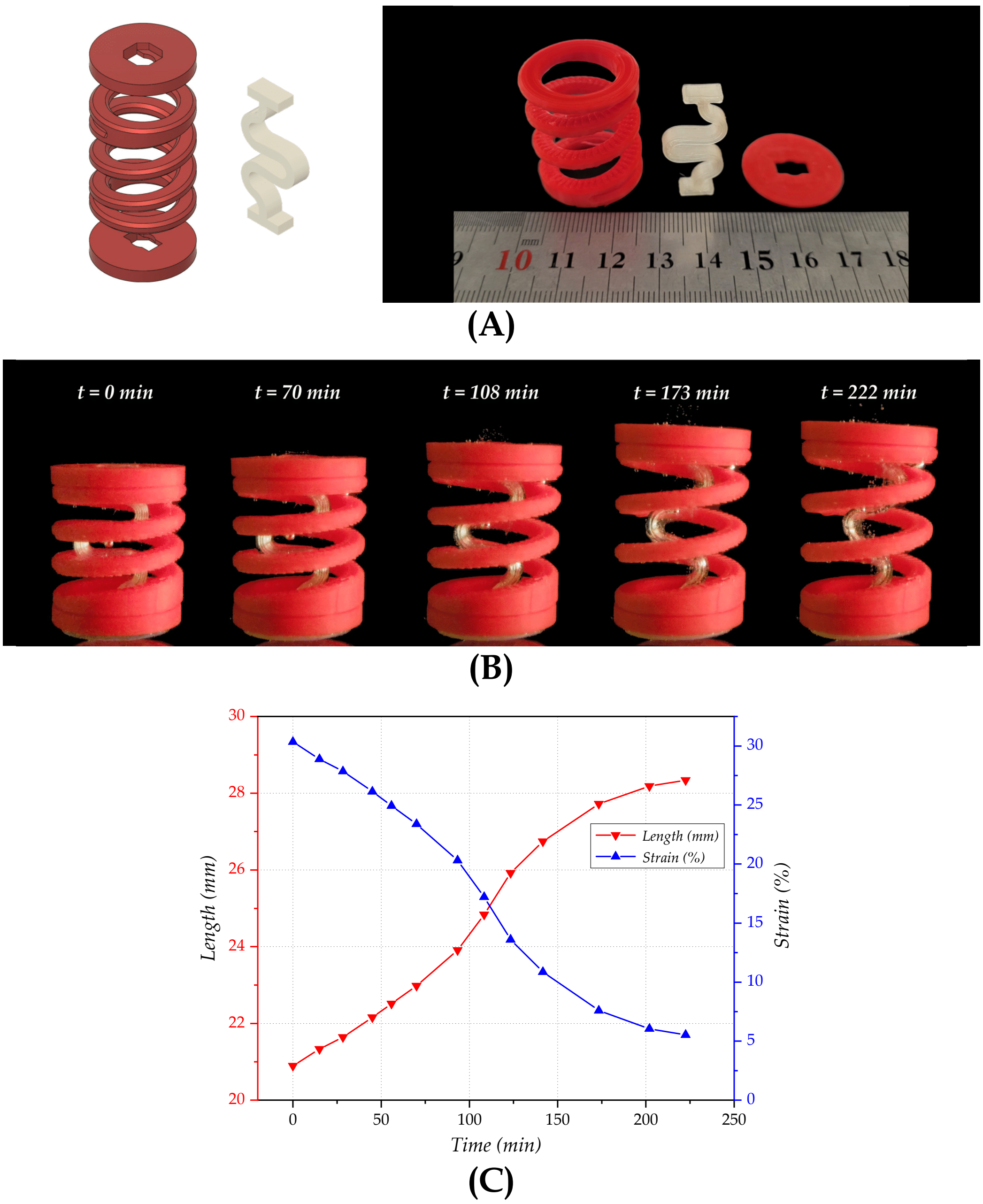

Figure 6.20: (A) CAD models and prototypes of the 4D-printed car shock absorber, (B) Key frames from the shape-morphing test, and graphs showing the evolution of (C) length and strain over time.

6.5. Discussion

The triggering strategy of the actuators proposed in this study is based on the hydrolytic degradation of PVA, a phenomenon that causes a progressive loss of its mechanical properties and enables the release of the elastic energy stored in an "active" component. From a design point of view, this exponential decrease in stiffness and increase in ductility of PVA under immersion is particularly advantageous for 4D printing applications, as it allows the programming of controlled shape changes over time.

The tests carried out demonstrate that the PVA degradation varies according to the geometry of the part. In two-dimensional configurations, erosion is mainly superficial because the water does not significantly penetrate the interior. In three-dimensional geometries, degradation occurs through a combination of surface and bulk erosion. Initially, this results in a linear decline in mechanical resistance due to surface damage. However, as degradation advances, the decline becomes exponential, reaching a critical threshold where catastrophic failure occurs. At this point, the material loses its structural integrity and transitions into a hydrogel-like state due to predominant bulk erosion (Figure 3.14) [176,367]. This behavior was observed in the shape-shifting actuator where PVA progressively transformed into a viscous and amorphous matter. This phenomenon is attributed to the greater surface area in contact with the water in three-dimensional pieces, which facilitates infiltration throughout the volume. It has also been described that PVA undergoes a reduction in crystallinity at the start of dissolution, followed by a period of stabilization and finally almost full dissolution [372].

During water immersion, bubble formation was observed in all samples, caused by the release of air trapped during printing as the PVA dissolves (Figure 6.9, Figure 6.11C and Figure 6.20B). In future work it would be interesting to clarify whether the internal stress exerted by PETG on the PVA can accelerate hydrolytic degradation. Both erosion and hydrolytic damage follow an exponentially decreasing trend that is directly correlated with the ratio of exposed surface area-to-volume (Figure 6.13). This finding offers the possibility of designing areas with different degradation rates using the same polymer. It has also been shown that the infill pattern does not have a significant effect on the degradation of solid parts, allowing the dynamics of the mechanical properties to be extrapolated simply by rescaling the coefficients of the exponential curve, while preserving the exponents.

In terms of mechanical response, the PVA tensile specimens with a quasi-isotropic pattern exhibited a brittle fracture. This failure started in the layers oriented at 90° with respect to the load, progressed through the fracture of the oblique layers and culminated in the collapse of the layers at 0°. In contrast, the flexural specimens with rectilinear pattern showed greater ductility, suggesting that the orientation of the layers with respect to the load direction favors a better distribution of stresses in the material. This behavior is confirmed by the test of a serpentine spring (Figure 6.21), similar to the one used in the 4D car shock absorber, printed with perimeters aligned with the load, the results of which showed the plastic deformation capacity of PVA, in line with what has been reported by other authors [373].

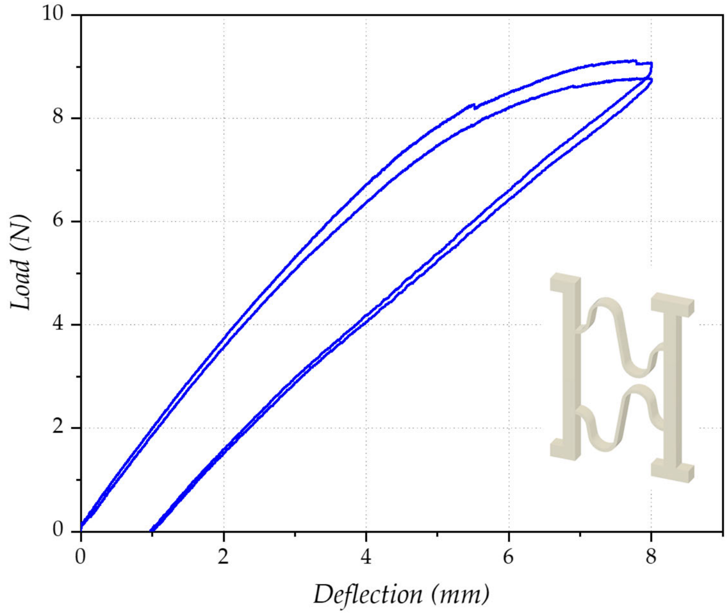

Figure 6.21: Load-deflection curve of a 3D printed PVA serpentine spring. This demonstrates that PVA, when 3D printed with its fibers aligned with the load direction, exhibits plastic deformation capability.

Although the design of infill patterns that adapt to stress distribution is advantageous in the production of actuators, standard tensile specimens printed with these patterns failed in undesirable areas, such as cross section changes, rather than in the extensometer region. As printed PVA behaves similarly to a unidirectional composite, its tensile properties can be estimated from flexure tests as described in [374].

To avoid unwanted failures in the tensile specimens, laser cutting of rectangular specimens is proposed as an alternative, which would allow a more accurate assessment of the PVA behavior printed with a rectilinear pattern.

On the other hand, understanding the mechanical evolution of PVA in aqueous environments is key to the development and adaptation of finite element models that integrate the progressive degradation of its mechanical properties due to hydrolytic damage [368,375]. These models would optimize the design and performance of 4D actuators driven by controlled degradation.

Regarding PETG, the stress relaxation results align with those reported in the literature [376]; however, this study is the first to quantify the effect of water immersion on the stress relaxation behavior of this material. Water acts as a plasticizer, increasing the mobility of the amorphous chains and reducing stiffness, which accelerates stress relaxation [377,378]. This phenomenon explains why the shape recovery ratio of the damper does not reach 100%. However, PETG was chosen for its relatively superior stability compared to polymers such as PLA, which suffers greater energy dissipation [379–381], making it difficult to recover shape after PVA degradation.

Furthermore, the difference in modulus between PETG and PVA means that less PVA is required in the design of elastic energy storage actuators, as the stiffness of the spring is directly related to the material's modulus of elasticity (see Spring mechanics).

The biocompatibility of 3D-printed PETG structures has been previously documented [382–384]. In this study, high viability of hMSCs was observed after six days of direct contact with PETG structures, aligning with an increase in cell number and metabolic activity over time. Additionally, to the best of current knowledge, this study represents the first evaluation of the biocompatibility of 3D-printed PVA. The 3D-printed PVA structures exhibit promising cytocompatibility, as indicated by the increased metabolic activity of hMSCs cultured in the presence of PVA over time. The observed increase in metabolic activity is consistent with previous findings, where dissolved PVA has been associated with enhanced growth and migration of human cells [385].

To assess the long-term effects of acute PVA exposure, the same samples were analyzed at different time points. Since PVA largely dissolves within 24 hours and is likely removed through PrestoBlue medium and expansion medium changes, future studies should investigate the repeated addition of PVA samples with each medium change to better understand the effects of continuous exposure.

Taking together, these results provide insight into the hydrolytic degradation and evolution of mechanical properties of 3D printed PVA, as well as stress relaxation in PETG under immersion. Both contributions lay the fundamentals for the design of degradation-controlled 4D actuators and the evaluation of their biocompatibility, thus expanding the applicability of these materials in tissue engineering and biomedical devices.

6.6. Conclusions

PVA has proven suitable as a degradable material for 4D mechanisms. Immersion in water triggers hydrolytic damage, reducing PVA's molecular weight, elastic modulus, yield stress, and tensile strength. As it degrades, PVA shifts from brittle to more ductile behavior. In solid forms, the infill pattern does not influence erosion rate; instead, the exposed surface area-to-volume ratio governs degradation kinetics. Cytotoxicity tests confirm that PVA dissolves rapidly without harmful effects, underscoring its excellent biocompatibility.

PETG, on the other hand, behaves as a ductile polymer with high elastic energy storage capacity, although water exposure plasticizes it and speeds stress relaxation. Despite this, it maintains strong mechanical properties under immersion and remains cell compatible.

Because PVA is stiffer yet degradable, it can serve as a temporary “lock”, gradually releasing the elastic energy stored in PETG as it breaks down. This principle was demonstrated in a 4D shock absorber, where the PETG spring released energy upon PVA degradation. Such a strategy holds promise for applications in engineering and biomedicine, ranging from controlled delivery systems to smart structures and implantable devices.

Combining the two polymers via FFF provides a quick, cost-effective, and scalable method for prototyping programmable actuators. With the appropriate configuration, this approach can be extended to more sophisticated systems, leveraging PETG’s flexibility and PVA’s controlled degradability to achieve precise, responsive shape transformations.

7. Comprehensive collection of shape-morphing actuators triggered by degradation

7.1. Introduction

This collection presents a library of documented designs (CAD models, blueprints and results from printing and experiments) of innovative shape-morphing actuators. These shape-morphing structures are aimed at being 4D printed and constitute basic geometrical concepts to be further developed towards different types of industrial applications. Within this PhD thesis, these applications deal with bone distraction and skin expansion, but applications are foreseen in areas like minimally invasive surgery, tissue engineering, robotics, transport, space technology, energy or architecture, to cite a few industrial fields that can benefit from 4D printed actuators. Although 4D printing is already becoming well established, normally it resorts to shape-memory and electroactive materials and to functional gradients of materials and geometries [23,262,267,309,340,342,343,345,346,350,352]. Among the different triggering stimuli for shape-morphing materials and structures, degradation has been employed to some extent [347,349] and biodegradable materials are often used for shape-morphing actuators [4,364,365]. But still, (bio)degradation-based shape-morphing triggering has not realized its remarkable capabilities for achieving large shape transformations, through single, multiple or progressive actuation steps. Despite leading to slow actuations, the potential for medical applications is clear, if biomedical biodegradable materials are used, because the healing and growth processes that benefit from evolutive devices are time consuming.

A huge variety of polymeric filaments, each with its own degradation rate, can be processed on multi extrusion fused filament fabrication (FFF) printers. By combining these materials, it becomes possible to manufacture complex shape morphing mechanisms whose motion is activated by the controlled breakdown of one or more components (for instance, upon immersion in water). Systematically articulating the design principles for such degradation driven actuators, and illustrating them through practical examples, will accelerate the adoption of this cost-efficient rapid prototyping pathway to 4D printing.

To investigate this potential, polymer combinations (PVA and PETG) are initially used for exploratory purposes. However, the designs developed can be adapted to use any combination of materials with different degradation rates. The final applications of these actuators are focused on biomedical applications, particularly through the combination of biodegradable metals (Mg and Zn) or a mixture of biodegradable and bioinert alloys and/or polymers. Beyond medicine, degradable metals, ceramics and polymers can also be integrated for other industrial applications.

Multi-material additive manufacturing technologies (AMTs) play a crucial role in enabling these complex transformations. Techniques such as material extrusion, material jetting, binder jetting, vat photopolymerization, powder bed fusion, sheet lamination and direct energy deposition promote geometrical complexity and facilitate the creation of these complex-shaped actuators. Fused filament fabrication has proved particularly useful for prototype development, while laser powder bed fusion is a promising approach for final solutions.

Regarding the structure of the collection, for simplified communication purposes and enhanced reusability and replicability of results, the library of CAD models to be shared as an open-source result is organized by families (Appendix B). In short, four main kinds of multi-material shape-morphing actuators are considered: 1) actuators including a degradable framework that temporarily restricts the movement of elastic portions of the multi-material structure; 2) actuators with interlocking elements that temporarily restrict the motion of elastic regions; 3) actuators based on the degradation of (a) plastically deformed region(s) that liberate other elastic regions; and 4) actuators incorporating a degradable softening anchor, which initially provides high stiffness to constrain the motion of the elastic structure but progressively softens as it degrades, enabling a controlled release of the shape-morphing mechanism.

Typically, each shape-morphing actuator of the library is associated with two CAD models: one for the rapidly biodegradable region and one for the slowly biodegradable region. Along this chapter and in the documented images of the library, the rapidly degradable regions are depicted in ivory white (corresponding with the pale yellowish color of rapidly degradable PVA regions) and the slowly degradable regions are depicted in red (corresponding to the red color of PETG regions).

Furthermore, within the different main families of shape-shifting actuators triggered by degradation, various initial and final geometrical configurations, dimensions, shapes, single- and multi-step actuators, progressive solutions and shape transformations are exemplified, according to the process of promoting creativity and the results presented in chapter 5. To provide an unequivocal classification of the shape-morphing actuators from the collection, a specific ontology was developed, described in that chapter, whose coding schemes are also applied to codify the collection, as summarized in Appendix C.

The ultimate purpose of this chapter is to generate and share knowledge about 4D printed shape-morphing actuators and devices triggered by degradation, promoting both their industrial applications and their social impact. To ensure an accessible approach, the following subsections summarize the design principles behind the different families of shape-shifting mechanisms developed, as well as the materials and methods employed in their production.

Moreover, a proof-of-concept based on a mechanism from the library is produced using Laser Powder Bed Fusion, with the aim of evaluating how rapid prototyping facilitates the analysis of shape changing and its adaptation to high-performance additive processes.

7.2. Design principles leading to main families of shape-morphing actuators

In the proposed approach, the creation of bimaterial shape-morphing actuators triggered by degradation is based on the combination of materials with different mechanical properties and degradation rates. A durable and flexible degradable material is used to form a deformable structure, and another short-lived degradable material is used as a temporary anchor. This anchor holds the structure in an initial configuration until its degradation allows the controlled release of the mechanical energy stored in the flexible structure. Depending on the system design, the release of the stored energy can occur in a single step, in several steps or progressively.

To evaluate the potential of these degradable structures, a library based on the combination of PETG and PVA has been developed using an exploratory approach to rapid prototyping. This approach enables the generation of several concepts that can be adapted to the design of shape-shifting implants made from biodegradable and/or biocompatible alloys such as zinc, magnesium or nitinol.

Depending on the printing technology and procedure, different configurations are possible. In the simplest version, separate structures are printed with two different materials: one flexible and slowly degradable, such as PETG, and the other more rapidly degradable, such as PVA. After printing, the flexible part is deformed into its temporary configuration (trained) and held in place by the degradable anchor(s). In the more complex version, multimaterial printing is used to produce a part in which the flexible and degradable regions are already integrated, avoiding assembly processes and subsequent handling. After printing, the flexible structure is deformed, and the degradable anchor comes into play.

From an energetic point of view, the mechanical deformation of the flexible structure introduces elastic potential energy into the PETG, which remains stored thanks to the constraint imposed by the degradable anchor. In this state, the system is metastable, as the stored energy can only be released when the anchor loses its structural integrity due to degradation (Table 6.1, Figure 6.5 - Figure 6.8). As the short-lived degradable material degrades, the mechanical restriction gradually disappears and the conversion of elastic potential energy into kinetic energy begins, causing the flexible structure to change shape. Depending on the design of the actuator and the rate of degradation of the anchor, the release of energy may be sudden, gradual or progressive. If the biodegradable anchor degrades uniformly and rapidly, the energy release is instantaneous, and the shape morphing occurs in a single step. On the other hand, if the degradation is programmed by the design of the material or the anchor's geometry, the release of energy can be spread over time, allowing a progressive and controlled change.

The energy conversion process is not completely efficient due to the presence of irreversibilities. During deformation, part of the potential energy is not converted into useful kinetic energy but is dissipated by three main mechanisms. Firstly, the viscoelasticity of PETG, which when in contact with the degradation medium (water) undergo plasticization due to creep and stress relaxation (Figure 6.18), altering its mechanical properties and reducing its ability to fully recover its initial shape (studied in the previous chapter) [386]. Secondly, mechanical hysteresis and irreparable deformation mean that the deformation and recovery of the material is not fully reversible [387]. Finally, fluid-structure friction losses also reduce the system efficiency. As the flexible structure moves to regain its stable shape, it interacts with its environment. This interaction introduces friction, which dissipates some of the kinetic energy in the form of heat and turbulence.

From a thermodynamic point of view, the energy evolution of the system is governed by the principle of energy conservation (see section 3.1.4). The total energy remains constant over time and is divided between the stored elastic potential energy, the kinetic energy released in motion and the energy dissipated by viscoelastic effects and friction. As a result, the proportion of energy available for shape shifting is always less than the initial stored energy, i.e. the shape recovery ratio is always less than 100%.

The efficiency of this process depends on several factors, such as the erosion rate of the degradable anchor, the geometry of the actuator and the mechanical properties of the flexible material. Consequently, different design principles or possibilities are explored, considering: 1) the structures and geometries of the anchorages and their actuation upon the shape-morphing structures, 2) the structures and geometries of the shape-morphing elements, and 3) the printing procedure, as explained below.

Building upon these findings, a novel approach to degradable structures with programmed activation has been developed, leading to the formulation of a patent currently under analysis: *Molina Aldareguia, J. M., Llorca Martínez, F. J., Patterson, J., Díaz Lantada, A., Solórzano Requejo, W. G., Kopp, A., Pöstges, S. "Structure comprising a first, rapidly degradable part and a second, slowly or non-degradable part"*. This patent, created in collaboration with IMDEA Materials Institute, Meotec GmbH, and Universidad Politécnica de Madrid, reflects the advancements made in optimizing degradable anchoring strategies and actuation mechanisms.

1) Structures and geometries of the anchorages and actuation upon the shape-morphing structures. For this design principle different families (or options) are considered

- ***Degradable framework*** (Figure 7.1). An external framework or anchoring structure is employed to fix the temporary geometry of the compliant shape-morphing structure. Its degradation leads to the release of the clamped structure and triggers the shape-morphing. Thus, a single cage or framework leads to a single-step actuation, while multiple frameworks with regions degrading at a different rate, for example imitating a nesting doll, or combining thicknesses within the biodegradable structure, allow for multi-step actuations, if the shape-morphing features of the compliant structure are also designed to enable them.

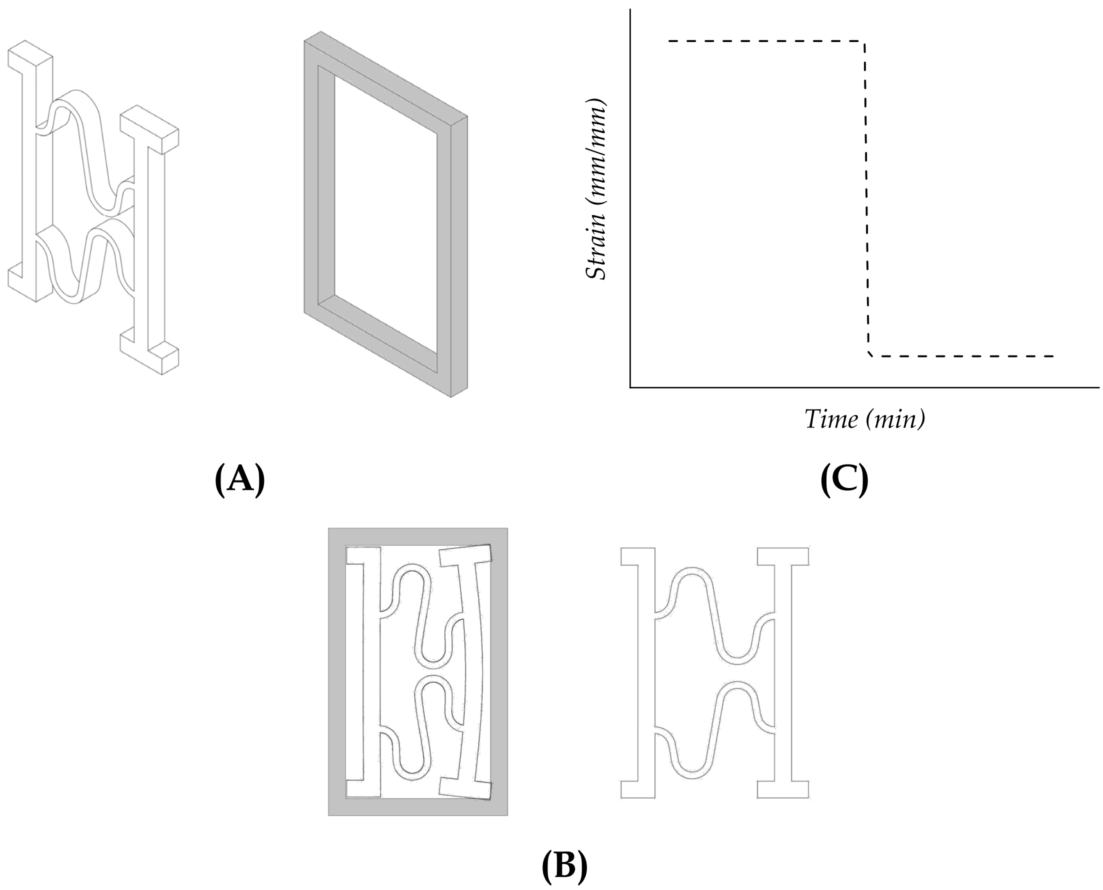

Figure 7.1: Scheme of a multi-material degradable framework-based actuator illustrating the metamorphosis triggered by degradation. This configuration includes a rapidly degradable locking framework (highlighted in gray) that clamps a slowly degradable elastically deformed region. (A) Parts constituting the actuator. (B) Shape change over time. (C) Strain evolution as time function.

- ***Degradable interlocking elements, pins, snap fits or threads*** (Figure 7.2). Instead of resorting to an external coffin or framework, it is also possible to employ smaller biodegradable regions and derived geometrical interlockings. These take inspiration from joints typically employed in the industry, like bolts, snap fits or screws. Single interlocking elements may lead to single-step or eventually progressive actuation, while designs including multiple interlocking elements allow multi-stepped actuations.

Progressive actuation is possible through special designs of the interlocking features, normally based on gradients of thickness or porosity. In specific cases the interlocking element may be printed as a single biodegradable element (for example, an external bar or pin that interlocks the shape-morphing structure through a designed hole or slot), which would be a simplified version of the biodegradable cage or framework explained above. However, bimaterial printing facilitates the simultaneous creation of the shape-morphing structure, in the long-lasting degradable material, and the short-living degradable interlocking elements. Hence, a single structure would be obtained, where shape-morphing regions interact with adjacent degradable interlockings during training.

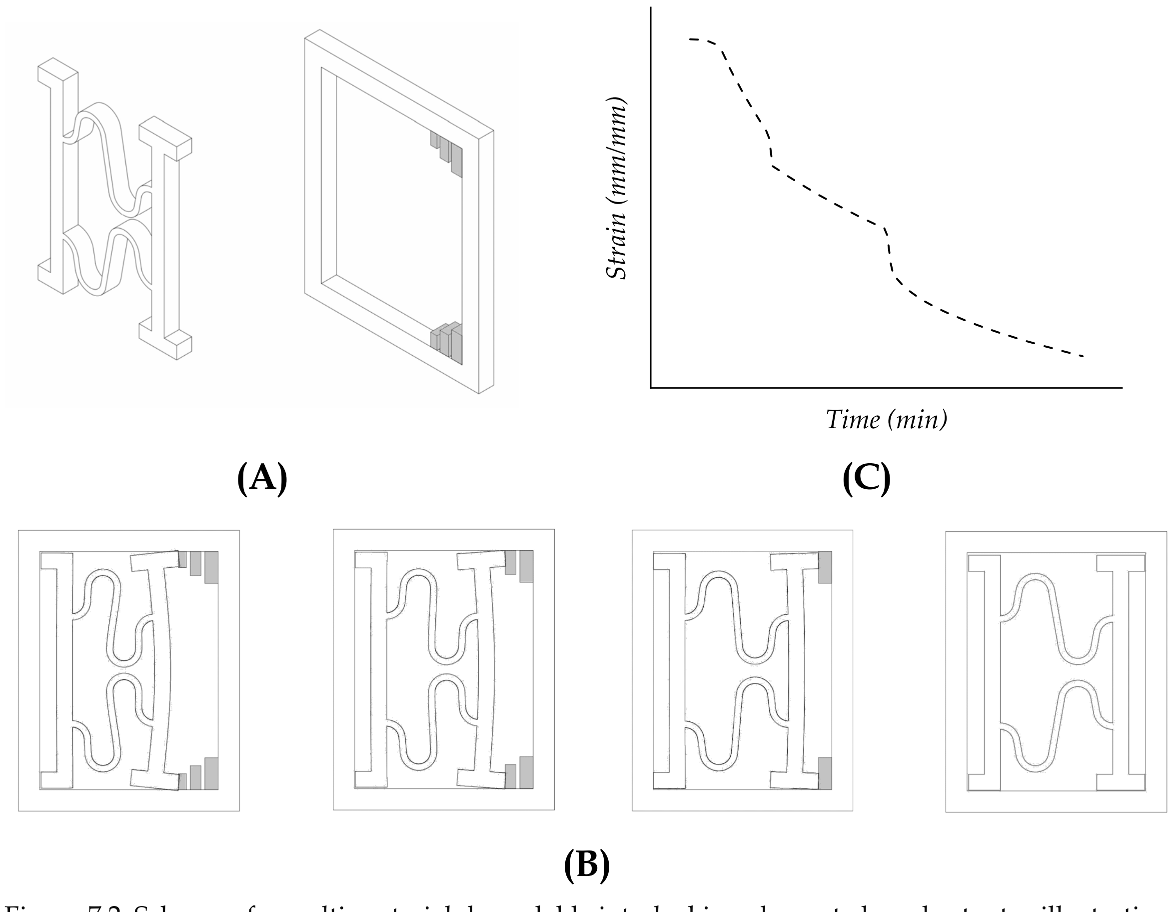

Figure 7.2: Scheme of a multi-material degradable interlocking elements-based actuator illustrating the metamorphosis triggered by degradation. This configuration includes a set of rapidly degradable interlocking elements (highlighted in gray) that selectively fix elastically deformed regions made of slowly degradable material and lead to a multi-stepped actuation process through degradation. (A) Parts constituting the actuator. (B) Shape change over time. (C) Strain evolution as time function.

- ***Plastic deformation of the degradable anchoring element*** (Figure 7.3). External degradable elements clamped against or acting upon the compliant shape-morphing structures and undergoing plastic deformation while bringing them to their temporary shape may be employed. Special designs with interwoven structures with degradable regions being plastically deformed through the interaction with the compliant material of the shape-morphing structure, which remains elastic, may be also an option. Thus, the degradable anchoring elements that are plastically deformed can be obtained, either as independent degradable parts, in the form of cages, frameworks, staples or rivets, or as biodegradable regions next to the shape-morphing compliant regions within bimaterial constructs. Both external and internal blocking elements or interwoven structures can be obtained in degradable material and act through plastic deformation upon the compliant shape-morphing structures, for temporally blocking them in their transitory shapes.

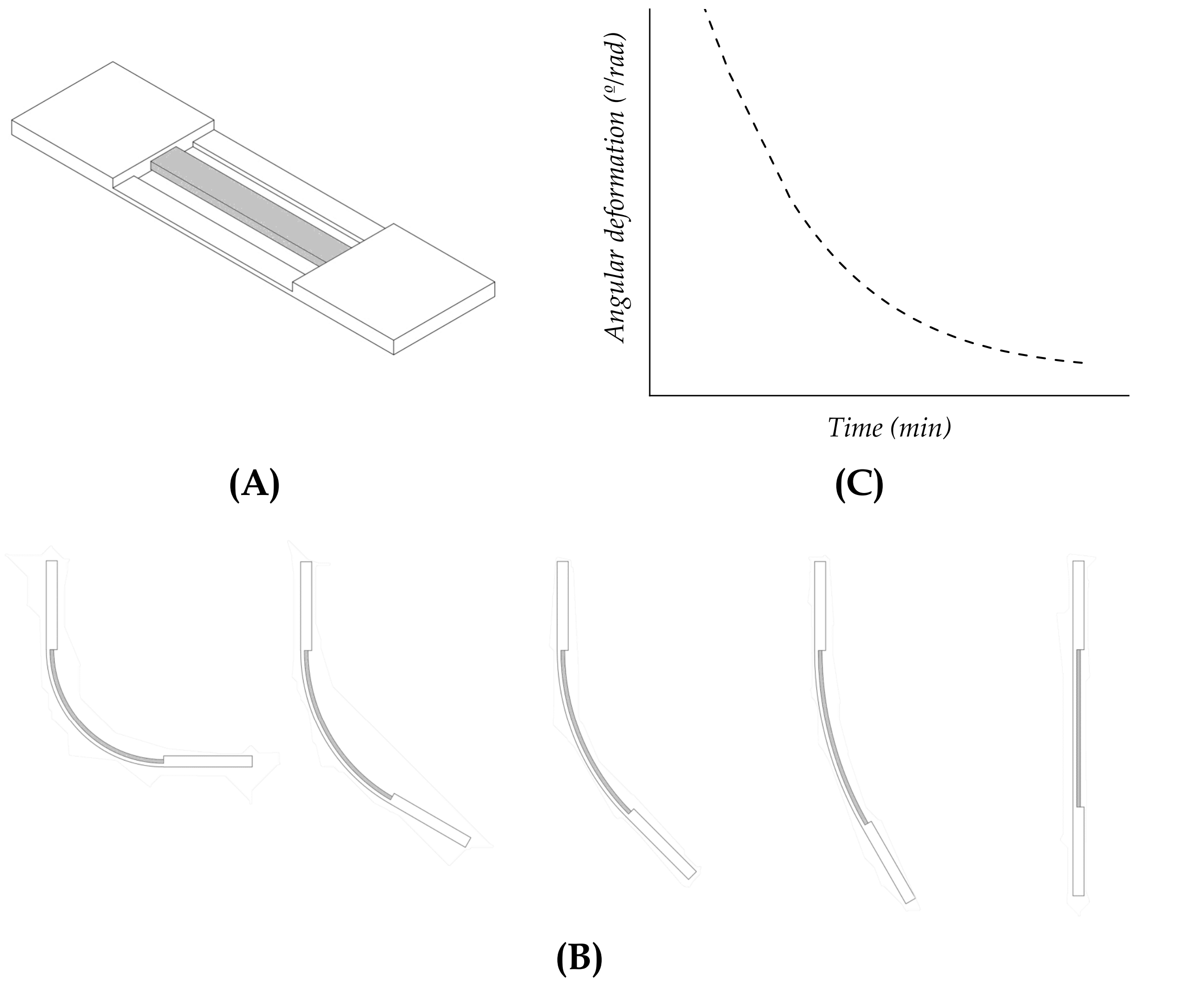

Figure 7.3: One configuration in which a region made of a rapidly degrading material is plastically deformed (highlighted in gray) together with a region made of slowly degrading material which is elastically deformed, leading to a bending structure that progressively returns to a straight position. (A) Part constituting the actuator. (B) Shape change over time. (C) Strain evolution as time function.

- ***Degradable softening anchor*** (Figure 7.4). It is based on the strategy of decreasing stiffness through controlled degradation, which allows a progressive and adaptable shape morphing activation. Contrary to methods that rely on the total and sudden degradation of the anchor, this strategy uses a fixing element, generally in the form of a spring, which has a high initial rigidity and prevents the movement of the flexible structure. As the degradable material of the anchor degrades, its stiffness gradually decreases, allowing a progressive release of the structure rather than a sudden separation. Depending on the design, the degradation can be homogeneous, resulting in a progressive and uniform deployment, or a stiffness gradient can be implemented by varying the thickness or composition of the material along the spring.

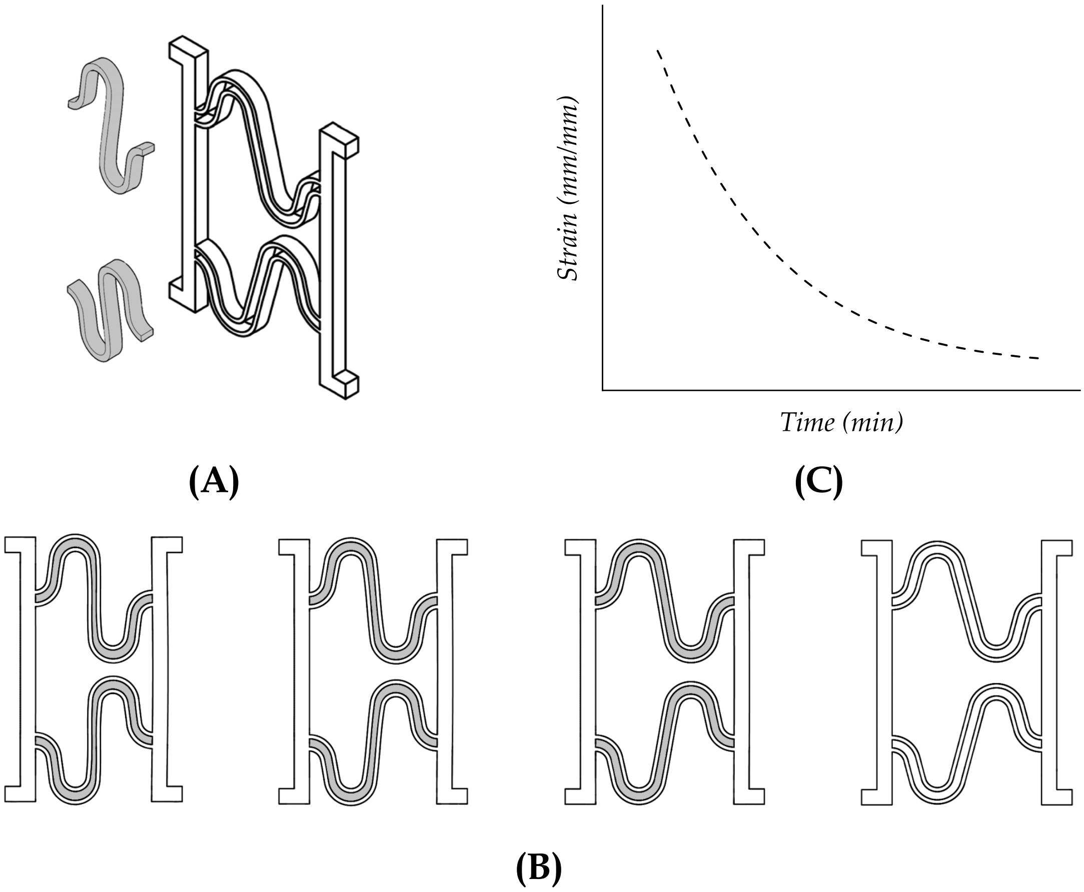

Figure 7.4: Schematic of a multi-material actuator based on a degradable softening anchor, illustrating the metamorphosis triggered by degradation. This configuration includes a serpentine spring with openings in its coils to place anchors made of a rapidly degradable material (highlighted in gray). These anchors compress the structure, which later returns to its original shape as the anchoring material softens when exposed to the degrading medium. (A) Parts constituting the actuator. (B) Shape change over time. (C) Strain evolution as a function of time.

2) Structures and geometries of the shape-morphing elements

- Promoting structural compliance for achieving shape-morphing properties. Structures typically employed in shape-morphing systems are also usable for the degradation-triggered transformations. To this end, it is essential to consider the compression of spring-based structures, whether linear, stiffening or softening, in configurations such as serpentine, helical, conical or torsional (for more details on its mechanical behavior see Spring mechanics section). Likewise, the folding of geometries inspired by origami art, the auxetic properties of advanced mechanical metamaterials, the structural variability of textiles and the use of kinematic mechanisms offer versatile solutions for designing “active” and flexible structures. These configurations not only provide structural adaptability but also allow for the storage and controlled release of potential energy, facilitating the shape changing in a programmed and efficient manner.

- These structural configurations can be combined, for creativity promotion purposes and increased versatility, with all the previously explained degradable anchorages, although only a selection of those is presented here and illustrated with rapid prototypes.
- Geometrical transformations for multi-purpose actuators. Most actuators follow this configuration, there are some exception. Depending on the application, actuators may require transformations across different geometric dimensions, including 1D, 2D and 3D. For symmetry reasons, only six of the possible transformations are analyzed in this study: 1D to 1D, 1D to 2D, 1D to 3D, 2D to 2D, 2D to 3D and 3D to 3D.

3) Printing procedure: mono- or multi-material

- Mono-material printing. Mono-material printing is adequate for printing the compliant shape-morphing structures and the degradable anchorages at different moments and using different materials and, subsequently, combining them to achieve a multi-material component made of single mono-material parts. This can work nicely for the framework-based degradable structures and for some specific alternatives of externally introduced degradable blocking elements or plastically deformable staples or rivets, to temporarily fix the shape-morphing structure, but does not exploit all the possibilities offered by AMTs.
- Multi-material printing. Multi-material printing avoids post-processes and also enables more complex geometrical features and interactions among multiple materials to be obtained. Indeed, a biodegradable external framework can interact with the outer boundaries of a shape-morphing structure but cannot directly reach and act within the core of the actuator. Through multi-material printing it is possible to reach higher geometrical complexity, including spatial modifications of thickness, functional gradients of composition, interwoven structures, which lead to a more versatile incorporation of blocking elements or easier elastic-plastic interactions among the degradable short-lived regions and the long-lasting compliant areas.

In the case of using multi-material printing technologies capable of processing more than two materials in the same construction or by using combinations of more than two parts made of more than two materials, the above principles apply and the shape-morphing possibilities, especially with regard to stepped actuations, may dramatically increase. Currently this study is limited to combining two materials, but the extension to three or more materials is conceptually direct.

Shape-morphing structures analyzed here are in most cases based on a compliant element that is compressed, bent or folded into a dimensionally lower object or a reduce-sized transitory shape during the shape-morphing training and that unfolds or expands due to degradation-triggered shape-morphing. Inversion of the movements or symmetric design principles can lead to dimensionally higher or enlarged objects that contract or fold after triggering the shape-morphing by degradation. This symmetric approach is not explored here, as the main objective of this PhD thesis is linked to implants applied in a minimally invasive way and capable of performing expansions and distractions, growing during the (bio)degradation process.

The following pages provide a detailed overview of the materials and methods employed in the rapid prototyping process, which was selected to demonstrate the aforementioned principles and illustrate them through a series of proof-of-concept mechanisms. Notably, a total of 50 conceptual bimaterial actuators have been designed, printed, and tested using polymeric combinations within the rapid prototyping route. The experimental results confirm the feasibility of shape-morphing devices activated by degradation, while the documented findings contribute to reinforcing the open science strategy of this study.

7.3. Materials and methods

7.3.1. Materials

To emulate the combination of materials with different degradation rates usable in bimaterial shape-morphing actuators triggered by degradation, polyethylene terephthalate glycol-modified (PETG) and poly(vinyl alcohol) (PVA) are employed. PETG is used for the compliant shape-morphing structure, while PVA, thanks to its rapid solubility in water, is used for the degradable anchorages for accelerated testing purposes. In a preliminary set of experiments the combination of poly(lactic acid) (PLA) and PVA was also employed, but the rapid plasticization of PLA in water led to stress relaxation within the compliant shape-morphing structures and did not provide adequate actuation after PVA degradation. For this reason, higher performing PETG was selected as an alternative to the initially planned PLA. The thermoplastic materials used in this research are purchased from Smart Materials 3D (Pol. Ind. El Retamar, c/ Tomillo 7, 23680 Alcalá la Real, Jaén, Spain) in the form of monofilaments with a 1.75 mm diameter.

7.3.2. Design and manufacturing resources

Shape-morphing structures were designed using Autodesk® Fusion 360 (Autodesk Inc., San Rafael, CA, USA). The PETG and PVA parts were separated into components to facilitate their being exported as independent .stl files. Fused filament fabrication (FFF) technique was employed to create bimaterial mechanisms triggered by degradation. For this purpose, a Bambu Lab X1 Carbon Combo printer (Austin, TX, USA), capable of using up to four different filaments, equipped with a hardened steel nozzle of 0.4 mm diameter was used. To generate the tool path for the 3D printer, Bambu Studio (Austin, TX, USA), an open-source slicing software based on Prusa Slicer, was employed. In this study, components were printed using either one or two filaments, depending on the design principles previously described. The print parameters were consistently configured for all printed specimens. A layer thickness of 0.2 mm, print speed of 50 mm/s, bed temperature of 70 °C, and nozzle temperatures of 220 ºC and 240 ºC were set for PVA and PETG, respectively. The structures were exclusively printed using perimeters with 100% density, and the seam was strategically placed in the least mechanically stressed area. To accommodate the printer's single extruder that requires filament changes, a prime tower was implemented. The dimensions were 25 mm in width, 45 mm^3 in volume, and featured a brim width of 1 mm.

7.3.3. Degradation testing setup

To investigate the shape evolution mechanism driven by hydrolytic degradation, a 12.0-megapixel high-resolution optical sensor with an f/1.5 lens and optical image stabilizer was used to capture images at regular intervals of one, ten or 60 seconds, depending on the degradation rate of the PVA anchors. To ensure consistency and prevent localized degradation, samples were carefully placed in a 200 mm × 150 mm × 50 mm glass container and fully immersed in 800 mL of water maintained at a constant temperature of 25 °C. This temperature was chosen to prevent the activation of any shape memory properties inherent to PETG [257,258], ensuring that the observed deformations were solely due to the degradation process. The camera was positioned either from the top or from the side, depending on the shape change of each mechanism (see Figure 7.5). The captured images were processed using ImageJ [254] to quantitatively analyze the shape shift and calculate the shape recovery ratio (equation (76)) for each actuator of the collection.

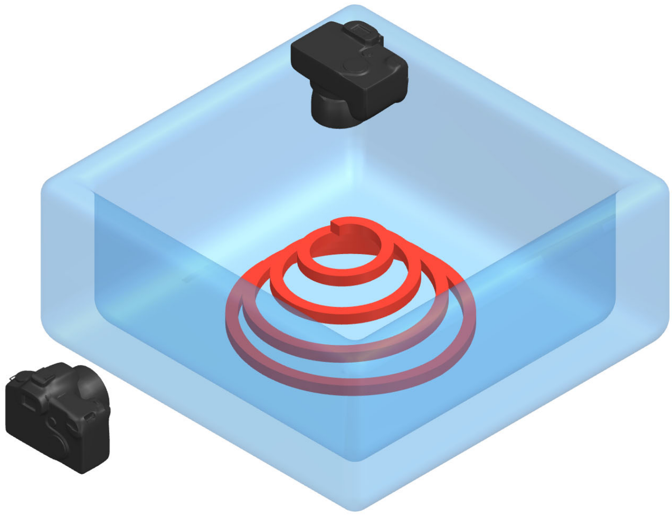

Figure 7.5: Experimental setup for the degradation test and camera positioning in top and side views.

7.4. Results

7.4.1. Library of shape-morphing actuators triggered by degradation

This section presents the results of the designed and rapid prototyped concepts of shape-shifting bi-material actuators triggered by the degradation of one of their components. The wide variety of combinations of dimensional transformations and geometric-structural alternatives to promote metamorphosis has led the designs to be grouped into four families according to the degradation strategy they adopt: external frameworks, internal interlocking elements, plastically deformed regions and anchors with gradual stiffness loss.

Within each family, the presented proofs-of-concept differ from each other for being: 1) printed with mono-material and muti-material approaches; 2) capable of achieving single- or multi-stepped, as well as progressive metamorphoses; 3) based on linear, planar or three-dimensional compliant structures; and 4) designed for different types of motions and transformations. In total, 50 conceptual actuators have been designed and documented, and tests on these actuators validate the possibility of inducing changes in shape through the controlled degradation of their components. Six of these are based on the degradation of an external framework (first family), eleven on the degradation of interlocking elements (second family), sixteen propose the concept of degrading plastically deformed regions to release elastically deformed regions (third family) and an additional set of seventeen actuators take advantage of the progressive softening of degradable anchorage to achieve gradual transformations (fourth family).

Table 7.1 provides a summary of key characteristics, including the representative design image, triggering strategy, printing process (mono- or multimaterial), and actuation type (single-step, multi-step, or progressive). It also details the dimensional and geometrical changes occurring as PVA degrades; the shape recovery ratio [371], which quantifies the extent to which the polymer regains its original shape after releasing stored potential energy, and the duration of the degradation test. Additionally, the table includes references to similar designs from the literature that inspired the actuators of this library, along with a hyperlink to Appendix B, which presents selected frames capturing the shape shifting of each mechanism.

Figure 7.6 - Figure 7.16 illustrate the evolution over time of the strain and angular deformation of the mechanisms, derived from the captured frames during the degradation test. To compare the performance of each family, the shape recovery ratio is plotted against test time in an Ashby-like diagram [388] (Figure 7.17), enabling the performance of these shape-morphing actuators to be evaluated together.

Table 7.1: Summary of prototyped and tested shape-morphing actuators with their shape recovery ratios after experimental quantification.

Actuator	Representative design image	Triggering strategy	Printing	Actuation	Dimensional change	Geometrical change	Shape recovery ratio (%)	Test time (min)	Ref.	Shape-morphing image
1		Degradable framework	Mono-material, two assembled parts	Single step	1D to 1D	Stretching	77.62	393	-	Figure B.1
2		Degradable framework	Mono-material, two assembled parts	Single step	3D to 3D	Stretching	79.67	206	-	Figure B.2
3		Degradable framework	Mono-material, two assembled parts	Progressive	2D to 3D	Expansion	88.05	78	-	Figure B.3
4	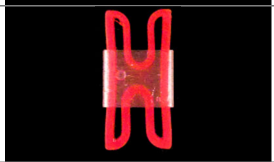	Degradable framework	Mono-material, two assembled parts	Single step	1D to 1D	Auxetic	77.07	45	[389]	Figure B.4
5		Degradable framework	Mono-material, five assembled parts	Multi-stepped	1D to 1D	Stretching	64.83	58	[390]	Figure B.5
6		Degradable framework	Mono-material, four assembled parts	Multi-stepped	2D to 2D	Expansion	-	-	[390]	Figure B.6

Actuator	Representative design image	Triggering strategy	Printing	Actuation	Dimensional change	Geometrical change	Shape recovery ratio (%)	Test time (min)	Ref.	Shape-morphing image
7		Degradable interlocking elements	Mono-material, two assembled parts	Single step	2D to 1D	Unfolding	78.24	175	-	Figure B.7
8	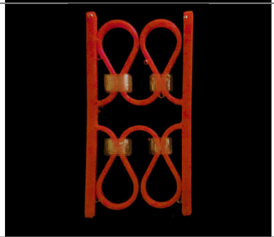	Degradable interlocking elements	Mono-material, five assembled parts	Multi-stepped	1D to 1D	Stretching	91.96	139	-	Figure B.8
9		Degradable interlocking elements	Multi-material, two assembled parts	Multi-stepped	1D to 1D	Stretching	54.53	1043	[391]	Figure B.9
10		Degradable interlocking elements	Multi-material, two assembled parts	Multi-stepped	1D to 1D	Stretching	52.31	1230	[391]	Figure B.10
11	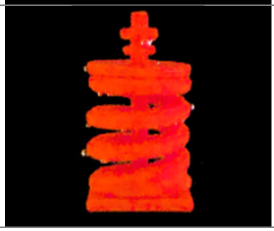	Degradable interlocking elements	Multi-material, three assembled parts	Multi-stepped	3D to 3D	Stretching	64.66	210	[392]	Figure B.11

Actuator	Representative design image	Triggering strategy	Printing	Actuation	Dimensional change	Geometrical change	Shape recovery ratio (%)	Test time (min)	Ref.	Shape-morphing image
12		Degradable interlocking elements	Multi-material, three assembled parts	Multi-stepped	3D to 3D	Stretching	71.78	145	[392]	Figure B.12
13		Degradable interlocking elements	Mono-material, seven assembled parts	Multi-stepped	2D to 3D	Expansion	77.38	210	-	Figure B.13
14	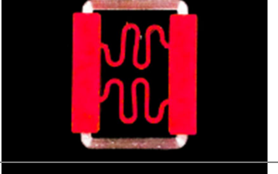	Degradable interlocking elements	Mono-material, three assembled parts	Single step	1D to 1D	Stretching	56.93	231	-	Figure B.14
15	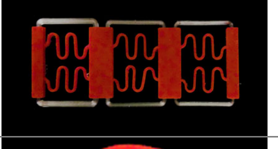	Degradable interlocking elements	Mono-material, seven assembled parts	Multi-stepped	1D to 1D	Stretching	90.43	227.1	-	Figure B.15
16		Degradable interlocking elements	Mono-material, two assembled parts	Single step	2D to 2D	Straightening	51.14	28.5	-	Figure B.16
17		Degradable interlocking elements	Multi-material, two assembled parts	Progressive	3D to 2D	Compressing	95.85	180	[393]	Figure B.17

Actuator	Representative design image	Triggering strategy	Printing	Actuation	Dimensional change	Geometrical change	Shape recovery ratio (%)	Test time (min)	Ref.	Shape-morphing image
18	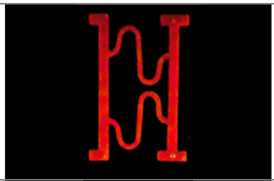	Degradable plastic deformed region	Bimaterial: printed in a single job	Progressive	1D to 1D	Stretching	9.01	30	-	Figure B.18
19		Degradable plastic deformed region	Bimaterial: printed in a single job	Progressive	1D to 1D	Stretching	9.12	15	-	Figure B.19
20		Degradable plastic deformed region	Multi-material, two assembled parts	Progressive	2D to 1D	Unfolding	88.39	135	[394]	Figure B.20
21	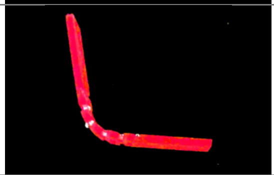	Degradable plastic deformed region	Bimaterial: printed in a single job	Progressive	2D to 1D	Unfolding	80.49	18	[395]	Figure B.21
22	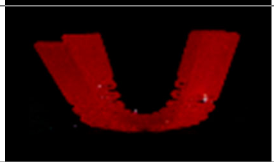	Degradable plastic deformed region	Bimaterial: printed in a single job	Progressive	3D to 2D	Origami	-	-	[395,396]	Figure B.22
23		Degradable plastic deformed region	Bimaterial: printed in a single job	Progressive	2D to 1D	Unfolding	30.34	27	[309,396,397]	Figure B.23

Actuator	Representative design image	Triggering strategy	Printing	Actuation	Dimensional change	Geometrical change	Shape recovery ratio (%)	Test time (min)	Ref.	Shape-morphing image
24	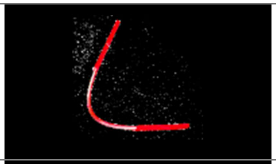	Degradable plastic deformed region	Bimaterial: printed in a single job	Progressive	2D to 1D	Unfolding	68.3	73	[309,396,397]	Figure B.24
25		Degradable plastic deformed region	Bimaterial: printed in a single job	Progressive	2D to 1D	Unfolding	61.06	28	[54,295,398]	Figure B.25
26		Degradable plastic deformed region	Bimaterial: printed in a single job	Progressive	2D to 1D	Unfolding	73.53	43	[54,295,398]	Figure B.26
27		Degradable plastic deformed region	Bimaterial: printed in a single job	Progressive	3D to 2D	Unfolding	72.63	60	[399]	Figure B.27
28	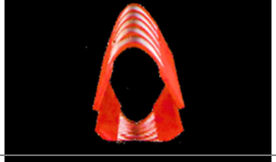	Degradable plastic deformed region	Bimaterial: printed in a single job	Progressive	3D to 2D	Unfolding	64.96	60	[399]	Figure B.28
29		Degradable plastic deformed region	Bimaterial: printed in a single job	Progressive	2D to 1D	Unfolding	-	-	[295,400,401]	Figure B.29

Actuator	Representative design image	Triggering strategy	Printing	Actuation	Dimensional change	Geometrical change	Shape recovery ratio (%)	Test time (min)	Ref.	Shape-morphing image
30	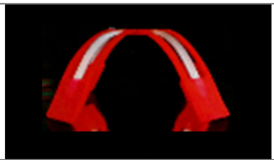	Degradable plastic deformed region	Bimaterial: printed in a single job	Progressive	3D to 2D	Origami	-	-	[295]	Figure B.30
31	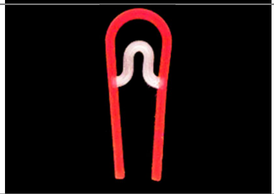	Degradable plastic deformed region	Bimaterial: printed in a single job	Progressive	2D to 2D	Straightening	87.71	25	[402,403]	Figure B.31
32		Degradable plastic deformed region	Bimaterial: printed in a single job	Progressive	2D to 1D	Straightening	77.95	70	[402,403]	Figure B.32
33		Degradable plastic deformed region	Bimaterial: printed in a single job	Multi-stepped	1D to 1D	Bistable	98.45	61	[404]	Figure B.33
34	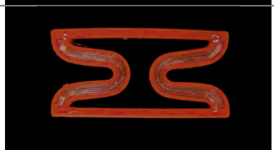	Degradable softening anchor	Mono-material, two assembled parts	Progressive	1D to 1D	Auxetic	60.85	450	[303,389]	Figure B.34
35	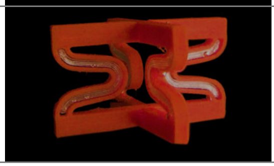	Degradable softening anchor	Mono-material, four assembled parts	Progressive	3D to 3D	Auxetic	-	-	[303,389]	Figure B.35

Actuator	Representative design image	Triggering strategy	Printing	Actuation	Dimensional change	Geometrical change	Shape recovery ratio (%)	Test time (min)	Ref.	Shape-morphing image
36	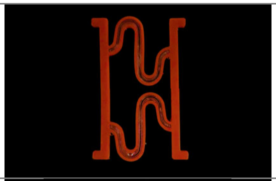	Degradable softening anchor	Mono-material, three assembled parts	Progressive	1D to 1D	Stretching	80.73	150	-	Figure B.36
37	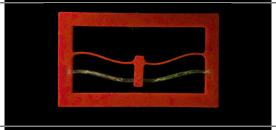	Degradable softening anchor	Mono-material, two assembled parts	Progressive	1D to 1D	Bistable	93.84	21	[404]	Figure B.37
38	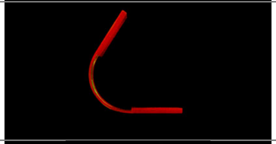	Degradable softening anchor	Mono-material, two assembled parts	Progressive	2D to 1D	Unfolding	92.49	26	[54,295,398]	Figure B.38
39	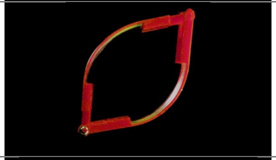	Degradable softening anchor	Mono-material, six assembled parts	Progressive	2D to 2D	Kusadama	-	-	[405]	Figure B.29
40	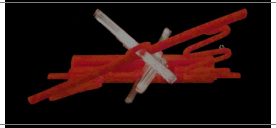	Degradable softening anchor	Mono-material, three assembled parts	Progressive	3D to 2D	Untwisting	90.87	23	[45]	Figure B.40
41	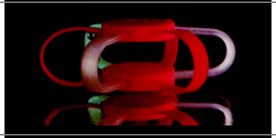	Degradable softening anchor	Mono-material, eight assembled parts	Progressive	3D to 3D	Expansion	76.43	100	[406]	Figure B.41
42	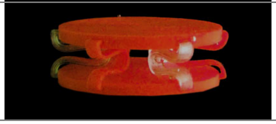	Degradable softening anchor	Mono-material, eight assembled parts	Progressive	3D to 3D	Auxetic	99.81	73	[407,408]	Figure B.42

Actuator	Representative design image	Triggering strategy	Printing	Actuation	Dimensional change	Geometrical change	Shape recovery ratio (%)	Test time (min)	Ref.	Shape-morphing image
43		Degradable softening anchor	Mono-material, two assembled parts	Progressive	3D to 3D	Stretching	81.77	223	[392]	Figure A.43
44	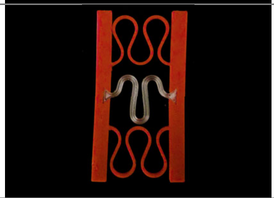	Degradable softening anchor	Mono-material, two assembled parts	Progressive	1D to 1D	Stretching	81.44	230	-	Figure B.44
45	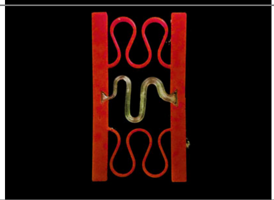	Degradable softening anchor	Mono-material, two assembled parts	Progressive	1D to 1D	Stretching	91.39	63	-	Figure B.45
46	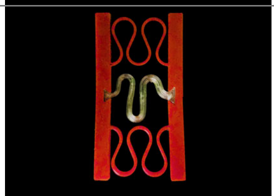	Degradable softening anchor	Mono-material, two assembled parts	Progressive	1D to 1D	Stretching	94.87	147	-	Figure B.46
47	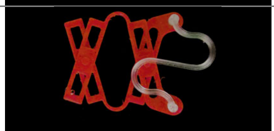	Degradable softening anchor	Mono-material, two assembled parts	Progressive	2D to 2D	Mechanism	54.4	108	[389]	Figure B.47
48	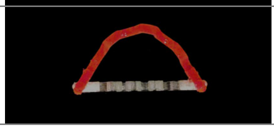	Degradable softening anchor	Mono-material, four assembled parts	Progressive	2D to 1D	Debuckling	87.71	22	[409–411]	Figure B.48

Actuator	Representative design image	Triggering strategy	Printing	Actuation	Dimensional change	Geometrical change	Shape recovery ratio (%)	Test time (min)	Ref.	Shape-morphing image
49	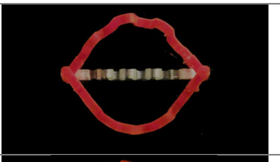	Degradable softening anchor	Mono-material, five assembled parts	Progressive	2D to 2D	Debuckling	55.6	26	[409–412]	Figure B.49
50	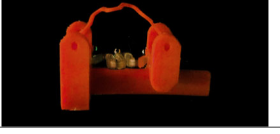	Degradable softening anchor	Mono-material, five assembled parts	Progressive	2D to 1D	Debuckling	96.6	112	-	Figure B.50

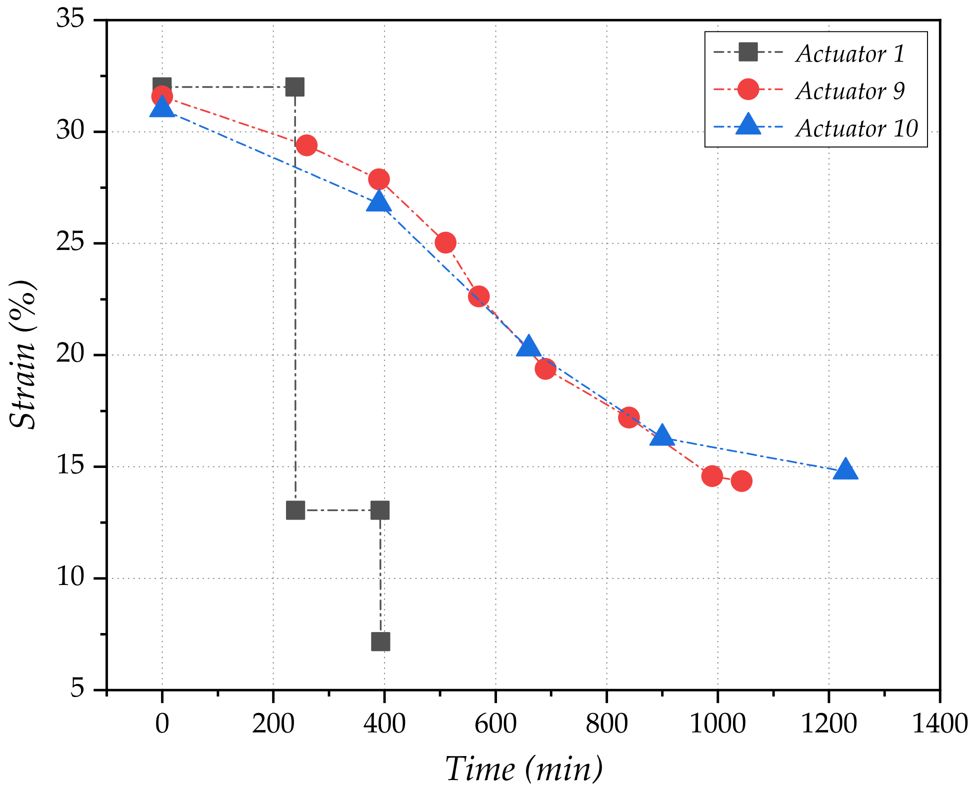

Figure 7.6: Comparative performance of actuators 1, 9 and 10.

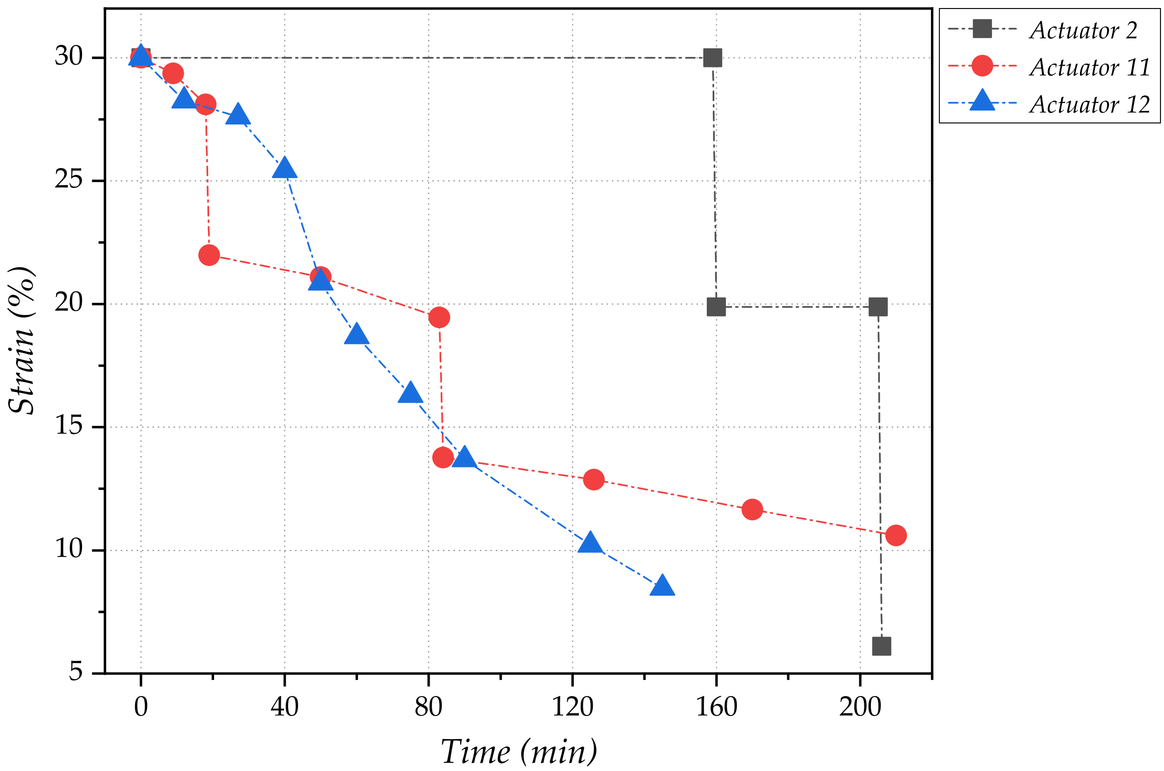

Figure 7.7: Comparative performance of actuators 2, 11 and 12.

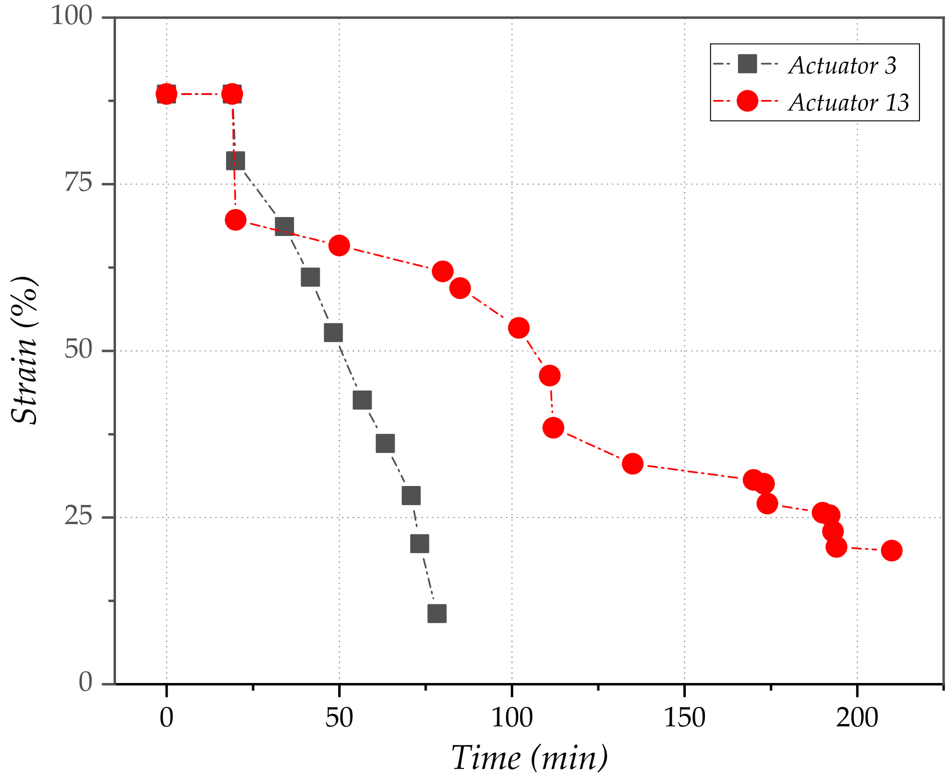

Figure 7.8: Comparative performance of actuators 3 and 13.

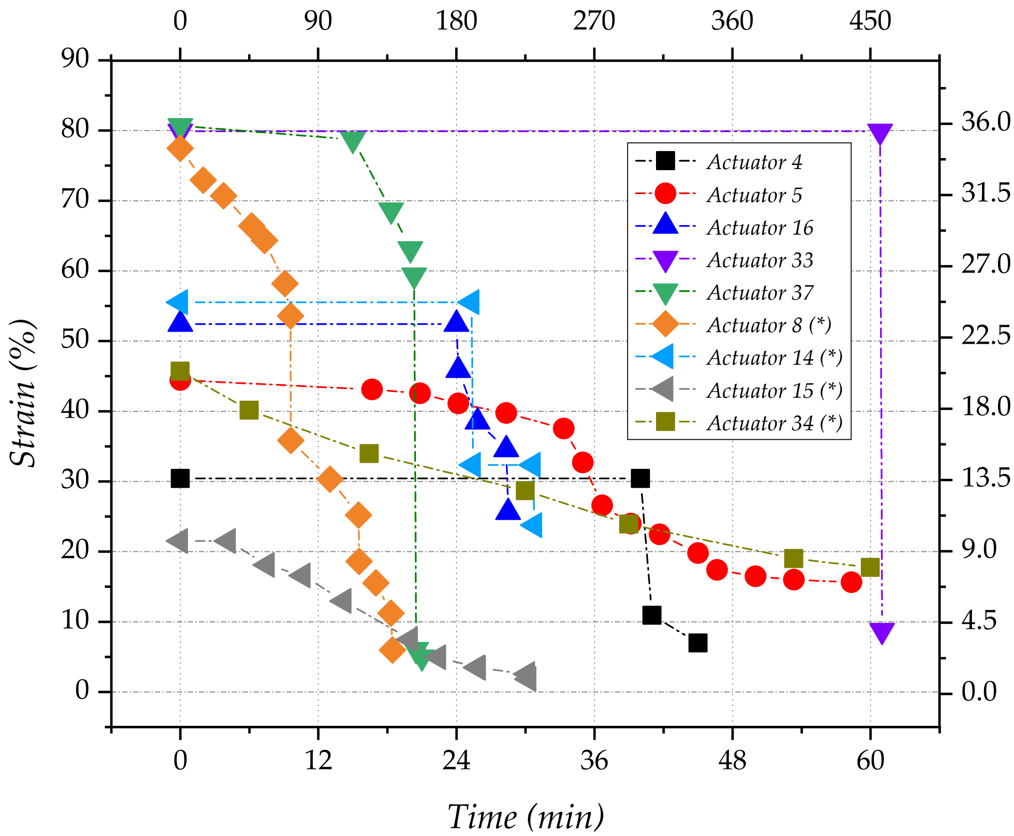

Figure 7.9: Comparative performance of actuators 4, 5, 8, 14, 15, 16, 33, 34 and 37. Parameters associated with auxiliary axes are marked with an asterisk (*).

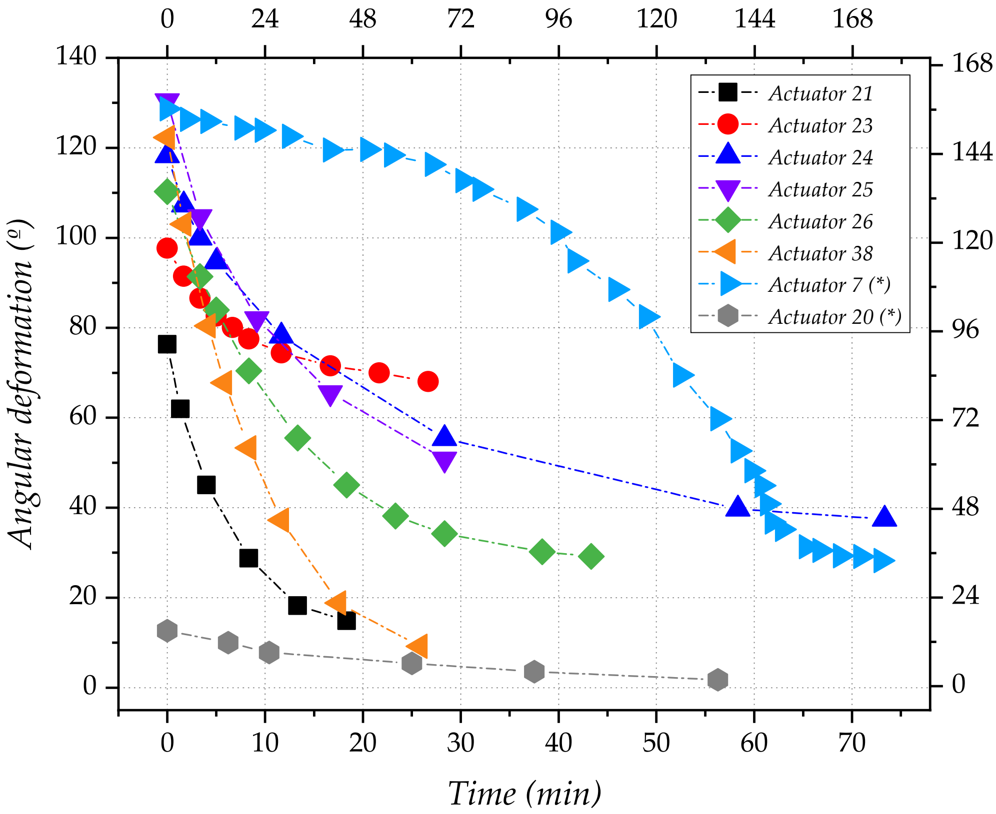

Figure 7.10: Comparative performance of actuators 7, 20, 21, 23, 24, 25, 26 and 38. Parameters associated with auxiliary axes are marked with an asterisk (*).

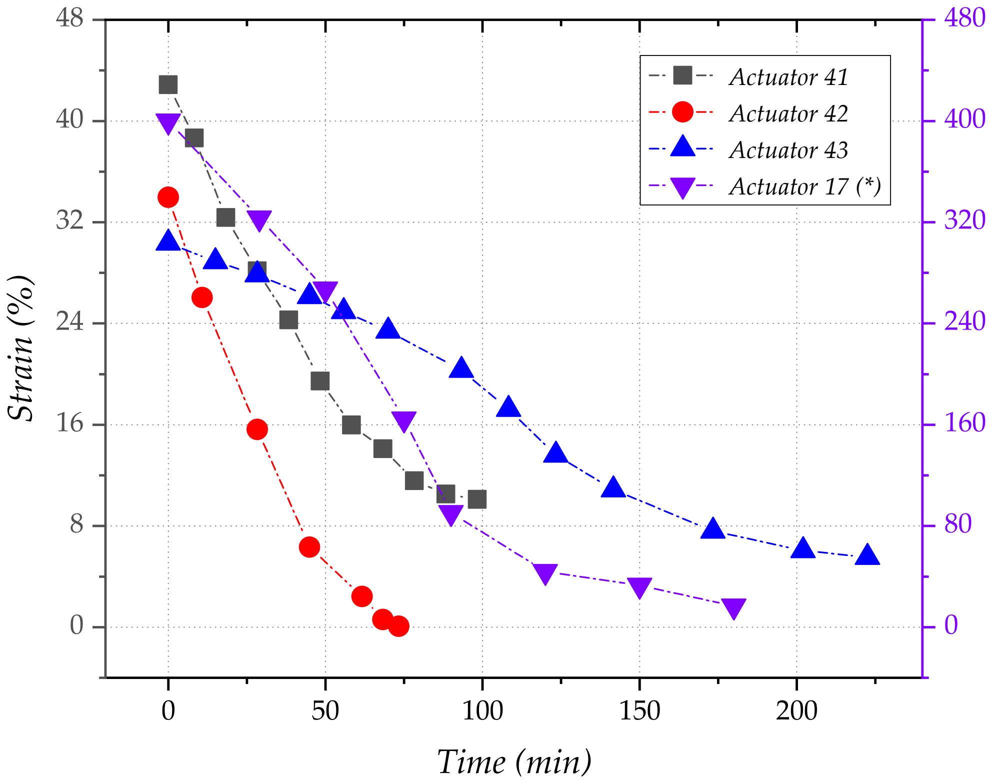

Figure 7.11: Comparative performance of actuators 17, 41, 42 and 43. Parameters associated with auxiliary axes are marked with an asterisk (*).

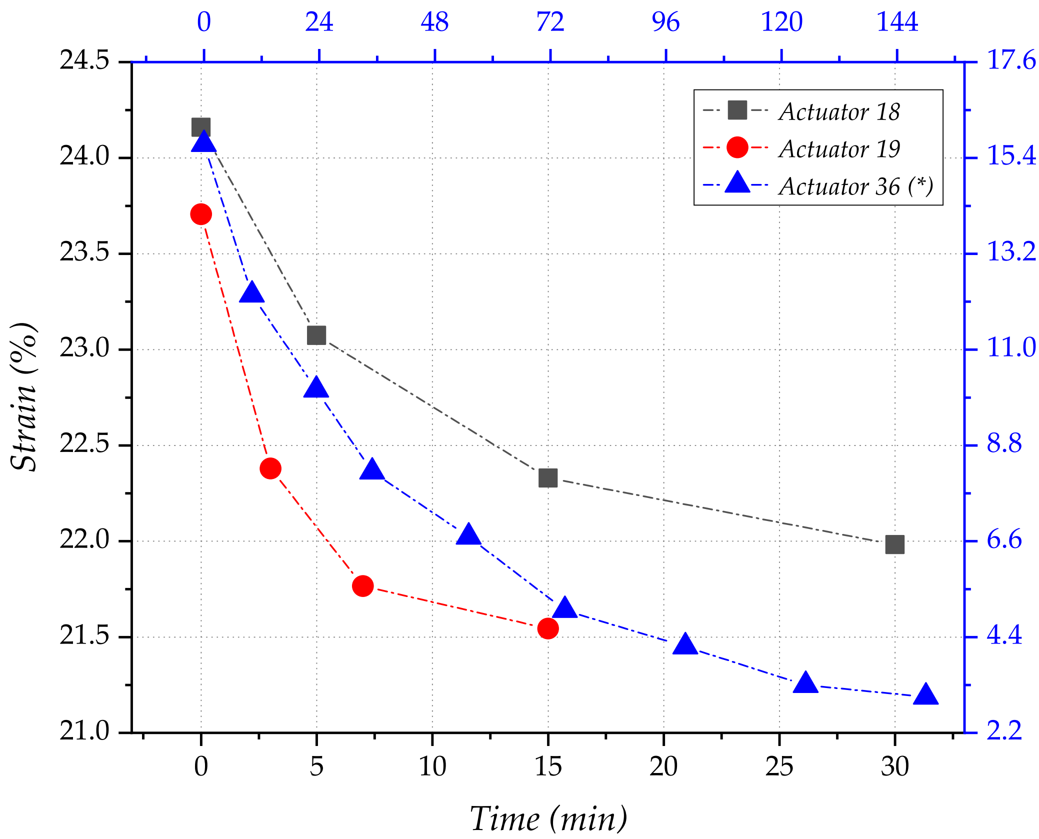

Figure 7.12: Comparative performance of actuators 18, 19 and 36. Parameters associated with auxiliary axes are marked with an asterisk (*).

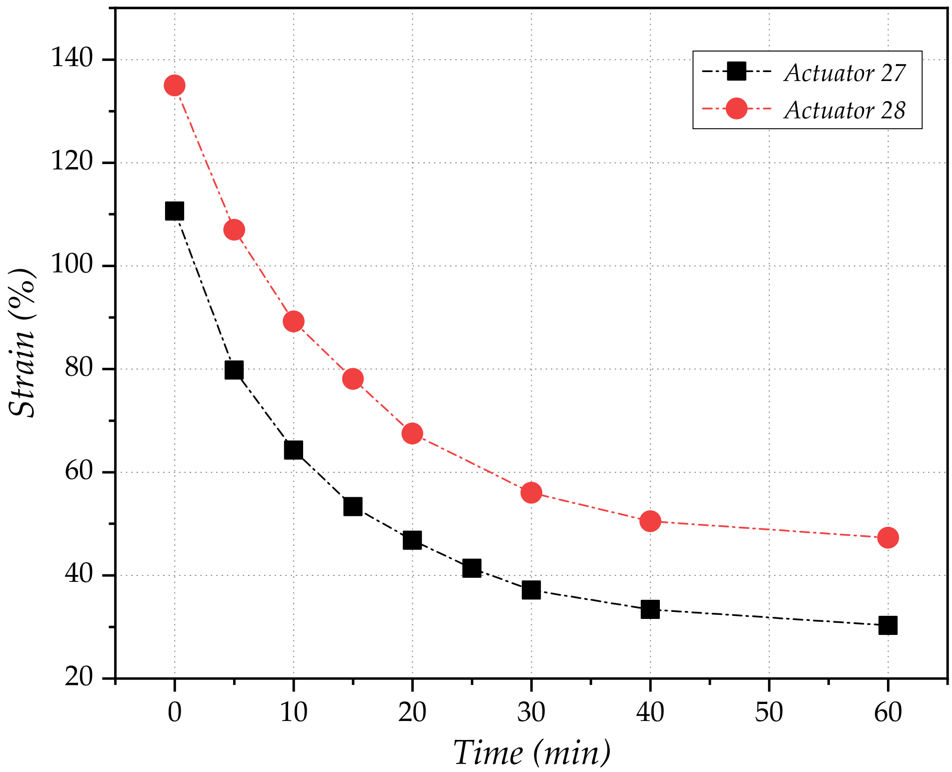

Figure 7.13: Comparative performance of actuators 27 and 28.

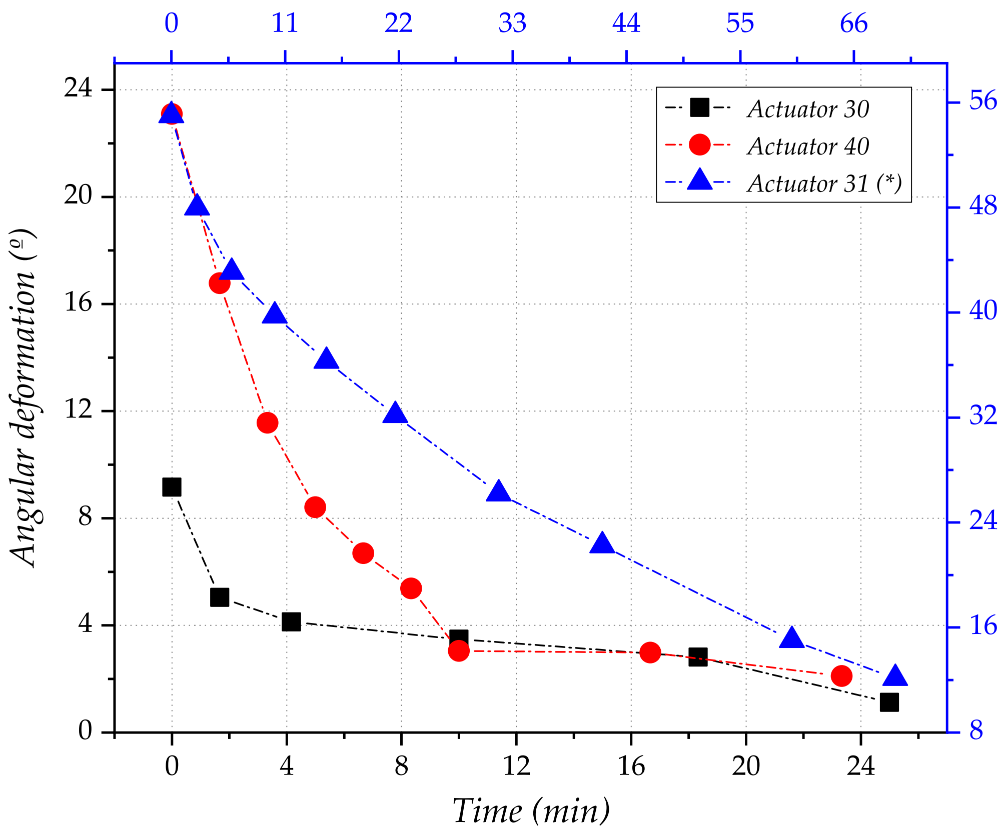

Figure 7.14: Comparative performance of actuators 30, 31 and 40. Parameters associated with auxiliary axes are marked with an asterisk (*).

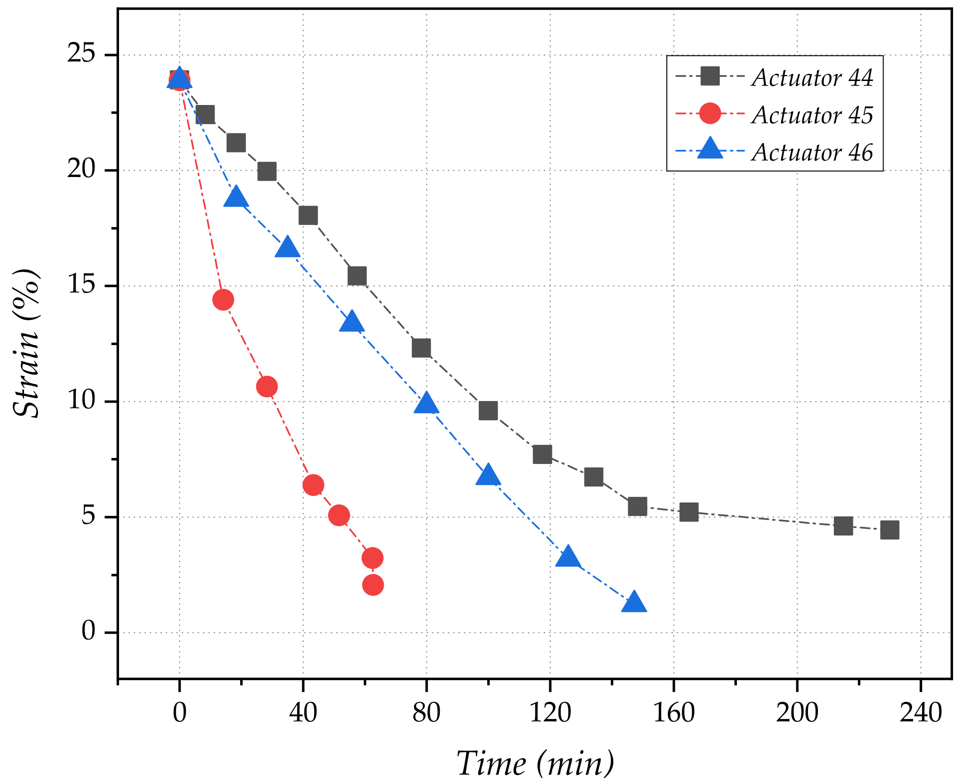

Figure 7.15: Comparative performance of actuators 44, 45 and 46.

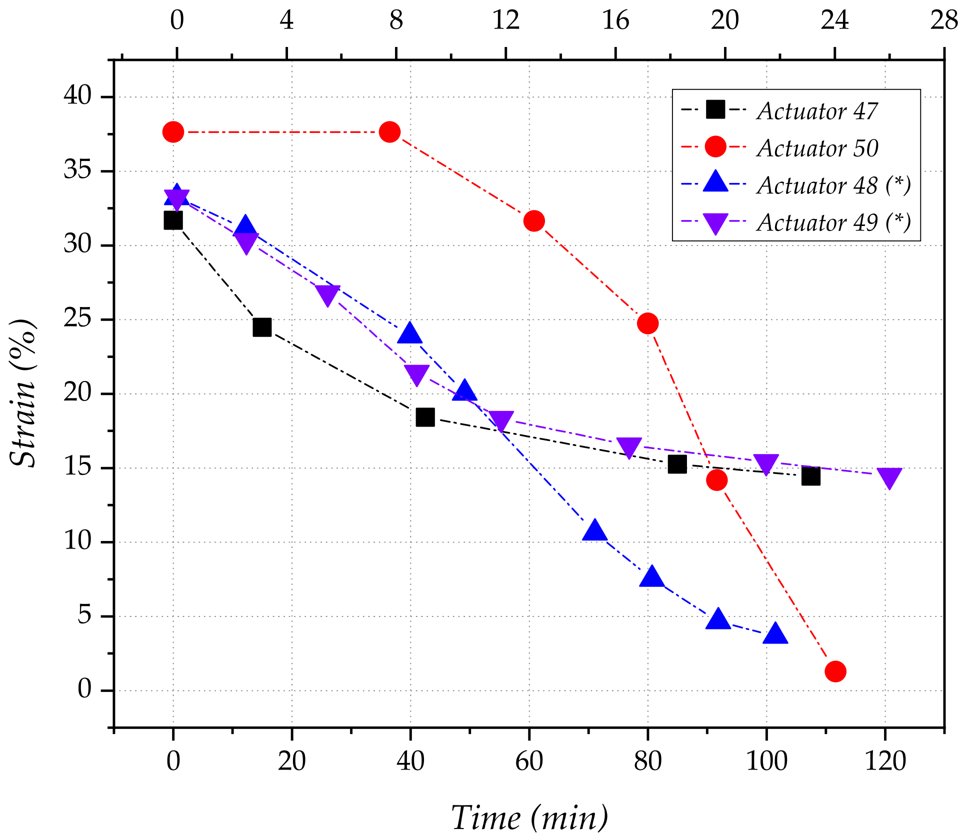

Figure 7.16: Comparative performance of actuators 47, 48, 49 and 50. Parameters associated with auxiliary axes are marked with an asterisk (*).

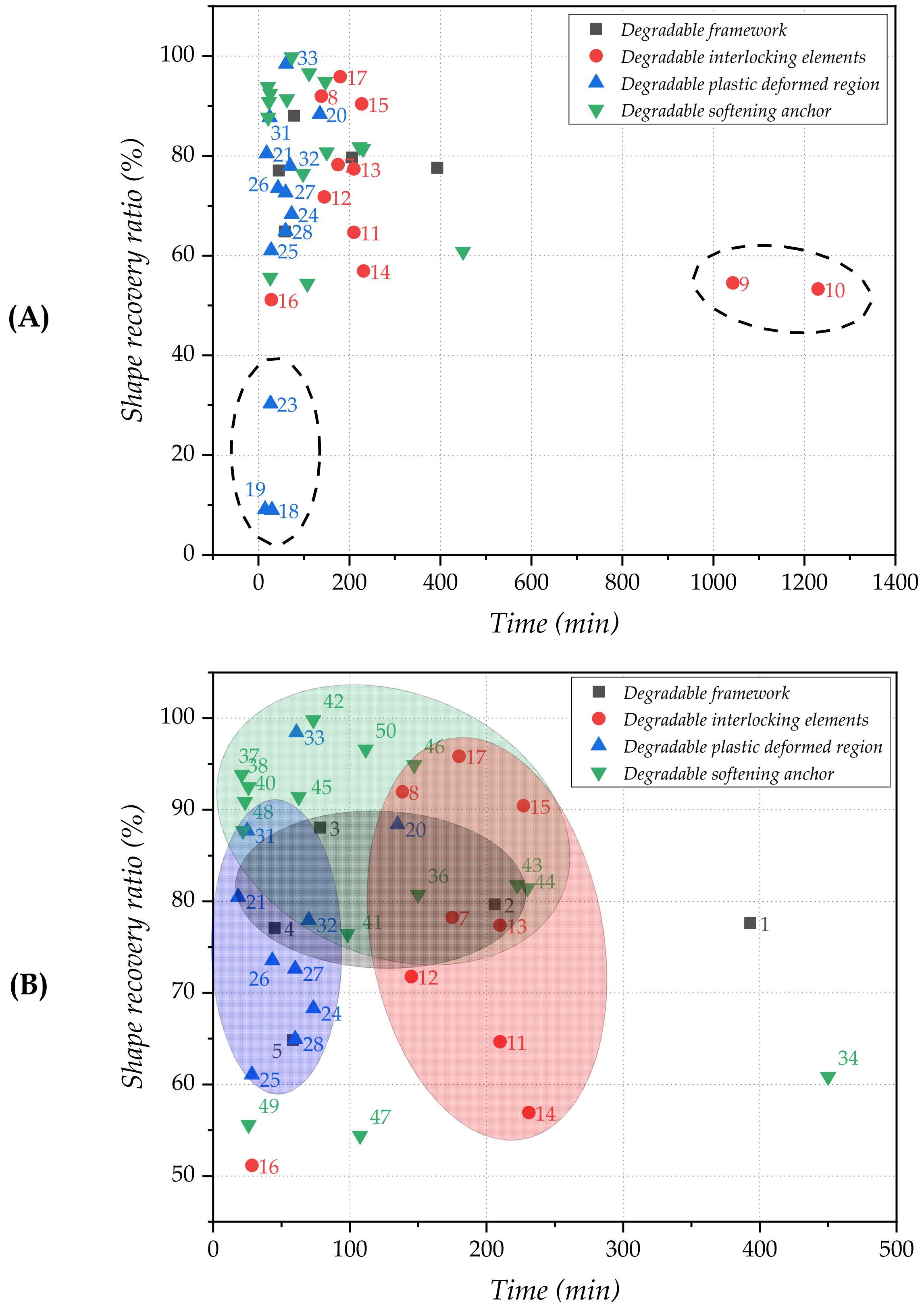

Figure 7.17: Ashby diagram of shape recovery ratio as a function of test time for (A) all mechanisms in the library, categorized by family and (B) with outliers removed for clearer analysis.

7.4.2. Proof-of-concept of a 4D printed shape-morphing metallic actuator

Although this PhD thesis focuses on polymeric actuators whose shape change is based on the degradation of one of their components, it is essential to determine whether the same concept can be applied to other materials and additive manufacturing processes. Consequently, within the framework of the BIOMET4D project that is funding this thesis, an actuator from the first family, that uses biodegradable frames, was designed with the aim of validating it in a metallic environment.

The production of the components followed a Design for Additive Manufacturing (DfAM) approach, considering the limitations of the Laser Powder Bed Fusion (LPBF) process and the materials selected. The flexible element was made of superelastic nitinol produced by Dr. Muzi Li and M.Sc. Oscar Contreras at IMDEA Materials Institute, while the degradable element was made of WE43meo alloy at Meotec GmbH, thanks to M. Eng. Simon Pöstges. Both IMDEA Materials and Meotec are members of the BIOMET4D consortium.

The design of this proof-of-concept is based on the fifth and eighth actuators from the mechanism library. It uses a serpentine spring with a pronounced angle of inclination to the horizontal as a flexible component, so that its walls remain vertical when compressed. This enables it to be assembled with two pairs of degradable frames of different thicknesses, allowing it to change shape in two stages. The final dimensions were defined in collaboration with Dr. Conall Quinn and Dr. Ted Vaughan from the National University of Galway (also BIOMET4D partners), who were responsible for the finite element modelling using Abaqus. Figure 7.18A shows the resulting configuration: a serpentine spring, initially compressed and held by anchors of 0.6 and 0.8 mm, where the tight fit between them guarantees the storage of potential energy by the spring. To compensate for possible inaccuracies in the LPBF process, anchors with two different tolerances (+0.1 and +0.2 mm) were printed, and finally the +0.2 mm ones were selected as they provided the best fit.

The assessment of this actuator was carried out by Dr. Jon Molina, Dr. Muzi Li, Dr. Vanesa Martínez and M. Eng. Guillermo Domínguez at IMDEA Materials Institute. The experimental set-up includes a transparent container measuring 90 × 70 × 55 mm^3, which allows the evolution of the actuator to be recorded in real time using a digital camera. This container is installed in a universal testing machine (Instron 5966) through its lower base, where the actuator is placed on a circular platform with a 45 mm diameter. The top of the container is open to enable a circular compression plate, attached to the machine crosshead, to descend into the container. A 100 N load cell measures the reaction force, while an LVDT with a maximum travel of 50 mm controls the separation between the compression plates, allowing the rate of expansion to be monitored. The system is connected to a thermo-bath to maintain the corrosion solution at 37°C (emulating the human body temperature) and a peristaltic pump (BT100M) is used to continuously recirculate the degrading medium.

During the test, the machine was programmed to maintain a constant load of 3 N during the entire experiment. In this way, as soon as the degradation of an anchor partially releases the spring, the load is released, and the machine raises the compression plate until the set point is restored. The chamber was then filled with a 3% NaCl solution buffered with Tris at pH 7.4. Figure 7.18B shows the various stages of the degradation process: after two minutes, dark corrosion products can be seen on the WE43MEO anchors; after about 60 minutes, the solution becomes opaque due to the high concentration of Mg^{2+} and the consequent increase in pH to 9.4. To reverse this alkalinization, 1 mL of acetic acid was added at 81 minutes, which immediately clarified the solution and reduced the pH to 5. Shortly afterwards, at 87 and 88 minutes, the thinner anchors broke, releasing the upper part of the spring and causing the first deformation. Thirty minutes later, the failure of the lower (thicker) anchors completed the second stage of the process, ending the test after approximately two hours. Figure 7.18C shows the evolution of the load and extension over time, highlighting the failure timing of each anchor and the corresponding reaction force and expansion at each stage. Notably, the mechanism achieved a shape-recovery ratio of 98.23%, exceeding that of the polymeric components analyzed in the previous section.

(A)

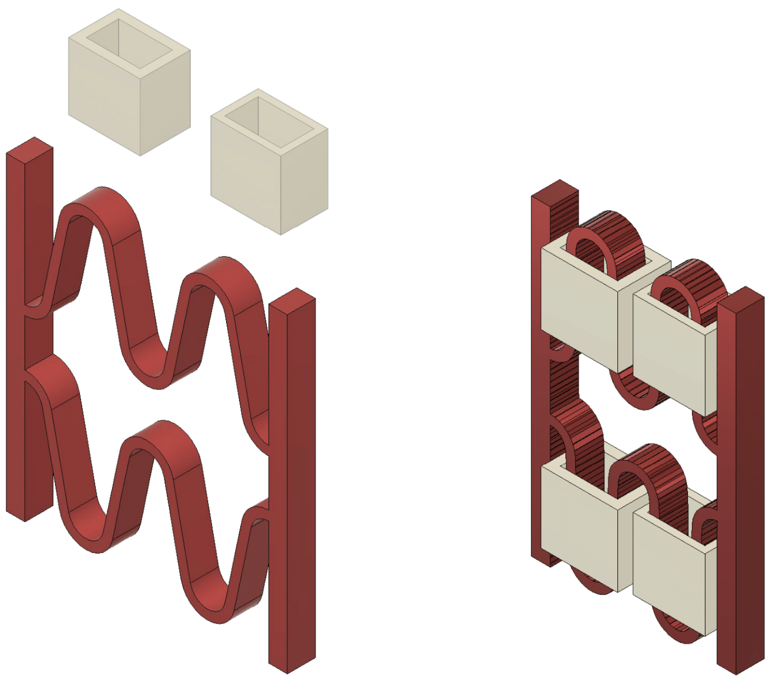

(B)

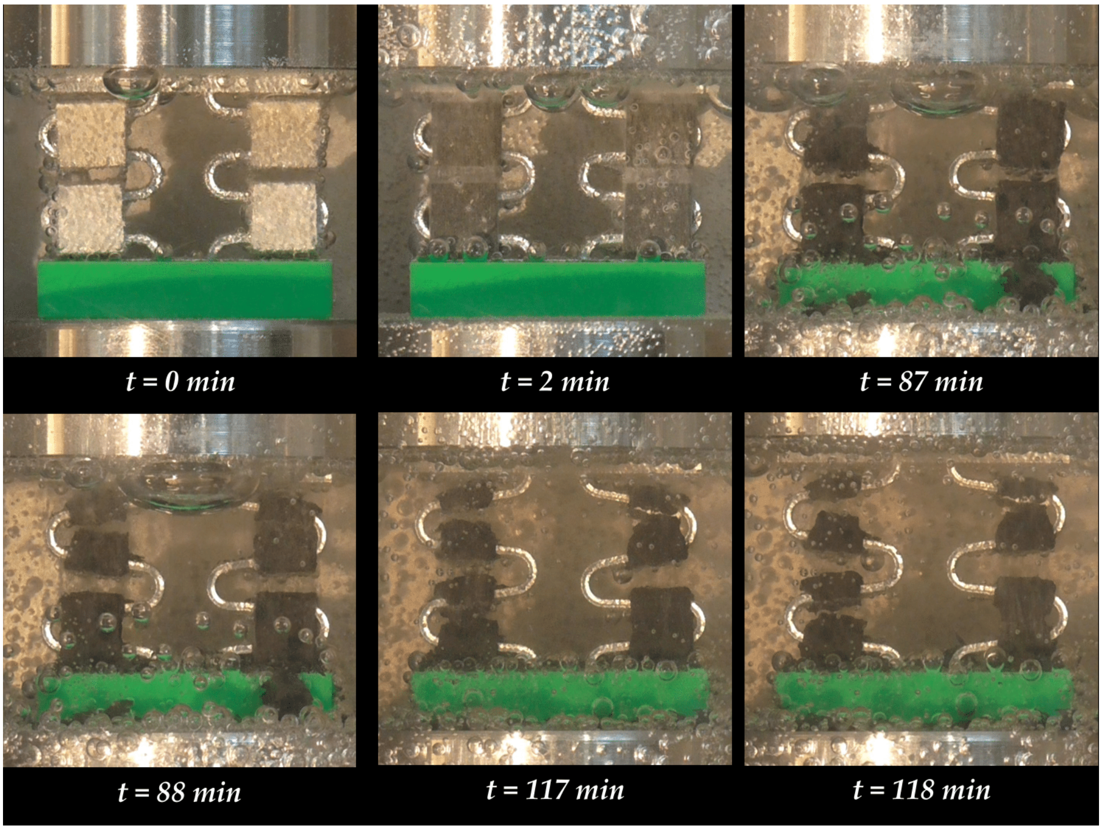

(C)

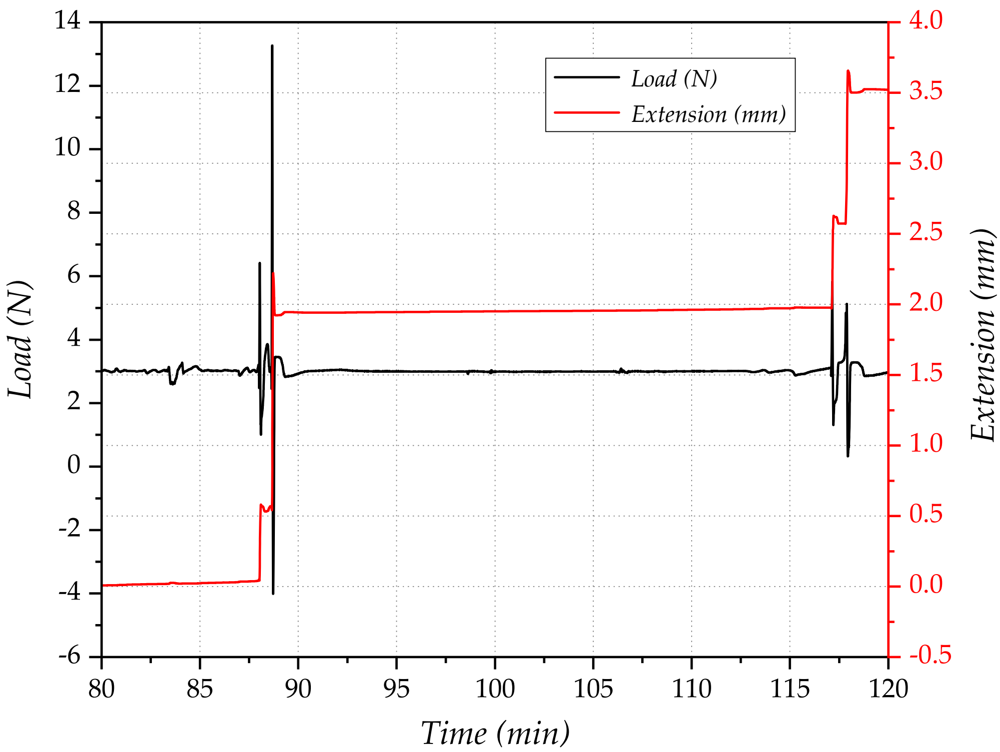

Figure 7.18: (A) Images of the components that constitute the degradable metallic actuator. The red parts represent superelastic nitinol, while the ivory-white ones correspond to WE43meo, the degradable material. (B) Shape evolution of the mechanism and (C) temporal variation of load and extension. Photographs courtesy of Dr. Muzi Li, M. Eng. Guillermo Domínguez, Prof. Dr. Jon Molina and Dr. Vanesa Martínez.

7.5. Discussion

The time-based analysis of the tests reveals how different types of anchoring affect the recovery capacity of similarly flexible elements. In Figure 7.6, Figure 7.7 and Figure 7.8, which employ serpentine, helical, and conical springs respectively, one can observe that longer test durations lead to increased residual deformation. This behavior arises from the viscoelastic nature of PETG [376] when in contact with water, reducing the shape recovery ratio and preventing the actuator from fully returning to its original shape. This outcome contrasts with the findings in the previous chapter regarding the increase in PETG viscosity when submerged in water.

In the family of actuators with a degradable frame, a one-step shape change was expected (Figure 7.1). However, actuators 1 and 2 (Figure 7.6 and Figure 7.7) exhibit a two-stage transformation. This is attributed to localized failures in the seam area during frame printing, which becomes the weakest point and is comparable to catastrophic pitting failures in metals. In smaller frames, such as in the fifth actuator, the PVA progressively deforms as it loses stiffness, allowing bulk erosion to predominate over surface damage. This observation inspired the fourth family, focused on the gradual loss of mechanical properties. In the case of biodegradable alloys, property degradation mainly occurs at the surface, unlike the relatively homogeneous erosion seen in PVA.

The second family of actuators uses interlocking components that release energy in a more stepwise fashion. Actuators 7, 8, 9, 10, and 13 illustrate a degradation process that advances in stages rather than a single abrupt shift. For bar-type anchors (actuators 14, 15, and 16), the shape change is not entirely instantaneous, leading to "steps" in the strain-time curve. A similar effect occurs in actuators 11, 12, and 17, where PETG rails restrict the motion of PVA; as the it degrades, the active structure is gradually released.

In the third family, which relies on plastic deformation in specific regions, the use of spring-shaped anchors is vital to induce the necessary strain for energy storage, especially when these springs adopt serpentine spring or straight beam configurations, as in actuators 31, 32, and 33. A key advantage of this family is the ability to fabricate all mechanism components using a multimaterial FFF process, eliminating the need for post-assembly.

The fourth family aims to enhance control over energy release by employing PVA anchors that progressively lose their mechanical properties. In Figure 7.15, which depicts actuators 44, 45, and 46, the same active element follows different shape-change paths by adjusting the anchor's thickness gradient. This phenomenon is largely driven by the ratio of exposed surface area-to-volume, which affects the PVA erosion rate, as discussed in Chapter 6. A similar approach is found in actuators 41, 42, and 43, which use the same topology for active and degradable components but adopt dimensions that increase rigidity in the degrading part, thus allowing a more controlled shape change (Figure 7.11).

More complex transformations can be achieved by combining simpler designs. Actuator 21, replicated four times, yields actuator 22, which functions like an origami. Actuator 26 transforms into actuators 27, 28, 29, and 30, and actuator 38, although from a different family, produces actuator 39. Actuator 34 progresses from a one-dimensional change to a three-dimensional one by joining two mechanisms in perpendicular planes (actuator 35). Actuator 48 evolves into 49, enabling uniform radial contraction. Actuator 14, which contains only one degradable region, can be repeated axially to create a multi-step device (actuator 15) with several degradable bars that regulate energy discharge. Notably, some mechanisms share the same shape but use different shape-morphing strategies: actuators 26 and 33 belong to the third family, whereas their counterparts 38 and 37 fall under the fourth. This design flexibility is crucial when aiming to extrapolate to high-performance materials, where certain approaches may prove unsuitable.

Actuator 47 stands out for its innovative kinematic chain. Meanwhile, actuators 48, 49, and 50 exploit the buckling of the serpentine spring, an initially undesired behavior, to create linear (actuator 50) or radial (actuators 48 and 49) expanders/contractors, using a PVA rail shaped as a serpentine spring that gradually loses stiffness and thereby directs the shape change. Twisting transformation has also been achieved in actuator 40, by combining a serpentine spring with a degradable anchor of the same topology, which allows the initial shape to be recovered.

In the Ashby diagram (Figure 7.17), comparing the shape recovery ratio with the transformation time, initially atypical values appear in actuators 9, 10, 18, 19, and 23. In actuators 18, 19, and 23, which include a degradable region subjected to plastic deformation, the flexible component accumulated permanent deformation during the "training" phase of the shape-change process, preventing it from fully returning to its original geometry. In contrast, in actuators 9 and 10 of the second family, the anchors' time-dependent resistance produces variations consistent with the inverse relationship between test duration and recovery capacity. Although this behavior may initially seem atypical, it is explained by that mechanism and becomes evident upon closer analysis.

Excluding these cases, most actuators exceed a 50% recovery, with an average near 80%, constrained by PETG's viscoelasticity, which induces plasticization during releasing stored potential elastic energy. Anchors that soften progressively exhibit the best performance, followed by biodegradable frames. The second and third families show a similar overall performance but differ in dispersion. The first family presents the smallest variability in the shape recovery ratio, whereas the fourth family demonstrates a higher spread in time, mainly due to its progressive energy release and lower associated stress relaxation.

When designing these systems, it is essential to select the transformation strategy best suited to the desired industrial application, recognizing that the active element itself can be adapted for different force-displacement behaviors, whether linear, softening, or stiffening (Figure 3.3). The experiment with alloys, presented in Figure 7.18, show recoveries approaching 98.23% thanks to nitinol's superelasticity. This confirms the feasibility of translating rapid prototyping concepts developed with polymeric materials to other AMT and high-performance materials, although the shape shift remains irreversible unless coupled again to a degradable element.

Combining degradable materials with shape-memory alloys also opens new possibilities. After the degradable segment erodes, a further shape change could be induced in the flexible component by regulating the temperature of the degrading medium. Even in PETG structures, which possess shape-memory properties, this research direction is promising [257,258]. Overall, bimaterial actuators triggered by controlled degradation show great potential in medical contexts, offering extensive opportunities for the design and additive manufacturing of medical devices that progressively evolve toward functional configurations.

7.6. Current challenges and future research

The application of shape-morphing actuators based on the controlled degradation of one of their components continues to pose significant challenges, particularly when transitioning from polymer-based prototypes to additively manufactured degradable metals. In this scenario, there is growing interest in combining nitinol, renowned for its superelasticity and shape memory properties, with zinc (Zn) and magnesium (Mg) anchors, which offer distinct degradation rates and specific mechanical characteristics.

On the one hand, nitinol can store large amounts of elastic energy and return to its original shape, making it highly suitable for designing flexible elements. At the same time, biodegradable metals such as Zn and Mg enable temporary anchoring that dissolves in a controlled manner under biological conditions, thereby releasing the energy stored in the nitinol component (or other elastic elements). However, combining these alloys raises several issues.

Differences in the degradation behavior and mechanical properties of Zn and Mg require detailed characterization because these alloys exhibit distinct performance in terms of strength, ductility, and corrosion rate. Designing an actuator that incorporates a superelastic component (nitinol) along with degradable metals demands accurate predictions of the mechanical interaction and corrosion kinetics of each material.

Integrating nitinol, Zn, and Mg through LPBF or other additive manufacturing processes requires considering the specific limitations of each technique (melting temperature, shielding gas, residual stresses, etc.), as well as DfAM, which must be adapted to the particularities of each alloy. It is also necessary to examine potential galvanic phenomena or incompatibilities among Zn, Mg, and nitinol, since the simultaneous presence of different metals in a single environment can accelerate or reduce degradation due to electrochemical effects. Additionally, when nitinol is held under compression by a Mg or Zn anchor, there is a risk that the superelastic structure may undergo creep, resulting in a loss of stored energy over extended periods.

In biomedical applications, safety and biocompatibility are paramount. The release of Mg or Zn ions must be carefully evaluated to ensure human tolerance and the absence of adverse effects. Even so, the possibility of leveraging nitinol's superelasticity alongside the biodegradability of Zn and Mg represents a highly promising avenue for temporary implants and smart medical devices.

The Finite Element Method (FEM) is pivotal in this research area, as it enables the integration of mechanical behavior and corrosion dynamics into a single model. Moreover, designing springs in various configurations, such as serpentine, helical, or conical, opens multiple pathways to control how the actuator releases its stored energy.

Ultimately, combining nitinol with Zn and Mg anchors brings together the advantages of shape memory, high deformability, and biodegradability, yet requires further advances in material characterization, FEM-based optimization, and the control of multimetal additive manufacturing. These efforts will guide the development of more versatile and reliable actuators for biomedical applications and other industrial sectors.

7.7. Conclusions

This chapter has yielded the largest available collection of shape-morphing actuators activated by degradation, to the author's best knowledge. It clearly demonstrates the feasibility of achieving multimaterial actuators capable of single-step, multi-step, and progressive shape transformations. The entire collection is documented, with the various designs grouped into four main families of actuators based on the structural configuration of the degradable anchoring elements: external frames, interlocking elements, plastically deformed regions, and anchors that gradually lose stiffness. These families enable a wide range of shape transformations, response speeds, and actuation approaches, as illustrated by the documented experiments.

In summary, a total of 50 bimaterial conceptual actuators have been designed, printed, and tested via a rapid prototyping route using polymeric combinations, conducted in parallel with advances in biodegradable metal additive manufacturing. These experiments confirm the feasibility of degradation-driven shape-shifting actuators in both polymers and alloys. Overall, most actuators exceed 50% shape recovery, with an average near 80%, although the viscoelasticity of PETG immersed in water limits complete recovery. Meanwhile, the metallic prototype combining a superelastic nitinol spring and biodegradable magnesium-based anchors achieved 98.23% recovery, showing that strategies initially developed for polymer systems can successfully transfer to higher-performance materials and processes such as LPBF.

The DfAM strategy presented here has focused on multimaterial printing, directly linking FFF (for prototyping) and LPBF (for industrial-scale production). Nevertheless, other AMT capable of processing multiple materials can also be applied to develop similar actuators, making use of a broad range of alloys, polymers, ceramics, and composites. In this way, the library can serve as a creative tool and a valuable resource for researchers and professionals interested in advanced materials and intelligent structures.

In conclusion, these results confirm the great potential of bimaterial actuators with controlled degradation to evolve into programmed functional configurations. Their proven effectiveness in both polymeric and metallic environments lay the groundwork for the development of smart biomedical devices, as well as for numerous industrial applications where shape changing and selective degradation offer decisive advantages.

8. Engineering shape-morphing medical devices for craniosynostosis and skin expansion

8.1. Introduction

Craniosynostosis is a congenital craniofacial disorder in which one or more sutures of the skull fuse prematurely [72,73]. This early fusion restricts brain growth and leads to deformities that, beyond aesthetic concerns, may compromise neurological, visual, and cognitive functions [73,77]. According to Virchow's law, cranial growth occurs perpendicularly to open sutures; in craniosynostosis, the fusion of these sutures disrupts normal skull development, resulting in deformities that vary depending on the affected suture(s) [72]. Timely diagnosis is crucial, as it allows for the implementation of therapeutic strategies to prevent complications such as increased intracranial pressure, visual impairments, and neurocognitive deficits [73,74,76].

Surgical procedures for craniosynostosis have significantly evolved. Traditional approaches include *open cranial vault remodeling*, in which the affected bones are removed, reshaped to a more appropriate shape, and securely repositioned [106]. Another method is *distraction osteogenesis*, where the sutures are gradually separated using screws, fixation pins, and extension arms, enabling incremental adjustments that stimulate osteogenesis and increase intracranial volume [10,107,108]. As a less invasive alternative, *endoscopic strip craniectomy* removes the fused suture through small incisions and is complemented by post-operative helmet therapy to guide skull remodeling [72,73]. Another technique, *spring-assisted cranioplasty*, involves implanting stainless steel springs over the affected suture to apply continuous, uncontrolled force, gradually expanding the cranial vault. However, once the desired shape is achieved, a secondary procedure is required to remove the springs [90,91].

Despite their innovative nature, these techniques present challenges such as the need for multiple interventions for implant removal, infection risks, and difficulties in achieving progressive and controlled expansion without manual adjustments or external devices [10,73,90].

In parallel, skin expanders have gained relevance in reconstructive surgery, including craniosynostosis treatments, as suture expansion also affects the surrounding skin [116,124]. Due to its viscoelastic properties, skin can undergo progressive expansion (*mechanical creep*) and generate new tissue through biological mechanisms (*biological creep*) [115,117,118]. However, traditional silicone-based inflatable expanders require weekly clinical visits over four to six months for saline or CO_2 injections, leading to patient discomfort, migration or rupture risks, and limitations in customizing expansion force [131,137].

Within this context, the emergence of "smart" implants that take advantage of controlled degradation to generate a gradual expansion is seen as a promising alternative both in the treatment of craniosynostosis and in reconstructive procedures. These implants can be made from degradable metals or polymers and are designed with geometries and materials that degrade at different rates. As their temporary anchors or structural frames disintegrate, stored elastic energy is released, driving the planned structural displacement. Although degradation is slower than other activation mechanisms (shape-memory or electroactive materials), this characteristic aligns with biological growth and bone remodeling or soft tissue regeneration. Additionally, this approach enables progressive expansion, reducing the need for additional surgeries for device adjustment or even removal [10,137].

Building on the creativity promotion framework introduced in Chapters 5 and 7, where an ontology for shape-morphing actuators was proposed and 50 shape-morphing concepts were generated based on the degradation of a component, this study applies the same methodology to the design of multimaterial medical devices fabricated via additive manufacturing, capable of shape morphing through degradation. This approach offers biomedical advantages by using resorbable and biocompatible materials, eliminating the need for implant removal.

This research focuses on the design and validation of two major applications of controlled-expansion degradable implants: 1) springs inspired by current spring-assisted cranioplasty technique, combining with the benefits of bone distractors to regulate suture expansion; 2) self-expanding skin expanders for soft tissue generation in reconstructive procedures, avoiding the complications of traditional implant.

For both applications, serpentine- and conical-shaped spring implants are proposed. These structures can store energy and release it progressively while enabling geometric transformations from a smaller to a larger dimension. Additionally, degradable anchors are considered to restrict or allow movement based on their immersion time in the degrading medium (body fluids, water, etc.).

To validate the functionality of these systems, specific test benches were developed. In the case of craniosynostosis, the medical imaging of a minipig was used to create an anatomical model simulating cranial vault changes. Multimaterial prototypes were manufactured using rapid prototyping techniques with PETG and PVA, evaluating their expansion capabilities in a controlled environment. The ultimate goal is to transfer these design strategies to metallic or polymeric materials with metallic reinforcements, ensuring optimal resorption profiles in the human body and expanding their potential clinical applications.

This chapter sets the groundwork for the development of adaptative implants and expanders to contribute to the treatment of craniosynostosis and tissue expansion, offering less invasive solutions with fewer surgical interventions. Throughout the document, the advantages and challenges of programmed degradation-based approaches are analyzed, while the experimental validation seeks to demonstrate the feasibility of a new generation of biodegradable medical devices capable of transforming in synchrony with the patient's physiology. In doing so, this research establishes a precedent for future developments in biomedical engineering and opens possibilities for adaptation in various industrial and technological applications.

8.2. Materials and methods

8.2.1. Test bench development

To evaluate the performance of various degradation-activated actuators in craniosynostosis applications, specific test benches were developed based on medical imaging data. The model used for the test bench was derived from computed tomography (CT) scan of a six-week-old minipig, provided by the surgeons of the Gregorio Marañon Hospital and selected for its physiological similarities to human bone regeneration processes. Minipigs exhibit a bone metabolism and regeneration rate of 1 - 1.5 mm/day, closely resembling that of humans [413]. By six months of age, their physiological growth is complete, and at four weeks old, their dental development corresponds to that of a 9 - 12-month-old human infant. Moreover, as demonstrated by Sanger et al. [414], minipigs are capable of tolerating craniotomies, further validating their suitability as an animal model for this study.

CT scan was obtained with slice thicknesses of 0.7 mm in the axial plane and 0.194 mm in the coronal and sagittal planes, producing images with a resolution of 768 × 768 pixels. Image segmentation was performed using 3D Slicer 5.6.2 (https://www.slicer.org), employing tools such as thresholding, grow from seeds, level tracing, smoothing, painting, and erasing. A window value of 304 Hounsfield units was used, following [415]. The average Hounsfield unit value of the segmented volume was 735, falling between cortical and trabecular bone, consistent with the bone development of a 6-week-old minipig. The segmented 3D model was exported as an STL file, and errors were corrected using Meshmixer 3.5 (Autodesk Inc., Mill Valley, CA, USA) to obtain the final model (Figure 8.1A).

The 3D cranial model was scaled up by a factor of 1.6 to enable the manufacturability of shape-morphing implants using Fused Filament Fabrication (FFF) technology. A standard fronto-orbital advancement procedure was emulated to treat metopic and coronal synostoses, involving the repositioning of the frontal bones and supraorbital bar [103,416]. The model was imported into NX 2206 (Siemens PLM Solutions), where osteotomy planning and cutting guide design were performed. A virtual osteotomy was carried out to separate fused sutures and create a 3 mm gap between bones. The aim was to use shape-morphing devices to double this gap to at least 6 mm.

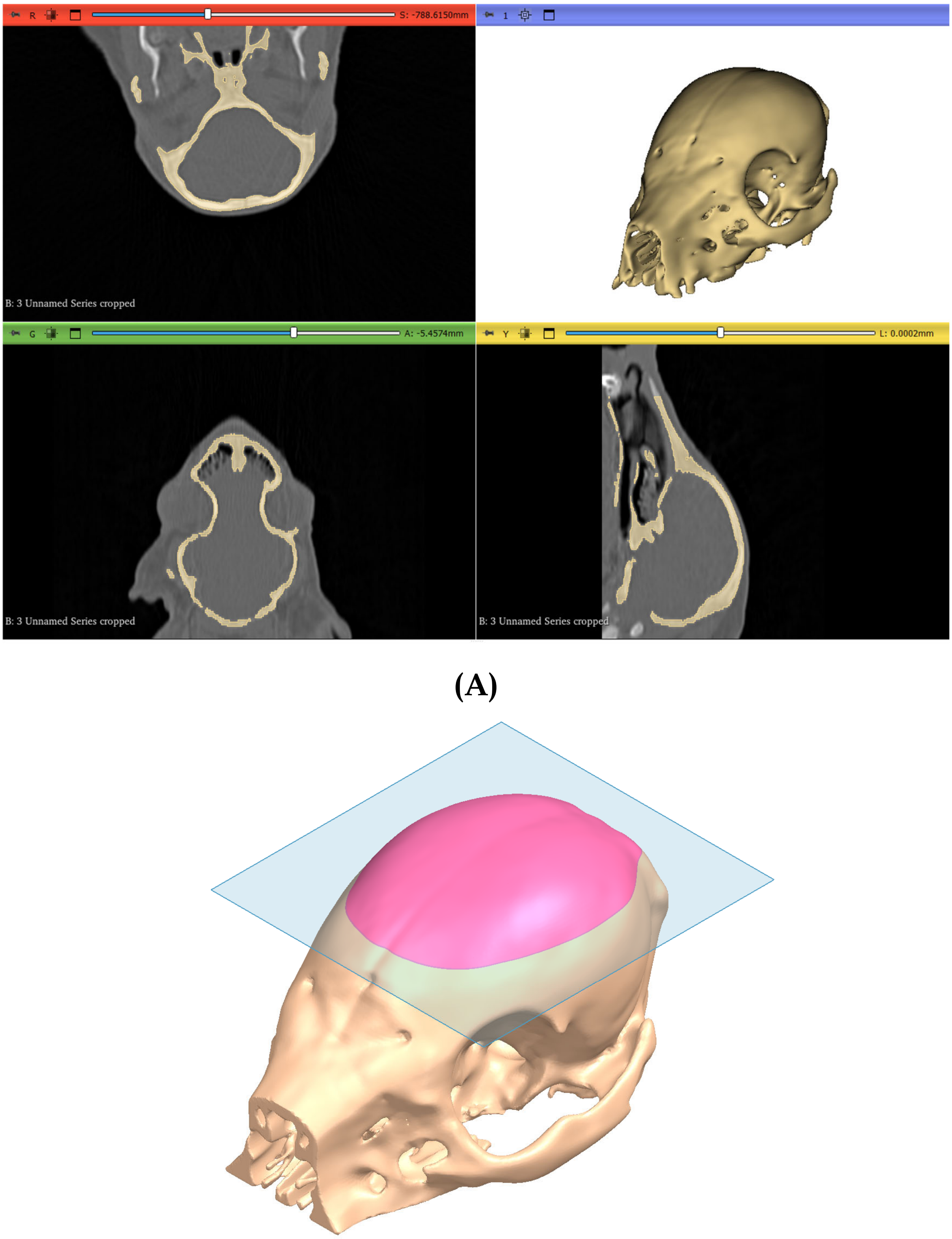

(A)

(B)

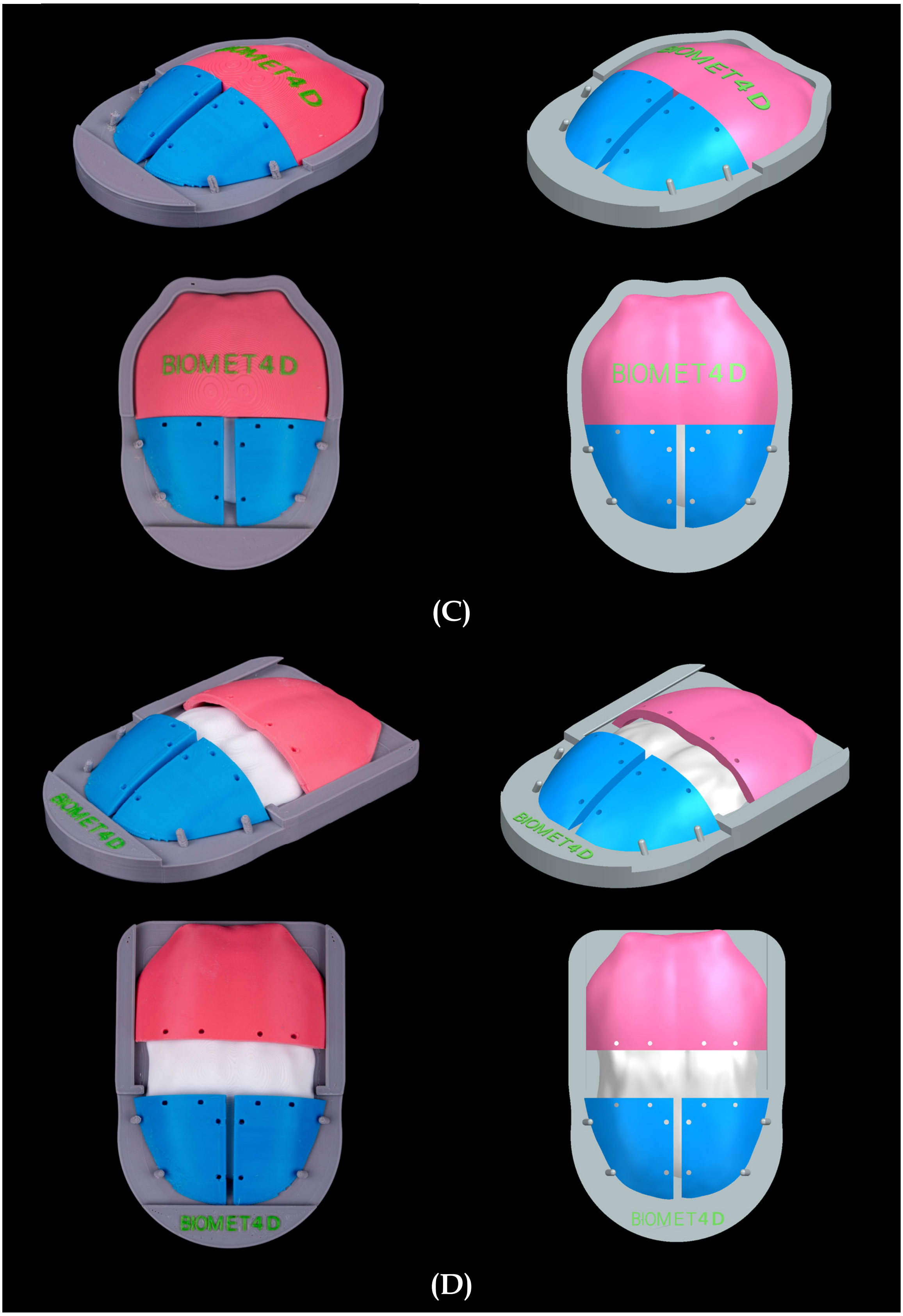

Figure 8.1: (A) Segmentation of the minipig's cranial model and (B) design of test benches based on the upper part of its skull to simulate (C) metopic and (D) metopic-bicoronal suture conditions. Photographs courtesy of Álvaro Troyano and Dr. Adrián Martínez. Special thanks to Dr. Santiago Ochandiano for the mini-pig CT.

To evaluate the performance of the shape-morphing craniosynostosis springs, two test benches were developed. The first was designed to assess the implants' ability to distract the metopic suture, and the second to evaluate tridimensional remodeling by distracting both the metopic and coronal sutures, simulating a bicoronal defect caused by syndromic craniosynostosis. Both test benches used only the upper portion of the cranial model (Figure 8.1B). To achieve the hinged effect for metopic expansion, 70° inclined stops were placed to allow the frontal bones to rotate without displacement, replicating the expansion observed in children treated with spring-assisted devices [250] (Figure 8.1C and D). For the coronal defect, a rear-open slide guide was added to accommodate and direct the expansion of the posterior cranium (Figure 8.1D).

The test benches were fabricated using the Bambu Lab X1 Carbon Combo printer (Bambu Lab, Austin, TX), capable of printing with four filaments simultaneously via its Automatic Material System and equipped with a 0.4 mm hardened steel nozzle. Frontal bones were printed using FLEX 93A filament in blue, while the remaining components were printed in PLA of various colors (gray, pink, green and white). All filaments were supplied by Smart Materials 3D (Pol. Ind. El Retamar, c/ Tomillo 7, 23680 Alcalá la Real, Jaén, Spain) as 1.75 mm diameter monofilaments.

As the test bench operates submerged in water, the PLA parts were designed with eight perimeters, two top layers, and no bottom layers to allow water access. A 15% gyroid infill was used, with the remaining print settings following the "Strength" configuration of the Bambu Studio slicer (Bambu Lab, Austin, TX), featuring a 0.2 mm layer height. FLEX 93A parts were printed with a speed of 30 mm/s for all layers and infill, a travel speed of 50 mm/s, and a fully dense structure built using only perimeters.

For the skin expansion test bench, Autodesk Fusion 360 (Autodesk Inc., San Rafael, CA, USA) was used to design: (1) a base flange, (2) an intermediate cylinder with fixation slots, and (3) a circular base with four perforations to allow water entry (Figure 8.2). These components were also produced using the same printer and blue PLA filament. Configurations were consistent with the cranial test bench, except those components (1) and (2) were printed using perimeters only, while part (3) was divided into two sections: (3.1) was printed using perimeters, and (3.2) with a 32% gyroid infill.

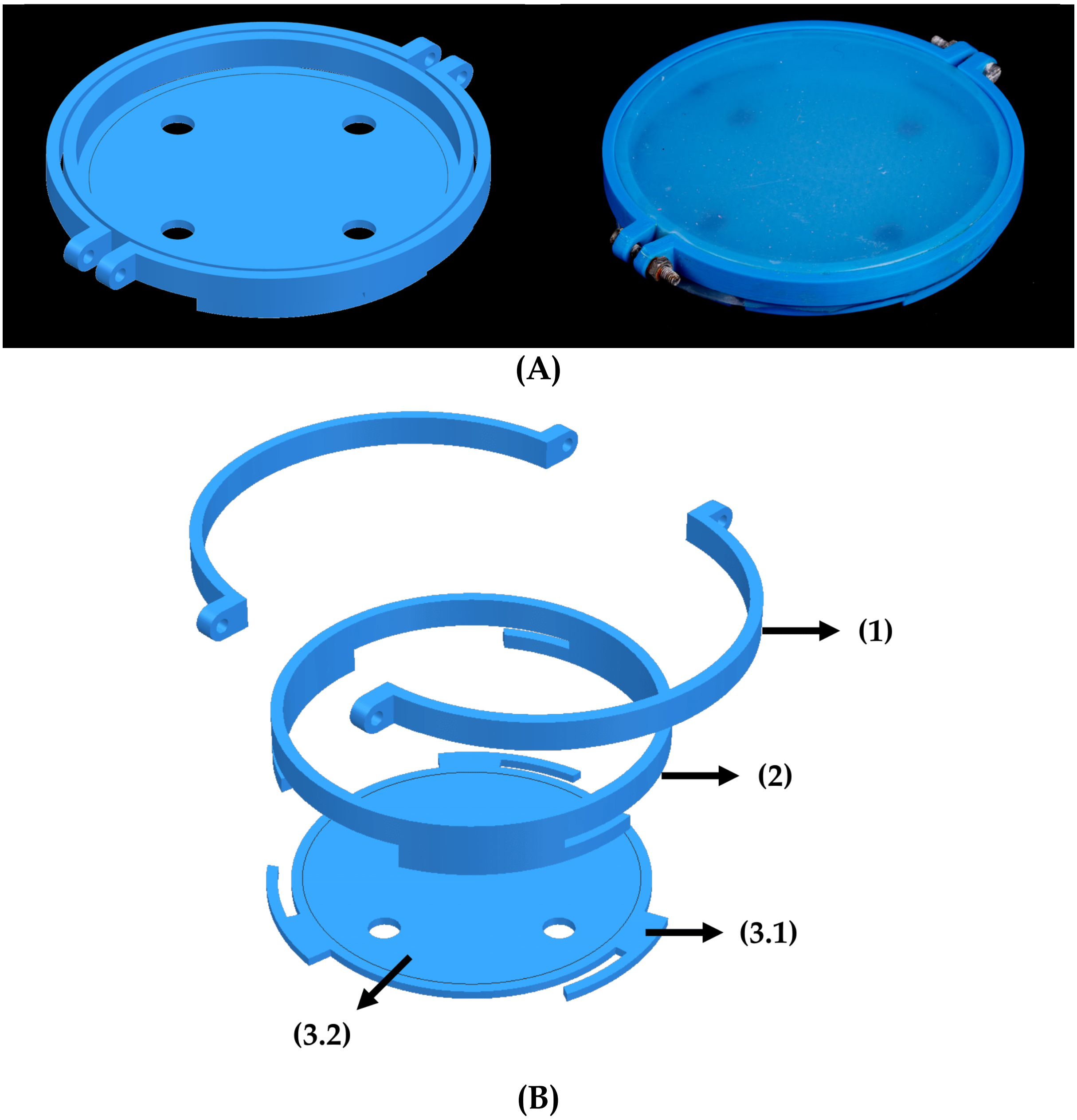

Figure 8.2: (A) Skin expansion test bench design and (B) its components. Photographs courtesy of Álvaro Troyano. Special thanks to Pedro Ortego for his invaluable help in the development of the silicone membranes.

Artificial skin membranes were created to simulate the mechanical properties of epidermal and dermal tissue during expansion. PlatSil Gel-0030 (Feroca, Madrid, Spain), a translucent platinum silicone was used for this purpose. Silicone was prepared by mixing equal parts of components A and B, following the manufacturer's instructions. The mixture was poured into a custom PLA mold with a diameter of 15 mm and a wall thickness of 1.2 mm. After curing for 4 hours at 25 °C, thin silicone discs with a uniform thickness of 0.5 mm were obtained. These discs were subsequently integrated into the test bench assembly, serving as the expandable membrane to evaluate the devices' performance in stretching artificial tissue.

8.2.2. Design and fabrication of shape-morphing medical devices

The design of shape-morphing implants for cranial bone distraction and skin expansion was guided by the most promising actuators identified in Chapter 7. These actuators were adapted and dimensionally modified to suit the specific requirements of the developed test benches. For craniosynostosis applications, actuators 5 and 31 were customized to create two active components: a serpentine and an omega-shaped springs. These elements were designed to store and release elastic energy upon compression, with the omega-shaped spring mimicking current solutions used in maxillofacial practice (Figure 2.5) [92,93,100]. Degradable anchors, serving as passive components, included degradable frames and springs that enabled a gradual or stepwise energy release. These devices were engineered to maintain the initial 3 mm gap defined during virtual osteotomy and progressively expand it by 3 mm or more as specific components gradually degraded in a controlled manner.

For skin expansion applications, actuators 13 and 42 were adapted using conical and auxetic serpentine springs with interlocking and softening biodegradable anchors respectively. Additionally, one non-telescopic mechanism was developed in collaboration with Dr. Adrián Martínez and inspired by interwoven wire patterns resembling wicker basket structures. In this case, degradable components passed through the woven fibers to stabilize the dome-like structure in its compressed state. To standardize performance comparisons, all skin expansion devices were constrained to fit within a 56 × 56 × 25 mm^3 cube, ensuring consistent evaluation of the silicone membrane expansion under equivalent conditions.

All actuators were designed using Autodesk Fusion 360, except for the wicker-inspired mechanism, which was generated using a Python script to define a unit cell geometry. This geometry was then imported into nTop (nTopology Inc., New York, NY, USA) to create a conformal design that resulted in a structure resembling a wicker-based mechanism following the methodology described by Martínez Cendrero [417].

The devices were fabricated using a Bambu Lab X1 Carbon Combo printer, employing PETG and PVA filaments (1.75 mm diameter) sourced from Smart Materials 3D. PETG was used for energy-absorbing components, while PVA was employed for degradable elements. In all cases, a mono material approach was used to produce flexible and degradable parts, which were then assembled to create a multimaterial implant/actuator. Printing parameters were consistently applied across all samples: a layer thickness of 0.2 mm, a printing speed of 50 mm/s, a bed temperature of 70 °C, and nozzle temperatures of 220 °C and 240 °C for PVA and PETG respectively. All structures were printed exclusively using perimeters with 100% density, strategically oriented on the printing platform to avoid the use of supports. Additionally, the seams were placed in areas of minimal mechanical stress. In the case of the auxetic spring, it consists of two caps and three helical springs, which were printed separately and assembled to form the actuator.

For the wicker-based mechanism, which could not be fabricated with FFF technology, a Phrozen Sonic Mighty 4K LCD printer (Phrozen 3D Tech Co, Ltd, Hsinchu City, Taiwan) was used with Phrozen Aqua Gray 4K photopolymer resin (Phrozen 3D Tech Co, Ltd, Hsinchu City, Taiwan). The printing process involved a layer exposure time of 2.4 seconds, a layer height of 100 μm, and post-curing for 3 minutes. Masks for the printer and slicing configurations were prepared using Chitubox software (Chitubox, Zhongcheng Future Industrial Park, Hangcheng Avenue, Baoan District, Shenzhen, Guangdong, China 518128).

Table 8.1: Summary of shape-shifting implants for the treatment of craniosynostosis and skin expansion triggered by degradation. The red parts correspond to the pieces made of PETG, the ivory-white ones to the pieces made with PVA and the grey ones to those produced using the light-curing resin Phrozen Aqua Gray 4K.

Shape-morphing implant	**Abbrev.**	**Flexible/active component**		**Degradable component**	
Craniosynostosis springs	C1	Serpentine spring	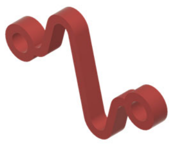	Two frames of 0.8mm thickness	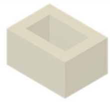
	C2			One frame of 0.8mm-thickness and another of 1.2mm-thickness	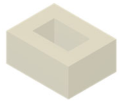
	C3			Deformed biodegradable serpentine spring	
	C4	Omega-shaped spring		Frame of 1.2mm thickness	
	C5			Deformed biodegradable serpentine spring	
Skin expander devices	SE1	Conical spring	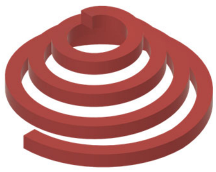	Frame of 1.6mm-thickness	
	SE2			Anchoring elements from 3.2 to 5.2 mm thickness in 0.4mm intervals	
	SE3	Auxetic spring	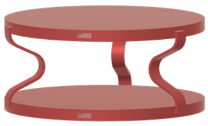	Deformed biodegradable serpentine spring	
	SE4	Wicker-based mechanism	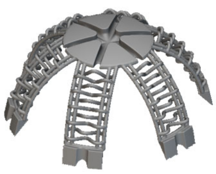	Degradable bar of 1.6x1x80mm^3	

8.2.3. Experimental validation

To evaluate the mechanical properties of the flexible structures, compression tests were performed using an Instron 5966 mechanical testing machine (Instron, Norwood, Massachusetts, USA) equipped with a 100 N load cell. The experimental protocol consisted of a loading and unloading cycle at a constant crosshead speed of 2 mm/min. A LVDT sensor with a maximum travel of 50 mm was employed to ensure accurate displacement measurements. Two samples of each flexible structure were tested. The deformation exerted during the loading cycle corresponded to the strain applied during energy storage to produce shape transformation. This approach enables the determination of the potential elastic (strain) energy contained in the implant, which is subsequently released during its metamorphosis.

In parallel, the implicit Finite element method (FEM) was used to analyze the mechanical behavior of the actuators and assess the feasibility of accurately estimating the reaction force. The simulations were conducted using Ansys Workbench 2022 R2, employing the Transient Structural module. The numerical model was developed based on the PETG quasi-isotropic mechanical properties, obtained from the mechanical characterization described in Chapter 6. The only implant that has not been simulated is the wicker-based mechanism, as no mechanical properties were available to characterize its behavior.

To realistically simulate the compression of the structures, a uniform mesh of quadratic hexahedral elements was generated, with partitions applied to the volume to minimize distortions (Figure 8.3A). Rigid planes were defined as contact surfaces, enabling controlled compression and release. In the case of the conical spring, a specific reference plane was introduced at the base to accurately measure the reaction force. Contact interactions between the actuators and the planes were modeled using perfectly rough frictional contact boundary condition.

Since the actuators undergo significant deformations, the large displacement option was activated, incorporating the elastoplastic properties of PETG, with an elastic modulus of 1790.884 MPa, a Poisson's ratio of 0.38, a density of 1.27 g/cm^3, and the stress-strain plastic curve presented in Figure 8.3B. The bases of all mechanisms were fixed, and the compression plane displacement was defined as the boundary condition. In each case, both the reaction force at the fixed support and the displacement of the actuator at the contact point with the compression plane were measured.

To facilitate the simulation of the auxetic and omega-based springs, geometric modifications were introduced. In the case of the auxetic spring, a hole was added to the cap and base to simplify mesh generation. For the omega spring, attachment elements were added, and out-of-plane parts were removed to better mimic the experimental compression test, which will be analyzed in more detail later (Figure 8.3A).

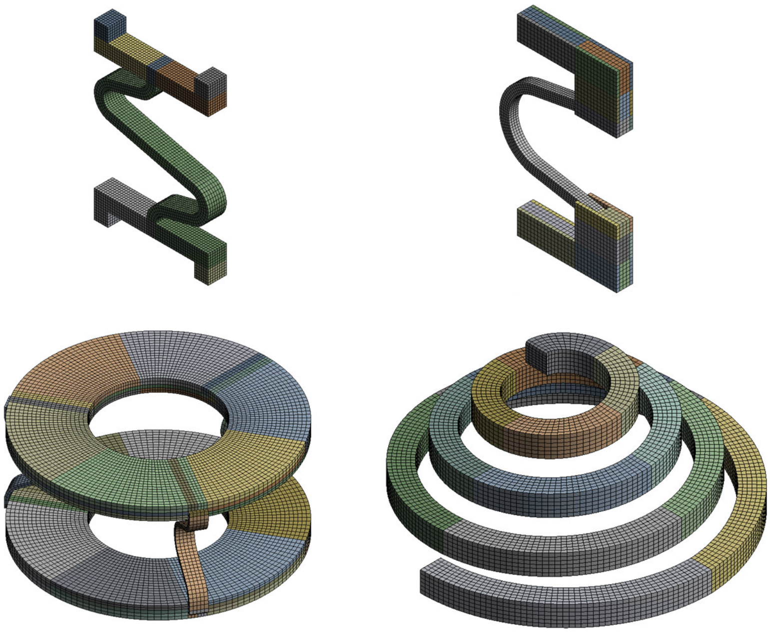

(A)

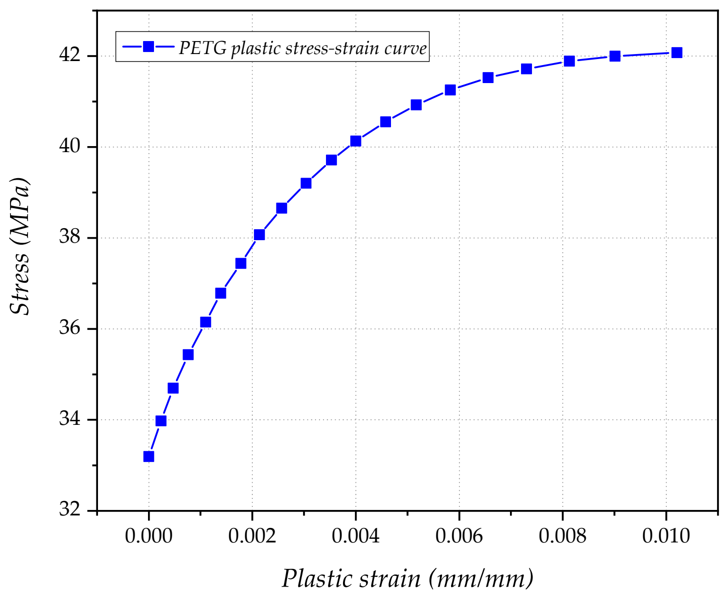

(B)

Figure 8.3: Meshes of the flexible structures composing the shape-morphing medical devices, obtained from ANSYS. The different colors correspond to the volume partitions applied to obtain a uniform mesh. (B) Plastic stress-strain curve of PETG printed with the quasi-isotropic infill pattern, characterized in Chapter 6.

To investigate the shape-morphing behavior of smart shape-morphing implants triggered by degradation, high-resolution optical sensors with a 12.0-megapixel resolution, an f/1.5 aperture, and optical image stabilization were employed. The specimens were photographed at regular intervals of either one or ten seconds, depending on the degradation rate of the anchoring elements. To ensure detailed tracking from multiple angles, two strategically positioned cameras captured their shape change: one recording the side and other the top views. This setup enabled a precise temporal monitoring of the implant's metamorphoses (Figure 8.4). To quantitatively analyze the shape change of every shape-morphing implant, the captured images were processed using ImageJ [254].

To maintain consistent experimental conditions and prevent localized degradation, the samples were carefully placed at the center of a glass container measuring 200 × 150 × 50 mm³. The container was filled with 800 mL of water, which was maintained at a constant temperature of 25 °C throughout the experiment. Complete submersion of the samples ensured uniform exposure to the degradation medium, allowing for reliable and reproducible results.

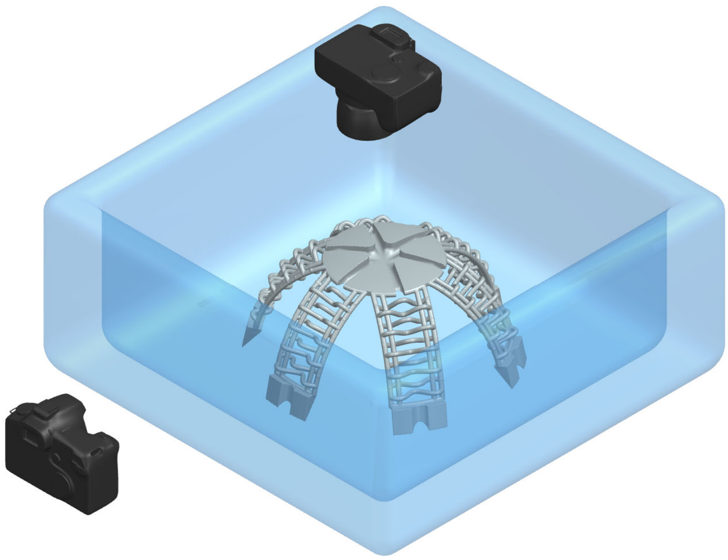

Figure 8.4: Experimental setup for the degradation test and camera positioning in top and side views to monitor the metamorphoses of degradation-activated implants for craniosynostosis and skin expansion treatment.

8.3. Results

8.3.1. Mechanical performance of shape-morphing devices

As mentioned in the previous chapter, the mechanical behavior of the active structure is fundamental, since the energy stored during the training of the device causes a change in shape when its anchoring elements degrade. Through the compression test, it is possible to calculate this absorbed energy by means of the area under the force-displacement curve, thus determining the amount of energy that will be released during degradation. Furthermore, analyzing the actuator's mechanics allows a prediction of how this force will act on the surrounding tissue with which the implant will interact throughout its lifespan.

Figure 8.6 to Figure 8.10 illustrate the force-displacement curves of the 4D printed flexible actuators, together with comparative photographs of the experimental tests and the FEM simulations. It can be seen that the active structures exhibit two different behaviors: some, such as the conical spring and the wicker-based structure, show a non-linear response with increasing stiffness, while others, such as the serpentine spring, the auxetic and the omega-shaped, exhibit a linear behavior with an almost constant spring rate.

Regarding the energy stored in the shape-morphing medical devices (Figure 8.5), in the case of craniosynostosis, the omega-shaped spring stores the greatest amount of strain energy. On the other hand, for the skin expander, the conical spring and the wicker-based structure show similar performance, although the auxetic spring stores the most energy. However, these active mechanisms are not completely elastic, both the tests and the simulations show the presence of permanent deformation, especially in the auxetic spring and the wicker-based structure. This implies that not all the elastic energy will be converted into kinetic one to induce the actuator's shape shifting, which introduces an irreversibility that must be considered in the design phase.

In this context, FEM simulations have proven to be an accurate tool for estimating the loading curve, although they present differences in the unloading due to the permanent deformation of the mechanisms. This is explained by the use of mechanical properties based on quasi-isotropic infill orientation (from Chapter 6), instead of the properties of the perimeters used in the production of the components. Even so, these simulations are valuable in the design process, as they enable the optimization of elastic energy storage capacity while minimizing residual deformation. This not only improves device efficiency but also reduces the need to manufacture and test multiple prototypes, lowering the costs and time associated with this iterative process.

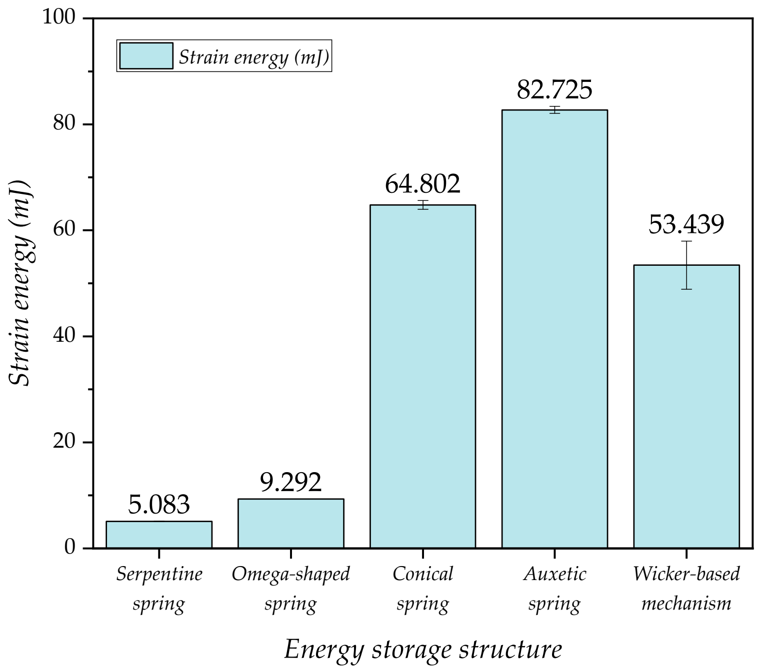

Figure 8.5: Mean strain energy of degradation-activated flexible implants, with error bars indicating standard deviation.

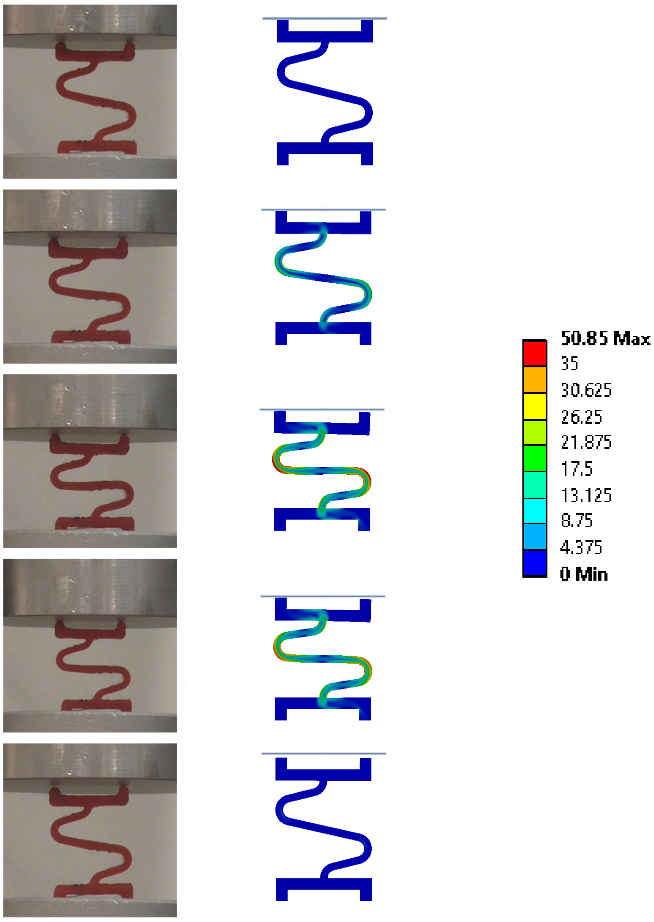

(A)

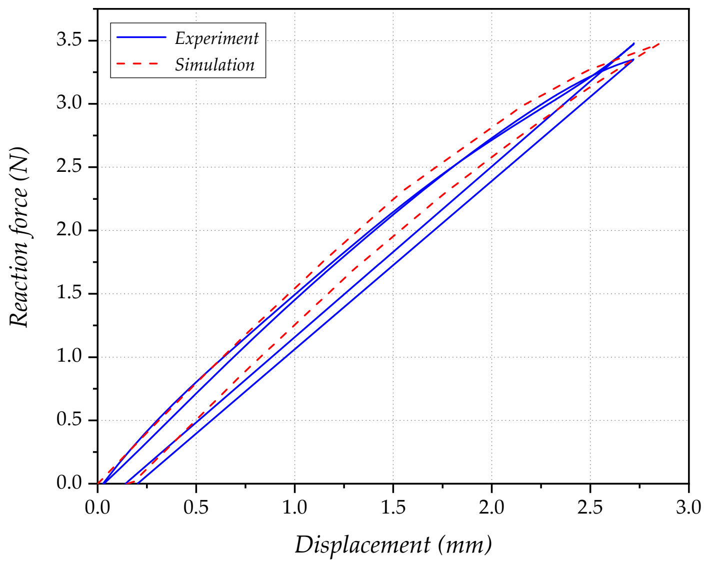

(B)

Figure 8.6: (A) Photographs of the serpentine spring during compression test, alongside the elastoplastic simulation performed in ANSYS, representing the von Mises stress field. (B) Force-displacement graph comparing simulation results with experimental data. Special thanks to Dr. Vanesa Martinez for her invaluable help in conducting the tests.

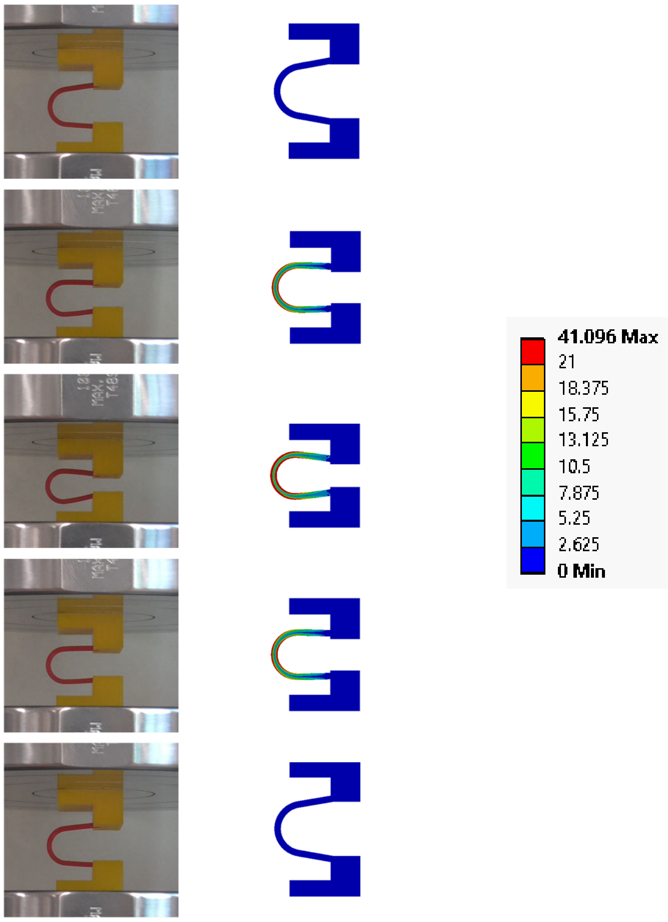

(A)

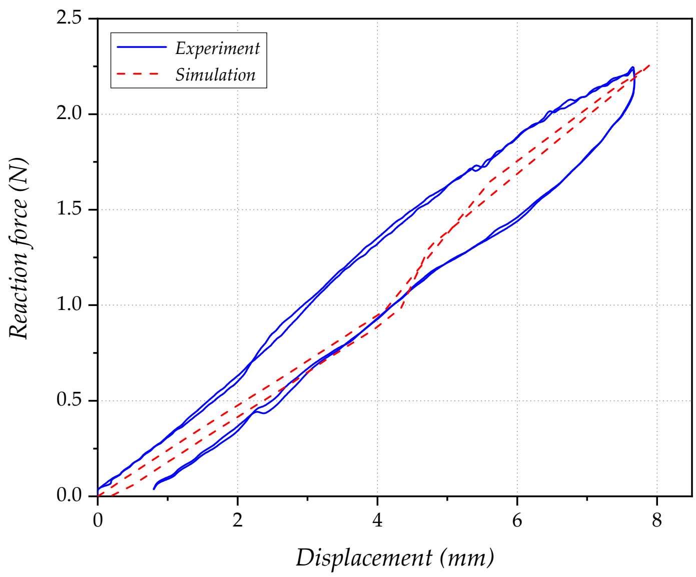

(B)

Figure 8.7: (A) Photographs of the omega-shaped spring during compression test, alongside the elastoplastic simulation performed in ANSYS, representing the von Mises stress field. (B) Force-displacement graph comparing simulation results with experimental data. Special thanks to Dr. Vanesa Martinez for her invaluable help in conducting the tests.

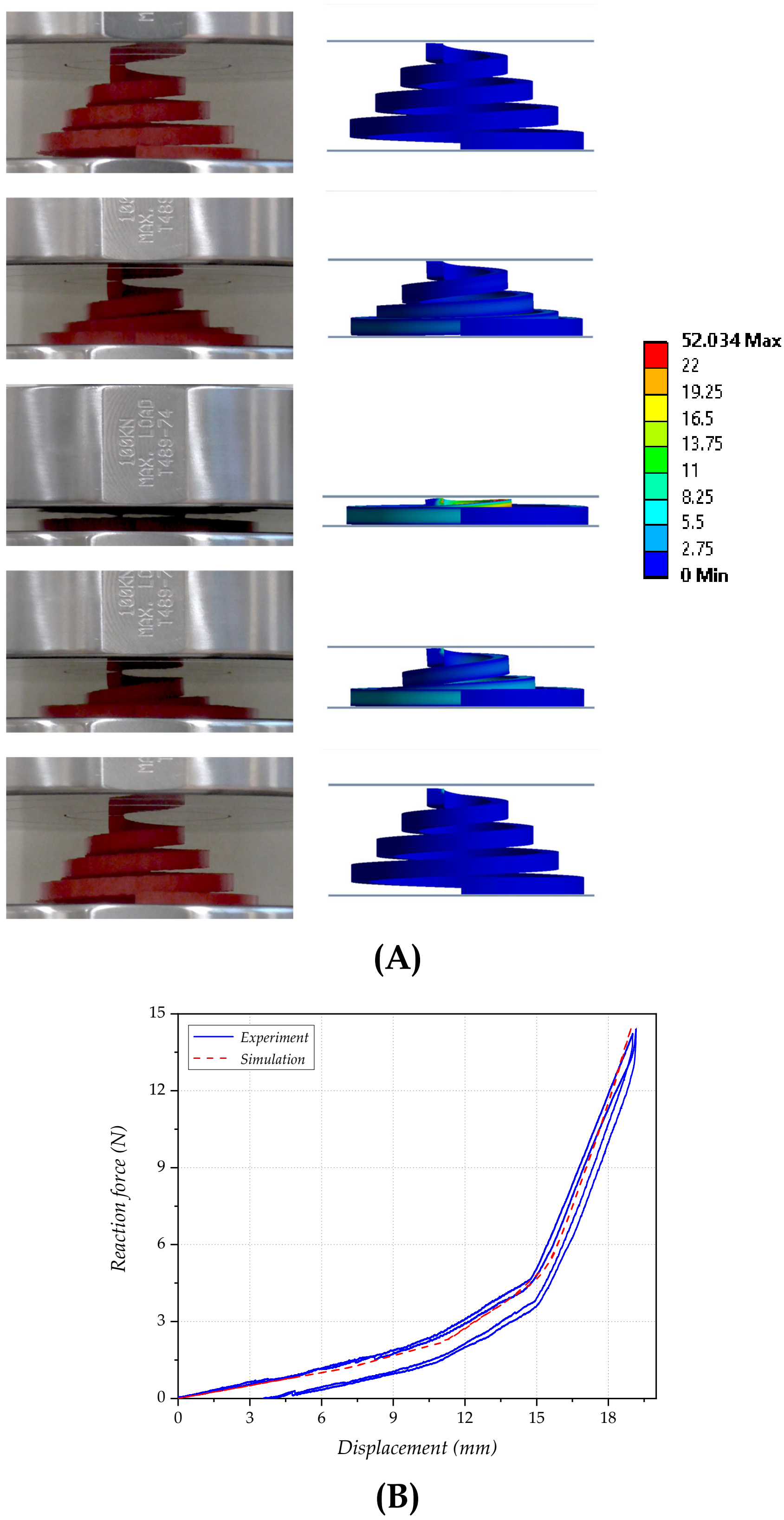

Figure 8.8: (A) Photographs of the conical spring during compression test, alongside the elastoplastic simulation performed in ANSYS, representing the von Mises stress field. (B) Force-displacement graph comparing simulation results with experimental data. Special thanks to Dr. Vanesa Martinez for her invaluable help in conducting the tests.

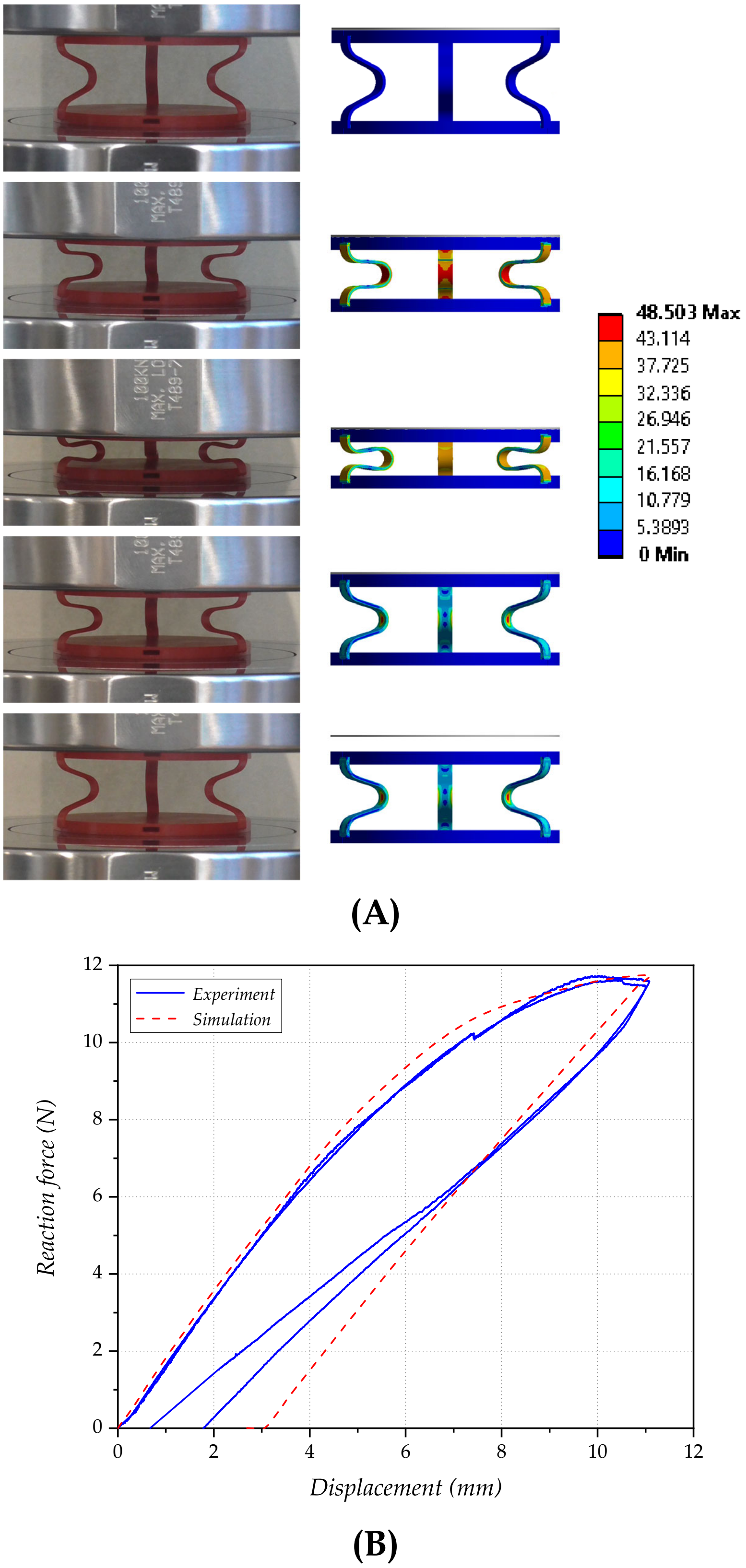

Figure 8.9: (A) Photographs of the auxetic spring during compression test, alongside the elastoplastic simulation performed in ANSYS, representing the von Mises stress field. (B) Force-displacement graph comparing simulation results with experimental data. Special thanks to Dr. Vanesa Martinez for her invaluable help in conducting the tests.

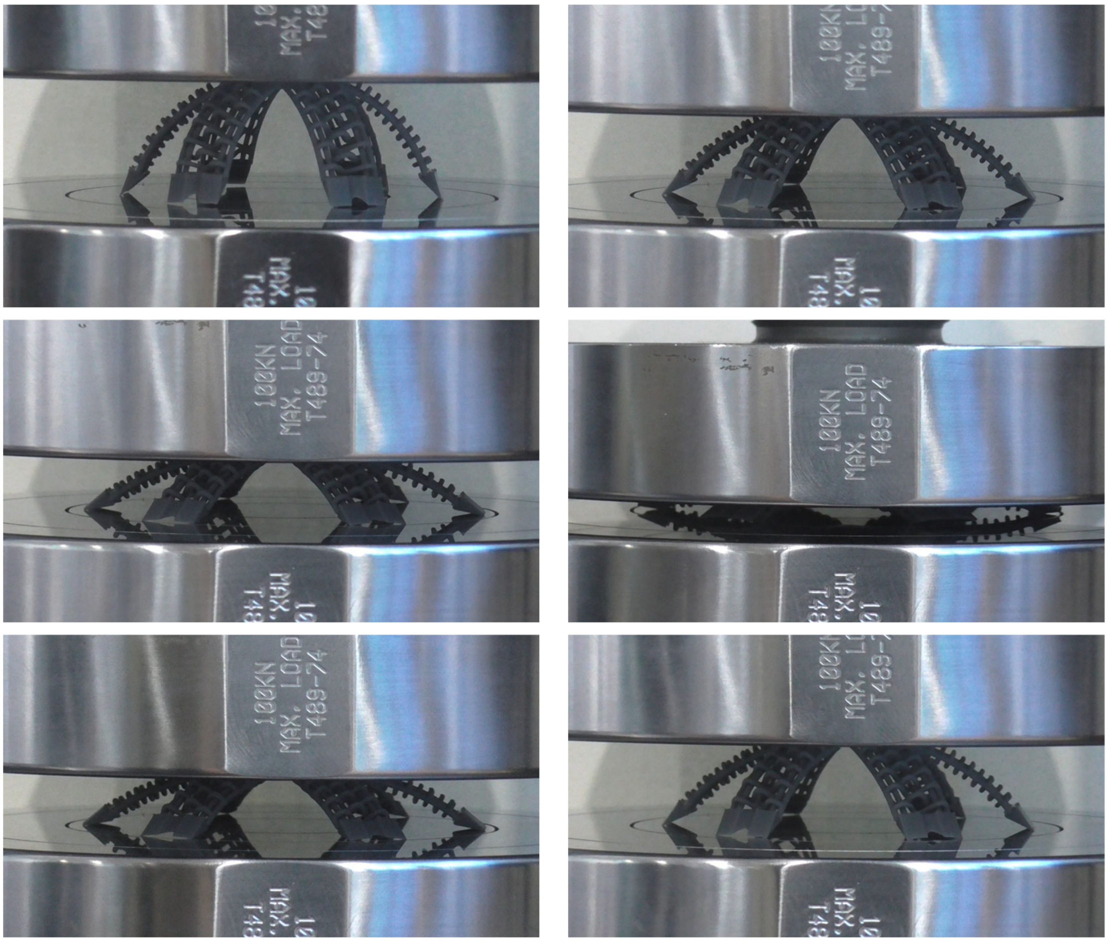

(A)

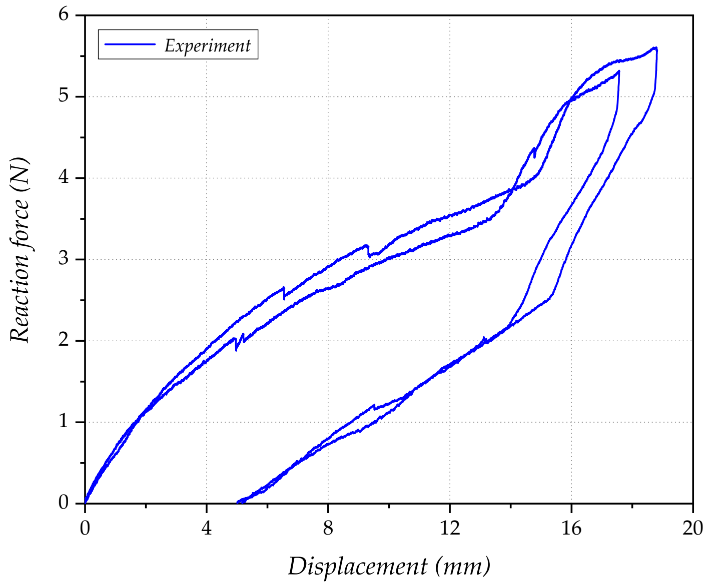

(B)

Figure 8.10: (A) Photographs of the wicker-based mechanism during compression test. (B) Force-displacement graph comparing simulation results with experimental data. Special thanks to Dr. Vanesa Martinez for her invaluable help in conducting the tests.

8.3.2. Degradable performance of shape-morphing devices

To ensure fair comparison conditions, the primary parameter assessed was the perpendicular distraction achieved at the suture, measured in millimeters over time (Figure 8.11). Results show that, despite using identical active structures, the type of degradable anchors significantly influenced the release of stored elastic strain energy during shape morphing.

Theoretically, devices with the same active components should achieve equivalent distraction. However, variations were observed due to the viscoelastic relaxation of the PETG in water, which is discussed in Chapter 6. Over time, the polymer's elastic modulus decreased, dissipating the stored energy and, consequently, the distraction achieved [376,386]. A clear inverse relationship between distraction and time was identified, with greater distraction occurring over shorter periods, and vice versa which was also demonstrated in the degradation-activated 4D mechanism library developed in Chapter 7.

Most devices exhibited linear distraction behavior, which aligns with the objective of achieving controlled and progressive expansion. However, devices with degradable frames (C1, C2, and C4) designed for stepwise distraction, based on the catastrophic failure of the anchors, exhibited distinct behaviors. For instance, the serpentine spring device with a 0.8 mm frame performed differently from one with a combination of 0.8- and 1.2-mm frames. Longer testing times translated to prolonged distraction periods, clinically relevant for avoiding re-synostosis during craniosynostosis treatment.

Thin degradable frames facilitated water penetration between PVA layers, accelerating bulk erosion and resulting in progressive expansion rather than stepwise failure (C1 and C2). For thicker frames, as in device C4, delayed softening enabled catastrophic failure, first in one plane and subsequently in the other. This behavior produced the two-step pattern observed in Figure 8.11 and Figure 8.16. Despite the failure, surrounding materials restricted spontaneous opening, ensuring a gradual expansion. This phenomenon has been described by surgeons who employ the spring in maxillofacial surgery procedures where expansion is not controlled [94].

An alternative anchoring strategy involved using a degradable spring with greater stiffness than the active element (C5 implant). As the degradable material eroded and its elastic modulus decreased, the anchoring stiffness was reduced, allowing the flexible structure to gradually release stored energy. This approach ensured a linear distraction behavior, which depended on both the initial stiffness of the degradable spring and its degradation rate. To design such springs, finite element analysis (FEA) was used to determine the geometry in its deformed state. This ensured pre-compression of the active structure, enabling it to store energy and release it progressively (Figure 8.17).

The C3 implant follows the same strategy; however, instead of assembling the deformed spring with the flexible component, it is implanted between the flexible structures along the metopic suture, an alternative strategy that can be implemented by physicians during surgery (Figure 8.15). This modular approach enables the regulation of stored energy by adjusting the active components, as well as controlling the shape-morphing implant’s lifespan and distraction rate through the selection of degradable elements. This design strategy surpasses the 3mm expansion threshold between sutures, making it extremely suitable for this clinical scenario. However, their lifetime is shorter than other implant designs.

Tests conducted using the metopic suture bench demonstrated the feasibility of controlled distraction. To explore the potential for tridimensional remodeling in cases of syndromic craniosynostosis, additional tests were performed on a model with metopic and bicoronal sutures. Springs C1 and C3 were placed at each suture, respectively. Results reveal that the perpendicular movement at each suture influenced the other due to their distinct motion types: rotational separation at the metopic suture and translational movement at the coronal suture (Figure 8.12 and Figure 8.18).

Friction between the parietal bone and the test bench introduced delays in both mechanisms. Initial energy release was insufficient to achieve simultaneous distraction, particularly for the bicoronal suture, where an additional spring was added for symmetry. Despite these challenges, the study demonstrated that combining springs along different sutures can achieve controlled cranial remodeling, a promising solution for syndromic craniosynostosis.

Images of shape changes over time for devices C1, C2, C3, and C4, as well as the tridimensional remodeling with combined C1 and C3 devices, are shown in Figure 8.13, Figure 8.14, Figure 8.15, Figure 8.16, Figure 8.17 and Figure 8.18 respectively.

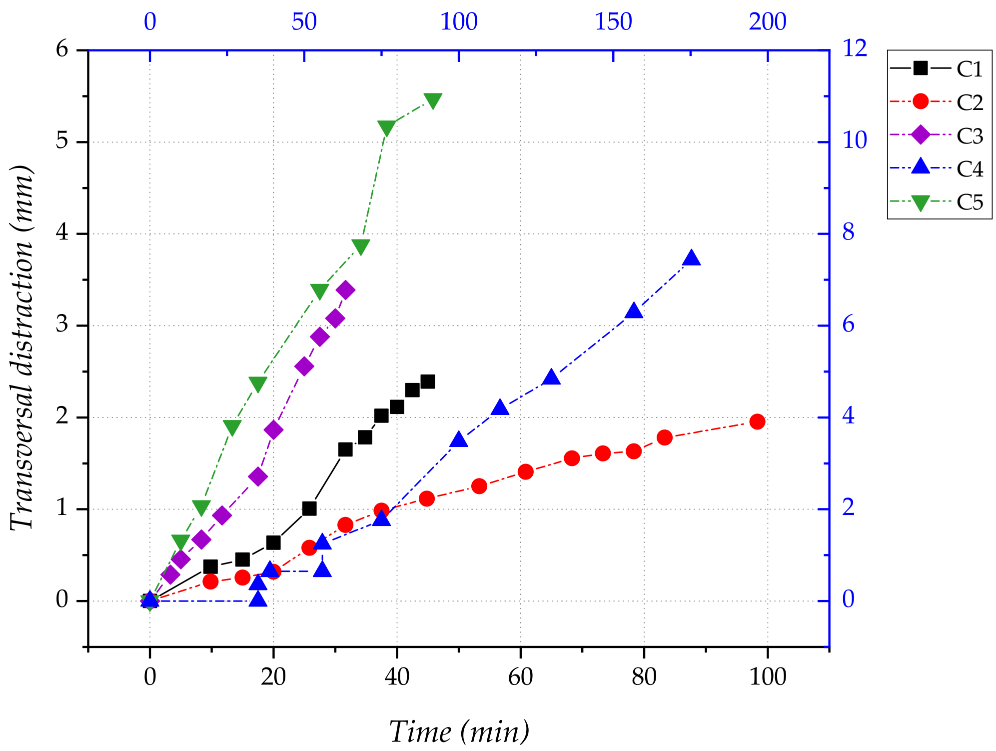

Figure 8.11: Comparison of metopic distraction achieved by different shape-morphing implants.

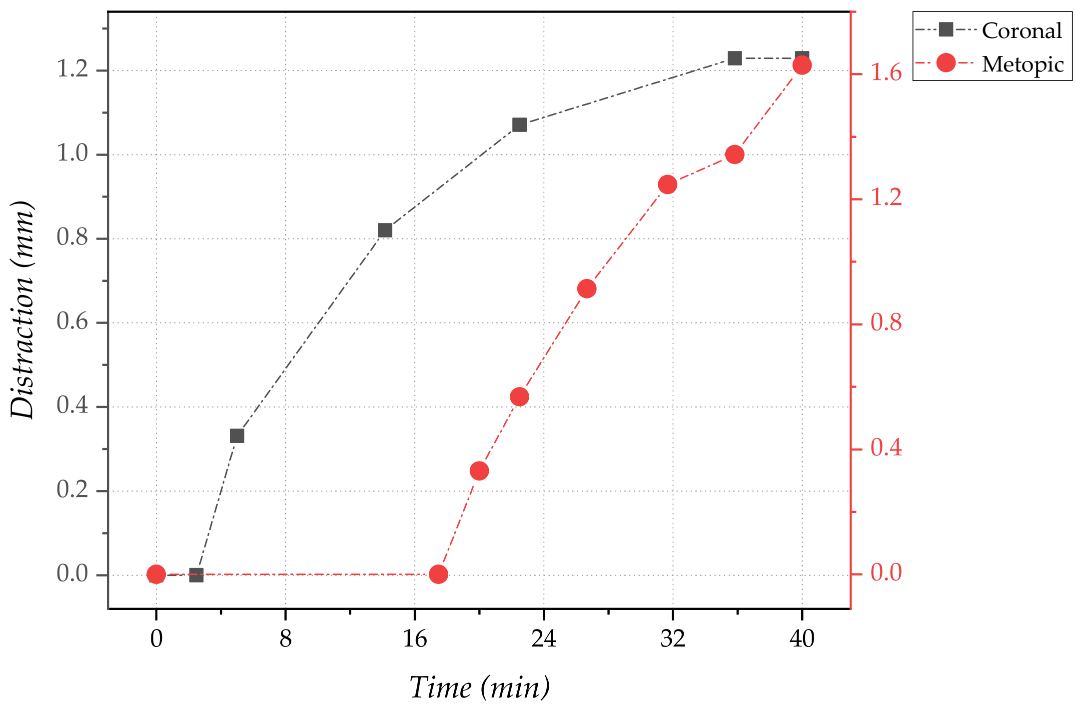

Figure 8.12: Comparison of distraction progression in coronal and metopic sutures.

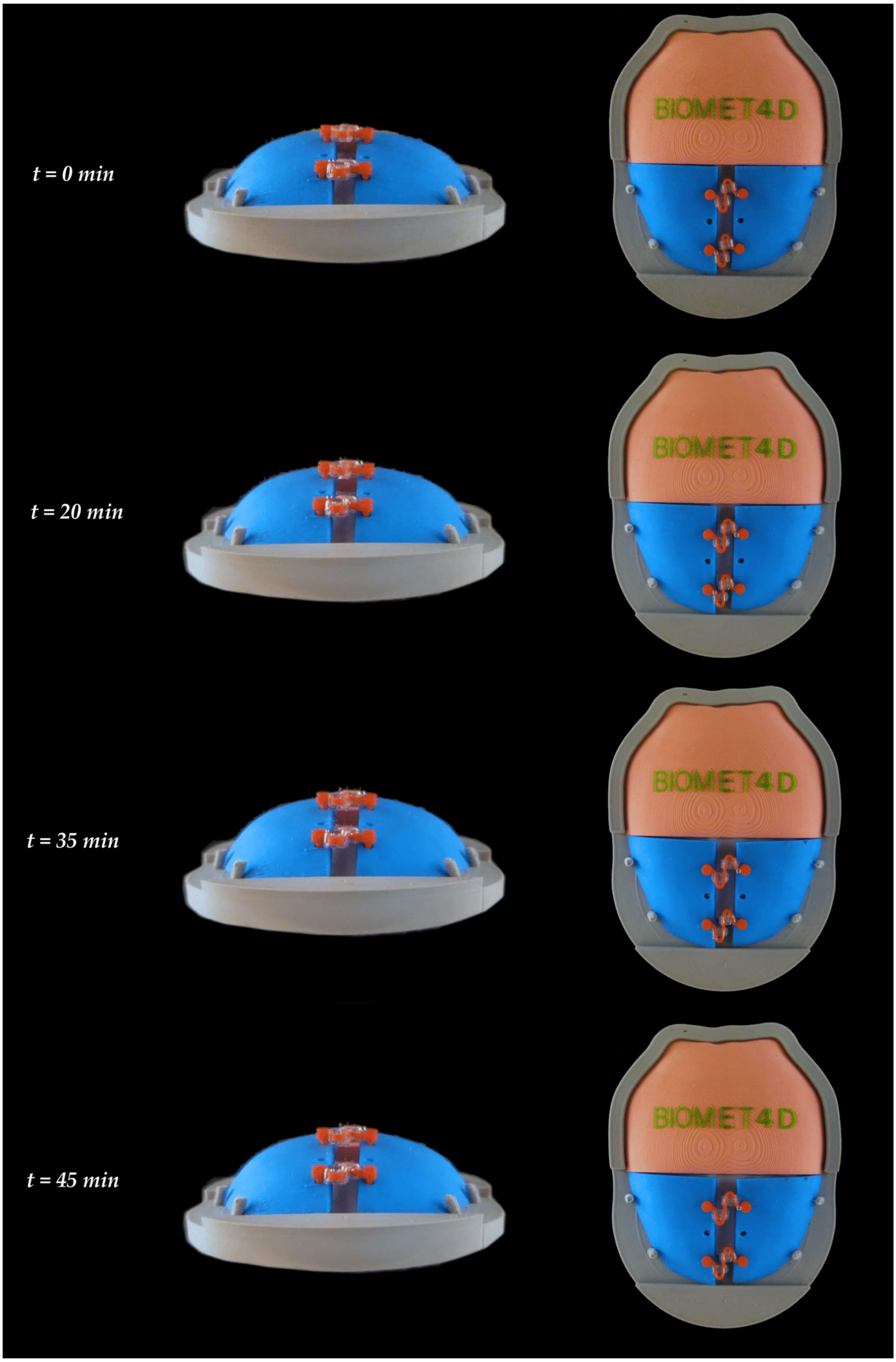

Figure 8.13: Evolution of degradation over time of the shape-morphing implant C1.

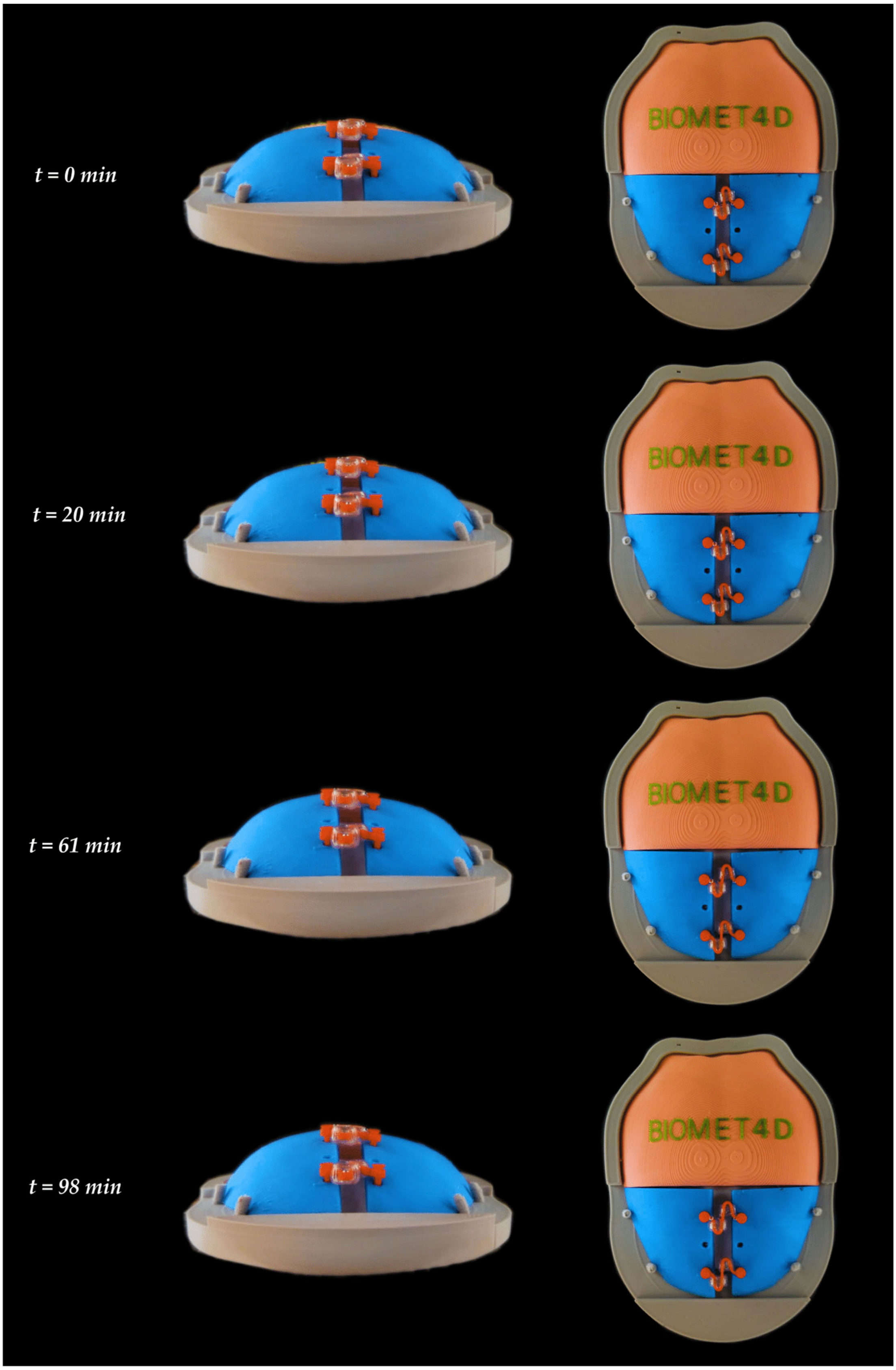

Figure 8.14: Evolution of degradation over time of the shape-morphing implant C2.

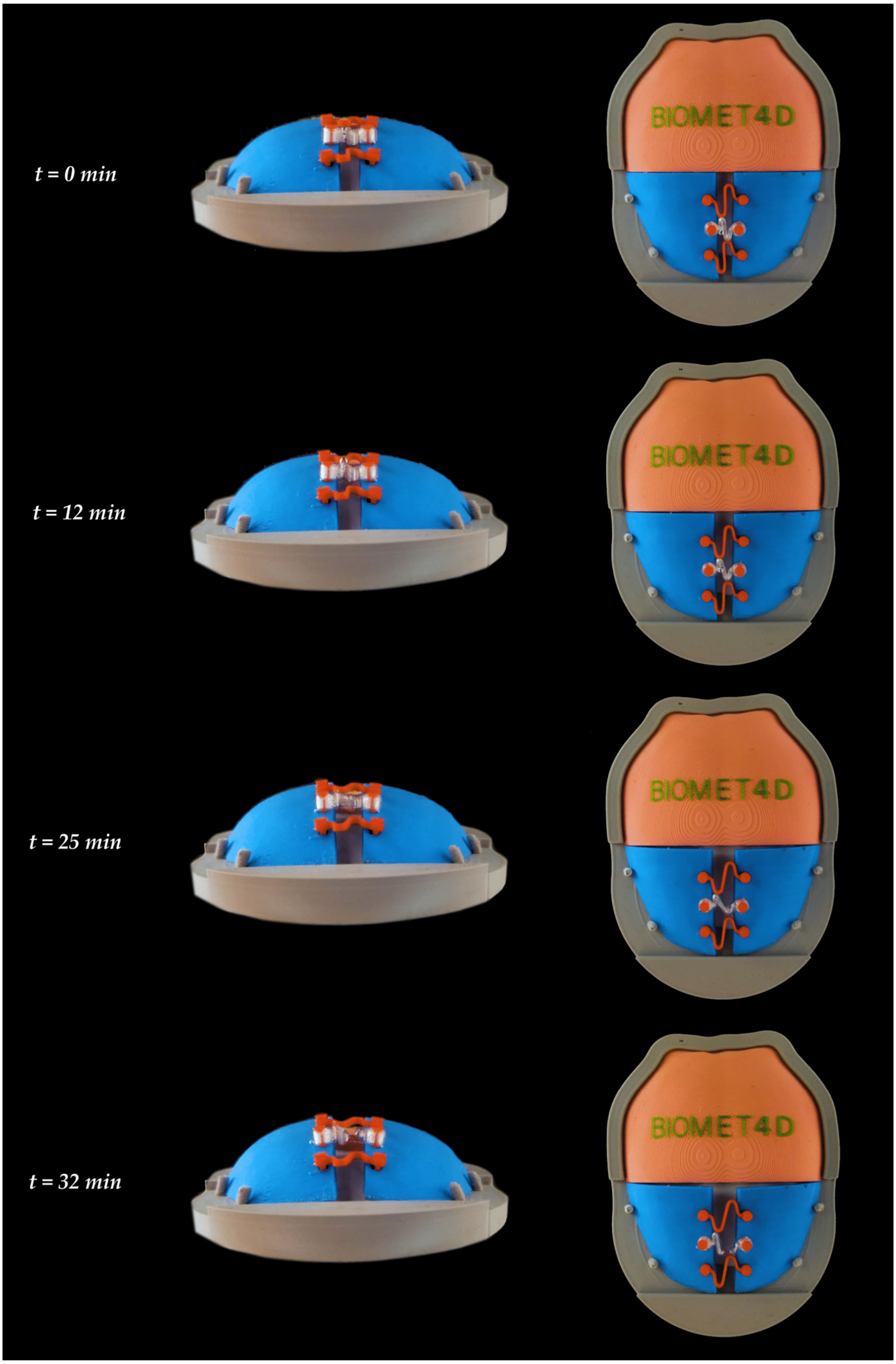

Figure 8.15: Evolution of degradation over time of the shape-morphing implant C3.

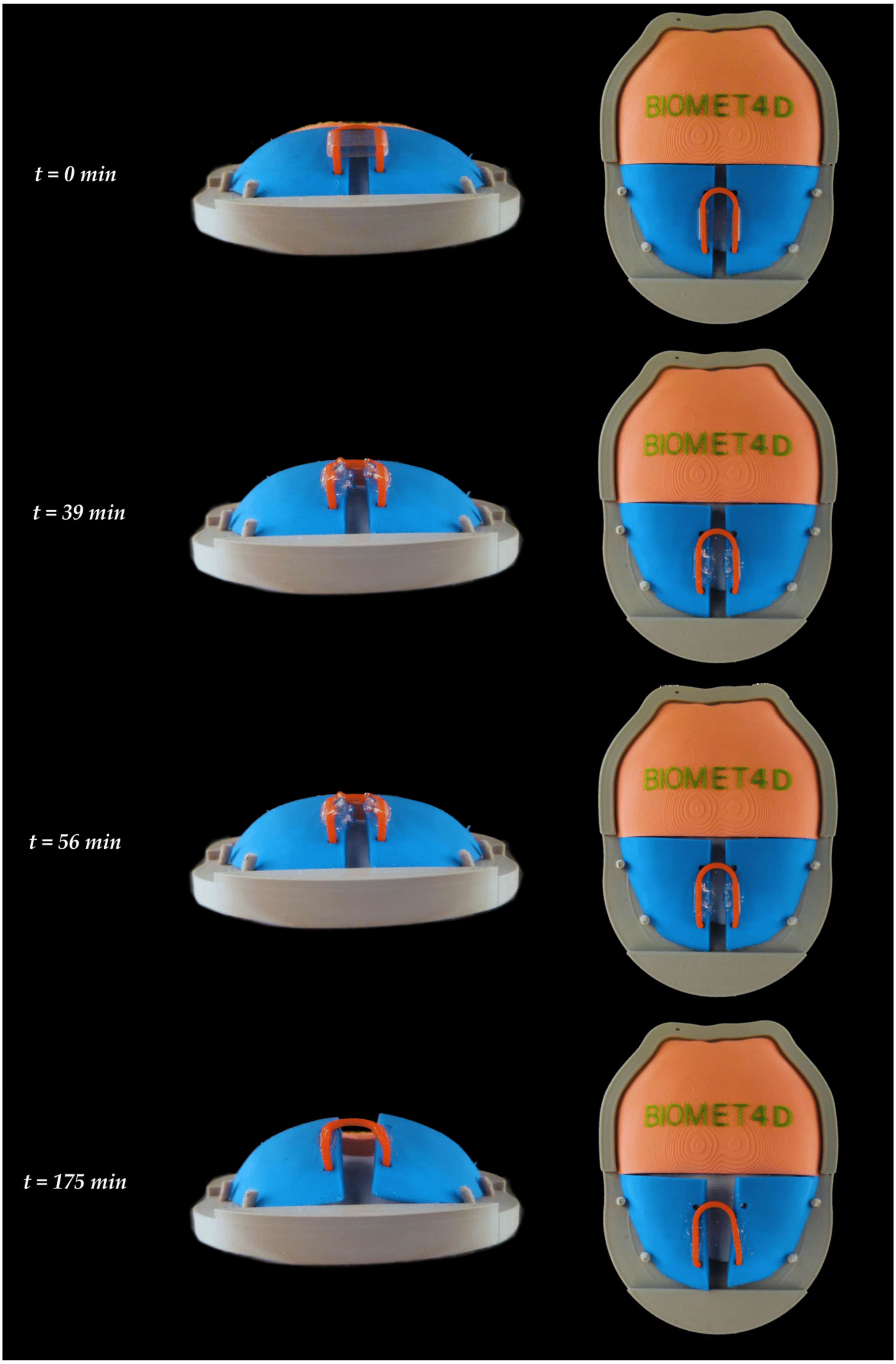

Figure 8.16: Evolution of degradation over time of the shape-morphing implant C4.

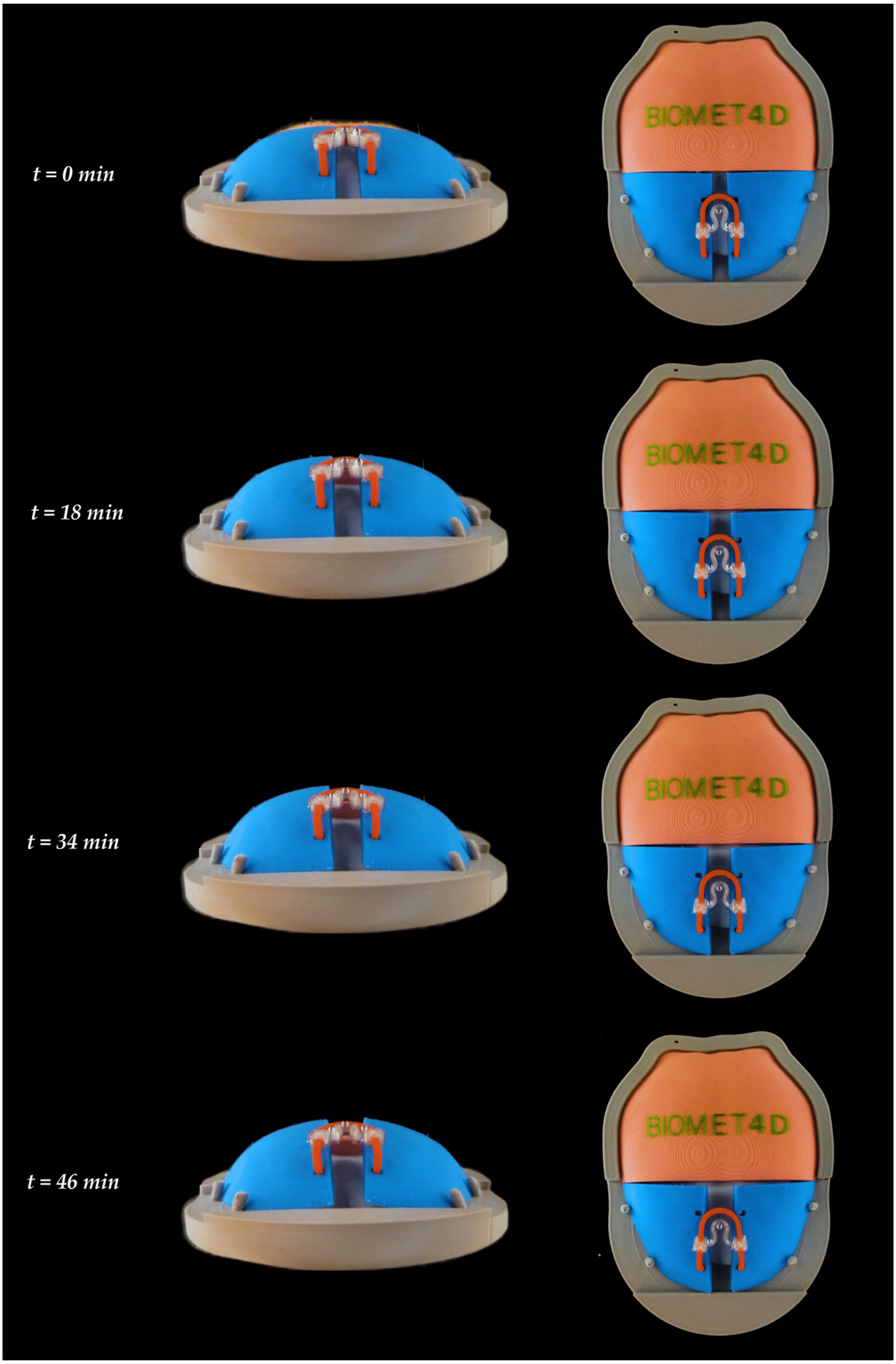

Figure 8.17: Evolution of degradation over time of the shape-morphing implant C5.